THESE

En vue de l'obtention du grade de Docteur,

délivré par

L'Ecole Normale Supérieure de Lyon

Ecole Doctorale N°206

Ecole Doctorale de Chimie (Chime, Procédés, Environnement)

Discipline : Chimie

Soutenance publique prévue le 14/09/2023, par :

Adrien HELLIER

Molecular simulation of the genesis of supported Pt catalytic active phases

Simulation moléculaire de la genèse de la phase active d'un catalyseur platine supporté

Devant le jury composé de :

Corinne LACAZE-DUFAURE, Professeure des universités, Toulouse INP	Rapportrice
Gianfranco PACCHIONI, Professeur, Università di Milano Bicocca	Rapporteur
David LOFFREDA, Directeur de Recherche, ENS de Lyon	Examinateur
Xavier CARRIER, Professeur des universités, Sorbonne Université	Examinateur
Céline CHIZALLET, Ingénieure de recherche - hdr, IFPEN	Examinatrice
Pascal RAYBAUD, Ingénieur de recherche - hdr, IFPEN	Directeur de thèse

Acknowledgements

I would like to take these few lines to thank the people who have been involved in this PhD project.

First, I would like to thank both my supervisors Pascal and Céline for giving me the opportunity to learn at their side during these last three years. I am deeply grateful for your time, advice, corrections, answers, and numerous proofreading whenever I needed them throughout my PhD journey. This work would not have been the same without your continuous help. You both have been great supervisors, scientifically and humanly.

I extend my thanks to the members of the jury, Corinne Dufaure-Lacaze, Gianfranco Pacchioni, David Loffreda and Xavier Carrier who kindly accepted to evaluate this work. A special thanks to Corinne, who gave me a taste for theoretical chemistry back at school, and who has helped me on many occasions in my journey dedicated to the study of this subject.

I conducted this research within the Catalysis, Biocatalysis and Separation direction of IFPEN, and I would like to thank both Luc Nougier, Director of the direction and Emmanuelle Guillon, Chief of the R065 department for providing the opportunity to pursue my PhD in their department. I am grateful to Marie-Claude and Isabelle for their continuous help regarding administrative matters. Additionally, I would like to thank both Christelle Legens and Ana Teresa Fialho Batista for their involvement in the experimental XAS part of this thesis, and I express my gratitude to Yves Joly, for his valuable time and the numerous insights on the calculation of XANES spectra.

I am grateful to my fellow PhD and post-doctoral colleagues who shared the office with me during these three years and who have made some long days more enjoyable. Thanks to Amit, Thomas, Thomas (the old one), Massoud, Adrien, Romain, Alberto, Monika, Nawras, Akif and Celestine. Thanks also to Pierre and Emmanuel who will start their own PhD at IFPEN after I left, I hope you will enjoy it.

Mom et Dad, I would like to express my deepest appreciation for everything you have done for me over the years. I happily thank Romain, Apo and my family for showing genuine curiosity about what I did during these last three years.

Finally, I would like to keep these last words for thanking Lorena, who has been by my side throughout this entire thesis and who has done so much.

Abstract

This thesis aims to explore, through a quantum approach, the evolution of oxychlorinated platinum complexes $PtO_xCl_y(OH)_z(H_2O)_n$ supported on γ-alumina during the activation steps of these catalysts, involving calcination and complete reduction. Experimental observations from the literature reveal that chlorine promotes the existence of isolated platinum atoms after reduction. However, to date, the mechanisms involved remain unknown. Therefore, the objective of this thesis is to improve the understanding of the reactions involved in these steps, as well as the role of chlorine in stabilizing isolated platinum atoms, using density functional theory (DFT).

The study of these unsupported complexes at a high level of theory (RPA) allowed the evaluation of the relevance of various exchange correlation functionals to describe reaction energies of the expected reactions during the activation steps. The stability of the intermediates under preparation conditions was assessed by calculating thermodynamic diagrams and systematically searching for transition states connecting these intermediates. During calcination, three species are predicted according to the chlorine content: PtO_2, $PtOCl_2$, and $PtCl_4$. During reduction, chlorine stabilizes $PtCl_2$ (+II) on a specific alumina site, hardening its reduction by H_2 and which potentially correspond to the observed isolated atomic species. The comparison of experimental XANES spectra with those simulated from DFT models allowed to propose a quantitative description of the species expected after calcination and revealed a specific signature reflecting the amount of chlorine coordinated to platinum.

Résumé

Cette thèse vise à explorer, par une approche quantique, l'évolution de complexes de platine oxychlorés $PtO_xCl_y(OH)_z(H_2O)$ supportés sur alumine gamma durant les étapes d'activation de ces catalyseurs, impliquant calcination et réduction complète. La littérature expérimentale relative à la preparation de ces systèmes révèle que le chlore favorise l'existence d'atomes isolés à l'issue de la réduction. Toutefois, à ce jour, les mécanismes impliqués restent inconnus. L'objectif de cette thèse est donc, grâce à la théorie de la fonctionnelle de la densité (DFT), d'améliorer la compréhension des réactions se déroulant lors de ces étapes, et de déterminer le rôle du chlore concernant la stabilisation d'atomes de platine isolés.

L'étude de ces complexes en l'absence de support à un haut niveau de théorie (RPA) a permis d'évaluer la pertinence des fonctionnelles d'échange et de corrélation choisies pour calculer les énergies des réactions rencontrées durant les étapes d'activation. La stabilité des intermédiaires dans les conditions de préparation a été évaluée par le calcul de diagrammes thermodynamiques et la recherche systématique des états de transition reliant ces intermédiaires. Lors de la calcination, trois espèces sont prédites en fonction de la quantité de chlore : PtO_2, $PtOCl_2$ et $PtCl_4$. Lors de la réduction, le chlore stabilise $PtCl_2$ (+II) sur un site d'alumine particulier. Cette espèce est difficilement réductible par H_2 et pourrait correspondre aux espèces atomiques isolées observées expérimentalement. La comparaison de spectres XANES expérimentaux avec ceux simulés à partir des modèles DFT développés durant cette thèse a permis de proposer une description quantitative des espèces attendues après calcination et de révéler une signature spécifique dans ces spectres traduisant la quantité de chlore coordinée au platine.

Acknowledgements i
Abstract ii
Résumé iii
Introduction 9
Chapter I : ***State of the art*** 15
I.1. Catalytic Reforming 16
I.1.1. Objectives 16
I.1.2. Reactions encountered 16
I.1.3. Bifunctional catalyst 17
I.1.4. Catalysts features 18
I.2. Alumina support 19
I.2.1. General formation and use 19
I.2.2. Surface features 20
I.2.3. DFT studies of alumina 23
I.3. Catalyst preparation 26
I.3.1. Impregnation 26
I.3.2. Drying 27
I.3.3. Calcination 28
I.3.4. Reduction 31
I.4. DFT studies of alumina supported platinum catalysts 34
I.4.1. Metallic Pt nanoclusters under reductive conditions 34
I.4.2. Metallic Pt nanoclusters under oxidative conditions 37
I.5. Conclusions and strategy 41
I.6. References 43
Chapter II : ***Theoretical background*** 49
II.1. Electronic structure calculation 50
II.1.1. Schrödinger equation 50
II.1.2. Variational principle 51
II.2. Density Functional Theory approach 52
II.2.1. Hohenberg and Kohn theorems 53
II.2.2. N-representability 57
II.2.3. Kohn Sham DFT 59
II.2.4. Exchange correlation functionals 61
II.2.5. Dispersion corrections 68
II.3. ACFDT-RPA 70

II.4. Periodic boundary calculations 75
II.4.1. Plane waves 75
II.4.2. Pseudopotential: PAW method 76
II.5. Thermodynamics 79
II.5.1. Vibration calculations 79
II.5.2. Statistical thermodynamics 80
II.6. First order saddle points of the PES 84
II.6.1. CI-NEB 85
II.6.2. Dimer method 88
II.6.3. IRC 90
II.7. X-Ray Adsorption Near Edge Structure 91
II.7.1. Main principle 91
II.7.2. FDMNES 93
II.8. Conclusions 95
II.9. References 96
Chapter III : ***$PtO_xCl_y(OH)_z(H_2O)_n$ Complexes Under Oxidative And Reductive Conditions : Impact of the Level of Theory on Thermodynamic Stabilities*** 101
III.1. Introduction 102
III.2. Computational methods 105
III.3. Results and discussion 107
III.3.1. Platinum complexes 107
III.3.2. Impact of the level of theory on relevant reaction energies 110
III.3.3. Thermodynamic stability 114
III.3.4. Impact of the exchange-correlation functional 118
III.4. Conclusion 120
III.5. References 122
III.6. Supporting information 125
Chapter IV : ***Identification of Platinum Single Atoms on Chlorinated γ-Alumina Support by Density Functional Theory Calculations and X-Ray Adsorption Spectroscopy*** 141
IV.1. Introduction 142
IV.2. Methods 145
IV.2.1. Catalyst preparation 145
IV.2.2. XAS characterization 145
IV.2.3. DFT calculations 146
IV.2.4. Pt complex hydration and OH/Cl exchange reactions under consideration 147
IV.2.5. Thermodynamic stability evaluation 147

IV.2.6. XANES simulations 148
IV.3. Results 149
IV.3.1. XANES experiments 149
IV.3.2. EXAFS experiments 149
IV.3.3. DFT calculations: structural, electronic and energetic trends 152
IV.3.4. Thermodynamics of calcination 161
IV.4. Discussion 164
IV.4.1. Comparison of DFT structures with EXAFS results 164
IV.4.2. Comparison of DFT structures with HERDF-XANES 167
IV.5. Conclusion 169
IV.6. References 172
IV.7. Supporting Information 177
Chapter V : ***Genesis of Alumina Supported Platinum Catalytic Active Phase : Chlorine Induced Stabilization of Platinum Single Atoms During Reduction*** 193
V.1. Introduction 194
V.2. Computational methods 197
V.2.1. Total energy calculation at 0 K 197
V.2.2. Supercell model and platinum species and reactions considered. 197
V.2.3. Thermodynamic corrections 201
V.2.4. Determination of transition states 201
V.3. Results 202
V.3.1. Electronic and Energetic properties of relevant reduction intermediates 202
V.3.2. Thermodynamic aspects of reduction 212
V.3.3. Kinetic aspects of the reduction of Pt complexes 214
V.4. Discussion 229
V.5. Conclusion 234
V.6. References 236
V.7. Supporting Information 240
Conclusion and perspectives 275

Introduction

Catalysts have become an indispensable tool in our society by playing a significant role in numerous industrial applications. Involved in the production of approximately 30% of Europe's gross domestic products and in the processing of 80% of all manufactured products, their importance is undeniable.[1] Heterogeneous catalysts have come a long way since their initial use in Döbereiner's lighter,[2] and their intrinsic properties (easy separation and regeneration, chemical stability, among others…) have made them essential in several industrial processes.[3] Their versatility and effectiveness stem from the considerable attention they have received from the research community as exemplified by several Noble prizes awarded to pioneers in the field, such as P. Sabatier, L. Langmuir and G. Ertl, who further helped set up heterogeneous catalysts as a core area of contemporary science.

Among the plethora of heterogeneous catalysts developed, platinum (Pt) supported on gamma-alumina (γ-Al_2O_3) is of paramount importance as being employed in a wide range of major industrial processes such as refining, petrochemistry, pollution abatement, biomass conversion, plastic recycling, inter alia.[3–9] Pt/γ-Al_2O_3 systems are traditionally prepared through the impregnation of the support with aqueous solution of metallic complexes, followed by a drying step.[10] The catalyst is then exposed to O_2 and high temperatures during the calcination step where changes in the platinum coordination sphere are expected[11]. Finally, the supported complexes are reduced under H_2 at high temperature to obtain the catalyst.[3,9]

In many cases, the Pt/γ-Al_2O_3 catalyst is prepared in combination with dopant elements which are used to boost their activity, selectivity or stability. This is in particular true for the catalytic process of naphtha reforming during which heavy naphtha petroleum cut is transformed into usable high-octane fuel, and where Pt/γ-Al_2O_3 is usually doped with chlorine to increase the acidity of the alumina support and to achieve better dispersion of the metallic phase.[9,12] The use of chlorine in Pt/γ-Al_2O_3 is inherited from the work of Haensel et al.[13] who showed in 1949 that adding chlorine during the preparation of the catalyst led to better catalytic performance with respect to the catalysts used at that time. Moreover, it has been recently shown that chlorine could also promote the stabilization of single atom catalysts (SAC), which are a new type of supported catalysts that could offer new reactivities while maximizing the efficiency of valuable resources.[14] Since this pioneer report, a

considerable amount of work has been dedicated to the tuning of the catalytic active phase to improve the catalysts performance, notably through the addition of co-metals or modification of the support.

Being able to efficiently tune catalyst active phase would enable a more efficient utilization of the noble metals usually used in heterogeneous catalysts. Tailoring the active phase to obtain specific properties can be done during the catalyst preparation. However, this requires a deep understanding of the intricated phenomena which take place during the various preparation steps and such task remains extremely challenging from an experimental point of view.[15] For instance, the mechanisms behind the role of chlorine on the dispersion on Pt remain unknown at the atomic scale.

Ab initio approaches have emerged as valuable tools, notably for rationalizing experimental observations.[15–17] With the evolution in their theoretical framework and computational power it is now possible to study heterogeneous catalysts at an atomic scale. Among the various methods developed, the density functional theory (DFT)[18] has been widely adopted notably due to its interesting accuracy/cost ratio, enabling the study of systems with hundreds of electrons while maintaining good accuracy. Although numerous theoretical studies have been dedicated to the study of Pt/γ-Al_2O_3, most of them have focused on the properties of the catalyst after reduction while the evolution of the metallic precursor during the preparation steps remains less studied.

The objective of the present research work is to gain a comprehensive understanding of the atomic scale mechanisms governing the formation of the platinum active phase on the alumina support. Due to the presence of the chlorine dopant, platinum oxy-chloride precursors will be considered from their state after drying to the formation of reduced Pt(0) upon reduction. The investigation aims to unravel the nature of the intermediates encountered during the formation of Pt(0) as well as their dependence on the preparation steps conditions. Given the experimental importance of chlorine for the Pt/γ-Al_2O_3 systems, a peculiar attention will be devoted to its impact during both preparation steps and on its role on the increase of the platinum single atoms ratio observed after reduction.

To achieve these objectives, it is proposed to investigate through periodical Kohn-Sham DFT[19] calculations the nature of the single atom platinum complexes, supported on the (100)-γ/Al_2O_3 surface, during the calcination and reduction steps. The evolution of the coordination sphere, oxidation degree, preferential adsorption site and relative stability of platinum species will be described as a function of the preparation conditions and precursors nature. The validation of the predicted ab initio model will be done through comparison with experimental X-ray adsorption spectroscopy (XAS) measurements. Finally, a search for key transition steps will be done to unveil the potential kinetic limitations and how they are modified in presence of chlorine.

In the first chapter of this work, the general and fundamental knowledge on the Pt/γ-Al_2O_3 catalyst will be presented through a description of the catalytic reforming. The importance of the γ-Al_2O_3 oxide support will also be briefly discussed in addition to the numerous models used to describe it. The impact of chlorine on the active phase is underlined and the gaps on our understanding of the mechanisms involved during the calcination and reduction steps will be emphasized. A dedicated review of the DFT studies that have been performed on similar systems will be conducted to show the scarcity of studies dedicated to the investigation of the evolution of platinum precursors during the calcination and reduction steps. By highlighting the limited knowledge in this area, it is emphasized the importance and novelty of the proposed research aiming to fill this critical gap in our understanding of the catalyst formation process.

The second chapter is dedicated to the theoretical framework underlying the methodologies employed. Principles of the Kohn-Sham DFT are discussed in addition to details on the exchange-correlation functionals. Technical details related to the use of periodical DFT with a planewave basis set are quickly presented. Some attention is devoted to the description of the adiabatic connection fluctuation dissipation theorem (ACFDT) within the DFT framework and how it allows to express and calculate the correlation energy under the random phase approximation (RPA). Finally, a brief description of the XAS theory and details about the FDMNES[20] software are provided.

In the third chapter, $[Pt(O^{2-})_x(Cl^-)_y(HO^-)_z(H_2O)_n]^0$ complexes are studied in gas phase. The results presented in this chapter have been published in ChemPhysChem in 2023.[21] This study allows to determine the intrinsic properties of the platinum complexes and paves the way for understanding the impact of the support. By taking into account the calcination and reduction operating conditions, a thermodynamic description of the platinum complexes stability under calcination and reduction conditions is proposed. A benchmark of exchange-correlation functionals is done to justify the selection done in this work.

The fourth chapter is dedicated to a study on supported Pt(IV) species during the calcination step. The chapter is structured as a journal paper as we intend to submit it in a near future. The structural and energetical features of the complexes are calculated and compared to the results obtained in chapter III to highlight the impact of the surface. Based on thermodynamic considerations of the calcination step conditions, a description of the expected species depending on the calcination conditions is proposed. The ab initio predicted models are successfully compared to experimental XAS results from the previous PhD work of A-T. Fialho Batista.[22]

In the fifth chapter, the reduction of supported single atom platinum complexes is considered with a focus on the relation between the nature of the platinum species obtain after calcination and the reduction products. Based on the findings regarding the species than can be expected after the calcination, numerous single atom

platinum species with oxidation degrees ranging from IV to 0 are proposed to describe the species that could be present during the reduction under H_2. Their structural and energetical properties are detailed and the impact of the support is highlighted by comparison with results from chapter III. The relative stability of the platinum species during the reduction step as a function of the temperature and H_2 pressure is calculated. Finally, the impact of chlorine on the reduction of key platinum complexes is described from a kinetic point of view, and their free energy profiles are quantified to rationalize the observed increase in the proportion of single atom on the (100) γ-Al_2O_3.

Finally, conclusions drawn from our work and key findings are summarized in the last chapter. On this basis, possible perspectives are proposed in order to go beyond the PhD work's contribution dedicated to the understanding of supported platinum species during their preparation.

References

1. Catlow, C. R., Davidson, M., Hardacre, C. & Hutchings, G. J. Catalysis making the world a better place. *Philosophical transactions. Series A, Mathematical, physical, and engineering sciences* **374** (2016).
2. Batis, H. & Chastrette, M. La catalyse : de Berzelius au Traité de Grignard. *L'act. Chim.* **275** (2004).
3. Ertl, G., Knözinger, H., Schüth, F. & Weitkamp, J. *Handbook of Heterogeneous Catalysis, 2nd ed.,* (Wiley-VCH; Weinhei, 2008).
4. Sattler, J. J. H. B., Ruiz-Martinez, J., Santillan-Jimenez, E. & Weckhuysen, B. M. Catalytic dehydrogenation of light alkanes on metals and metal oxides. *Chem. Rev.* **114,** 10613–10653 (2014).
5. Chen, A. & Holt-Hindle, P. Platinum-based nanostructured materials: synthesis, properties, and applications. *Chem. Rev.* **110,** 3767–3804 (2010).
6. Farrauto, R. J. & Heck, R. M. Catalytic converters: state of the art and perspectives. *Catal. Today* **51,** 351–360 (1999).
7. Zhang, F. *et al.* Polyethylene upcycling to long-chain alkylaromatics by tandem hydrogenolysis/aromatization. *Science* **370,** 437–441 (2020).
8. Huber, G. W., Cortright, R. D. & Dumesic, J. A. Renewable alkanes by aqueous-phase reforming of biomass-derived oxygenates. *Angew. Chem. Int. Ed.* **43,** 1549–1551 (2004).
9. Antos, G. J. & Aitani, A. M. (eds.). *Catalytic naphtha reforming.* 2nd ed. (Marcel Dekker, New York, 2004).
10. Marceau, E., Carrier, X. & Che, M. Impregnation and Drying. In *Synthesis of Solid Catalysts,* edited by K. P. de Jong (Wiley-VCH Verlag GmbH & Co. KGaA, Weinheim, Germany, 2009), pp. 59–82.
11. Lieske, H. Reactions of platinum in oxygen- and hydrogen-treated Pt/gamma-Al2O3 catalysts I. Temperature-programmed reduction, adsorption, and redispersion of platinum. *J. Catal.* **81,** 8–16 (1983).
12. Batista, A. T. F. *et al.* Atomic Scale Insight into the Formation, Size, and Location of Platinum Nanoparticles Supported on γ-Alumina. *ACS Catal.* **10,** 4193–4204 (2020).
13. V. Haensel. *Alumina-Platinum-Halogen Catalyst And Preparation Thereof. U.S. Patent 2,479,109* (1949).
14. Kaiser, S. K., Chen, Z., Faust Akl, D., Mitchell, S. & Pérez-Ramírez, J. Single-Atom Catalysts across the Periodic Table. *Chem. Rev.* **120,** 11703–11809 (2020).
15. Chizallet, C. & Raybaud, P. Density functional theory simulations of complex catalytic materials in reactive environments: beyond the ideal surface at low coverage. *Catal. Sci. Technol.* **4,** 2797–2813 (2014).
16. Chizallet, C. Achievements and Expectations in the Field of Computational Heterogeneous Catalysis in an Innovation Context. *Top. Catal.* **65,** 69–81 (2022).
17. Valero, M. C. & Raybaud, P. Computational chemistry approaches for the preparation of supported catalysts: Progress and challenges. *J. Catal.* **391,** 539–547 (2020).
18. Hohenberg, P. & Kohn, W. Inhomogeneous Electron Gas. *Phys. Rev.* **136,** B864-B871 (1964).
19. Kohn, W. & Sham, L. J. Self-Consistent Equations Including Exchange and Correlation Effects. *Phys. Rev.* **140,** A1133-A1138.
20. Bunău, O., Ramos, A. Y. & Joly, Y. The FDMNES code. *International tables for crystallography - X-ray Absorption* **I** (2021).
21. Hellier, A., Chizallet, C. & Raybaud, P. PtOxCly(OH)z H2O)n Complexes under Oxidative and Reductive Conditions: Impact of the Level of Theory on Thermodynamic Stabilities. *Chemphyschem* **24,** e202200711 (2023).
22. Ana Teresa Fialho Batista. Atomic scale insight into platinum based catalysts supported on chlorinated gamma-alumina. PhD thesis, 2016-2019.

Chapter I

State of the art

I.1. Catalytic Reforming

I.1.1. Objectives

One of the key processes in the petroleum refining and petrochemical industry is the catalytic reforming process which is used in refineries to transform low-octane petroleum cuts into usable high-octane gasoline that are compliant with regulation and technical constraints.[1] These cuts are made of a mixture of linear alkanes with 6 to 12 carbon atoms, cycloalkanes (or naphthene), aromatics and alkenes in some cases. Depending on its composition, the naphtha can be divided into two categories. The straight run (SR) naphtha, (or heavy naphtha) which comes from the atmospheric distillation of crude oil, and the synthetic naphtha which come from another unit (typically FCC or visbreaker) of the refining plant. The proportions of each of these components can vary a lot according to the provenance of the crude oil and/or with the kind of refined products wanted.

I.1.2. Reactions encountered

The set of reactions encountered during the transformation of naphtha requires the use of a bi-functional catalyst combining metallic and acid sites. Relatively harsh conditions are used with temperature of around 500°C and a H_2 pressure, usually between 1 to 10 bars according to the active phase and process, which needs to be carefully considered.

The main wanted reactions during the catalytic reforming are:

- Dehydrocyclization corresponds to a combination of dehydrogenation and cyclization reactions, and it ends up with the highest increasing of research octane number (RON), while H_2 is produced.
- Dehydrogenation occurs on metallic sites of the catalyst. It mainly occurs on naphthene or alkanes, while H_2 is produced.
- Hydroisomerization is the one with the lightest gain in term of RON. First the alkane dehydrogenation occurs on the metallic site, then the isomerization takes place on the acidic sites of the catalyst. H_2 is produced during the alkane dehydrogenation.

The main unwanted reactions during the catalytic reforming are:

- Hydrocracking leads to low RON products. They consist into the breaking of C-C bond, while H_2 is consumed. These short alkanes can still be used in other fields, such as petrochemistry, or even as GPL for the C_1H_4 and C_2H_6.

- Hydrogenolysis: is very similar to hydrocracking, the main difference is the location of the broken C-C bond. In this case, terminal C-C bonds are cut while H_2 is consumed.
- Coking: is responsible for the deactivation of catalyst. Coke is the product of the polymerisation of heavy dehydrogenated compounds. It is favored by a low pressure in H_2.

H_2 is a key species in the encountered reactions, being a product during two of the desired reactions, and reactant in two of the unwanted chemical reactions. One can expect that reducing H_2 pressure to the lowest would be sought. Unfortunately, this hypothetical diminution of $P(H_2)$ will favor coking, which will lead to a decrease of the catalytic performances. A subtle balance is required to favor the desired products, without degrading the catalyst. However, the optimization of these reactions is not limited to the pressure in H_2 used and a major part of the complexity of the system lies on the bifunctional catalysts used.

I.1.3. Bifunctional catalyst

The transformation of naphtha trough catalytic reforming requires the use of bifunctional catalysts. The use of bifunctional catalysts implies that multiple active sites either metallic or acidic are involved in the reactions previously detailed (**Table I-1**).

Reaction	**Active site**
Hydroisomerization	Acid, Metal, Acid + Metal
Dehydrogenation	Metal
Dehydrocyclization	Acid + Metal
Hydrocracking	Acid + Metal
Hydrogenolysis	Metal
Coking	Acid, Metal, Acid + Metal

Table I-1 - Encountered reactions during catalytic reforming and their respective catalytic active sites

Metallic sites catalyze the desired dehydrogenation and hydroisomerization but also favor the unwanted hydrogenolysis and coking of the catalyst. The acidic sites also catalyze the isomerization and are responsible of the catalyst's coking. The intervention of both sites is needed for the dehydrocyclization and hydrocracking. Finally, both the isomerization and coking can also be catalyzed through a combined action of the metallic phase and through both active sites. For a given reaction the mechanisms are not the same according to the involved site.

Moreover, the dehydrocyclization of n-paraffins, which highly increases the RON, requires bifunctional catalysts. the paraffin is dehydrogenated on a metallic site, before getting isomerized and cyclized on acid sites through carbocation intermediates to get a cyclic intermediate which will be dehydrogenated on a metallic site to obtain

an aromatic.[2,3] The use of a bifunctional catalyst in this case allows to accelerate the reaction while obtaining a better selectivity.[2]

The use of bifunctional catalyst for the catalytic reforming allowed Weisz[4] to get higher conversion rate than with the respective mono-functional catalysts. We can note that the use of bifunctional catalysts for the catalytic reforming started before this work of Weisz, and the first patent for the system Pt/γ-Al_2O_3(-Cl) dates back to 1949.[5] Bifunctional catalysts impose spatial constraints on the active phase and involved intermediates. Both sites need to be close enough to avoid diffusional limitation of the intermediates to obtain high-rate conversion. This led Weisz to define the intimacy criterion[4], which is the optimal distance between two active sites allowing to get no diffusional limitations of the intermediates.

I.1.4. Catalysts features

Nowadays, the use of supported platinum with or without co-metal is common in the catalytic reforming industry. Before the use of such catalysts, chromia catalysts were firstly used, but they lead to unsuitable behavior to be used in reforming conditions.[6] Supported catalysts used in today's refining plants for catalytic reforming can be divided into three categories:[1]

- Monometallic platinum supported on chlorine doped γ-Al_2O_3. Those are used in semi-regenerative units.
- Bimetallic platinum-rhenium supported on chlorine doped γ-Al_2O_3. Those are used in semi-regenerative and cyclic units.
- Bimetallic platinum-tin supported on chlorine doped γ-Al_2O_3. Those are used in continuous regenerative units.

The first industrial use of monometallic platinum supported on chlorine doped γ-Al_2O_3 dates back to 1949. Developed by Haensel[5] at UOP, the 'platforming' process used chlorine (or fluorine) to increase the acidity of the support, in combination of small amount of platinum for the metallic function. They were used in semi-regenerative (SR) or fixed-bed units. Those catalysts were extremely sensible to coke, leading to economic loses in such semi-regenerative units, that is why in 1968 rhenium was first added by Chevron.[7] Bimetallic platinum-rhenium supported on chlorine doped γ-Al_2O_3 allows to increase the lifetime of the catalyst by reducing coking and stabilizing the metal phase. The impact of rhenium on the coke formation could be either due to the hydrogenating of the coke,[8] or to the cracking of the coke precursors[9] before they form the coke. The high activity of Re-Pt catalyst in hydrogenolysis, required to do a sulphurisation passivation step to avoid getting to much small hydrocarbons.[1] The Re/Pt ratio can be tuned to promote new behavior, and increasing the quantity

of rhenium allows to get a more effective catalyst for heavy cuts, by producing more aromatics while being more resistant to coke, which allow lower operating pressures[10]. Another widespread bimetallic industrial catalyst is Pt/Sn supported on chlorine-doped γ-Al_2O_3. It is used in continuous regenerative units where the addition of tin is responsible for multiscale effects on the catalyst. It decreases the deactivation rate of the catalyst while increasing its resistance to agglomeration, which is needed in continuous regenerative units. From a chemical point of view, the tin allows to obtain, among other properties, a better selectivity due to the reduction of the activity of the highly acidic site of the support which are responsible of the cracking reactions. At the same time, tin does not interfere with the less acid sites which are needed for the desired reactions of dehydrocyclization and isomerization.

I.2. Alumina support

Al_2O_3 (or aluminum oxide) is a material used in vast number of domains such as electronics, optics, biomedicine, mechanical engineering and catalysis[11]. γ-Al_2O_3 is the most used polymorph as a support for metallic catalysts, in particular in refining, because of its high surface area, thermal stability and acid-basic properties. While being used for decades, the structure of γ-Al_2O_3 is still highly debated[12].

I.2.1. General formation and use

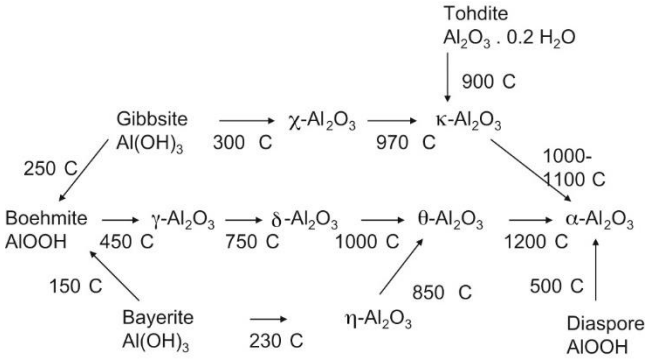

Figure I-1 - Main transformations of alumina polymorphs. Taken from[13]

γ-Al_2O_3 is a metastable polymorph of alumina obtained during the dehydration of boehmite into the high temperature stable α-Al_2O_3 polymorph (**Figure I-1**). The crystal structure of the γ-Al_2O_3 was investigated by Lippens and de Boer[14] who considered it to be a cubic defective spinel. The defective character comes from the fact that only one cation is present in the Al_2O_3 stoichiometry (compared to AB_2X_4, where A and B are cations, and X is the anion) and so vacancies are expected among the cations with the general formula given by $\square Al_8O_{12}$ with □ being the vacancy. The oxygen anions are in a cubic close packed arrangement, while the A^{2+} and B^{3+}

cations usually occupy tetrahedral (T_d) and octahedral (O_h) sites. If A^{2+} occupies T_d and B^{3+} occupies the O_h site the structure is referred as normal spinel, if this is the other way, then it is an inverted spinel, and finally if the cations occupy sites independently of their nature this is a random spinel. As cations are missing in the Al_2O_3 stoichiometry (compared to the spinel) the vacancies can be either T_d or O_h sites but to this date, the nature of the vacancies sites are not known. However, the spinel nature of the γ-Al_2O_3 is not a certitude and XRD analysis showed that part of the Al cations may occupy non-spinel sites[15–18].

The uncertainties regarding the crystal arrangement of the γ-Al_2O_3 are also present in quantum simulations where many models exist. Ferreira et al.[19] considered a spinel model while other authors such as Krokidis et al.[18] or Paglia et al.[17] proposed a non-spinel type model to describe γ-Al_2O_3. To build the atomic model of γ-Al_2O_3, Krokidis et al.[18] considered that the transformation of the boehmite into γ-Al_2O_3 occurred in two steps. First a transfer of protons accompanied by the removal of water in the boehmite occur though the collapsing of the structure, then aluminum atoms migrate from octahedral sites to tetrahedral ones to form the γ-Al_2O_3 arrangement [18]. Hydrogen spinel with protons occupying the cationic vacancies was also considered by Sohlberg et al.[20] but this model was then refuted[16].

I.2.2. Surface features

I.2.2.a) Morphology

As the morphological properties of γ-Al_2O_3 are determined by the boehmite due to the topotactical nature of the transformation, many boehmite materials with different properties were developed leading to various γ-Al_2O_3. For example, high surface area γ-Al_2O_3 can be obtained by calcination of nanocrystalline (pseudo)boehmite. In that case, the γ-Al_2O_3 will mainly exhibit a rhombic, lamellar, fibrous or block morphology inherited from the precursor as observed by TEM. As an example, the preparation of boehmite by precipitation of soluble aluminum salts (UOP process) will give rise to fibrous plate-like structure (**Figure I-2**) while the Ziegler (or ALFOL) process tend to produce bulky boehmites.[13]

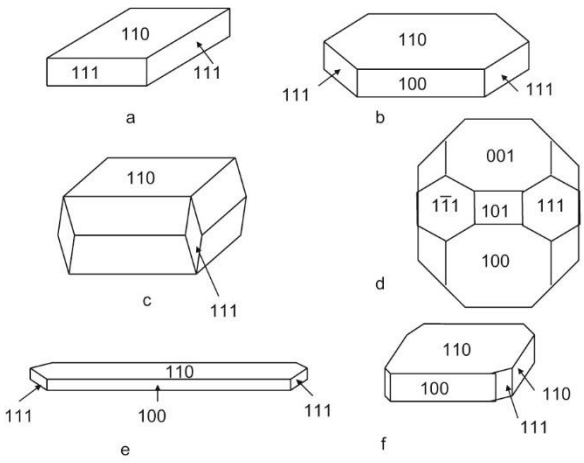

Figure I-2 - Main γ-Al_2O_3 nanocrystals morphologies[13]. A) rhombic crystal b) lamellar crystal c) bulkier particle d) cubo-octahedral crystal e) fibrous f) platelet model

The rhombohedral boehmite is one of the most commonly formed, for this morphology the predominant face is the basal one (010). Experimentally, the (110) surface was found to be the most exposed one and accounts for around 70% of the total surface, while the (100) and (111) surface share the remaining 30% according to Nortier et al.[21] who used electron microscopy. By using neutron diffraction analysis, Beaufils and Barbaux.[22] found that the (110) surface represented 83% of the total surface and the remaining 17% were attributed to the (100) surface. Similar results on the facets exposition were found by Digne et al.[23,24] by using Krokidis' models.

I.2.2.b) Surface hydroxyls

Adsorbed water on the surface can be found as undissociated coordinated H_2O but also as dissociated hydroxyls. These hydroxyls are observed by IR analysis and as the corresponding spectra are highly dependent of the environment these vibrations are a way to characterize the oxides and to get important information on the nature of the surface sites. In the case of γ-Al_2O_3, seven OH bands are expected above 3000 cm^{-1} [25]. Many models have been developed in order to understand the IR spectrum of γ-Al_2O_3.

The first one was developed by Peri[26], who used the dried (100) surface of a defective spinel bulk and made a relation between $\nu(OH)$ and the number of surrounding oxygen ions. This first model is limited by the fact that only the (100) surface is considered. This model was considered as a good one until the seventies.

Then, Tsyganenko and Filimov[27] developed a model by considering a spinel like model for the bulk and the (100) and (111) surfaces. In their analysis they concluded that the different vibrations are due to the different number of metallic atoms in the coordinative sphere of the oxygens. This analysis leads to an explanation for three of the five observed frequencies (at this time, only 5 frequencies were expected above 3000 cm^{-1}), the two

remaining ones were attributed to the effect of the different coordination sphere of the bonding atoms. In the same vein of work (considering the coordination sphere of atoms) Morterra et al.[28] considered the coordination sphere of the Al cations but this description even if good for α-Al_2O_3 was not adapted the transitions alumina.

Knözinger and Ratnasamy[29] developed a model by considering (110), (100) and (111) surface of a defective spinel structure. They explained the difference of vibration by considering the net formal charges of the hydroxyl groups. This model was one of the most used for a long time. They assumed that no reconstruction or migration of ion could happen during the dehydration of boehmite. The net charge is determined by the charge of the OH group and the charge of the linked Al. They established that the highest frequencies correspond to the most negative charges, or in other words, to the most basic hydroxyls. The model has some drawbacks such as the fact that no reconstruction of the surface was considered, moreover no cation vacancies are taken into account and finally no edges or high index planes are considered. A similar approach was proposed by Tsyganenko and Mardilovich.[30]

Busca et al.[31] pushed the Knözinger and Ratnasamy model further by considering different spinel structure (normal, inverse, defective) to take into account the cationic vacancies of the defective spinel and the impact of the coordinative sphere of the aluminum bonded to the hydroxyl group. These considerations induce small differences with the Knözinger and Ratnasamy model.

Later on, Digne et al.[23,24] revisited this assignment by means of DFT calculations as explained in section I.2.3.

I.2.2.c) Chlorination effects

As presented in the previous section, the chlorination of the alumina support is influential in catalytic reforming to enhance its acidity or to redisperse platinum. Various mechanisms, with different chlorinating agent were studied to describe the chlorination of the γ-Al_2O_3.

For the chemisorption of gaseous HCl, two main reactions were invoked.[32–34] The first one involves the exchange of HCl with a surface hydroxyl leading to the formation of water (by eliminating a surface hydroxyl) and the formation of an Al-Cl bond. The other one occurs in absence of an existing hydroxyl, HCl dissociates on the surface to form a μ_1 hydroxyl and Al-Cl. Both were considered after experimental evidence that the chlorination by gaseous HCl leads to a diminution of some hydroxyls' bands and the apparition of a new band around 3500 cm^{-1}. It was observed that the most basic OH are the first to be exchanged.[32,35] No HCl band was observed by infrared (IR) spectroscopy.[33,34] Tanaka[34] observed that the newly formed (OH) are more ionic than the already

existing one without chlorine, and they explained it by the heterolytic dissociation of HCl which give rise to long range interactions between the chlorine atom and the hydrogen of the newly formed adjacent hydroxyl.

The adsorption of gaseous Cl_2 at different temperatures was considered by Marczewski et al.[36] and on a dry γ-Al_2O_3, the amount of chlorine on the surface increase with the temperature. As for the HCl agent, they observed by IR examination a diminution of the OH bands for frequencies between 3700 and 3800 cm^{-1}. On the basis of these observations, they conclude that the adsorption of gaseous Cl_2 could occur through the exchange of two surface hydroxyls by chlorine and the formation of a hypochlorite surface group and water. Based on chemical observations, they proposed that the complexation of chlorine into OCl_2 was a possibility. They also note that in contrary of the chlorination by HCl which leads to the formation of Brønsted acid sites[34], Cl_2 chlorination creates both Brönsted and Lewis acid centers at low temperature but only Lewis acid sites at high temperature. Other vectors of chlorination for the alumina can be considered such as CCl_4 or $AlCl_3$.[36]

I.2.3. DFT studies of alumina

I.2.3.a) Morphology

Using the non-spinel γ-Al_2O_3 bulk proposed by Krokidis et al.[18], Digne et al.[23,24] constructed three relevant surface models ((100), (110) and (111)) by cleaving the bulk and relaxing the obtained surfaces. They studied the surface state under realistic conditions and were able to determine different hydration states according to the temperature and water pressure for the different facets.

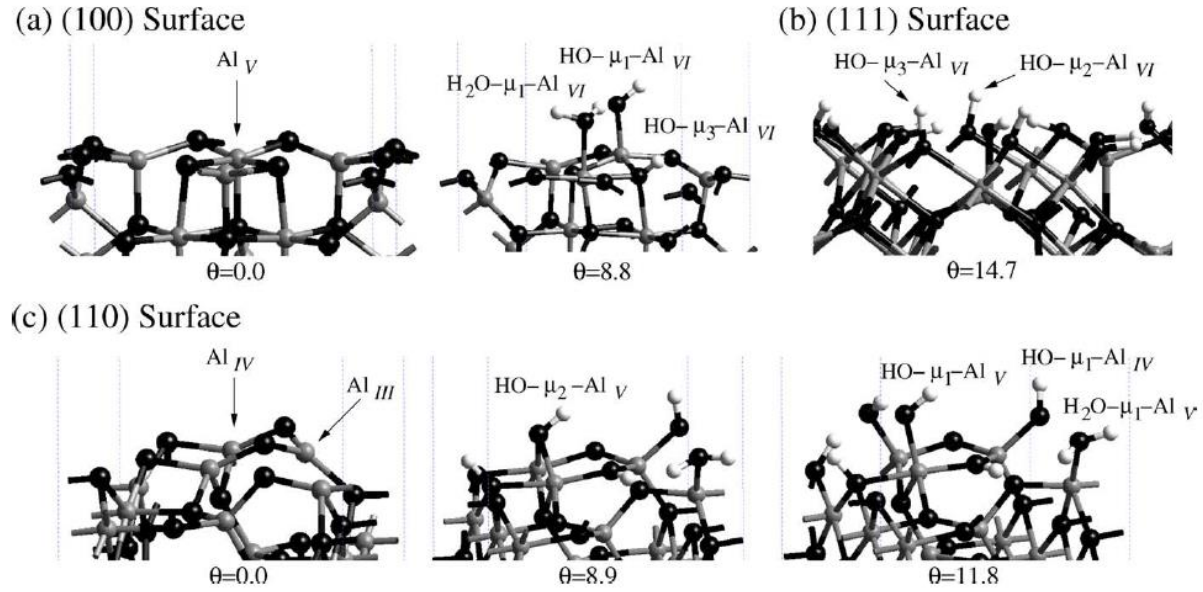

Figure I-3 - Atomistic models for the (100) (a), (110) (c) and (111) (b) γ-Al_2O_3 surface for various hydration rate (exprimed in (OH)/nm²). The various coordinations of the aluminum atoms are indicated. Taken from ref.[24]

The dehydrated (100) surface exhibits octahedral Al_V and tetrahedral Al_{IV}, while the dehydrated (110) surface presents Al_{IV} in octahedral and tetrahedral positions, but also Al_{III} in tetrahedral positions (**Figure I-3**). The presence of under coordinated Al_{III} on the (110) surface with a strong Lewis acid character is responsible for the difference of hydration energy between the two surfaces.[23] While the (100) surface was calculated as dehydrated for temperature above 600 K, thermodynamic calculations showed that the full dehydration of the (110) surface is supposed to occur around 1150 K, a temperature for which the metastable γ-Al_2O_3 is supposed to become α-Al_2O_3. The (111) surface was not found stable if dehydrated, even for simulation temperature as high as 1200 K. It was found that this last surface was more stable if fully hydrated until 800 K.[24] Latter on, Wischert et al.[37] proposed a competing model for the (110) surface exhibiting local reconstruction of Al_{IV} site. More recently Pigeon et al.[38] revisited all the alumina surfaces by considering the topotactic transformation of boehmite slabs, which reveals a new model for the (110) surface located on the basal plane of alumina, exhibiting numerous isolated μ_2-OH groups compatible with NMR experiments.

Following a proposal made by Busca[39], atomistic models of alumina edges were constructed by Batista et al.[40] Based on a nano-rod structure the (110)-(100) edge was simulated (**Figure I-4**), such a model induces two possible terminations: aluminum (bright blue edge in **Figure I-4**) and oxygen (dark blue edge in **Figure I-4**). This methodology was transposed recently[41] for the construction of models of the $(110)_b$-(100) and $(110)_l$-$(110)_b$ edges, where $(110)_b$ and $(110)_l$ stand for basal and lateral versions of the (110) surface, differentiated since the work of Pigeon et al.[38] The hydroxyl groups present at the $(110)_b$ surface and at the edges appeared to be key in the assignment of the 1D and 2D ^{1}H proton NMR spectra of various γ-Al_2O_3 samples.[40,41]

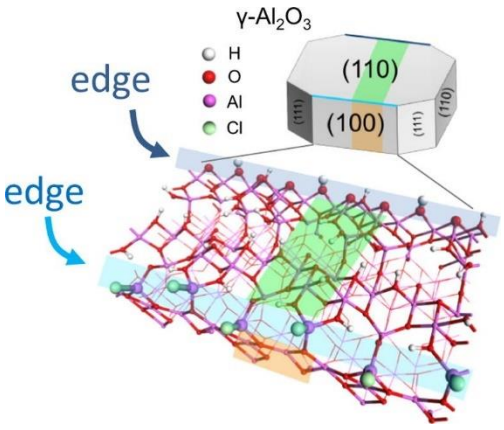

Figure I-4 - Chlorinated and hydroxylated edge model constructed from the (100) and (110) surfaces of Digne et al.[23] The edge in the front (light blue) correspond to aluminum sites baring chlorine atoms, while the edge in the back (dark blue) is made of oxygen and hydroxyls.

Digne et al.[23,24] used their models of the γ-Al_2O_3 to make a density functional theory (DFT) study (PW91 GGA functional) of the infra-red hydroxyls for the (100), (110) and (111) surfaces (**Figure I-3**). In their study they found that hydroxyl coverage of the surface was dependent of the temperature and water pressure, and at 500 K, the predicted hydroxyl coverage for the different surface are: θ_{110}=11.8, θ_{100}=8.8 and θ_{111}=14.7 OH.nm^{-2}. They found, as in the model of Knözinger, that OH frequencies were impacted by the aluminum in the coordinative sphere of the corresponding oxygen, but they differ in the attribution of some bands. Indeed, the highest stretching (calculated at 3842 cm^{-1} with DFT[23], against 3785-3800 cm^{-1} observed experimentally) is attributed to a μ_1-Al_{IV} of the (110) surface while Knözinger predicted that an Al_{VI} was implicated. Digne's model was able to highlight the impact of the surface orientation on the OH frequencies showing the impact of the boehmite precursor in the IR signature of the γ-Al_2O_3. The anharmonicity of the potential was corrected by using a value provided by a previous work on boehmite hydroxyls[42] also inspired by calculations on zeolites. One has to keep in mind that the hydroxylated surfaces are subject to interactions due to the H-bonding network and whose effect are not very well reproduced at the level of calculation used.

I.2.3.b) Chlorination

Chlorination of γ-Al_2O_3 was also studied at the DFT-GGA level by Digne et al.[35] on the previously detailed models. For all the considered surfaces (100), (110) and (111), the substitution of OH by Cl is mainly endothermic at low chlorine coverage. This is particularly true for the OH-μ_2 and OH-μ_3 groups while the OH-μ_1 sites are slightly more prone to be exchanged by giving isoenergetic reaction at 0K (**Figure I-3**). In any cases, the presence of hydrogen bonds tends to destabilize the chlorine exchange, and the highly hydroxylated surface (111) exhibits the most endothermic energies for the substitution of OH by chlorine. This DFT study, coupled

with an IR analysis allowed them to deduce from the disappearance of bands located at 3794 and 3775 cm^{-1} (measured experimentally) that at the very low chlorine content (~1 Cl nm^{-2}) the most labile OH (OH-μ_1 on (110) and (100) surfaces) are the first to be exchanged. It can be noted that at this low chlorine coverage, the exchange of the OH-μ_2 and OH-μ_3 is not observed by IR. The impact of the chlorination of the surface on the μ_2 and μ_3 vibrations is also treated. By replacing one OH-μ_1 by chlorine, the hydrogen bonds of the remaining hydroxyl groups are weakened, leading to a broadening of their bands. Higher chlorine contents were considered for the (110) surface, and destabilization is expected at high chlorine coverage due to electronic repulsion between chlorine atoms. Batista et al.[40,41] extended the study of the substitution of hydroxyl groups for chlorines on alumina edge models. They found that μ_1-OH from the edge are more prone to be exchanged by chlorine than the ones on the surfaces. This was confirmed by ^{1}H NMR spectroscopy, with the selective decay of a 0 ppm signal upon increase of the chlorine loading. This 0 ppm signal was simultaneously attributed to isolated μ_1-OH at the edge thanks to the DFT models.

I.3. Catalyst preparation

The preparation steps of the catalyst are of paramount importance to obtain the desired properties. One can tune the acidity of the support's surfaces and both the dispersion and reduction states of the catalyst during these steps. As it was explained before, there is a thin line between wanted and unwanted reactions encountered during catalytic reforming, that is why the understanding of the mechanisms at work during the genesis of the active phase is primordial. Three main objectives are aimed during the preparation of industrial reforming catalyst, first the support should have the desired mechanical properties and porosity, secondly a highly dispersed state for the platinum is expected, and finally the acid sites need to be at the right strength. The preparation of the previously described catalysts can be divided into four steps: the impregnation step, the drying step, the calcination step and finally the reduction step.

I.3.1. Impregnation

The impregnation of monometallic platinum catalyst is usually done with precursors such as hexachloroplatinic acid (H_2PtCl_6) if chlorine is wanted in the system, or platinum nitrate $Pt(NH_3)_4(NO_3)_2$ otherwise. Usually, a diffusional impregnation is used to prepare the monometallic platinum catalyst even though this is a relatively slow method (few hours are needed to ensure a good distribution of Pt). During the diffusional impregnation, the dry alumina is first saturated with water, or hydrochloric acid, and then immersed in an aqueous solution containing H_2PtCl_6 which diffuses to the center of the support's pores.[1,43]

The alumina support being an oxide support, complicated reactions involving charged interfaces, surface hydroxyls or pH effects need to be considered and multiple models were built in order to describe the adsorption of chlorinated platinum precursors during impregnation.[1] Because of the presence of hydroxyls at the oxide surface this last can be charged differently with the pH of the solution. This charge comes from the surface hydroxyls which can be gradually protonated with H^+ available in the solution. That effect leads to the definition of the point of zero charge (PZC), which defines the pH corresponding to a neutral surface, for the alumina PZC ∈ [8;9]. We can also retain that the oxide surface acts as a buffer in a solution, leading to changes in the pH solution and hence different surface state. This last effect was showed using the mass titration technique which consists in the addition of oxide solids in a solution whose pH is being monitored.[44]

Mass titration technique can be used to determine the PZC. The principle is the following: once being in contact with a solution at a different pH than the oxide's PZC, protons from the solution are adsorbed (or released from the support if pH_{sol} > PZC) on the surface which leads to a change of the solution's pH. This driving force exists as long as charged hydroxyls are present on the oxide. The process is repeated until a plateau is reached, at this point the solution's pH gives the PZC. Hence, if present in sufficient amount, an oxide will act as a buffer on the pH of the bulk immersive solution. This buffering effect on the pH leading to the fact that different pH can co-exist at the surface and in the solution is extremely important.

Indeed, the precursor can exchange up to two chlorines for hydroxyls or water ligands depending on the pH.[45] This makes the description of the impregnation more complex, as each of these species is supposed to interact differently with the oxide surface.[46,47]

During the impregnation, even in presence of H_2PtCl_6 precursors, HCl is added to obtain a uniform distribution of Pt on the support. Two hypotheses exist to explain that phenomenon, the first one describes the Cl^- anion as a competitor to $PtCl_6^{2-}$ during its adsorption on the surface leading to a deeper diffusion into the pore and by extension a more uniform deposition of the platinum.[48] Another hypothesis is that Cl^- does not act as a competitor, but instead reduces the adsorption equilibrium constant leading again to a more uniform deposition by allowing the platinum to visit the deepest pores of the support.[46]

I.3.2. Drying

A drying step is used to eliminate the aqueous solution from the pores, and usually follow the impregnation step. The drying step is also suspected to be involved in the grafting of the platinum species to the surface. EXAFS study showed the coordination sphere of the platinum after drying was $PtCl_4(O\{H\})_2$,[49] with the uncertainty regarding the protonation level of the oxygens being due to the EXAFS method. The suspected

process of this grafting involves the exchange of Cl of the coordinative shell for OH on the alumina surface, which could be deprotonated later. This hypothesis is based on the decrease of the ^{195}NMR (Nuclear Magnetic Resonance) signal intensity after this drying step. This was interpreted by Shelimov et al.[50] as the fact that the adsorption of platinum on the surface leads to lower symmetry and higher chemical shift anisotropy for the Pt complexes which became not detectable by NMR. The conditions of drying are highly impactful on the state of the anchored platinum. For soft drying conditions (20°C and under vacuum), it is suspected that Cl^- does not form covalent bond with Al^{3+} of the surface, but instead are in electrostatic interaction with protonated group (OH_2^+) of the surface giving rise to a reversible phenomenon, and the not grafted species could be reobtained after rewetting the dried solid.[49] Under harsher conditions (90°C), the drying step leads to irreversible changes and rewetting does not restore the species post-impregnation. Treating the sample with an HCl solution is expected to changes the coordination of the platinum and leads to the formation of $[PtCl_6]^{2-}$.[49]

The becoming of the exchanged Cl depends on the drying conditions. For soft drying, it is expected that the chlorine stays on the surface by being electrostatically linked to a protonated hydroxyl of the surface.[49] In the case where harsher conditions are used, the removing of Cl was suggested to happen with the formation of HCl[47] but later studies[49] show that no HCl can be evidenced, and that the Cl/Al molar ratio was only slightly affected by the drying under 90°C. The authors conclude[49] that the chlorine takes the place of a surface hydroxyl bonded to an aluminum.

I.3.3. Calcination

The drying step is usually followed by calcination under dry air, typically between 500 and 600 °C. During it, platinum is expected to be mainly under the form of oxidized single atoms (SA), but if the platinum loading is high enough, dimers and trimers can appear.[51,52] Slightly bigger weakly cohesive clusters (up to pentamer) were also observed by Batista et al.[53] if the platinum loading was high enough to saturate all available surface site. Batista et al.[53] analyzed by HR-HAADF-STEM two different samples after calcination, at distinct platinum loading (0.3% and 1%). Pt_n clusters with n<5 were only visible for the 1% Pt sample. (**Figure I-5**). No impact of chlorine loading on the clustering in the oxide state was observed and similar results were found for other platinum loading and oxidizing conditions by Dessal et al.[54] and Bradley et al.[55] who also observed dimers and trimers in absence of chlorine. The presence of single atoms for the low loading of platinum is also supported by a comparison done by Batista during her PhD thesis[56] between XANES spectra obtained from both experiments and ab initio simulations. However, as they emphasized it, the species considered for the calculation of the XANES spectra are chlorine free, while Batista et al.[53] observed by EXAFS that chlorine is in close vicinity of the platinum.

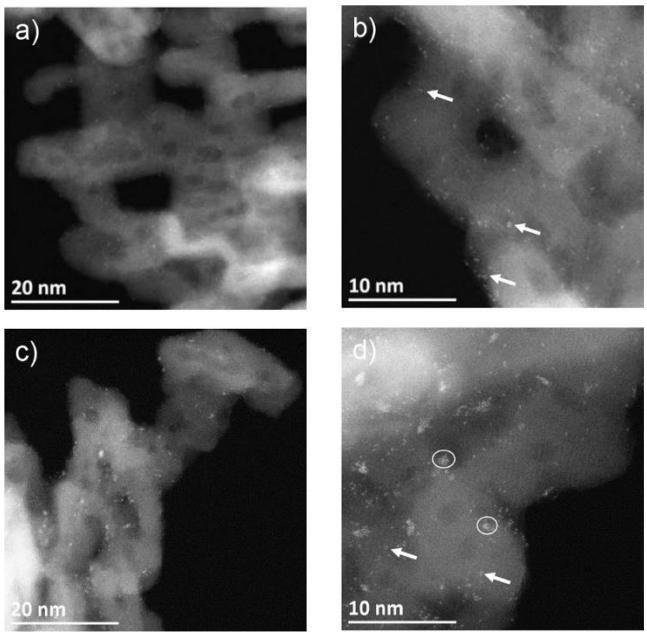

Figure I-5 - HR-HAADF-STEM image of oxide catalysts for 0.3%wt Pt (a,b) and 1%wt Pt(c,d) for 1.3%wt Cl. Arrows highlight single atoms and circles show clusters[53]

The impact of the support on the highly dispersed state of platinum was studied by Bradley et al.[55] thanks to HAADF-STEM. They used three oxide supports: γ-Al_2O_3, TiO_2 and SiO_2 on which they adsorbed platinum. After calcination, they observed that more clusters have been formed on SiO_2 than on γ-Al_2O_3 and even more than on TiO_2. This ranking can be explained by the strength of the Pt-support and ligand-support bonds. On TiO_2 the complex is more strongly anchored and hence aggregation into clusters is limited. This same phenomena was observed by Lee et al.[57], with the clustering of oxidized platinum during calcination occurring on supports having weak interactions with platinum such as SiO_2. However, despite the nature of the surface, this clustering was also observed when the platinum loading was too high (between 5 and 10%). The support might also be impactful on the speciation of platinum during calcination. This was proposed by Lambert et al.[58] who found that the self-reduction of chlorinated Pt(IV) into Pt(II) and then Pt(0) through the releases of Cl_2 was possible only on SiO_2 and not on Al_2O_3 due to the nature of the interaction between chlorine and the support. The formation of the volatile $PtCl_2$ was used to explain the formation of large crystallites upon reduction as no redispersion was observed during this last step.

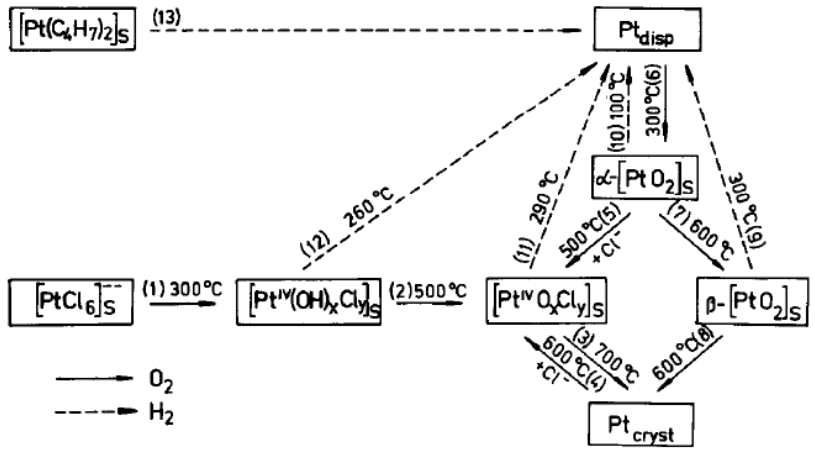

Figure I-6 - Reaction pathways of supported Pt species under O_2 (full arrow) and H_2 (dashed arrows). +Cl indicates reaction with chloride. Taken from ref[59]

Experimental studies have been devoted to the nature of the species and their evolution during calcination. Lieske et al.[59] and Lietz et al.[60] suggested through a combined Temperature Programmed Reduction (TPR) and UV analysis that grafted platinum atoms are expected to form neutral $Pt(IV)Cl_x(OH)_y$, $Pt(IV)Cl_xO_z$, β-PtO_2 or α-PtO_2 depending on both the precursors and conditions of calcination (**Figure I-6**). The first two species were observed after being treated under O_2 at temperatures between 300°C and 600°C. The distinction between the hydroxylated and oxo species was based on the different reduction temperatures and different UV-vis spectra[60]. In the absence of chlorine, the oxidation of the previously dried sample gives α-PtO_2 which can then be transformed in the chlorinated form of the complexes with a HCl treatment. The work of Batista et al.[53] corroborates the presence of $PtCl_x(O\{H\})_y$ after calcination in presence of chlorine through EXAFS analysis. In the cases where the platinum was found to be well isolated and that no Pt-Pt bond was observed (0.3% Pt loading), the chlorine loading changes the coordination sphere of the supported platinum on γ-Al_2O_3, replacing oxo (or hydroxy) ligands for chlorine. They considered two loading in chlorine, for the lower one (0.3% wt Cl), they fitted an EXAFS model to a platinum with 5 oxygens and one Cl as neighbors, while for the high loading in chlorine (1.4%wt Cl), they observed changes in the platinum's coordination sphere with 3 chlore and 3 oxygens in close proximity to the Pt. In both cases, the platinum was expected to be octahedral and chlorinated, even with very few chlorines available in the system. The presence of oxychlorinated complexes after calcination in presence of chlorine is also supported by older work from Berdala et al.[61] or more recently by Gracia et al.[62] and Svintsitskiy et al.[63]

A summary of Batista et al. [53] EXAFS results is displayed **Table I-2** and compared to the works of Berdala et al.[64] and Gracia et al.[62] who also studied by EXAFS similar complexes after calcination but with different conditions.

	Gracia et al.[62]			Berdala et al.[61]				Batista et al.[53]			
Catalyst	1.5% Pt/Al_2O_3	1.5% Pt/Al_2O_3 - 2.1%Cl		0.3%Pt/Al_2O_3-2.2%Cl		1.5%Pt/Al_2O_3-2.1%Cl		1%Pt/Al_2O_3-1.4%Cl		0.3%Pt/Al_2O_3-1.4%Cl	
Calcination temperature	250 °C	300°C		530 °C				520 °C			
Path	Pt-O	Pt-O	Pt-Cl	Pt-O	Pt-Cl	Pt-O	Pt-Cl	Pt-O	Pt-Cl	Pt-O	Pt-Cl
R(Å)	2.06	2.03	2.31	2.04	2.34	2.03	2.32	2.00	2.31	2.00	2.31
CN	5.9	3.5	2.5	5.5	1.7	5.5	1.7	3.8	2.2	3.3	2.7

Table I-2 - EXAFS results for Pt/Al_2O_3(-Cl) samples calcinated with various conditions (CN = coordination number)

Oxidative atmosphere can also be used to redisperse the platinum after sintering of the catalyst.[59,62,65–69] During these oxychlorination steps, the presence of chlorine, which can be added through a HCl treatment is necessary to redisperse the Pt. This redispersion is accompanied by an increase of the Pt oxidation state[59] which is associated with the formation of $PtCl_xO_y$ species (**Figure I-6**). The formation of these oxychlorinated species was supposed to be necessary to achieve the Pt redispersion.[59] In the case of re-oxidation of reduced platinum without chlorine in the system, the Pt-Pt distances observed by EXAFS are the same than in the reduced state, showing the necessity of the presence of chlorine in the catalyst for the redispersion.[62] However, the nature of the chlorinating agent is not important. For catalysts calcinated from chlorine free precursor, the same behaviour than for chlorinated precursors was observed after treating them with HCl during the oxychlorination step. In that case, the same redispersion was observed than the one expected with chlorinated precursors[59,62] By studying oxychlorination of sintered platinum catalyst on γ-Al_2O_3 Galisteo et al.[70] found that the diameter of the sintered systems has an impact on the redispersion and that , the redispersion was better for the smaller clusters.

By using ^{27}Al MAS NMR, Kwak et al.[71,72] showed that in the oxide state, Pt (assumed to be PtO, although this is strongly questionable) are mainly bonded to Al_V abundantly present on the (100) alumina surface but no chlorine was considered in their study. The form and location of chlorine atoms during the oxidation is still not established, but the hypothesis that the chlorine stays on the surface is supported by the observed regeneration of chlorinated Pt(IV) after multiple cycles of oxidation/reduction without the need of add chlorine in the system.[59]

I.3.4. Reduction

After the calcination step, follows the reduction. This step takes place under a reductive agent such as H_2 at temperature between 500 to 550°C and induces a change of the Pt oxidation states from Pt(IV) or Pt(II) species to Pt(0). Simultaneously, the sintering of the isolated Pt atoms is expected to happen during this step, leading to

the formation of dispersed Pt(0) cluster of about 0.9 nm in diameter[53,73] that can coexist with Pt single atoms [52,53]. The ratio SA/cluster is increased by high chlorine loading[56,74]. If no chlorine is in the system, the presence of SA is not a certitude. Dessal et al.[54] only observed small cluster after reduction at 300 K while Bradley et al.[55] argue from HAADF-STEM evidences that SA, dimers and 0.6-1nm NP coexist on Al_2O_3.

The formation of clusters is favored by the use of high temperatures and reductive atmosphere such as H_2. For a low loading in Pt (0.35%wt Pt) formation of cluster is expected to start around 350°C and is followed by gradual growth in cluster size for temperature up to 700°C.[73] The dispersion of the platinum over the alumina surface during the reduction is impacted by multiple factors such as the support, the loading in chlorine and platinum, and the nature of the anchoring sites. Lee et al.[75] used different alumina supports with various BET surface areas to show that the dispersion of the platinum increases with the number of anchoring sites available and start decreasing as soon as the amount of platinum exceeds an intrinsic threshold relative to the support. The impact of the Pt dispersion and morphology dependence on the number of anchoring site is supported by other works.[51,72]

Clusters of various shapes and sizes were observed experimentally. For Pt loading lower or equal to 1% Pt, the majority of the clusters are expected to be comprised between 0.6 and 1.2 nm[53,73–75]. For higher loading in platinum, bigger clusters are observed because of the saturation of the available anchoring sites on the support[53,75]. Experimental analysis such as STEM[55,73] reveals that clusters are mainly flat bi-planar. Borges et al.[76] showed that in absence of chlorine flatter NP were observed. The coordination number of the cluster's platinum is usually found to be around 4 and 8 both for chlorinated[62,64,77,78] and unchlorinated supports[62,64,79,80]. A few other works, such as the ones of Sinkler et al.[73] or Batista et al.[53] found a lower coordination: Sinkler et al.[73] found a CN of 3.3 for such systems supported on chlorinated γ-Al_2O_3. Batista et al.[53], for two loading in platinum (0.3% and 1%) at 1.4% chlorine loading, reported respectively a CN of 3 and 3.2.

The doping of the support by Cl has an impact on the interaction between the support and the cluster. By depleting electronically the oxygen of the support, chlorines allows platinum atoms to be more strongly bonded to the support[81]. The higher the amount of chlorine is, the higher the proportion of single atoms platinum is according to Batista et al.[53,74]. They also observed that for the highest chlorine loading they considered (1.4%) the SA population becomes independent to the platinum loading. This resistance against sintering but also against reduction was observed by Svintsitskiy et al.[63]. In their work, they observed by XRD and TEM that in case of unchlorinated sample, heating at 250°C under H_2 was responsible of sintering into particles of averaged size of 1.3 nm, while this size could reach 3 nm at 600°C. These results are corroborated by XPS analysis which reveals the presence of metallic clusters, $Pt(OH)_2$ and/or PtO for the unchlorinated sample under H_2 at 250°C. In the other hand, chlorinated samples were more resilient to this phenomenon and no metallic patterns could be

observed by XRD even at 600°C under H_2 and the average NP's size was 0.9nm. Moreover, chlorinated species were more resilient against reduction and only a very small amount of Pt(0) with a dispersed character is observed by the authors through XPS analysis. EXAFS analysis made by the same authors tends to corroborate the previously described behaviours, even though they highlighted the missing existence of reference XANES spectra for chlorinated species and the difficulties to assign some of these spectra. This lack of relevant models is a strong motivation for the present work.

EXAFS observations about the presence of Pt-Cl bond after reduction are not unanimous. While Batista et al.[53] and Gracia et al.[62] found that under H_2 at temperature of 300°C and 500°C respectively no Pt-Cl bonds can be observed, for slightly lower reduction temperature under H_2 (250°C) Svinsitskiy et al.[63] found that the number of Pt-Cl bond was around 1.5. One has to keep in mind that the absence of Pt-Cl bond detected by EXAFS (which provides an average value over the whole sample) could be also the result of a too low number of Pt-Cl instead of a real impossibility to make Pt-Cl bond after reduction. Based on XPS, Smolikov et al.[82] proposed that oxidized platinum (+II) with Pt-Cl bonds might resist to the reduction process. Based on time-of-flight secondary ion mass spectrometry, Zhou et al.[83] also argued that chlorine might stay bounded to the platinum during the reduction but also after the use of the catalyst for reactions such heptane reforming. This is also in line with the hypothesis of Marceau et al.[84,85] on the fact that chlorine might be present on the post-reduction platinum. In this case, the hypothesis is based on a decrease of activity in oxidation reaction for catalysts prepared from chlorinated precursors.

The impact of chlorine on platinum is not universal and depends on the support as highlighted by the work of Radivojevic et al.[86] who observed that the sintering of chlorinated platinum species ($PtCl_x$) was easier than the sintering of PtO_x if supported on SiO_2. On SiO_2 more dispersed NPs were observed for the chlorine free systems unlike what is observed on γ-Al_2O_3. Huizinga et al.[87] also showed that the nature of the support impacts the stability of the complexes during reduction, but they also made a link between the calcination conditions and the reduction. The decomposition of PtO_2 (obtained from chlorine free precursors) was easier on TiO_2 or SiO_2 rather than on γ-Al_2O_3 where it was found stable until 750 K which is 100 K above the stability of bulk PtO_2. Simultaneously, they found that by doing calcinations at higher temperatures, the platinum complexes were reduced at lower temperature and that more H_2 was consumed during the reduction.

All the γ-Al_2O_3 surfaces are not equivalent, each surface or edge may show different surface Al and O(H) sites with various coordination numbers leading to a change in the adsorption strength. The various faces also exhibit different hydration degrees for same conditions which again modify the surface chemistry and so one can expect to have preferred anchoring sites for the platinum. Kovarik et al.[88] studied high loading platinum ($5\%_{w/w}$) on unchlorinated γ-Al_2O_3 and found that the preferred sites of the NPs are the (110) and (111) surfaces. It

should be noted that such a high loading in platinum is not representative of a population of highly dispersed Pt atoms, but it corresponds rather to large clusters. Batista et al.[53] used smaller Pt loadings (0.3%$_{w/w}$ and 1%$_{w/w}$) which are more relevant of the case of reforming, and they observed that the majority of nanoparticles (70%) is mostly located on the edges of the crystallites or on other edge-like defaults. The higher concentration of Cl atoms in close vicinity of edges as shown by ^{1}H NMR and DFT[40], was invoked to justify such preference. The location of single atoms was not evaluated as they are below the resolution attainable in electron tomography of such samples.

I.4. DFT studies of alumina supported platinum catalysts

Numerous ab initio calculations, usually at the DFT level, were performed to rationalize some of the experimentally observed and previously described phenomena for various oxide supported metal. Indeed, ab initio calculations provide atomic scale information that can be combined to statistical models, to model desired systems under realistic conditions. These results can also be used symbiotically with experimental methods such as IR, RMN or XANES to gain knowledge on the catalysts at an atomistic scale. Due to the catalyst targeted in the present work, we focus in the present bibliographic section exclusively on previous DFT studies dealing with alumina supported platinum clusters (of various sizes).However, as it will be shown, we immediately noticed that there is a lack of DFT studies addressing the numerous challenges of the catalytic preparation (discussed in the previous section) as this observation was also made in a recent perspective article by Corral-Valero and Raybaud.[11] For that reason, we focus in what follows on the DFT studies which were devoted to the behaviours of metallic Pt clusters (of various sizes) either under reductive conditions or under oxidative ones.

I.4.1. Metallic Pt nanoclusters under reductive conditions

Earlier DFT models of metallic Pt_{13} were constructed by Hu et al.[89] on two alumina surface models developed by Digne et al.[23,24] to compare with the observed geometries by STEM[55,73]. The dehydrated (100) surface and the (110) hydrated one at 8.9 OH/nm² were used as surface models for the alumina support. The type of the surface was found to be able to modify the stable morphology of the Pt_{13}. Two layers bi-planar cluster were the most stable on the (100) surface while 3D spherical clusters were favored on the hydrated (110) surface (**Figure I-7**). In the bi-planar case, the stabilization of the cluster results from the formation of Pt-O and Pt-Al bonds through which the surface atoms are electronically depleted at the profit of the cluster which becomes anionic. On the hydrated surface, such bonds with the support are not possible due to the OH blocking the interaction of the platinum atoms with Al and O sites of the alumina network, and thus the cluster is bonded to the oxygen atoms

of the hydroxyls. These weaker bonds could be responsible for the fact that the supported cluster has a similar structure as the one found in gas phase[90]. Similar conclusions on the relation between the hydroxylation level of the surface and the geometry of the cluster were deduced by Erfani et al.[91] on bigger clusters (22 and 44 Pt). They observed a change on the geometry, going from a 3D cluster in case of lowly interacting cluster to a bi-planar one in case of strong interactions cluster/support and back again to a 3D geometry if the hydroxylation of the surface exceeds a specific threshold.

The question of the migration of surface groups such as OH and H was also investigated by Hu et al.[89] They showed that OH spillover is not possible for thermodynamic reasons, while the H transfer was possible and responsible for the depletion of the electronic charge of the cluster, making it cationic. These results of charge transfers are in agreement with other DFT works done on smaller cluster (Pt_6).[92]

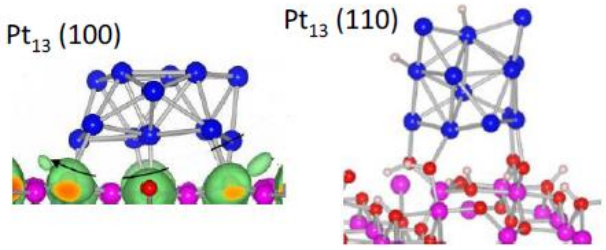

Figure I-7 - Most stable Pt cluster morphology on the dry (100) and hydrated (110) γ-Al_2O_3 surfaces

The effect of H2 pressure in the reductive environment was also studied by Mager-Maury et al.[93] They focused on the impact of H_2 on the reconstruction of the Pt_{13} clusters. On the dehydrated (100) γ-Al_2O_3 surface they found that a reconstruction into a cuboctahedral morphology occurs (**Figure I-8**, **a)** into **b)**) if enough hydrogens are adsorbed on the cluster (more than 18 hydrogens). The hydrogen spillover was found to be accompanied of a partial loss of the metallic nature of the cluster and a weaker interaction with the support. At high H coverage, all the platinum sites are occupied by a hydrogen (hydride in nature), and at this point the cluster is not expected to be chemisorbed.

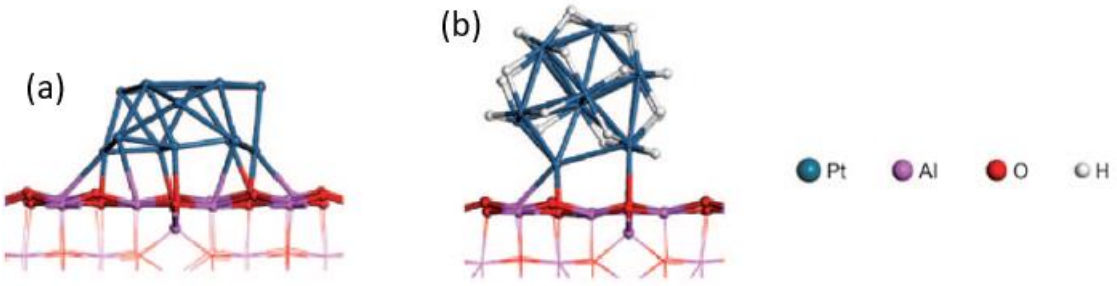

Figure I-8 - Most stable Pt_{13} according to the ratio H/Pt[93]. Calculations are done on the (100) γ-Al_2O_3 surface.

The work of Gorczyca et al.[94] illustrates how DFT models can help for the interpretation of experimental XAS analysis. They used Ab Initio Molecular Dynamic (AIMD) to determine the most stable geometries for various H_2 coverage. The discrimination of the various optimized morphologies was done after comparison with experimental XAS spectra. On the (100) surface, Pt_{13} remained biplanar even for 18 hydrogens, while on (110), a 3D morphology is observed even though it is strongly distorted compared to the case without hydrogen. They found that hydrogen pressure was more impactful on the hydrogen coverage than the temperature. This work highlights the symbiotic behavior between XANES analysis and DFT models in the description of Pt nanostructures at an atomic level. The combination of XANES experiments and FDMNES[95,96] simulations of XANES for various DFT model was able to reveal the presence of H adsorbed on the Pt cluster. Also, the combination of Inelastic Neutron Scattering (INS) experiments with INS simulations made on DFT models further confirmed the adsorption and reconstruction of H atoms on Pt clusters.[97]

Smaller systems were also considered by Mager-Maury et al.[98] who studied by DFT the stability of $Pt_{1<n<5}$ and Pt_{13} clusters in presence of chlorine atoms and on various alumina surface models. The possible stabilization of these smaller clusters was considered through ligands migration phenomenon. Both the dehydrated (100) and hydrated (110) surfaces at different coverages were considered as support for the complexes. At this point, we can note that they consider that the (100) surface could not be chlorinated due to the absence of surface hydroxyl to make the exchange with HCl. As they considered various size of clusters, they analyzed the sintering process and found out that this process is mainly driven by the stabilization of the Pt_{13} particle over the small ones. Without migration of protons, hydroxyls or chlorines, small clusters are stabilized by the high amount of chlorine on the (110) surface. In case of proton's migration, the level of chlorination has an impact of the relative stability of the species. If no chlorine is present, the H migration is globally stabilizing, however if the surface is chlorinated then the migration of proton is destabilizing, especially for Pt_1. The migration of chlorine atoms and hydroxyls onto the platinum clusters leads to different results. While the migration of OH stabilizes Pt_2 and Pt_3 but destabilizes all the others, the migration of one chlorine is always stabilizing independently of the number of Pt. They used this argument, and especially the fact that in presence of chlorine Pt_3 is observed as a local minimum to explain the ability of chlorine to limit the sintering of metallic Pt during reductions done in presence of Cl. This question of the role of Cl on the stabilization of Pt species during the catalyst's preparation will be at the core of the present work.

The impact of the type of surface on the stabilization of smaller clusters on the support was also observed by Liu et al.[99] who studied the growth of small clusters ($Pt_{1<n<4}$) on the γ-Al_2O_3 and found that sintering is easier on gas phase than on the (110) γ-Al_2O_3 surface. Similarly, Mei et al.[71] studied the role of the Al_V during the sintering on the dehydrated (100) surface. They found that the formation of a dimer was unfavorable, but if dimer was

formed, then the sintering process become thermodynamically favored. The formation of dimers from monomers is not only thermodynamically unfavored but also kinetically due to the strong interaction with Al_V. These results are also valid for PtO.[71]

The location of the clusters on the γ-Al_2O_3 platelet was analyzed by Mager-Maury et al.[98]. Both the dehydrated (100) and the hydrated (110) (11.8 OH/nm²) surfaces are similar in term of adsorption of the Pt_{13} cluster. The binding energies were calculated at -397 kJ/mol for the (100) surface and -416 kJ/mol for the (110) surface. More recently, Batista et al.[53] found that these values are close to the ones obtained for the adsorption of the Pt_{13} on the edge-like model of γ-Al_2O_3. For the Al-side of the hydrated (110)-(100) edge (**Figure I-4**), a binding energy of -409 kJ/mol, and -404 kJ/mol were calculated on the same side but saturated with chlorine. The other edge side (O-side) gives very similar binding energy (-403 kJ/mol). Different exchange correlation functionals were used for the two works, and Batista et al.[53] considered a correction for the long range interaction while Mager-Maury et al.[98] did not, even though the results are similar and they show that edges are as stabilizing as the surfaces for Pt_{13}.

I.4.2. Metallic Pt nanoclusters under oxidative conditions

The impact of an oxidative atmosphere was studied at a DFT level on the previously presented Pt_{13} clusters by Sangnier et al.[100]. They studied the behavior of metallic Pt clusters made of 13 atoms supported on the dehydrated (100) γ-Al_2O_3 surface of Digne et al.[23,42] during the adsorption of O_2. By using DFT they were able to define the most stable site for the adsorption of dissociated O_2 and observed the symbiotic behavior of the support and the cluster during the adsorption of O_2 as the most stable cases were found for the oxygen atoms which act as bridges (**Figure I-9**). They found out that the bridging mode remains the most stabilizing adsorption mode for oxygens and that the two-layer like structure was stable up to 12 oxygen. $Pt_{13}O_{14}$ and $Pt_{13}O_{16}$ appear to be the intermediate case for the transition into a hemispheric geometry which become the most stable structure up to $Pt_{13}O_{26}$. For larger oxygen loadings, the disintegration of this hemisphere starts, and adsorption of undissociated O_2 is observed. The adsorption of O_2 is always stabilizing although the adsorption energy ranges from -130 kJ/mol for the first O_2 to around -80 kJ/mol for 16th O_2 molecule. The stability of these clusters is evaluated for different conditions of temperature and O_2 pressure and shows the high capacity of Pt_{13} to be oxidized by O_2 even at high temperatures (**Figure I-9**). Their study was done on the dehydrated (100) surface of Digne et al.[23,24] and considers that the surface stayed dehydrated for the wide range of investigated temperatures.

Similarly to what was previously presented for the supported Pt_{13}, the support also impacts the geometry of smaller entities such as Pt_2O_4. The role of surface on the geometries of oxidized species is highlighted by comparing the work of Xu et al.[101] who studied by AIMD, among other species, the gas phase Pt_2O_4 while Dessal et al.[54] studied similar, but supported, species which exhibits strong deformation upon adsorption.

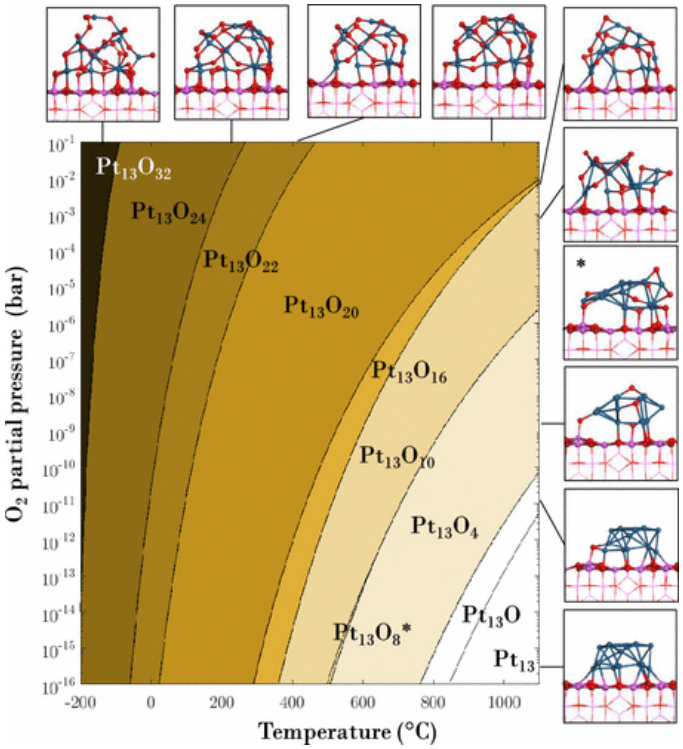

Figure I-9 - Most stable $Pt_{13}O_x$ structures according to the partial pressure in O_2 and the temperature. Taken from ref.[100]

Dessal et al.[54] predicted that the formation of the cluster was unlikely to happen during the calcination, as it was expected from an experimental point of view. By using the previously presented DFT model[100] for $Pt_{13}O_{22}$ and optimized PtO_4 and Pt_2O_4 models (**Figure I-10**) they calculated the stabilizing effect of the O_2 on single atoms platinum. Under 300°C and $P(O_2)$ = 0.2 bar, no sintering is expected. The sintering of these oxidized complexes would be favored from an entropic point of view due to the desorption of O_2 but the gain is not enough to compensate the enthalpy loss. Oxygens stabilize the platinum by anchoring them to the surface through ligand-surface bonds. However, no chlorine was considered in the study.

Under H_2, Pt_1H_2, Pt_2H_6 and $Pt_{13}H_{36}$ are expected as the most stable systems for each platinum stoichiometry. They noticed that hydrogen atoms behave differently from oxygen atoms as they cannot participate to the anchoring of the platinum to the surface through ligand-surface bonds. In this case, the sintering is thermodynamically favored as represented in **Figure I-10**. They conclude that the sintering process under H_2 was driven by enthalpic contribution as the ratio H/Pt increased despite the high temperatures considered and

hence the entropic losses. However, once the cluster is formed, the desorption of the hydrogen is favored by high temperature and the formation of a Pt_{13} cluster without hydrogen is then possible at 700°C.

Finally, they show that the formation of PtO_4 from $Pt_{13}O_{22}$ is not expected during the calcination as the sintering is thermodynamically unfavored. However, they notice that the oxidation of a $Pt_{13,}$ which can be formed during the reduction, could lead to $Pt_{13}O_{22}$.

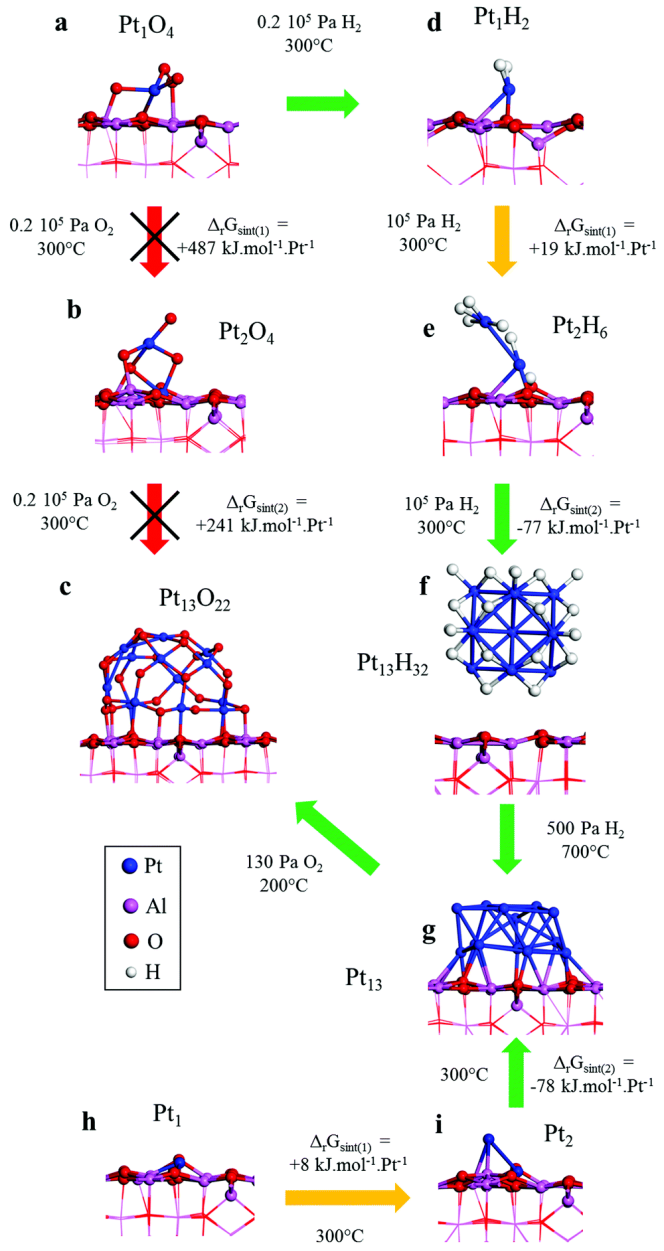

Figure I-10 - Most stable systems found by DFT calculations for various aggregation levels and proposition for a pathway leading to the formation of oxidized cluster. The green arrows represent exogenic reactions, while red ones are for endergonic ones. Orange arrows are used for systems with similar Gibbs free energy. Taken from ref[54]

Zhou et al.[102] studied the effect of chlorine on the redispersion of Pt_1 supported on the (100) and (110) γ-Al_2O_3 surface of Digne et al.[23,24]. In their study, they considered two steps, the evaporation of platinum from an agglomerated Pt cluster and then the adsorption of oxidized platinum species on the surface. The two species considered are PtO_2 and $Pt(OH)_2Cl_2$. They compute the Gibbs free energy to consider the impact of the atmosphere. They argue that chlorine facilitates the redispersion of Pt through the formation of $PtCl_2(OH)_2$ that is easier to evaporate from Pt_{bulk} than PtO_2. However, some hypotheses that were made could be questioned,

the adsorption sites retained for the Pt(0) on the (100) surface are not the same as expected by Mager-Maury et al.[98] despite having the similar level of theory and the same surface. Finally, their thermodynamic estimations consider that HCl and O_2 pressures are both fixed at 1 atm during the process.

I.5. Conclusions and strategy

Platinum active phases supported on γ-Al_2O_3 are involved as catalysts in many industrial processes including naphtha reforming. The combination of a metallic center and an acidic center through the use of bifunctional catalysts enhances both the activity and the selectivity compared to their mono-functional counterparts. In catalytic reforming, the addition of chlorine is beneficial due to an increase of the support acidity and a higher dispersion of the active phase. Because of the nature of the encountered reactions a fine tuning of the catalyst properties is required to increase the activity, selectivity, and lifetime of the catalyst.

Such control on the active phase can be obtained during the preparation of the catalyst. The latter usually occurs in four steps: impregnation, drying, calcination and reduction. Due to their high industrial interest, Pt/ γ-Al_2O_3 catalysts were subject to many experimental studies to gain insight on the nature of the species during these steps. Chlorine, which induces higher performances, lead to the formation of oxychlorinated species during calcination. During reduction, a better resistance against both reduction and sintering is observed when the chlorine content increases. However, and despite the numerous studies dedicated to the subject, the knowledge on these systems is mainly focused on the mesoscale and many questions on the exact atomic nature of the intermediates formed during the preparation remain unanswered, while it could help achieve a better control on these catalysts.

Theoretical studies, mostly using DFT, were found to be a precious tool to get insights on the atomic description of the species of interest that can be encountered after calcination and reduction steps. However, until now, the majority of these studies were done on the species expected at the end of the considered activation steps, and none of them focused on the evolution of the precursors during calcination or reduction steps. Hence, the reactivity of metallic Pt clusters supported on alumina surfaces and the effect of H_2 or O_2 environment on such Pt clusters were studied in detail. By contrast, no atomistic study of supported oxychlorinated platinum ($PtO_xCl_y(OH)_z(H2O)_n(H2)_m$) exists at the DFT level, and the evolution of the Pt coordination sphere (chlorine, oxygen, hydroxyl, water or dihydrogen ligands) and its oxidation degree (from +IV to 0) was never studied within a DFT approach, to the best of our knowledge. Understanding these properties during the genesis of the active phase could be of great help in better rationalizing the complex activation steps of the catalyst and controlling the final properties of the reduced catalyst.

In the present work, we thus propose to study this missing piece of knowledge on the transformation of the platinum intermediates from the beginning of the calcination step to the formation of the metallic platinum at the end of reduction step. All along this study a peculiar attention will be paid to unravelling the role of chlorine, whose impact is well known but not understood. Doing so, we thus propose to address some of the computational challenges in the field as identified in a recent perspective.[11]

A periodic DFT approach will be used to provide a thermodynamic analysis of the species nature as well as their dependence on the preparation conditions encountered during the genesis of the catalysis. The proposed models will be confronted to XAS experiments to evaluate their relevance. Beyond thermodynamic properties, kinetics and thus activation barriers are key components that will be modelled under reduction atmosphere.

Within these objectives we will first study by DFT, the gas phase platinum complexes that have been experimentally observed (Chapter III). In order to evaluate the relevance of various exchange-correlation functionals in the description of the reactions that can be encountered during both calcination and reduction, we will benchmark exchange-correlation functionals of various kinds against a higher-level method, namely ACFDT-RPA. This gas phase study will also help quantifying the impact of the γ–alumina support considered in the following chapters.

The evolution of γ–alumina supported Pt(IV) as a function of the conditions used during calcination will be presented in Chapter IV and a fruitful comparison with XAS (XANES and EXAFS) results will be carried out. Finally, the reduction step will be studied in Chapter V. Platinum complexes from oxidation degree +IV to 0 will be considered to evaluate what species are thermodynamically expected according to the reduction conditions. A kinetic study of the reduction of relevant intermediates from Pt(IV) to Pt(0), through the activation of the H_2 molecule, will be done to decipher the role of the chlorine in the stabilization of single atom.

Beforehand, the next chapter (**Chapter II**) will be dedicated to a presentation of the theoretical methods employed during this thesis.

I.6. References

1. Antos, G. J. & Aitani, A. M. (eds.). Catalytic naphtha reforming. 2nd ed. (Marcel Dekker, New York, 2004).
2. Davis, B. H. Alkane dehydrocyclization mechanism. *Catal. Today* **53,** 443–516 (1999).
3. Davis, B. H. & Venuto, P. B. Paraffin dehydrocyclization. *J. Catal.* **15,** 363–372 (1969).
4. Weisz, P. B. Polyfunctional Heterogeneous Catalysis. *Adv. Catal.,* 13, 137–190 (1962).
5. Haensel, V. *Alumina-Platinum-Halogen Catalyst And Preparation Thereof. U.S. Patent 2,479,109* (1949).
6. Pines, H. & Goetschel, C. T. Alumina: Catalyst and Support. XXIV. 1 Discussion of the Mechanism of the Aromatization of Alkanes in the Presence of Chromia—Alumina Catalysts 2,3. *J. Org. Chem.* **30,** 3530–3536 (1965).
7. Kluksdahl, H. E. *Reforming a sulfur-free naphtha with a platinum-rhenium catalyst. US. Patent, 3,415,737* (1968).
8. Augustine, S. The effect of Re, S, and Cl on the deactivation of Pt/γ-Al2O3 reforming catalysts. *J. Catal.* **115,** 217–232 (1989).
9. Sorrentiono, C, M, Pellet, R. J. & Bertolacini, R. J. *Reforming catalyst containing a group VIII noble metal, a group VIII non-noble metal, and gallium on separate support particles. U.S Patent 4,469,812A* (1984).
10. Grau, J. M. & Parera, J. M. Naphtha reforming capacity of catalysts with different metallic functions. *Ind. Eng. Chem. Res.* **28,** 1596–1600 (1989).
11. Valero, M. C. & Raybaud, P. Computational chemistry approaches for the preparation of supported catalysts: Progress and challenges. *J. Catal.* **391,** 539–547 (2020).
12. Prins, R. On the structure of γ-Al2O3. *J. Catal.* **392,** 336–346 (2020).
13. Busca, G. Structural, Surface, and Catalytic Properties of Aluminas. Adv. Catal., 57, 319–404 (2014).
14. Lippens, B. C. & Boer, J. H. de. Study of phase transformations during calcination of aluminum hydroxides by selected area electron diffraction. *Acta Cryst.* **17,** 1312–1321 (1964).
15. Smrcok, L., Langer, V. & Krestan, J. γ-alumina: a single-crystal X-ray diffraction study. *Acta crystallogr. C Struct. Chem.* **62,** i83-4 (2006).
16. Wolverton, C. & Hass, K. C. Phase stability and structure of spinel-based transition aluminas. *Phys. Rev. B* **63** (2000).
17. Paglia, G., Rohl, A. L., Buckley, C. E. & Gale, J. D. Determination of the structure of γ-alumina from interatomic potential and first-principles calculations: The requirement of significant numbers of nonspinel positions to achieve an accurate structural model. *Phys. Rev. B* **71** (2005).
18. Krokidis, X*.,* Raybaud, P., Gobichon, A. E., Rebours, B., Euzen, P. & Toulhoat H. Theoretical Study of the Dehydration Process of Boehmite to γ-Alumina. *J. Phys. Chem. B* **105,** 5121–5130 (2001).
19. Ferreira, A. R*.,* Martins, M. J. F., Konstantinova, E., Capaz, R. B., Souza, W. F., Chiaro, S. S. X. & Leitao, A. A. Direct comparison between two structural models by DFT calculations. *J. Solid State Chem.* **184,** 1105–1111 (2011).
20. Sohlberg, K., Pennycook, S. J. & Pantelides, S. T. The bulk and surface structure of γ-alumina. *Chem. Eng. Commun.* **181,** 107–135 (2000).
21. Nortier, P., Fourre, P., Saad, A. M., Saur, O. & Lavalley, J. C. Effects of crystallinity and morphology on the surface properties ofalumina. *Appl. Catal.* **61,** 141–160 (1990).
22. Beaufils, J.-P. & Barbaux, Y. Détermination, par diffraction différentielle de neutrons, des faces cristallines exposées par des supports de catalyseurs en poudre. *J. Chim. Phys.* **78,** 347–352 (1981).
23. Digne, M., Sautet, P., Raybaud, P., Euzen, P. & Toulhoat, H. Hydroxyl Groups on γ-Alumina Surfaces: A DFT Study. *J. Catal.* **211,** 1–5 (2002).
24. Digne, M., Sautet, P., Raybaud, P., Euzen, P. & Toulhoat, H. Use of DFT to achieve a rational understanding of acid-basic properties of γ -alumina surfaces. *J. Catal.* **226,** 54–68 (2004).
25. Morterra, C. & Magnacca, G. A case study: surface chemistry and surface structure of catalytic aluminas, as studied by vibrational spectroscopy of adsorbed species. *Catal. Today* **27,** 497–532 (1996).
26. Peri, J. B. A Model for the Surface of γ-Alumina 1. *J. Phys. Chem.* **69,** 220–230 (1965).

27. Tsyganenko, A. A. & Filimonov, V. N. Infrared Spectra of Surface Hydroxyl Groups and Crystalline Structure of Oxides. *Spectrosc. Lett.* **5,** 477–487 (1972).
28. Morterra, C., Ghiotti, G., Garrone, E. & Boccuzzi, F. Infrared spectroscopic characterization of the α-alumina surface. *J. Chem. Soc., Faraday Trans. 1* **72,** 2722 (1976).
29. Knözinger, H. & Ratnasamy, P. Catalytic Aluminas: Surface Models and Characterization of Surface Sites. *Catal. Rev.* **17,** 31–70 (1978).
30. Tsyganenko, A. A. & Mardilovich, P. P. Structure of alumina surfaces. *Faraday Trans.* **92,** 4843 (1996).
31. Busca, G., Lorenzelli, V., Ramis, G. & Willey, R. J. Surface sites on spinel-type and corundum-type metal oxide powders. *Langmuir* **9,** 1492–1499 (1993).
32. Kytökivi, A., Lindblad, M. & Root, A. IR and 1 H NMR studies on the adsorption of gaseous hydrogen chloride on γ-alumina. *Faraday Trans.* **91,** 941–948 (1995).
33. Peri, J. B. Infrared Study of the Reaction of Hydrogen Chloride with the Surface of γ-Alumina and Its Effect on Surface "Acid" Sites 1. *J. Phys. Chem.* **70,** 1482–1491 (1966).
34. Tanaka, M. & Ogasawara, S. Infrared studies of the adsorption and the catalysis of hydrogen chloride on alumina and on silica. *J. Catal* **16,** 157–163 (1970).
35. Digne, M., Raybaud, P., Sautet, P., Guillaume, D. & Toulhoat, H. Atomic scale insights on chlorinated gamma-alumina surfaces. *J. Am. Chem. Soc.* **130,** 11030–11039 (2008).
36. Marczewski, M., Derewinski, M. & Malinowski, S. The influence of gaseous chlorine on the chemical and catalytic properties of alumina. *Can. J. Chem. Eng.* **61,** 93–97 (1983).
37. Wischert, R., Laurent, P., Copéret, C., Delbecq, F. & Sautet, P. γ-Alumina: the essential and unexpected role of water for the structure, stability, and reactivity of "defect" sites. *J. Am. Chem. Soc.* **134,** 14430–14449 (2012).
38. Pigeon, T., Chizallet, C. & Raybaud, P. Revisiting γ-alumina surface models through the topotactic transformation of boehmite surfaces. *J. Catal.* **405,** 140–151 (2022).
39. Busca, G. The surface of transitional aluminas: A critical review. *Catal. Today* **226,** 2–13 (2014).
40. Batista, A. T., Wisser, D., Pigeon, T., Gajan, D., Diehl, F., Rivallan, M., Catita, L., Gay, A. S., Lesage, A., Chizallet, C. & Raybaud, P. Beyond γ-Al2O3 crystallite surfaces: The hidden features of edges revealed by solid-state 1H NMR and DFT calculations. *J. Catal.* **378,** 140–143 (2019).
41. Batista, A. T. F., Pigeon, T., Meyet, J., Wisser, D., Rivallan, M., Gajan, D., Catita, L., Diehl, F., Gay, A. S., Chizallet, C., Lesage, A. & Raybaud, P. Structure, Location, and Spatial Proximities of Hydroxyls on γ-Alumina Crystallites by High-Resolution Solid-State NMR and DFT Modeling: Why Edges Hold the Key. *ACS Catal.* **13,** 6536–6548 (2023).
42. Raybaud, P., Digne, M., Iftimie, R., Wellens, W., Euzen, P. & Toulhoat, H. Morphology and Surface Properties of Boehmite (γ-AlOOH): A Density Functional Theory Study. *J. Catal.* **201,** 236–246 (2001).
43. Marceau, E., Carrier, X. & Che, M. Impregnation and Drying. In *Synthesis of solid catalysts,* edited by K. P. de Jong (Wiley-VCH, Weinheim, 2009), pp. 59–82.
44. Noh, J. S. & Schwarz, J. A. Estimation of the point of zero charge of simple oxides by mass titration. *J. Colloid Interface Sci.* **130,** 157–164 (1989).
45. Spieker, W. A., Liu, J., Miller, J. T., Kropf, A. J. & Regalbuto, J. R. An EXAFS study of the co-ordination chemistry of hydrogen hexachloroplatinate(IV). *Appl. Catal. A* **232,** 219–235 (2002).
46. Spieker, W. A. & Regalbuto, J. R. A fundamental model of platinum impregnation onto alumina. *Chem. Eng. Sci.* **56,** 3491–3504 (2001).
47. Shelimov, B., Lambert, J.-F., Che, M. & Didillon, B. Initial Steps of the Alumina-Supported Platinum Catalyst Preparation: A Molecular Study by 195Pt NMR, UV–Visible, EXAFS, and Raman Spectroscopy. *J. Catal.* **185,** 462–478 (1999).
48. Maatman, R. How to Make a More Effective Platinum-Alumina Catalyst. *Ind. Eng. Chem.* **51,** 913–914; (1959).

49. Shelimov, B., Lambert, J.-F., Che, M. & Didillon, B. Molecular-level studies of transition metal–support interactions during the first steps of catalysts preparation: platinum speciation in the hexachloroplatinate/alumina system. *J. Mol. Catal. A Chem.* **158,** 91–99 (2000).
50. Shelimov, B., Lambert, J.-F., Che, M. & Didillon, B. Application of NMR to Interfacial Coordination Chemistry: A 195 Pt NMR Study of the Interaction of Hexachloroplatinic Acid Aqueous Solutions with Alumina. *J. Am. Chem. Soc.* **121,** 545–556 (1999).
51. Yao, H., Sieg, M. & Plummerjr, H. Surface interactions in the Pt/-AlO system. *J. Catal.* **59,** 365–374 (1979).
52. Dessal, C., Len, T., Morfin, F., Rousset, J. L., Aouine, M., Afanasiev, P & Piccolo L. Dynamics of Single Pt Atoms on Alumina during CO Oxidation Monitored by Operando X-ray and Infrared Spectroscopies. *ACS Catal.* **9,** 5752–5759 (2019).
53. Batista, A. T. F. Baaziz, W., Taleb, A. L., Chaniot, J., Moreaud, M., Legens, C., Aguilar-Tapia, A., Proux, O., Hazemann, J. L., Diehl, F., Chizallet, C., Gay, A. S., Ersen, O. & Raybaud, P. Atomic Scale Insight into the Formation, Size, and Location of Platinum Nanoparticles Supported on γ-Alumina. *ACS Catal.* **10,** 4193–4204 (2020).
54. Dessal, C., Sangnier, A., Chizallet, C., Dujardin, C., Morfin, F., Rousset, J. L., Aouine, M., Bugnet, M., Afanasiev, P. & Piccolo, L. Atmosphere-dependent stability and mobility of catalytic Pt single atoms and clusters on γ-Al_2O_3. *Nanoscale* **11,** 6897–6904 (2019).
55. Bradley, S. A., Sinkler, W., Blom, D. A., Bigelow, W., Voyles, P. M. & Lawrence, F. A. Behavior of Pt Atoms on Oxide Supports During Reduction Treatments at Elevated Temperatures, Characterized by Aberration Corrected Stem Imaging. *Catal. Lett. (Catalysis Letters)* **142,** 176–182 (2012).
56. Fialho Batista, A. T. Atomic scale insight into platinum based catalysts supported on chlorinated γ-alumina. Ph.D., 2016-2019.
57. Lee, J., Jang, E. J., Oh, D. G., Szanyi, J. & Kwak, J. H. Morphology and size of Pt on Al_2O_3: The role of specific metal-support interactions between Pt and Al_2O_3. *J. Catal.* **385,** 204–212 (2020).
58. Lambert, J. F. Marceau, E., Shelimov, B., Lehman, J., Le Bel de Penguilly, V., Carrier, X., Boujday, S., Pernot, H. & Che, M. Thermal chemistry of oxide-supported platinum catalysts: A comparative study. *Stud. Surf. Sci. Catal., **130***, 1043-1048 (2000).
59. Lieske, H., Lietz, G., Spindler, H. & Völter, J. Reactions of platinum in oxygen- and hydrogen-treated Pt/γ-Al_2O_3 catalysts I. Temperature-programmed reduction, adsorption, and redispersion of platinum. *J. Catal.* **81,** 8–16 (1983).
60. Lietz, G., Lieske, H., Spindler, H., Hanke, W. & Völter, J. Reactions of platinum in oxygen- and hydrogen-treated Pt/γ-Al_2O_3 catalysts II. Ultraviolet-visible studies, sintering of platinum, and soluble platinum. *J. Catal.* **81,** 17–25 (1983).
61. Berdala, J., Freund, E. & Lynch, J. P. Environment of platinum atoms in a H_2PtCl_6/AL_2O_3 catalyst: Influence of metal loading and chlorine content. *J. Phys. Colloques* **47,** C8-269-C8-272 (1986).
62. Gracia, F. J., Miller, J. T., Kropf, A. J. & Wolf, E. E. Kinetics, FTIR, and Controlled Atmosphere EXAFS Study of the Effect of Chlorine on Pt-Supported Catalysts during Oxidation Reactions. *J. Catal.* **209,** 341–354 (2002).
63. Svintsitskiy, D. A. Kibis, L. S., Stadnichenko, A. I., Slavinskaya, E. M., Romanenko, A. V., Fedorova, E. A., Stonkus, O. A., Doronkin, D. E., Marchuk, V., Zimina, A., Casapu, M. & Grunwaldt, J. D. Insight into the Nature of Active Species of Pt/Al_2O_3 Catalysts for low Temperature NH_3 Oxidation. *ChemCatChem* **12,** 867–880 (2020).
64. Berdala, J., Freund, E. & Lynch, J. P. Genesis of the metallic phase in a highly dispersed catalyst formed from Pt acetylacetonate on alumina. *J. Phys. Colloques* **47,** C8-265-C8-268 (1986).
65. Le Normand, F., Borgna, A., Garetto, T. F., Apesteguia, C. R. & Moraweck, B. Redispersion of Sintered Pt/Al_2O_3 Naphtha Reforming Catalysts: An in Situ Study Monitored by X-ray Absorption Spectroscopy. *J. Phys. Chem.* **100,** 9068–9076 (1996).
66. Mordente, M. G. V. & Rochester, C. H. Infrared study of the effects of oxychlorination on Pt dispersion in Pt/Al_2O_3 catalysts. *J. Chem. Soc., Faraday Trans. 1* **85,** 3495 (1989).

67. Franck, J. P. & Martino, G. Deactivation and Regeneration of Catalytic-Reforming Catalysts. In *Figueiredo (Ed.) – Progress in Catalyst Deactivation,* pp. 355–397.
68. Morgan, K., Goguet, A. & Hardacre, C. Metal Redispersion Strategies for Recycling of Supported Metal Catalysts: A Perspective. *ACS Catal.* **5,** 3430–3445 (2015).
69. Cholley, T. Etude de la redispersion de phase bimétallique à base de platine supportées sur alumine chlorée ou neutralisée. PhD, 1997.
70. Galisteo, F. C., Mariscal, R., Lopez Granados, M., Fierro, J. L. G., Daley, R. A. & Anderson J. A. Reactivation of sintered Pt/Al_2O_3 oxidation catalysts. *Appl. Catal. B. Env.* **59,** 227–233 (2005).
71. Mei, D. Kwak, J. H., Hu, J., Cho, S. J., Szanyi, J., Allard, L. F. & Peden, C. H. F. Unique Role of Anchoring Penta-Coordinated Al^{3+} Sites in the Sintering of γ-Al_2O_3 -Supported Pt Catalysts. *J. Phys. Chem. Lett.* **1,** 2688–2691 (2010).
72. Kwak, J. H. Hu, J. Mei, D., Yi, C. W., Kim, D. H., Peden, C. H. F., Allard, L. F. & Szanyi, J. Coordinatively unsaturated Al^{3+} centers as binding sites for active catalyst phases of platinum on γ-Al_2O_3. *Science (New York, N.Y.)* **325,** 1670–1673 (2009).
73. Sinkler, W. Sanchez, S. I., Bradley, S. A., Wen, J., Mishra, B., Kelly, S. D. K. & Bare, S. Aberration-Corrected Transmission Electron Microscopy and In Situ XAFS Structural Characterization of Pt/γ-Al_2O_3 Nanoparticles. *ChemCatChem* **7,** 3779–3787 (2015).
74. Batista, A. T. F. Chizallet, C., Diehl, F., Taleb, A. L., Gay, A. S., Ersen, O. & Raybaud, P. Evaluating acid and metallic site proximity in Pt/γ-Al_2O_3-Cl bifunctional catalysts through an atomic scale geometrical model. *Nanoscale* **14,** 8753–8765 (2022).
75. Lee, J., Jang, E. J. & Kwak, J. H. Effect of number and properties of specific sites on alumina surfaces for Pt-Al_2O_3 catalysts. *Appl. Catal. A Gen.* **569,** 8–19 (2019).
76. Borges, L. R. Lopez-Castillo, A., Meira, D. M., Gallo, J. M. R., Zanchet, D. & Bueno, J. M. C. Effect of the Pt Precursor and Loading on the Structural Parameters and Catalytic Properties of Pt/Al_2O_3. *ChemCatChem* **11,** 3064–3074 (2019).
77. Ramallo-López, J. M. Requejo, F. G., Craievich, A. F., Wei, J., Avalos-Borja, M. & Iglesia, E. Complementary methods for cluster size distribution measurements: supported platinum nanoclusters in methane reforming catalysts. *J. Mol. Catal. A Chem.* **228,** 299–307 (2005).
78. Vaarkamp, M., Miller, J. T., Modica, F. S. & Koningsberger, D. C. On the Relation between Particle Morphology, Structure of the Metal-Support Interface, and Catalytic Properties of Pt/γ-Al_2O_3. *J. Catal.* **163,** 294–305 (1996).
79. Frenkel, A. I. Small, M. W., Smith, J. G., Nuzzo, R. G., Kvashnina, K. O. & Tromp, M. An in Situ Study of Bond Strains in 1 nm Pt Catalysts and Their Sensitivities to Cluster–Support and Cluster–Adsorbate Interactions. *J. Phys. Chem. C* **117,** 23286–23294 (2013).
80. Bus, E. & van Bokhoven, J. A. Hydrogen chemisorption on supported platinum, gold, and platinum-gold-alloy catalysts. *PCCP* **9,** 2894–2902 (2007).
81. Stakheev, A. Y. Zhang, Y., Ivanov, A. V., Beava, G. N., Ramaker, D. E. & Koningsberger, D. C. Separation of Geometric and Electronic Effects of the Support on the CO and H_2 Chemisorption Properties of Supported Pt Particles: The Effect of Ionicity in Modified Alumina Supports. *J. Phys. Chem. C* **111,** 3938–3948 (2007).
82. Smolikov, M. D., Belyi, A. S., Nizovskll, A. L., Smirnova, I. E., Semikolenov, A. S. & Duplyakin, V. K. New data about platinum state in reduced Pt/Al_2O_3(Cl) catalysts. *React. Kinet. Catal. Lett.* **37,** 437–442 (1988).
83. Zhou, Y., Wood, M. & Winograd, N. A time-of-flight SIMS study of the chemical nature of highly dispersed Pt on alumina. *J. Catal.* **146,** 82–86 (1994).
84. Marceau, E., Che, M., Saint-Just, J. & Tatibouët, J. M. Influence of chlorine ions in $Pt/A1_2O_3$ catalysts for methane total oxidation. *Catal. Today* **29,** 415–419 (1996).
85. Marceau, E., Lauron-Pernot, H. & Che, M. Influence of the Metallic Precursor and of the Catalytic Reaction on the Activity and Evolution of $Pt(Cl)/\delta$-Al_2O_3 Catalysts in the Total Oxidation of Methane. *J. Catal.* **197,** 394–405 (2001).

86. Radivojević, D., Seshan, K. & Lefferts, L. Pt/SiO_2 catalyst preparation: high platinum dispersions by using low-temperature treatments. Stud. Surf. Sci. Catal. **162**, 529-536 (2006)
87. Huizinga, T., van Grondelle, J. & Prins, R. A temperature programmed reduction study of Pt on Al_2O_3 and TiO_2. *Appl. Catal.* **10,** 199–213 (1984).
88. Kovarik, L. Genc, A., Wang, C., Qiu, A., Pedens, C. H. F., Szanyi, J. & Kwak, J. H. Tomography and High-Resolution Electron Microscopy Study of Surfaces and Porosity in a Plate-like γ-Al_2O_3. *J. Phys. Chem. C* **117,** 179–186 (2013).
89. Hu, C. H., Chizallet, C., Mager-Maury, C., Corral-Valero, M., Sautet, P., Toulhoat, H. & Raybaud, P. Modulation of catalyst particle structure upon support hydroxylation: Ab initio insights into Pd_{13} and Pt_{13}/γ-Al_2O_3. *J. Catal.* **274,** 99–110 (2010).
90. Hu, C. H., Chizallet, C., Toulhoat, H. & Raybaud, P. Structural, energetic, and electronic trends in low-dimensional late-transition-metal systems. *Phys. Rev. B* **79** (2009).
91. Erfani, G. S., Hong, S. & Rahman, T. S. Effects of γ-Al_2O_3 Support on the Morphology and Electronic Structure of Pt Nanoparticles. *J. Phys. Chem. C* **123,** 16893–16901 (2019).
92. Vayssilov, G. N. & Rösch, N. Reverse hydrogen spillover in supported subnanosize clusters of the metals of groups 8 to 11. A computational model study. *PCCP* **7,** 4019–4026 (2005).
93. Mager-Maury, C., Bonnard, G., Chizallet, C., Sautet, P. & Raybaud, P. H_2-Induced Reconstruction of Supported Pt Clusters: Metal-Support Interaction versus Surface Hydride. *ChemCatChem* **3,** 200–207 (2011).
94. Gorczyca, A., Moizan, V., Chizallet, C., Proux, O., Del Net, W., Lahera, E., Hazemann, J. L., Raybaud, P. & Joly, Y. Monitoring morphology and hydrogen coverage of nanometric Pt/γ-Al_2O_3 particles by in situ HERFD-XANES and quantum simulations. *Angew. Chem., Int. Ed. Engl.* **53,** 12426–12429 (2014).
95. Bunău, O., Ramos, A. Y. & Joly, Y. The FDMNES code. *International tables for crystallography - X-ray Absorption* **I** (2021).
96. Guda, S. A., Guda, A. A., Soldatov, M. A., Lomachenko, K. A., Bugaev, A. L., Lamberti, C., Gawelda, W., Bressler, C., Smolentsev, G., Soldatov, A. & Joly, Y. Optimized Finite Difference Method for the Full-Potential XANES Simulations: Application to Molecular Adsorption Geometries in MOFs and Metal-Ligand Intersystem Crossing Transients. *J. Chem. Theory. Comput.* **11,** 4512–4521 (2015).
97. Vottero, E., Carosso, M., Ricchebuono, A., Jiménez-Ruiz, M., Pellegrini, R. Chizallet, C., Raubaud, P., Groppo, E. & Piovano, A. Evidence for H_2-Induced Ductility in a Pt/Al_2O_3 Catalyst. *ACS Catal.* **12,** 5979–5989 (2022).
98. Mager-Maury, C., Chizallet, C., Sautet, P. & Raybaud, P. Platinum Nanoclusters Stabilized on γ-Alumina by Chlorine Used As a Capping Surface Ligand: A Density Functional Theory Study. *ACS Catal.* **2,** 1346–1357 (2012).
99. Liu, Y., Cen, W., Feng, G., Chu, Y., Kong, D & Yin, H. First principles study on the adsorption of Ptn (n=1–4) on γ-Al_2O_3(110) surface. *Appl. Surf. Sci.* **313,** 424–431 (2014).
100. Sangnier, A., Matrat, M., Nicolle, A., Dujardin, C. & Chizallet, C. Multiscale Approach to the Dissociative Adsorption of Oxygen on a Highly Dispersed Platinum Supported on γ-Al_2O_3. *J. Phys. Chem. C* **122,** 26974–26986 (2018).
101. Xu, Y., Shelton, W. A. & Schneider, W. F. Effect of particle size on the oxidizability of platinum clusters. *J. Phys. Chem. A* **110,** 5839–5846 (2006).
102. Zhou, X., Zhang, Y. & Wang, J. DFT study on the regeneration of Pt/γ-Al_2O_3 catalyst: The effect of chlorine on the redispersion of metal species. *Appl. Surf. Sci.* **545,** 148988 (2021).

Chapter II

Theoretical background

II.1. Electronic structure calculation

II.1.1. Schrödinger equation

Three years after the famous equation of Schrödinger in 1926, Dirac wrote "The fundamental laws necessary for the mathematic treatment of a large part of physics and the whole of chemistry are thus completely known, and the difficulty lies only in the fact that application of these laws lead to equations too complex to be solved".[1] These words still echo as a sad triumph, but tremendous progress has been made during the last eighty years.

Using Dirac notations and without accounting for time-dependent interaction, nor relativistic effect, the electronic states of a quantum system are described by the Schrödinger equation:

$$\widehat{H}|\Psi\rangle = E|\Psi\rangle \qquad \textbf{1}$$

with $\widehat{H}$, the Hamiltonian operator of the system, and $\Psi = \Psi(x_1, x_2, \dots, x_n, R_1, R_2, \dots, R_M)$ the wave function of n electrons located at the coordinates x_i ($x_i = (r_i, \sigma_i), with\ r_i \in \mathbb{R}^3\ and\ \sigma_i \in \{\uparrow, \downarrow\}$), and M nuclei at positions $R_i\ with\ R_i \in \mathbb{R}^3$. E is the energy of the system.

Even if it is already a simplification of a much complex problem, this equation was found to be impossible to solve analytically for a system with more 2 and more electrons. Hence, approximations must be done in order to find a solution. The Born-Oppenheimer Approximation (BOA) is important in quantum chemistry and the following descriptions are done by assuming it. From a qualitative point of view, the BOA stands that nuclei and electrons have uncoupled movements. In other words, electrons adapt immediately at the nucleus positions. Under BOA, the Hamiltonian $\widehat{H}$ can be simplified to its electronic part $\widehat{H}_{elec}$ which can be written (using atomic units as in the whole chapter):

$$\widehat{H}_{elec} = -\sum_i \frac{1}{2}\nabla_i^2 + \sum_{i<j} \frac{1}{|r_i - r_j|} - \sum_i v_{ne}(i) \qquad \textbf{2}$$

With r_i and r_j the position of the *i* and *j* electron, and $v_{ne}(i)$ is the external potential in which the electrons evolve with Z_A the atomic number of the nucleus A and R_A the position of the nucleus A as in:

$$v_{ne}(i) = -\sum_A \frac{Z_A}{|r_i - R_A|} \qquad \textbf{3}$$

In this case, the electronic wavefunction depends explicitly on the electrons coordinates but only parametrically on the nuclear coordinates. The first term of $\widehat{H}_{elec}$ is the kinetic energy operator, the second one is electron-electron repulsion while the third one is the coulombic attraction between nuclei and electron external potential. In order to get the total energy of a system, one has to add the electronic repulsion between the fixed nuclei. In that case it is possible to write it as following:

$$E_{tot} = E_{elec} + \sum_{A<B} \frac{Z_A Z_B}{R_{AB}} \quad \textbf{4}$$

With E_{elec} obtained from **Eq.1**, Z the atomic number of each nucleus and R_{AB} the distance between two nuclei A and B. From now we will only consider electronic Hamiltonians and electronic wavefunctions hence the subscript $elec$ will be dropped.

II.1.2. Variational principle

The variational principle states that the energy associated to the ground state (GS) wavefunction is a lower bound of the energies obtained from approximated wavefunction.

For a given state Ψ its energy can be calculated as:

$$E[\Psi] = \frac{\langle \Psi | \widehat{H} | \Psi \rangle}{\langle \Psi | \Psi \rangle} \quad \textbf{5}$$

where:

$$\langle \Psi | \widehat{H} | \Psi \rangle = \int \mathrm{d}^3 \Psi^* \widehat{H} \Psi \quad \textbf{6}$$

If we expand a normalized state Ψ_{trial} as a linear combination of the eigenstates of $\widehat{H}_{elec}$ such as:

$$\Psi_{trial} = \sum_k c_k |\Psi_k\rangle \quad \textbf{7}$$

The energy is given by:

$$E[\Psi_{trial}] = \sum_{k,k'} c_k^* c_{k'} \langle \Psi_{k'} | \widehat{H} | \Psi_k \rangle \quad \textbf{8}$$

As $\widehat{H}$ is a Hermitian operator, its eigenfunctions $|\Psi_k\rangle$ are orthonormal, hence we have:

$$E[\Psi_{trial}] = \sum_k |c_k|^2 E_k > E_0 \sum_k |c_k|^2 = E_0 \quad \textbf{9}$$

with E_k the energy of the kth eigenstate that are all superior or equal to E_0. The last equality comes from the normalized property of Ψ_{trial}, and the orthonormality between $\{|\Psi_k\rangle\}$:

$$\langle \Psi_{trial} | \Psi_{trial} \rangle = 1 = \sum_{k,k'} c_{k'}^* c_k \delta_{kk'} = \sum_k |c_k|^2 \quad \textbf{10}$$

Hence, the energy of an approximate wavefunction is always higher than the ground state wavefunction, Ψ_0. Moreover, the variational principle for the ground state energy shows that the quality of a given wavefunction can be described by its energy, the lower the energy, the better the wavefunction. Thus, by minimizing the energy, one can enhance $|\Psi_{trial}\rangle$. The result remains true in the extension to a set of $\{|\Psi_k\rangle\}$ that are not orthonormal between them.[2]

II.2. Density Functional Theory approach

The electronic wavefunction $\Psi(x_1, x_2, \dots, x_N)$ totally describes the system. However, because of the important number of coordinates (4N: $x_i = (r_i, \sigma_i), with\ r_i \in \mathbb{R}^3\ and\ \sigma_i \in \{\uparrow, \downarrow\}$) such quantity is not easy to manipulate, but still remains at the center of numerous methods developed to solve the Schrödinger equation. However, as they were not used in this work, we will not describe them, and we will focus on an alternative: The density functional theory (DFT) method which is based on the one-electron density $\rho(r)$ rather than the multibody wavefunction.

The main idea of DFT is that : "*the knowledge of the ground-state density for any electronic system (with or without interactions) uniquely determines the system*".[3] That statement allows to reduce the dimension of the electronic problem to 3. DFT allows to study bigger systems at a cheaper cost than what will be required if multibody wavefunctions were used. For a N-electrons system, the density $\rho(r)$ can be written as following:

$$\rho(r) = \langle \Psi | \hat{n}(r) | \Psi \rangle = N \sum_{\sigma_i} \int d^3 r_2 \dots d^3 r_N \Psi^*(x, x_2, \dots, x_N) \Psi(x, x_2, \dots, x_N) \quad \textbf{11}$$

With $\int \rho(r) dr = N$ and the density operator $\hat{n}(r) = \sum_i \delta(r - r_i)$.

The first model based on the electronic density was proposed in 1927 by Thomas and Fermi, [4,5] but the hard approximations made in this model makes it unusable to describe binding molecules, and thus chemical systems. DFT as it is known and used nowadays, took birth in two papers, the first in 1964 by Hohenberg and Kohn[6] and the second in 1965 by Kohn and Sham.[7] The first paper shows that all the wanted information that one needs about a system can be calculated using the electronic density while the second one provides a scheme to calculate properties using this formulation. This is after these two milestones that DFT started to become prolifically useable for quantum chemists, in fact, between 1980 and 2010 two of the three most cited physicists were working on DFT.[8]

II.2.1. Hohenberg and Kohn theorems

The first theorem of Hohenberg and Kohn states that: the ground state density of a bound system of interacting electrons determines its external potential up to an additive constant.[6]

First let us redefine the Hamiltonian operator in a more concise way that will be useful in the next parts:

$$\hat{H} = \hat{T} + \hat{W}_{ee} + \hat{V} \qquad \textbf{12}$$

With $\hat{T}$ the kinetic-energy operator, $\hat{W}_{ee}$ the electron-electron operator and $\hat{V}$ the external potential operator which does not have to be only the Coulomb potential. The $\hat{V}$ component of the Hamiltonian is the only external contribution to the systems; hence we can consider that $\hat{T}$ and $\hat{W}_{ee}$ are the same for all N-electron systems. As it will be useful later, we will also rewrite the operator $\hat{V}$ in term of the density operator.

$$\hat{V} = \sum_i v(r_i) = \int d^3 r v(r)\hat{n}(r) \qquad \textbf{13}$$

In order to prove the first HK theorem, we have to establish that both relations A and B in **Figure II-1** are true.

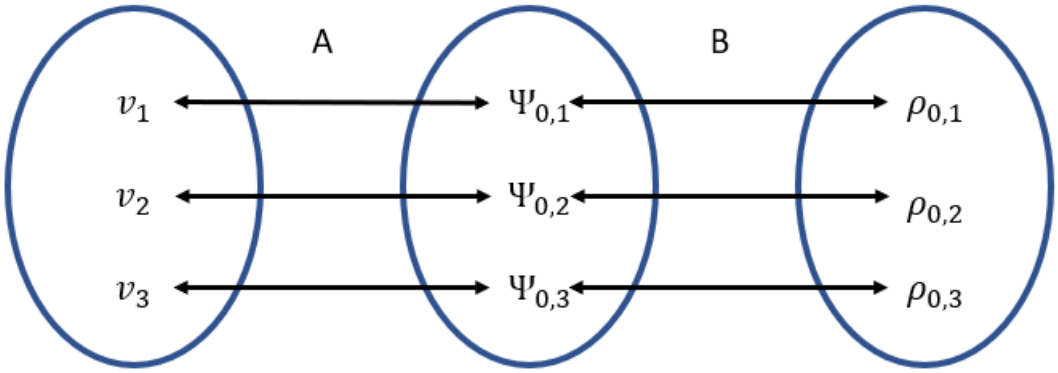

Figure II-1. Representation of the bijective mapping between external potential (v_i), associated ground states ($\Psi_{0,i}$), and the ground state densities ($\rho_{0,i}$).

Let us first consider the A mapping. The fact that for a given v_i there is only one $\Psi_{0,i}$ is immediate from the Schrödinger equation and the restriction to non-degenerate ground state. To prove that there is no Ψ_0 being the ground state for two v that differs by more than a constant can be proved by *reductio ad absurdum*. Let us assume that $|\Psi_0\rangle$ is the ground state obtained from two v:

$$\hat{H}|\Psi_0\rangle = \left[\hat{T} + \hat{W}_{ee} + \hat{V}\right]|\Psi_0\rangle = E_0|\Psi_0\rangle \quad \textbf{14}$$

$$\hat{H}'|\Psi_0\rangle = \left[\hat{T} + \hat{W}_{ee} + \hat{V}'\right]|\Psi_0\rangle = E'_0|\Psi_0\rangle \quad \textbf{15}$$

We would have after subtraction:

$$\left[\hat{V} - \hat{V}'\right]|\Psi_0\rangle = [E_0 - E'_0]|\Psi_0\rangle \quad \textbf{16}$$

From the form of the $\hat{V}$ and $\hat{V}'$ given in **Eq.13** we see that as v and v' differ by more than a constant while the difference $E_0 - E_0{}'$ is constant. Hence, as long as $|\Psi_0\rangle$ does not vanish, there is a contradiction. Thus, there is a one-to-one correspondence between the external potential and the ground state wavefunction. The non-vanishing nature of Ψ is not supposed to be an issue for realistic systems.[9]

Regarding the second part of the bijective mapping presented in **Figure II-1**, the fact that $|\Psi_0\rangle$ determines uniquely the ground state density come directly from **Eq.11**. It remains to show that only one $|\Psi_0\rangle$ can be obtained from a given ρ_0. The proof, as for the first map, is done by *reductio ad absurdum*.

First, let's $\rho(r)$ be the nondegenerate ground state of a N-electrons system in the potential $v(r)$. We call $|\Psi\rangle$ the ground state wavefunction and E the associated energy. Let's suppose that there is another potential ($v'(r)$) with $|\Psi'\rangle$ as ground state and which give the same $\rho(r)$. They both satisfy the Schrödinger equation, and let's denote *H* and *H'* the corresponding Hamiltonians to *E* and *E'*.

We can express the energy E and E' as following:

$$E = \langle \Psi | H | \Psi \rangle = \int v(r)\rho(r)dr + \langle \Psi \left| \hat{\hat{T}} + \widehat{W}_{ee} \right| \Psi \rangle \quad \textbf{17}$$

$$E' = \langle \Psi' | H' | \Psi' \rangle = \int v'(r)\rho(r)dr + \langle \Psi' \left| \hat{\hat{T}} + \widehat{W}_{ee} \right| \Psi' \rangle \quad \textbf{18}$$

By definition of the ground state and the nondegenerate hypothesis, we can write that:

$$E' = \langle \Psi' | H' | \Psi' \rangle < \langle \Psi | H' | \Psi \rangle \quad \textbf{19}$$

And it follows that:

$$E' < E + \int [v'(r) - v(r)]\rho(r)dr \quad \textbf{20}$$

Because of dummies indices, it comes immediately:

$$E < E' + \int [v(r) - v'(r)]\rho(r)dr \quad \textbf{21}$$

Finally, by summing equation (20) and equation (21) we can write that:

$$E + E' < E + E' \quad \textbf{22}$$

Hence, Hohenberg and Kohn showed that the ground state density of a system determines uniquely its external potential and its ground state wavefunction (**Eq.23**).

$$v_{ne}(r) \Leftrightarrow |\Psi_0\rangle \Leftrightarrow \rho_0(r) \quad \textbf{23}$$

By showing that, it is possible to write that any observable $\hat{O}$ of the ground state can be written as a functional of the density ρ_0.

$$O[\rho_0] = \langle \Psi_0[\rho_0] \left| \hat{O} \right| \Psi_0[\rho_0] \rangle \quad \textbf{24}$$

Especially we can write the energy E_v of a system under the external potential v as a functional of the electronic density $\rho_0(r)$.

$$E_0[\rho_0] = \langle \Psi_0[\rho_0] \left| \hat{T} + \widehat{W}_{ee} + \hat{V} \right| \Psi_0[\rho_0] \rangle \quad \textbf{25}$$

We can introduce now the universal functional $F_{HK}[\rho]$ which is the sum of the kinetic and the electron-electron interaction energy: $T[\rho] + W_{ee}[\rho]$. As we said, such functional is supposed to be independent of the system.

$$F_{HK}[\rho] = \langle \Psi_0[\,\rho] \big| \hat{T} + \hat{W}_{ee} \big| \Psi_0[\rho] \rangle \qquad \textbf{26}$$

It is possible to rewrite the energy of a system under a potential ν by using the universal functional of Hohenberg and Kohn:

$$E_\nu[\rho] = F_{HK}[\rho] + \int d^3 r \rho_0(r) \nu(r) \qquad \textbf{27}$$

The second theorem of Hohenberg and Kohn states that *the exact ground state density minimizes the ground state energy*. In other words, the functional E[$\rho(r)$] reaches a minimum when $\rho(r) = \rho_0(r)$ with ρ_0 the ground state density. This is easily demonstrated by considering the link between the ground state density and the ground state wavefunction and by applying the variational principle. Hence, one can obtain the ground state energy E_0 by minimization of the functional $E[\rho]$ over ρ.

$$E_0 = \min_{\rho} E[\rho] \qquad \textbf{28}$$

The implication of such a variational principle means that the ground state density can be minimized thanks to the following variational equation:

$$\frac{\delta}{\delta \rho(r)} \left\{ E_\nu[\rho(r)] - \mu \left(\int d^3 r \rho(r) - N \right) \right\} = 0 \qquad \textbf{29}$$

With μ a Lagrange multiplier and *N* the number of electrons in the system. This formulation allows to keep a density corresponding to the *N* electrons of the system. By definition of $E_v[\rho]$, the Euler-Lagrange equation can be rewritten as:

$$\frac{\delta F_{HK}[\rho]}{\delta \rho(r)} + v(r) = \mu \qquad \textbf{30}$$

However, to apply the variational principle to the trial density, the density must be *v*-representable.

II.2.2. N-representability

By definition, a *v-representable* density is a density associated to an antisymmetric ground-state wave function of an electronic Hamiltonian with a given external potential $v(r)$.

Hence, the mapping between the density and the wave function of a ground state as proposed by Hohenberg and Kohn relies on the fact that the density needs to be *v*-representable, otherwise the functional of the density is not defined. This is especially true for the universal functional of Hohenberg and Kohn (**Eq.26**). For the same reasons, the second theorem of Hohenberg and Kohn (the variational principle) also requires that the density if *v*-representable. However, there is not certitude that a given density will be *v*-representable, and in fact many densities do not fulfil this condition.[10] The main issue with this definition is that not all the conditions to the *v*-representability are known.[11] It is then impossible to restrict the search only over densities that are *v*-representable. That is an important constraint as both theorems of Hohenberg and Kohn[6] are made for *v*-representable densities.

Hopefully, if a study is limited to the ground state, then a weaker restriction is needed to apply the HK theorems: the N-representability. A density is said N-representable if it can be obtained from an antisymmetric wavefunction. The conditions to be a N-representable density are known, and a density $\rho(r)$ is N-representable if:

$$\rho(r) > 0, \int \rho(r)dr = N, \int ||dr|\nabla\rho^{1/2}(r)|^2 < \infty \qquad \textbf{31}$$

Hence, in that case, only the B-maps on **Figure II-1** is required. The remaining problem is that one can easily obtain the density from the wavefunction, but there is an infinite number of anti-symmetric wavefunction that give the same density. How is it possible to determine the ground state in that case? The answer comes from the work of Levy[12] in 1979 and Lieb[11] in 1983 who proposed to minimize the energy of the system by using a 'constrained-search' formulation.

Let's call Ψ_0 the ground state wavefunction and Ψ_{ρ_0}a wavefunction that also give the same ρ_0 ground state density. From the minimum-energy principle, it is possible to write:

$$\langle\Psi_{\rho_0}|\hat{H}\,|\Psi_{\rho_0}\rangle \geq \langle\Psi_0\big|\hat{H}\big|\Psi_0\rangle \qquad \textbf{32}$$

That it is possible to develop as:

$$\langle \Psi_{\rho_0} | \hat{\mathrm{T}} + \widehat{W}_{ee} | \Psi_{\rho_0} \rangle + \int dr v(r) \rho_0(r) \geq \langle \Psi_0 | \hat{\mathrm{T}} + \widehat{W}_{ee} | \Psi_0 \rangle + \int dr\, v(r) \rho_0(r) \quad \textbf{33}$$

Hence, we have:

$$\langle \Psi_{\rho_0} | \hat{T} + \widehat{W}_{ee} | \Psi_{\rho_0} \rangle \geq \langle \Psi_0 | \hat{T} + \widehat{W}_{ee} | \Psi_0 \rangle \quad \textbf{34}$$

which leads to a new functional usually called the Levy-Lieb Functional:

$$F_L[\rho_0] = \min_{\Psi \to \rho_0} \langle \Psi | \hat{T} + \hat{V}_{ee} | \Psi \rangle \quad \textbf{35}$$

The functional is equal to the previous HK functional if the density is v-representable. But by using the $F_L[\rho_0]$ functional there is no need for the density to be v-representable, the N-representability is enough. The term 'constraint' come from the fact that the search of the density in the minimization process is done not over all the N-particle Hilbert space, but only over the wavefunctions that give a density ρ_0 corresponding to the ground state density. In that case, the v-representability is not needed anymore, but one must limit his study to the ground state properties of a system.

The search of the ground state energy can now be done through a double minimization by using the Levy-Lieb functional as following:

$$E_0 = \min_{\rho} \left[\min_{\Psi \to \rho} \langle \Psi | \hat{H} | \Psi \rangle \right] \quad \textbf{36}$$

$$E_0 = \min_{\rho} \left[F_L[\rho] + \int dr\, v(r) \rho(r) \right] \quad \textbf{37}$$

First the minimization is done through all the wavefunctions associated to the same ρ and then the minimization is done through all the densities ρ.

The formalization of such a minimalization can be done by introducing a Lagrange multiplier μ (as it was done for the F_{HK}) to keep the number of electrons constrained during the minimization:

$$\delta \{ F_L[\rho] + \int d^3 r v(\mathrm{r}) \rho(r) - \mu \left(\int d^3 r\, \rho(r) - N \right) \} = 0 \quad \textbf{38}$$

which is equivalent to the Euler equation:

$$\frac{\delta F_L[\rho]}{\delta \rho(r)} + v(r) = \mu \quad \textbf{39}$$

II.2.3. Kohn Sham DFT

As primordial as the two theorems of Hohenberg and Kohn are for modern DFT, they do not allow the calculation of electronic structures. Indeed, they ensure the existence of a universal functional but do not provide a way to calculate it. And that is where the work of Kohn and Sham[7] is needed. Their idea was to replace the system by a fictitious noninteracting one subject to an external potential V_{KS}. In that case the term $\widehat{W}_{ee}$ in **Eq.12**. vanishes and the Hamiltonian for a noninteracting system can be written as a sum of single-particle Hamiltonians:

$$\widehat{H}_{KS} = \hat{T}_{KS} + \hat{V}_{KS} = \sum_i^N \hat{h}_{KS} = \sum_i^N \left(-\frac{1}{2}\nabla_i^2\right) + \sum_i^N v_{KS}(r) \quad \textbf{40}$$

To study a noninteracting system, then it is possible to use a single slater determinant of one electron orbitals ϕ_i to describe it. In that case, one can easily calculate the kinetic energy and density as following:

$$T_{KS} = -\frac{1}{2}\sum_i^N \int dr\, \phi_i^*(r)\nabla^2\phi_i(r)\,;\ \rho = \sum_i^N |\phi_i|^2 \quad \textbf{41}$$

The energy of the KS system is then:

$$E_{KS}[\rho(r)] = T_{KS}[\{\Psi\}] + \int d^3r v_{KS}(r)\rho(r) \quad \textbf{42}$$

The idea of Kohn and Sham is that this fictitious system will have the same density as the real one by using an effective external potential ν_{KS}. However, by considering only the kinetic part of a non-interacting system, terms are missing to get the 'real' kinetic energy functional ($T[\rho]$ as defined in the universal functional) of the 'real' interacting system. The next step is to introduce the exchange correlation energy E_{XC} which allows to add these missing terms in the energy of the system as follows:

$$E_{KS}[\rho(r)] = T_{KS}[\rho(r)] + E_v[\rho(r)] + E_{xc}[\rho(r)] + E_H[\rho(r)] \quad \textbf{43}$$

or by developing it a little bit more:

$$E_{KS}[\rho(r)] = T_{KS}[\rho(r)] + \int d^3r v(r)\rho(r) + E_{XC}[\rho(r)] + \frac{1}{2}\int d^3r d^3r' \frac{\rho(r)\rho(r')}{|r-r'|} \quad \textbf{44}$$

E_v comes from the external potential created by the nucleus; T_{KS} is the kinetic term of a noninteracting system and $E_H$the classical Coulombic repulsion term (or Hartree term), the remaining part of the energy is the exchange correlation energy. In other words, the exchange correlation energy is the energy that is missed by considering only the classical part of the electron-electron interaction and the kinetic energy of a noninteracting system. This becomes clearer by rewriting the exchange correlation energy functional as:

$$E_{xc}[\rho] = (T[\rho] - T_{KS}[\rho]) + (W_{ee}[\rho] - V_H[\rho]) \quad \textbf{45}$$

With $T[\rho]$ and $W_{ee}[\rho]$ coming from the 'real' potentials. The exchange correlation energy- functional contains both kinetic and potential energies. It is exact, but its exact form remains unknown, and approximations are necessary. At this point, we can note that despite being called the 'exchange-correlation' functional, it also contains a kinetic-energy contribution.

By decomposing the energy like they did, Kohn and Sham got an exact formulation of the energy functional of the system and a way to calculate $V_H[\rho]$ and $T_s[\rho]$ by using a single Slater determinant of one electron orbitals ϕ_i previously introduced in equation (**Eq.41**).

As both the interacting and noninteracting systems are subject to the minimization principle, they both fulfil the associated Euler-Lagrange equation. Moreover, as ν_{KS} is built to reproduce the density of the interacting system, then one can write the following equality:

$$\frac{\delta F_L[\rho]}{\delta\rho(r)} + v(r) = \frac{\delta T_{KS}[\rho]}{\delta\rho(r)} + \nu_{KS}(r) \quad \textbf{46}$$

From the definition of $F_L[\rho]$ and $E_{XC}[\rho]$, we can write the Kohn Sham potential as follows:

$$\nu_{KS}(r) = v(r) + \frac{\delta V_H[\rho(r)]}{\delta\rho(r)} + \frac{\delta E_{XC}[\rho(r)]}{\delta\rho(r)} \quad \textbf{47}$$

The KS potential being thus defined, we can obtain from the definition of Hamiltonian in **Eq.40**, the so-called Kohn-Sham equations:

$$-\frac{1}{2}\nabla^2\phi_i^{KS} + \nu_{KS}\phi_i^{KS} = \epsilon_i\phi_i^{KS} \quad \textbf{48}$$

With the density sets as:

$$\rho(r) = \sum_i^N |\phi_i^{KS}(r)|^2 \quad \textbf{49}$$

Because of the dependence of the KS-potential v_{KS} to the density, these equations are solved self-consistently. Once solved, the KS equations provide from the knowledge of ϕ_i^{KS} the GS energy and density, with an incertitude related to the exchange-correlation term.

In the end, orbitals were re-introduced in the DFT, but one must keep in mind that these orbitals are fictitious ones and are created only from a dummy system with the same density as the real one. They should not have any physical senses. That being said, the Kohn-Sham orbitals energies are commonly used, but their properties need to be considered with great care.[13]

Finally, Kohn and Sham provided a practical way to calculate ground state observables under the framework described Hohenberg and Kohn. The definition (**Eq.43**) is exact, but the exchange correlation term is unknown and need to be approximated in practice. Hence, the quality of the KS-DFT calculations depends on the quality of the approximation made on E_{XC}.

II.2.4. Exchange correlation functionals

The exchange correlation potential, and by extension, the exchange correlation energy functional must be approximated. Even though its existence is assured, its expression is unknow and its approximation is the milestone of many DFT related works. As the quality of a calculation is highly dependent on the choice of the functional, many functionals have been developed throughout the years, leading to more and more complex expressions. In 2001, Perdew ranked the various approximations through a 'Jacob's ladder' made of various rung of increasing complexity.[14] In the first rung stands the simplest approximation, the local density approximation while in the highest rung stand the fully non-local approximations. In this part, we will only present the exchange correlation functionals used in this thesis.

II.2.4.a) Some constraints on the exchange-correlation functionals

Before discussing exchange-correlation functionals approximation, let us detail two important quantities for exchange-correlation functionals: the exchange and correlation holes.

An expression to the exchange-correlation hole can be obtained by considering the pair density $\rho_2(r_1, r_2)$ which describes the probability to find two electrons at r_1 and r_2 independently of the positions of the others. For a system described by a wavefunction $\Psi[\rho]$ the pair density can be written as:

$$\rho_2(r_1, r_2) = N(N-1) \sum_{\sigma_i} \int d^3r_3 \dots d^3r_N \Psi^*(x_1, x_2, \dots, x_N)\Psi(x_1, x_2, \dots, x_N) \quad \textbf{50}$$

We can decompose $\rho_2(r_1, r_2)$ by introducing the exchange-correlation hole $h_{xc}(r_1, r_2)$ such as ρ_2 becomes:

$$\rho_2(r_1, r_2) = \rho(r_1)[\rho(r_2) + h_{xc}(r_1, r_2)] \quad \textbf{51}$$

Because $\rho_2(r_1, r_2) > 0$, we have:

$$h_{xc}(r_1, r_2) \geq -\rho(r_2) \quad \textbf{52}$$

After rearrangement of **Eq.51** and integration over r_2 we get the sum rule for the exchange-correlation hole:

$$\int h_{xc}(r_1, r_2) dr_2^3 = -1 \quad \textbf{53}$$

The next step is to separate the exchange contribution and the correlation one. By considering a single-determinant wavefunction (such as the KS one) no correlation is accounted for, thus we can rewrite:

$$\rho_2^{KS}(r_1, r_2) = \rho(r_1)[\rho(r_2) + h_x(r_1, r_2)] \quad \textbf{54}$$

For the same reasons, the exchange hole satisfies:

$$h_x(r_1, r_2) \geq -\rho(r_2) \; and \int h_x(r_1, r_2) dr_2^3 = -1 \quad \textbf{55}$$

The last important property of the exchange hole is its non-positivity:

$$h_x(r_1, r_2) \leq 0 \qquad \textbf{56}$$

This can be demonstrated by writing the exchange energy as a function of the one-particle density matrix defined in terms of the KS occupied orbitals (as it is not intended to go through the density matrices, this is not presented here, however, proofs can be found in various books/papers.[15–17] We can still note that ρ and ρ_2 are the diagonal elements of the one and two particle density matrices respectively.)

Finally, the exchange energy functional can be rewritten in term of the exchange hole as:

$$E_X[\rho] = \int d^3r_1 d^3r_2 \rho(r_1)\epsilon_X[\rho](r_1);\ with\ \epsilon_X[\rho](r_1) = \frac{1}{2}\int \frac{h_X(r_1, r_2)}{|r_1 - r_2|} d^3r_2 \qquad \textbf{57}$$

This last step also requires the use of the two-particle density matrix to first express the exchange energy.

A similar development can be done for the correlation hole which is defined as:

$$h_c(r_1, r_2) = h_{xc}(r_1, r_2) - h_x(r_1, r_2) \qquad \textbf{58}$$

We get immediately from the sum rules of the exchange-correlation and exchange hole the sum rule for the correlation hole:

$$\int d^3r_2 h_c(r_1, r_2) = 0 \qquad \textbf{59}$$

Finally, to exhibit the dependence of $E_C[\rho]$ to the correlation hole we must consider the adiabatic connection formalism. The principles of this concept will be detailed in the section dedicated to the ACFDT-RPA (**II.3**), here we will only consider the results as given in Toulouse's work.[16] After some work, the correlation energy can be rewritten as a function of correlation hole as:

$$E_C[\rho] \int d^3r \epsilon_c[\rho](r_1)\,; with\ \epsilon_c[\rho](r_1) = \frac{1}{2}\int \frac{d^3r_2}{|r_1 - r_2|}\int_0^1 d\lambda h_c^\lambda(r_1, r_2) \qquad \textbf{60}$$

With $\int_0^1 d\lambda h_c^\lambda(r_1, r_2)$ the coupling constant hole. λ is a coupling constant used to represent the level of interaction of a system along the adiabatic connection.

The h_c^λ is subject to the same sum rule that h_c:

$$\int d^3 r_2 h_c^{\lambda}(r_1, r_2) = 0 \quad \textbf{61}$$

Finally, h_c^{λ} is also subject to the cusp condition:[18]

$$h_c^{\lambda'}(r, r) = \lambda h_c^{\lambda}(r, r) \quad \textbf{62}$$

With $h_c^{\lambda'}(r, r)$ the first order derivative of the spherically averaged correlation hole that we can write as following, with r_{12} the distance between the electron r_1 and r_2, $S(r_1, r_{12})$ is the sphere centered at r_1 with a radius of r_{12}.

$$h_c^{\lambda'}(r_1, r_2) = \frac{\partial}{\partial r_{12}} \left(\frac{1}{4\pi r_{12}^2} \int_{S(r_1, r_{12})} h_c(r_1, r_2 + r_{12}) dr_{12} \right)_{r_{12}=0} \quad \textbf{63}$$

II.2.4.b) Local Density Approximation

The first approximation, called the Local Density Approximation (LDA) was already present in the work of Kohn and Sham in 1965.[7] The idea is to calculate the exchange correlation energy of a system by assimilating it to a homogeneous electron gas. Despite not being a very realistic model for most of the chemical systems, it has the enormous advantage to be a system whose exchange energy is exactly known.

In the LDA model, one assumes that the exchange correlation energy can be written as follows:

$$E_{XC}^{LDA} = \int dr^3 \, \rho(r) \epsilon\big(\rho(r)\big) \quad \textbf{64}$$

With $\epsilon(\rho)$ the exchange correlation energy per particle which can be then split into two contributions as follows:

$$E_{XC}[\rho] = E_X[\rho] + E_C[\rho] \quad \textbf{65}$$

The exchange contribution is evaluated based on the model of a uniform electron gas. For such a system, it can be shown that the exchange energy per electron is:[15]

$$\epsilon_X = -\frac{3}{4\pi}\frac{(9\pi/4)^{1/3}}{r_s} \quad \textbf{66}$$

With r_s the Seitz radius (the radius of a sphere which on average contains one electron). It must be noted that this exchange energy is due to the Pauli exclusion principle.

Such an expression does not exist for the correlation energy part, but quantum Monte Carlo simulations done by Ceperley and Alder in 1980[19] were used to fit parametrized functions which satisfy the two known limits. Indeed, the correlation contribution can be expressed in term of r_s in two distinct cases: the high density ($r_s \to 0$) with weak correlation and the low density ($r_s \to \infty$) with strong correlation. The two most used are the parametrizations of Vosko, Wilk and Nusair in 1980[20] and the one of Perdew and Wang in 1992.[21] More details on the nature of the correlation energy per particle can be found in a recent review on the approximations done in DFT.[16]

In practice the LDA approximation is not so bad despite being built on strong simplifications. It gives good structural, elastic, and vibrational properties (even though the presence of d-metal deteriorates the results). However, the binding energies are way too negative, and the activation energies are not good either. The exchange part calculated under the LDA approximation is typically underestimated while the correlation one is overestimated. Moreover, the LDA suffers from self-interactions issues. It generally gets worse with small systems where the spatial variations of the density can be important, and it tends to be a better approximation as the systems growth and have slowly varying density.

Beyond the 'not so bad' results of the LDA lies the fact that the LDA is based on a physical system (the uniform electron gas). Hence it appears the LDA exchange hole fulfils the negativity and sum-rule (**Eq.55** and **Eq.56**) while the LDA correlation hole fulfils the sum-rule (**Eq.61**) and electron-electron cusp conditions (**Eq.62**). The spherical average of the exchange-correlation hole is also relatively well described by the LDA.[22] Moreover, there is an error cancelation between the exchange and the correlation energies.[23] Among the drawbacks of the LDA, there is a self-interaction error because the LDA correlation functional does not vanish even if the system only has one electron.

II.2.4.c) Generalized Gradient Approximation

The Gradient Expansion Approximation (GEA) functionals are built by assuming that the density is not homogenous and that its variations are important. In this new class of exchange correlation functionals,

corrective terms depending on the gradient of the density and higher-order derivative of the density are added to the LDA expression.

However, such a development did not lead to the expected accuracy. Indeed, while the LDA functional respected numerous physical properties for the exchange and correlation holes, the addition of the gradient of the density leads to the loss of the negativity and the respect of the sum rules for the exchange correlation holes. To avoid such failures, brute force restrictions were added in order to impose the validity of the sum rules and negativity of the exchange correlation holes, this new family of functional is called Generalized Gradient Approximation (or GGA).

The general form of the exchange correlation energy of a GGA functionals is the following (without the spin dependence):

$$E_{XC}^{GGA} = \int dr^3 \epsilon_{XC}^{GGA}(\rho(r), \nabla\rho(r)) \qquad \textbf{67}$$

With ϵ_{XC}^{GGA} a function relative to the GGA functional. Many GGA functionals were developed for various applications, leading to a very vast ecosystem. The one that will be mainly use in this work is the Perdew-Burke-Ernzerhof (PBE) functional.[24] GGA functionals are often called semi-local or non-local functionals due to their dependence to not only the density but also its gradient, this terminology can be confusing as it not based on a mathematical definition. As for the LDA, the value of the functional at a point r_1 is independent to the value of the functional at any other point r_2 of the space.

In general, GGA functionals are an improvement over the LDA. Many energy-related values such as the total energy, the atomization energy or the energy barrier are improved with the addition of the gradient of the density. Metallic, ionic, covalent, and even, in a relative extent, hydrogen bonds are well described but GGA (as for LDA) cannot grasp the dispersive forces in a system. Moreover, there is a tendency to overestimate the bond length.

The PBE exchange correlation functional, corrected for dispersion forces using the dDsC scheme, was used throughout this work. Its reasonable computational cost and good performances during the benchmark justify its application to study the platinum species during the calcination and reduction step of the catalyst preparation.

II.2.4.d) Meta-GGA

Following the family of the GGAs, come the meta-GGA functionals which depend not only on the gradient of the density but also on the Laplacian $\nabla^2\rho$ of it and on the kinetic energy density associated to a single determinant wave function (typically the KS one) τ. Without considering the spin, the exchange correlation functional can be written as follows:

$$E_{XC}^{mGGA} = \int dr^3 \epsilon_{XC}^{mGGA}\left(\rho(r), \nabla\rho(r), \nabla^2\rho(r), \tau(r)\right) \quad \textbf{68}$$

As for GGA, meta-GGA can be semiempirical as it is the case for the PKZB[25,26] one, or fully nonempirical with for example the TPSS[27] one. In general, meta-GGA functionals tend to give better results than the GGAs in term of electronic properties and geometries for most systems.

In this work, three meta-GGA were considered: SCAN, TPSS and RTPSS. However, due to their performance in our gas phase benchmark we did not used them to calculate properties of supported systems.

II.2.4.e) Hybrid functionals

In 1993, Becke proposed to add a fraction of the exact exchange to the GGA exchange correlation.[28] Three years after this first functional which was based on three parameters, he proposed a simpler functional based on the same idea:[29]

$$E_{XC}^{hyb} = aE_X^{exact} + (1-a)E_X^{GGA} + E_C^{GGA} \quad \textbf{69}$$

This functional, proposed by Becke, is known as the one-parameter hybrid functional (1H) (in opposition the first one based on 3 parameters was called 3H). The parameter 'a' is used to tune the amount of the 'exact' exchange added to the functional. The exact exchange considered is calculated according to the Hartree Fock method, but here the KS orbitals are used. In other approximations, exchange correlation functionals of other families such as LDA (in the case of the 3H[28] functional for example), or meta-GGA (in the case of the TPSSh) can also be used to build the final exchange correlation functional. In the most famous hybrid functional B3LYP,[30] a mix of one GGA functional (B88[31]) and LDA is used for the exchange part while another GGA (LYP[32]) is combined with an LDA part for the correlation. The VWN[20] parametrization was used for the LDA correlation part of the B3LYP. Adding a fraction of the HF exchange decreases the self-interaction error, however, adding too much of

it will worsen the results notably by diminishing the compensation of errors usually occurring between the local (or semilocal) exchange correlation functionals.

In a similar family as the hybrid functionals, can be classified the range separated hybrid functionals. The idea behind such functionals is that the approximation of the exchange correlation energy will not be the same as a function of the distance between electrons.

For example, the HSE[33] exchange correlation functionals use a mix of HF and PBE exchange for the short range, while for the long range, there is only the PBE exchange contribution. For the short-range description, the amount of HF for the exchange is fixed with a = 0.25. The general equation of the range separated hybrid HSE is the following:

$$E_{XC}^{HSE}[\Psi] = aE_X^{exact,sr,\mu}[\Psi] + (1-a)E_X^{PBE,sr,\mu}[\rho] + E_X^{PBE,lr,\mu}[\rho] + E_C^{PBE}[\rho] \qquad \mathbf{70}$$

With 'sr' and 'lr' standing for short and long range, μ is the range separation parameter and ψ the DFT wavefunction corresponding the electronic density ρ of the system.

In this work, we considered three hybrid functionals, namely B3LYP, PBE0 and HSE06. The latter one being a range-separated hybrid. Based on the benchmark results, single-point calculations were performed on supported systems to get the electronic energies at the HSE06 level.

II.2.5. Dispersion corrections

Unless using highly sophisticated functionals, one will miss the description of the London dispersion forces. Some widely used functional such as the PBE GGA can describe short range interactions such as the hydrogen bonds but will fail as the density of both fragments will stop overlapping. The principal reason of such failures is that these functionals are local.

In the same spirit as the 'Jacob's Ladder' of Perdew,[14] Klimes and Michaelides define a 'starway to heaven' classification of the description of the dispersive forces in DFT.[34] Two main approaches have been developed: the first simply adds to the electronic energy calculated through the KS workflow a semiempirical dispersion correction term accounting for the dispersion forces:

$$E_{disp} = -s\sum_{A=1}^{N}\sum_{B=1;B>A}^{N} f(R_{AB})\frac{C_6^{AB}}{R_{AB}^6} \qquad \mathbf{71}$$

With s a scaling parameter depending on the functional used, f a damping function, C_6^{AB} the London dispersion coefficient and R_{AB} the distance between the A and B atoms.

In this method called DFT-D by Grimme,[35] the London dispersion coefficients are tabulated.[36] In his first version, the DFT-D2,[35] Grimme only took into account the C_6^{AB} term, it was later refined through the DFT-D3[37] which also took into account the two-body term C_8 (which decays in $\frac{1}{R^8}$) and the three-body term C_9 (which decays in $\frac{1}{R^9}$). Different methods to determine the dispersion coefficients lead to different flavour of the DFT-D3.[38–40] In the same spirit, the dDsC[41,42] correction was developed by S. N. Steinmann and C. Corminboeuf. It is also based on a dispersive term which is added to the electronic energy, but the damping function and dispersion coefficient are charge density dependent and not only based on molecular geometry as previously. These corrections stand in the first and second step of the 'starway to heaven'. These methods successfully capture a part of the nonlocal component missing in the correlation functional at a small computational cost.

The next step of correction is made of the nonlocal van der Waals density functionals whose form is the following:

$$E_C^{nl} = \frac{1}{2}\int\int dr_1\, dr_2 \rho(r_1)\rho(r_2)\phi(r_1, r_2) \qquad \textbf{72}$$

With ϕ a correlation kernel similar to the Coulombic one, but more complicated and with an asymptotic behaviour in $\mathcal{O}(1/|r_1 - r_2|^6)$. Two main families exist, the van der Waals density functionals (vdW-DF)[43] and the Vydrov-Van Voorhis (VV)[44–46] functionals. They are more computationally expensive than the previously detailed methods, but they do not depend on empirical fitting.

The next and last step is fulfilled with methods going beyond the pairwise additivity.[34] There are various approaches such as methods named Many-Body dispersion (MBD) which derive from an atom centered approach, the ACFDT-RPA which uses KS-orbitals or multi-reference exchange correlation functionals. The Random Phase Approximation (RPA) is still a highly expensive method and can be compared to what post HF methods (notably MP2) are to the wavefunction world. Some functionals such as the range separated double hybrids are also able to correctly describe the long-range correlation. These functionals are inspired by a multideterminant extension of the KS scheme and the first of this kind was developed in 2005.[47]

In this work, dispersion corrections were included using the dDsC scheme to correct the PBE exchange correlation functional and with the optPBE exchange correlation functional.

II.3. ACFDT-RPA

ACFDT stands for Adiabatic Connection Fluctuation Dissipation Theorem and is one of the existing formulations which uses the random phase approximation (RPA) formalism. In this formulation, the goal is to obtain an exact expression for the exchange correlation energy thanks to the ACFD theorem by varying the electron-electron interaction of the system from 0 (KS system) to 1 (fully interacting system). However, the exact expression given by the ACFD formalism is not analytically solvable and RPA is one possible approximation that can be made to obtain the correlation functional, E_C, of a system.

The derivation of the correlation energy is done as follows.

In the adiabatic connection formalism, a coupling strength constant λ is used to link the non-interacting system ($\lambda = 0$) to the real one ($\lambda = 1$). By considering the Hamiltonian along the adiabatic connection:

$$\widehat{H}(\lambda) = \widehat{H}_0 + \lambda \widehat{H}_1(\lambda) \quad \textbf{73}$$

That can be developed as:

$$\widehat{H}(\lambda) = -\sum_{\mathrm{i}}^{\mathrm{N}} \frac{\nabla_i^2}{2} + \sum_{i}^{N} v_\lambda(r_i) + \sum_{i>j}^{N} \frac{\lambda}{2|r_i - r_j|} \quad \textbf{74}$$

where v_λ is the external potential dependent of λ. If $\lambda = 1$, then it represents the real external potential v. This potential varies along the variation of λ in order to keep the density of the system constant. We can note the approximation done on the kinetic part of the Hamiltonian which, in this formulation, does not depend on the coupling strength constant λ.

The reference Hamiltonian ($\lambda = 0$) describes a non-interacting system, similarly to the KS one:

$$\widehat{H}_0 = -\sum_{\mathrm{i}}^{\mathrm{N}} \frac{\nabla_i^2}{2} + \sum_{i}^{N} v_{KS}(r_i) \quad \textbf{75}$$

And the perturbative Hamiltonian $\widehat{H}_1$ is thus given by:

$$\widehat{H}_1 = \sum_{i>j}^{N} \frac{1}{2|r_i - r_j|} + \frac{1}{\lambda} \sum_{i}^{N} [v_\lambda(r_i) - v_{KS}(r_i)] \quad \textbf{76}$$

By denoting the ground state of such Hamiltonian by the normalized wavefunction $|\Psi_\lambda\rangle$ such as $\widehat{H}(\lambda)|\Psi_\lambda\rangle = E_\lambda|\Psi_\lambda\rangle$, we deduce from the Hellmann-Feynman theorem:

$$\frac{dE_\lambda}{d\lambda} = \left\langle \Psi_\lambda \left| \frac{\partial \widehat{H}_\lambda}{\partial \lambda} \right| \Psi_\lambda \right\rangle = \left\langle \Psi_\lambda \left| \sum_i^N \frac{\partial v_\lambda(r_i)}{\partial \lambda} + \sum_{i>j}^N \frac{1}{2|r_i - r_j|} \right| \Psi_\lambda \right\rangle \quad \textbf{77}$$

By using the density operator and the property that $\langle \Psi_\lambda|\hat{n}(r)|\Psi_\lambda\rangle = \rho(r)$ and the fact that the density is independent of the coupling factor λ we have:

$$\frac{dE_\lambda}{d\lambda} = \int d^3r \rho(r_1) \frac{\partial v_\lambda(r_1)}{\partial \lambda} + \frac{1}{2}\int d^3r_1 d^3r_2 \frac{\langle \Psi_\lambda|\hat{n}(r_1)\hat{n}(r_2)|\Psi_\lambda\rangle - \rho(r_1)\delta(r_1 - r_2)}{|r_1 - r_2|} \quad \textbf{78}$$

By integration between $\lambda = 0$ and $\lambda = 1$, the energy of the interacting system is given as:

$$E = E_0 + \int_0^1 \frac{dE_\lambda}{d\lambda} d\lambda \quad \textbf{79}$$

From the previous expression, we deduce:

$$E = E_0 + \int d^3r_1 \rho(r_1)[v_{\lambda=1}(r_1) - v_{KS}(r_1)] + \frac{1}{2}\int_0^1 d\lambda \int d^3r_1 d^3r_2 \frac{\langle \Psi_\lambda|\hat{n}(r_1)\hat{n}(r_2)|\Psi_\lambda\rangle - \rho(r_1)\delta(r_1 - r_2)}{|r_1 - r_2|} \quad \textbf{80}$$

With E_0 which can be obtained through:

$$E_0 = \langle \Psi_0|\widehat{H}_0|\Psi_0\rangle = T_{KS}[\rho(r)] + \int d^3r v_{KS}(r)\rho(r) \quad \textbf{81}$$

Hence, we have the following expression for the energy:

$$E = T_{KS}[\rho(r_1)] + \int d^3r_1 \rho(r_1) v_{\lambda=1} + \frac{1}{2}\int_0^1 d\lambda \int d^3r_1 d^3r_2 \frac{\langle \Psi_\lambda|\hat{n}(r_1)\hat{n}(r_2)|\Psi_\lambda\rangle - \rho(r_1)\delta(r_1 - r_2)}{|r_1 - r_2|} \quad \textbf{82}$$

Knowing that the ground state energy as written in the KS-DFT formalism:

$$E_{KS}[\rho(r_1)] = T_{KS}[\rho(r_1)] + \int d^3r_1 v(r_1)\rho(r_1) + E_{XC}[\rho(r_1)] + \frac{1}{2}\int d^3r_1 d^3r_2 \frac{\rho(r_1)\rho(r_2)}{|r_1 - r_2|} \quad \textbf{83}$$

Finally, the exchange correlation energy, E_{XC} is expressed as:

$$E_{XC} = \frac{1}{2}\int_0^1 d\lambda \int d^3r_1 d^3r_2 \frac{\langle\Psi_\lambda|\delta\hat{n}(r_1)\delta\hat{n}(r_2)|\Psi_\lambda\rangle - \rho(r_1)\delta(r_1 - r_2)}{|r_1 - r_2|} \quad \textbf{84}$$

Where we introduced the density fluctuation operator $\delta\hat{n}(r) = \hat{n}(r) - \rho(r)$.

This new expression of the exchange-correlation energy was obtained from the Adiabatic Connection theorem, now we will use the Fluctuation Dissipation Theorem (FDT) to get an expression of E_{XC} in term of an external perturbation to the system.

To avoid the calculation of the many-body wavefunction $|\Psi_\lambda\rangle$, we use the linear density response function χ, which describes the change in the density due to a perturbation in the external potential v. For the system dependent of λ, it is expressed as:

$$\chi^\lambda(r, r', \omega) = \frac{\delta n}{\delta v} \quad \textbf{85}$$

The FDT provides a relation between the density fluctuation operator and the response of the system, hence the problematic quantity $\langle\Psi_\lambda|\delta\hat{n}(r)\delta\hat{n}(r')|\Psi_\lambda\rangle$ can be written as:[48,49]

$$\langle\Psi_\lambda|\delta\hat{n}(r_1)\delta\hat{n}(r_2)|\Psi_\lambda\rangle = -\frac{1}{\pi}\int_0^\infty d\omega \mathrm{Im}\chi^\lambda(r_1, r_2, \omega) \quad \textbf{86}$$

The exchange correlation energy can then be rewritten as a function of χ^λ:

$$E_{XC} = \frac{1}{2\pi}\int_0^1 d\lambda \int \int_0^\infty d\omega\, d^3r_1 d^3r_2 \frac{\chi^\lambda(r_1, r_2, i\omega) - \rho(r_1)\delta(r_1 - r_2)}{|r_1 - r_2|} \quad \textbf{87}$$

The calculation of $|\Psi_\lambda\rangle$ along the integration path has been replaced by the calculation of χ^λ whose exact form is not known either. However, χ^λ and the response function of the non-interacting system $\chi^{\lambda=0}$ (or χ^{KS}) are linked through a Dyson equation such as:

$$\chi^\lambda_{RPA}(r_1, r_2, i\omega) = \chi^{KS}(r_1, r_2, i\omega) + \int d^3r_3 d^3r_4 \chi^{KS}(r_1, r_3, i\omega) \left[\frac{\lambda}{|r_3 - r_4|} + f^\lambda_{XC}(r_3, r_4, i\omega) \right] \chi^\lambda_{RPA}(r_4, r_2, i\omega) \quad \textbf{88}$$

With f^λ_{XC} the xc-kernel defined as:

$$f^\lambda_{XC}(r_1, r_2, i\omega) = \frac{\partial v^\lambda_{XC}(r_1)}{\partial \rho(r_2, \omega)} \quad \textbf{89}$$

This quantity is the new 'problematic' one that needs to be approximated. In the direct Random Phase Approximation (dRPA or more generally RPA), one approximates the λ dependent exchange correlation kernel to 0 and only the Hartree part of the kernel ($\frac{1}{|r_1 - r_2|}$) is kept. The correlation energy within the ACFDT-RPA[50] formalism can then be calculated.

The exchange contribution can be deduced from **Eq.87** and by considering that the exchange-correlation term is reduced to the exchange in case of a non-interacting system. Thus, by considering $\lambda = 0$ we have:

$$E_X = \frac{1}{2\pi} \int_0^1 d\lambda \int \int_0^\infty d\omega \, d^3r_1 d^3r_2 \frac{\chi^{KS}(r_1, r_2, i\omega) - \rho(r_1)\delta(r_1 - r_2)}{|r_1 - r_2|} \quad \textbf{90}$$

The expression of χ^{KS} is explicitly known in term of the KS orbitals and it can be shown that E_X is equivalent to the exchange energy in the Hartree-Fock theory but expressed with the KS orbitals.

$$E_X = \sum_{m,n} \int d^3r_1 d^3r' \frac{\phi^*_m(r_1)\phi_n(r_2)\phi^*_n(r_1)\phi_m(r_2)}{|r_1 - r_2|} \quad \textbf{91}$$

From there, we can rewrite the correlation energy E_c as $E_C = E_{XC} - E_X$. If we consider the RPA approximation, we have for E_C:

$$E_C^{RPA} = \frac{1}{2\pi}\int_0^1 d\lambda \int\int_0^\infty d\omega\, d^3r_1 d^3r_2 \frac{\chi_{RPA}^{\lambda}(r_1, r_2, i\omega) - \chi^{KS}(r_1, r_2, i\omega)}{|r_1 - r_2|} \quad \textbf{92}$$

By rewriting E_C with the formalism $Tr\{A(i\omega)B(i\omega)\} = \int d^3r d^3r' A(r, r', i\omega)B(r, r', i\omega)$ as in Niquet et al.[51] work.

$$E_C = \frac{1}{2\pi}\int_0^1 d\lambda \int_0^\infty d\omega\, \mathrm{Tr}\left\{\frac{\chi_{RPA}^{\lambda}(i\omega) - \chi^{KS}(i\omega)}{[r_1 - r_2|}\right\} \quad \textbf{93}$$

Finally, the integration over λ can be avoided from the fact that $f_{XC}^{\lambda} = 0$ in the RPA approximation. From **Eq.88**, we have the relation $\chi_{RPA}^{\lambda} = \frac{\chi^{KS}}{1-\lambda\chi^{KS}\alpha}$ where, for the sake of clarity the electron-electron operator is written as "α". Hence, from the derivation of the logarithm we have:

$$\mathrm{Tr}\left\{\frac{\chi_{RPA}^{\lambda}(i\omega)}{|r_1 - r_2|}\right\} = -\frac{\partial}{\partial\lambda}\mathrm{Tr}\left\{\ln\left[\frac{1 - \lambda\chi^{KS}(i\omega)}{|r_1 - r_2|}\right]\right\} \quad \textbf{94}$$

Finally, we can write the correlation energy as it is usually found under the ACFDT-RPA formalism:

$$E_C = \frac{1}{2\pi}\int_0^1 d\lambda \int_0^\infty d\omega\, \mathrm{Tr}\{\ln(1 - \chi^{KS}(i\omega)\alpha) + \chi^{KS}(i\omega)\alpha\} \quad \textbf{95}$$

With $\alpha(r_1, r_2) = \frac{1}{[r_1 - r_2|}$

In the VASP implementation of the ACFDT-RPA, the correlation energy is added to the Hartree-Fock energy calculated using KS orbitals. In this work, we will use orbitals obtained from GGA calculations. Hence the energy of the system is given by:

$$E = E_{HF}[\{\Psi_{KS}\}] + E_C^{RPA} \quad \textbf{96}$$

Using such a decomposition is advantageous on different points. First of all, by considering the Hartree-Fock exchange, one gets rid of the spurious self-interaction effect obtained by only considering the Hartree energy in the calculation of the exchange energy in KS-DFT. Secondly, the RPA correlation energy is

fully non-local and hence takes into account the long-range vdW interaction. However, there are some drawbacks due to the relatively harsh approximations made for the exchange-correlation kernel. Notably, the short-range correlation is not well described by the RPA. In order to improve the standard RPA presented here, various developments are undertaken. Among them we can note the RPA+, SOSEX, SE…39,52 but they do not constitute an absolute improvement over the standard RPA and each method can be better suited for specific calculations. More details on the performances of the RPA and on the protocol followed to calculate the correlation energy will be provided in the Chapter III.

II.4. Periodic boundary calculations

II.4.1. Plane waves

The wavefunctions which are the solutions of the KS equations need to be spawned in a basis set. As the work presented in this thesis was done by using the VASP periodic software[53,54] using only a plane wave basis set, we only detail this kind of basis set here. That being said, other families of basis sets exist with intrinsic pros and cons.

The plane waves basis set is particularly useful when periodic systems (solids, surfaces…) are studied. Such infinite systems require that the wavefunction is calculated for an infinite number of electrons and that all the wave functions are extended over the entire system. A way to solve these two problems is to use the Bloch's theorem.

The Bloch's theorem states that in a periodic solid each electronic wave function can be written as the product of a cell-periodic part and a wavelike part:

$$\psi_{nk} = e^{ik.r} u_{nk} \qquad \textbf{97}$$

With *n* an index allowing to order the wavefunction and k is a wave vector in the first Brillouin zone. As u_{nk} has the same periodicity as the system, it can be extended as:

$$u_{nk}(r) = \frac{1}{\sqrt{\Omega}} \sum_{G} c_{nk,G}\, e^{iG.r} \qquad \textbf{98}$$

With G the reciprocal lattice vector. The plane wave can then be extended through a finite grid of k-points to sample the first Brillouin zone. The number of plane waves used to expand the wave function is controlled by a quantity called the cutoff energy: E_{cut}. Ideally these plane waves should be expanded in an infinite basis set, but, for practical reasons, one has to use a finite basis set with a cutoff energy defined as:

$$E_{cut} = \frac{\hbar^2}{2m}|k+G|^2 \qquad \textbf{99}$$

The previous truncated expansion can be rewritten to keep only the wave function with a kinetic energy smaller than E_{cut}. Hopefully the coefficients for the small kinetic energy wave function are the most important.[55] In practice, one can use a higher value of cutoff in order to increase the number of plane waves and to reduce the magnitude of error in theory.

The plane waves basis set has many advantages: it allows an easy calculation of the forces stress through the Hellmann-Feynman theorem, does not suffer from the basis set superposition error (BSSE) and plane waves are orthogonal between each other's. But as the number of plane waves used depends on the volume of the cell, calculation of gas phase molecule (with the supercell approach) is expensive. Moreover, the description of the core electrons is a problem with a plane wave approach. Indeed, a very high number of plane waves are required to correctly describe the rapid oscillations of the wavefunction of such electrons. A way to bypass this issue is to use pseudopotentials to simplify the description of the core electrons.

Supported systems were calculated using an energy cutoff of $E_{cut} = 400$ eV. However, for gas phase systems, a higher cutoff of 800 eV was considered because of the pseudopotential requirement for the ACFDT-RPA calculations. In all cases, only the Γ point of the Brillouin zone was considered since big enough supercells were employed.

II.4.2. Pseudopotential: PAW method

II.4.2.a) Pseudopotential

All the electrons do not have the same impact on the chemistry of a system. The valence electrons are more important in the description of the chemistry of a system than the core electrons. This is the main idea behind the pseudopotential formalism: dividing the electrons into two groups, the valence electrons and the inner core electrons.

The idea of limiting the study to the valence electrons started with Fermi in 1934,[56] and Hellmann in 1935[57]. But the pseudopotentials did not receive much attention until 1959 and the work of Phillips and Kleinman.[58,59] Firstly, constructed thanks to experimental data and on the cancelation idea of Phillips and Kleinman, they took a new direction with Topp and Hopfield[60] by being obtained through ab initio calculations.

In practice, a radius cutoff r_c is defined beyond which the wavefunction is identical to the all-electron wavefunction. But for radius lower than r_c then the effect of all the core electrons is averaged through an effective potential. One can see a schematic comparison between a pseudopotential wavefunction and an all electron one in **Figure II-2**.

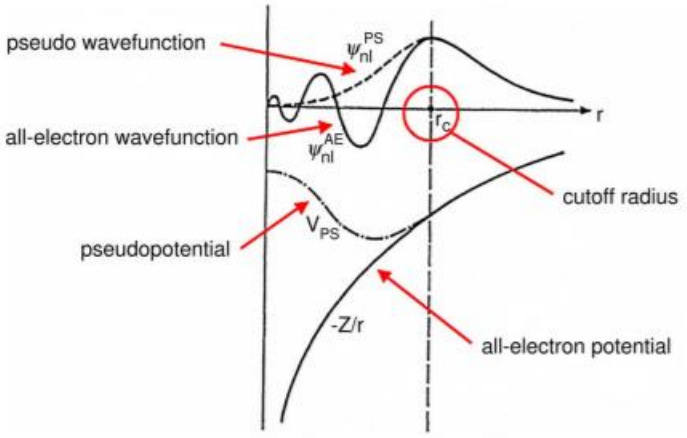

Figure II-2. Comparison between all electron and pseudo potential wavefunction according the distance to the nucleus.[55]

Many types of pseudopotentials exist, depending on what constraints they respect, how they are built and their properties. In this work, the calculations were done using the so-called PAW pseudopotentials.

II.4.2.b) PAW formalism

The idea of the Projector Augmented Wave[61] (PAW) is derived from older pseudo potentials[53,62,63] and was firstly developed by Blöchl.[64] The principle is to divide the all-electron wavefunction into a linear combination of wavefunctions and to link the true all electron wavefunction $|\Psi\rangle$ with some auxiliary smooth wavefunctions $|\widetilde{\Psi}\rangle$ thanks to a linear operator $\hat{\Gamma}$.

$$|\Psi\rangle = \hat{\Gamma}|\widetilde{\Psi}\rangle \qquad \textbf{100}$$

To do that the space is divided into two regions, the augmentation region around the atoms and the interstitial regions. The operator does not need to modify the wavefunction in the interstitial region (away from the nucleus) as the true all electron wavefunction is already smooth enough.

In the augmentation region, the all-electron (or true) wavefunction $|\Psi\rangle$ is expanded in a set of partial waves $|\phi\rangle$. These wavefunctions are solutions to the all-electron KS-DFT equation for isolated atom under the frozen core approximation. They will be used as a basis set to expand the true wavefunction near the nucleus ($|r - R_R| < r_{c,R}$):

$$|\Psi(r)\rangle = \sum_i c_i \ |\phi_i(r)\rangle \qquad \textbf{101}$$

With i an index referring to a site R, the angular momentum indices *(l,m),* the atom type and the reference energies of the corresponding KS-DFT equation. $r_{c,R}$ defines the radius of the augmentation region.

Then for each of the partial waves $|\phi_i\rangle$ a pseudo partial waves $|\widetilde{\phi}_i\rangle$ is generated thanks to $\hat{\Gamma}$. They are built to be smooth functions inside the augmentation sphere and to match the all-electron partial wavefunction $|\phi_i\rangle$ outside the augmentation sphere.

The pseudo wavefunction $|\widetilde{\Psi}\rangle$ can finally be expanded in term of the previously detailed quantity inside the augmentation region (102) and outside (103).

$$|\widetilde{\Psi}\rangle = \sum_i c_i \, |\widetilde{\phi_i}\rangle \qquad \textbf{102}$$

$$|\widetilde{\Psi}\rangle = |\Psi\rangle \qquad \textbf{103}$$

With c_i undetermined expansion coefficients. The last step is to introduce a projector function $|\widetilde{p_i}\rangle$ such as:

$$\langle \widetilde{p_i} | \widetilde{\phi_j} \rangle = \delta_{ij} \qquad \textbf{104}$$

Which allows to recover the c_i coefficient thanks to:

$$\langle \widetilde{p_i} | \widetilde{\Psi} \rangle = \mathrm{c_i} \qquad \textbf{105}$$

One can write the all-electron wave function thanks to the auxiliary functions in the various region as:

$$|\Psi\rangle = |\widetilde{\Psi}\rangle + \sum_i (|\phi_i\rangle - |\widetilde{\phi}_i\rangle) \langle \widetilde{p}_i|\widetilde{\Psi}\rangle \quad \textbf{106}$$

The expression **Eq.106** can be illustrated as in **Figure II-3** where the all-electron wavefunction is decomposed into a pseudo wavefunction with all electron contributions in the augmentation sphere.

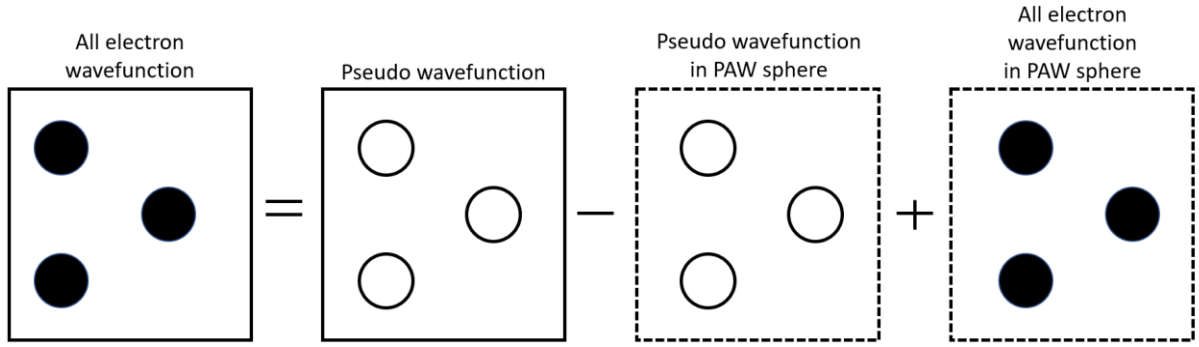

Figure II-3. Wavefunction representation in the PAW formalism[61]

II.5. Thermodynamics

Many properties can be obtained through the resolution of the Schrödinger equation, the electronic energy and the geometry are two of them. The electronic energy is calculated at 0K, so if one wants to extend its study to more realistic conditions and take into account the temperature or the pressure it is necessary to consider the enthalpy and entropy of a compound and their dependencies to the external environment. Such information can be obtained through ab initio calculations by considering statistical mechanics equations.

II.5.1. Vibration calculations

The calculation of the vibrational frequencies is needed in the construction of a thermodynamic models to account the effect of external atmosphere such as temperature or pressure. There are two ways to calculate them in VASP. The first one is by using a finite difference method and the second one is based on the density functional perturbation theory. Both methods rely on the harmonic approximation of the potential describing the elongated bond. In this manuscript, only the finite difference method will be presented.

The finite difference method is based on the calculation of the dynamical matrix. The dynamical matrix, which is a Hessian matrix of the potential energy for mass weighted coordinates, is then diagonalized in order to get the eigenvalues and eigenvectors. These two quantities will be respectively the frequencies and the normal modes.

The elements of the dynamical matrix can be defined as:

$$H_{i,j}^{m} = \frac{\delta^2 E}{\delta r_i \delta r_j} \frac{1}{\sqrt{M_i M_j}} \quad \textbf{107}$$

With M and r the mass and the atomic position of nuclei i and j. E is the potential energy surface. The finite difference method is the method used to calculate the second derivative of the potential energy. Each atom is displaced from its equilibrium position to a small amount, the gradient of the energy is calculated for these new positions and the Hessian can then be estimated. Different kinds of displacements can be used in practice. In this thesis the central differences scheme was used. In this particular method, atoms are displaced from their optimized positions in all the three directions, by positive and negative shifts.

II.5.2. Statistical thermodynamics

II.5.2.a) General considerations

Partition functions are key quantities to statistical thermodynamics, in a similar way to wavefunctions in quantum mechanics, all the macroscopic properties of a system can be calculated from them by applying the right operator. For a system of interacting particles, the partition function *Q* can be calculated by summing all potential energy states *i* of energy E_i of the system weighted by the Boltzmann's constant k.

$$Q = \sum_i e^{\frac{-E_i}{kT}} \quad \textbf{108}$$

Thermodynamic quantities such as the internal energy of the system *U*, the entropy *H*, the enthalpy *S* or the Gibbs free energy *G* can be derived from the partition function *Q*:[65,66]

$$U = kT^2 \left(\frac{\delta lnQ}{\delta T}\right)_V \quad \textbf{109}$$

$$H = U + kTV \left(\frac{\delta lnQ}{\delta V}\right)_T \quad \textbf{110}$$

$$S = kT \left(\frac{\delta lnQ}{\delta T}\right)_V + klnQ \quad \textbf{111}$$

$$G = kTV \left(\frac{\partial lnQ}{\partial V}\right)_T - kTlnQ \quad \textbf{112}$$

In the case of N non-interacting particles, *Q* can be expressed thanks to the molecular partition function *q*. For different particles, the relation is simply given by the product of all the N molecular partition functions (**Eq.113**). However, in the case of identical particles, it is necessary to account for the possible permutations among the particles that give rise to a same energy level E_i. In that case, the relation is given by **Eq.114** which take into account these permutations.

$$Q = q^N \quad \textbf{113}$$

$$Q = \frac{q^N}{N!} \quad \textbf{114}$$

Similarly to the partition function of the system, the molecular partition function q can be calculated by summing all potential quantum energy states *i* of energy ϵ_i weighted by the Boltzmann's constant k.

$$q = \sum_i e^{\frac{-\epsilon_i}{kT}} \quad \textbf{115}$$

Under the ideal gas, rigid rotor and harmonic oscillator approximation, it is possible to decompose the various contribution to the molecular partition function into non coupling terms describing the electronic, translational, rotational and vibrational contributions:[66]

$$q_{tot} = q_{elec} q_{trans} q_{rot} q_{vib} \quad \textbf{116}$$

This decomposition allows to decompose the internal energy, entropy, enthalpy and Gibbs free energy as follows:

$$U_{tot} = U_{trans} + U_{rot} + U_{elec} + U_{vib} \quad \textbf{117}$$

$$S_{tot} = S_{trans} + S_{rot} + S_{elec} + S_{vib} \quad \textbf{118}$$

$$H_{tot} = H_{trans} + H_{rot} + H_{elec} + H_{vib} \quad \textbf{119}$$

$$G_{tot} = G_{trans} + G_{rot} + G_{elec} + G_{vib} \quad \textbf{120}$$

In the case of the ideal gas, where $PV = nRT$ one can simplify the enthalpy to $H = U + nRT$, with n the number of mols. The Gibbs free energy, usually used in chemistry to compare relative stability between various compounds can be simply deduced from the previous quantities as $G = H - TS$.

The U_{elec} term is usually taken as the electronic energy calculated at 0K with the Schrödinger equation. This independence of the electronic energy to the temperature is a good approximation if the various electronic levels in the molecule are energetically well separated (larger than kT).[65] The partition functions q won't be detailed here, but can be found in various books.[66,67]

The different terms of the internal energy and entropy can be written as follows:

$$U_{vib}(T) = N_A \sum_{i=1}^{N_{vib}} h\nu_i \left(\frac{1}{2} + \frac{e^{-h\nu_i/kT}}{1 - e^{-h\nu_i/kT}} \right) \quad \textbf{121}$$

With N_A the Avogadro constant and U in $J.mol^{-1}$. The special case for $T = 0$ is called the zero-point energy (ZPE). N_{vib} depends on the geometry of the system, for a nonlinear one, then it equals $3N - 6$ but for a linear one it is $3N - 5$. If one considers non-linear gas phase molecules, then:

$$U_{trans}(T) = U_{rot}(T) = \frac{3}{2}RT \quad \textbf{122}$$

In the case of a linear molecule then $U_{rot} = RT$ as one degree of freedom disappears.

Entropic terms are given by:

$$S_{vib}(T) = R \sum_{i=1}^{N_{vib}} \left[\frac{h\nu_i}{kT} \frac{e^{-h\nu_i/kT}}{1 - e^{-h\nu_i/kT}} - \ln\left(1 - e^{-h\nu_i/kT}\right) \right] \quad \textbf{123}$$

$$S_{Trans}(T) = R \left[\frac{5}{2} + ln\left(\frac{RT}{P^\circ} \left(\frac{2\pi MkT}{h^2} \right)^{3/2} \right) \right] \quad \textbf{124}$$

$$S_{Rot}(T) = R \left[\frac{3}{2} + ln\left(\frac{\sqrt{\pi}}{\sigma} \left(\frac{8\pi^2 kT}{h^2} \right)^{3/2} (I_A I_B I_c)^{1/2} \right) \right] \quad \textbf{125}$$

$$S_{elec}(T) = Rln(g_0) \quad \textbf{126}$$

With $P°$ the normal pressure of the gas, M the molecular mass, I_A, I_B and I_C the principal moments of inertia and σ the rotational symmetry number. g_0 is the electronic degeneracy of the state (it equals 1 for a singlet, 2 for a doublet, etc…). The S_{elec} term was not considered in this work. As for the internal energy, N_{vib} depends on the geometry, for non-linear molecules $N_{vib} = 3N - 6$, while for linear ones $N_{vib} = 3N - 5$. The rotational component of the entropy is also simplified in the case of a linear molecule and is given by:

$$S_{Rot}(T) = R\left[1 + ln\left(\frac{8\pi^2 IkT}{\sigma h^2}\right)\right] \quad \textbf{127}$$

II.5.2.b) Practical estimations

In this thesis, the Gibbs free energy was computed with respect to the previous formulas to determine the relative stability of studied compound under various conditions as proposed by Reuter et al.[68] The way to calculate such quantity can changes with the studied element and the approximations done. In our case, three different ways of calculated G were used according to the state of the specie.

Supported cluster and surface:

In the case of supported cluster and surface, the contribution of the rotation and translation components of the Gibbs free energy were not calculated. In the case of expensive calculation, one can approximate the cancelation of the vibration part between the product and reactive for such systems. In our case, calculations were tractable at the desired level of theory and so vibrations were included to calculate the Gibbs free energy. Hence, the Gibbs free energy for supported clusters and surfaces G_{sup} was calculated as:

$$G_{supported}(T) = E_{elec} + H_{vib} - TS_{vib} \quad \textbf{128}$$

Gas phase complex:

In the case of gas phase complexes, the rotational and translational contributions were included, and the Gibbs free energy can be expressed as:

$$G_{complex}(T) = E_{elec} + H_{vib+trans+rot} - TS_{vib+trans+rot} \quad \textbf{129}$$

Atmosphere:

To take into account the impact of the (P, T) conditions, the chemical potential of the reactive species must be calculated. The chemical potential of an ideal gas at constant pressure P and temperature T can be derived from the Gibbs free energy:[69]

$$\mu = \left(\frac{\partial G}{\partial n}\right)_{T,P} \quad \textbf{130}$$

As the Gibbs free energy depends on both the pressure and the temperature it is possible to write:

$$dG = \left(\frac{\partial G}{\partial T}\right)_P dT + \left(\frac{\partial G}{\partial P}\right)_T dP = -SdT + VdP \quad \textbf{131}$$

In the ideal gas approximation, with $PV = nRT$:

$$\int_{P^\circ}^{P} \left(\frac{\partial G}{\partial P}\right)_T dP = \int_{P^\circ}^{P} VdP = \int_{P^\circ}^{P} nRT\frac{dP}{P} = nRTln\left(\frac{P}{P^\circ}\right) \quad \textbf{132}$$

And finally, for species that will be present in the atmosphere during the reaction (such as H_2O, H_2, HCl, O_2, etc…) the chemical potential is given by:

$$\mu(T, P) = \mu^0(T, P^\circ) + nRTln\left(\frac{P}{P^\circ}\right) \quad \textbf{133}$$

As the concept of reservoir of molecules will be applied to them, we will consider that their consumption during a chemical reaction won't change their pressure. A generic application of the previously detailed quantities can be written as:

$$\Delta_r G = \sum_i n_i \mu_i \quad \textbf{134}$$

II.6. First order saddle points of the PES

The research of first order saddle points on the potential energy surface (PES) is a necessary step to determine the activation barriers and thus the kinetic of a chemical reaction in the harmonic transition state theory (hTST).

The first order saddle points (commonly called transition state and abbreviated as TS) to describe a chemical reaction are usually found along the minimum energy path (MEP) that connects the initial and final states. Along this direction, the forces perpendicular to the path are nil and hence the maxima along the MEP are saddle points of the PES. Because of the high dimensionality of such space (3N with N being the number of atoms in the system), this search is far from being easy and numerous methods have been developed in order to ease this task. In this work, the research of activation barriers was done using two methods, the climbing image nudged elastic bond (CI-NEB) and the dimer, hence we will limit ourselves to describing only this two. It has to be noticed that other methods exist.

II.6.1. CI-NEB

The climbing image nudged elastic bond (CI-NEB)[70] can be seen as an upgrade to the NEB[71] method.

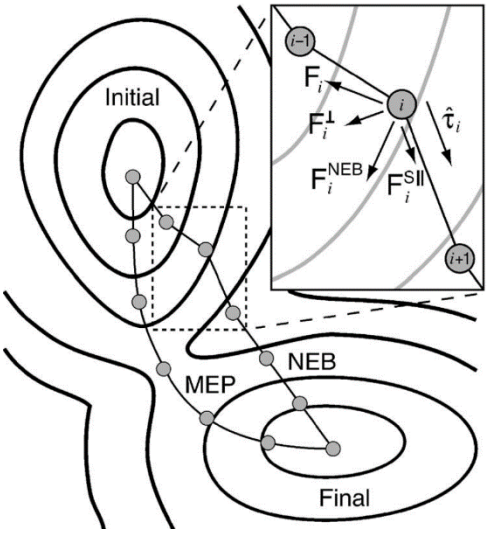

Figure II-4. Representation of MEP and NEB between an initial and final state. The forces decomposition according to the NEB formalism is presented. Taken from ref.[72]

The NEB is a method to find the MEP linking two states of interest (usually, the reactant and the product). A set of images (replicas) is built along the path, they will be the starting point of the MEP research. (**Figure II-4**) Several choices exist to create these images, most of the time, a simple interpolation between the reactant and product coordinates is done. According to the nature of the reaction a simple linear interpolation using the cartesian coordinates can be done or a preliminary change of the coordinate basis can be applied in order to facilitate the description of rotation. Finally, the chemical intuition or experience on the system can be put to good use in order to have an initial guess close to the MEP. To avoid that all the images before the maxima (let's consider that there is only one saddle point along the MEP for the sake of simplicity) end up being optimized as

the reactant and that all the images after the maxima end up as the product, fictitious forces are added between the images to maintain them at a given distance. A careful separation of the 'real' forces and the spring forces has to be done to not pollute the results. During the NEB procedure, a projection of the forces is done (that's the nudging part) to keep only the contribution of the spring, which is parallel to the path, and only the perpendicular component of the forces derived from the PES.[70] By considering a set of N images noted $[R_0,\ldots,R_i,\ldots,R_{N-1}]$ the forces acting on the replica *i* can be written as in **Eq.135**.

$$F_i = F_i^S|_{||} - \nabla E(R_i)|_{\perp} \quad \textbf{135}$$

Where $F_i^S|_{||}$is the sum of the spring's forces parallel to the local tangent (τ_i) at the replica i and $\nabla E(R_i)|_{\perp}$ describes the forces coming from the system's potential that are perpendicular to the same local tangent ($\hat{\tau}_i$). These two quantities are easily expressed as:

$$\nabla E(R_i)|_{\perp} = \nabla E(R_i) - \nabla E(R_i) \cdot \hat{\tau}_i \quad \textbf{136}$$

$$F_i^S|_{||} = k(|R_{i+1} - R_i| - |R_i - R_{i-1}|)\hat{\tau}_i \quad \textbf{137}$$

With the spring constant *k.* As it can be expected from the definition of the forces calculated for each replica, the definition of the normalized tangent $\hat{\tau}_i$ is an important point of the actual algorithm of the CI-NEB as developed by Henkelman et al..[73] Because of the discretized nature of the replicas, numerous definitions for the tangent to the MEP at an image *i* could be used. Currently, four definitions of $\hat{\tau}_i$ depending on the energies of the images *i-1, i* and *i+1* are implemented.

$$\tau_i = \tau_i^+ = R_{i+1} - R_i, if\ E_{i+1} > E_i > E_{i-1} \quad \textbf{138}$$

$$\tau_i = \tau_i^- = R_i - R_{i-1}, if\ E_{i-1} > E_i > E_{i+1} \quad \textbf{139}$$

$$\tau_i = \tau_i^+ \Delta E_i^{max} + \tau_i^- \Delta E_i^{min}, if\ E_{i+1} > E_{i-1}\ and\ (E_i > E_{i+1}\ or\ E_i < E_{i-1}) \quad \textbf{140}$$

$$\tau_i = \tau_i^+ \Delta E_i^{min} + \tau_i^- \Delta E_i^{max}, if\ E_{i+1} < E_{i-1}\ and\ (E_i < E_{i+1}\ or\ E_i > E_{i-1}) \quad \textbf{141}$$

$$\Delta \mathrm{E}_i^{max} = \max(|E_{i+1} - E_i|, |E_{i-1} - E_i|) \quad \textbf{142}$$

$$\Delta \mathrm{E}_i^{min} = \min(|E_{i+1} - E_i|, |E_{i-1} - E_i|) \quad \textbf{143}$$

$$\widehat{\tau_i} = \frac{\tau_i}{|\tau_i|} \quad \textbf{144}$$

Eq.138 and Eq.139 describe the cases where the image *I* is not a maximum nor a minimum while Eq.140 and Eq.141 are for images that are extrema. Eq.144 allows to get the normalized tangent.

Another main issue of the NEB is related to the equal space between the images. As defined by the previous equation, the NEB is built to keep an equal space between each image. One can guess that a lot of luck (or a lot of preliminary work) is required to have the saddle point described by a replica. That is where the CI (for Climbing Image) part is needed.[70] (Figure II-5)

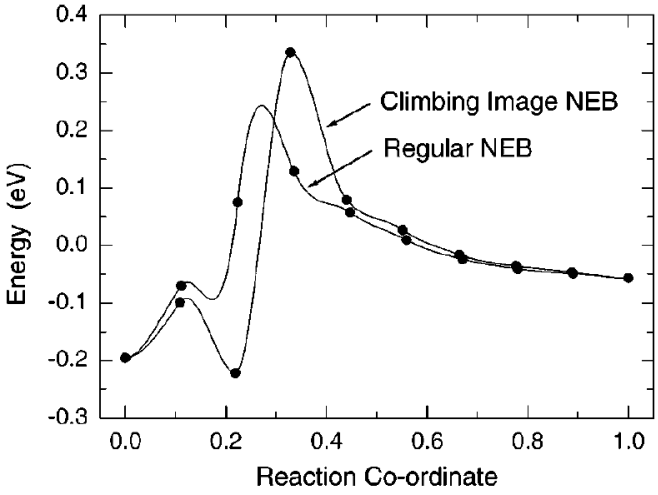

Figure II-5. Comparison of the different MEP calculated from a regular NEB and a CI-NEB for a given reaction. The dots represent the images along the path, the lines linking them are obtained after interpolation. With the CI-NEB the highest energy point (close to the TS) is well described by an image, while this is not the case for the regular NEB. Taken from ref.[70]

After a few iterations that follow the classical NEB precepts, the definition of the forces applied to the replica with the highest energy changes as:

$$F_{i_{max}} = 2\nabla E\left(R_{i_{max}}\right) \cdot \hat{\tau}_{i_{max}} \hat{\tau}_{i_{max}} - \nabla E(R_{i_{max}}) \quad \textbf{145}$$

Because of **Eq.145** the image i_{max} is not influenced by the spring, hence it can move closer or further away from its neighboring replica. The second difference is that the component along the elastic band is inverted. Hence this image will try to maximize its energy along the path defined by the replicas and minimize it in all other direction. Once the CI-NEB has converged, the path is supposed to be the MEP which will be described by the replicas, and the saddle point of interest will be correctly defined by the image with the highest energy.

In theory, if a sufficient number of replicas are considered along the path, the CI-NEB can deal with multiple extrema, being either meta-stable intermediate (local minima) or saddle points that are not the highest in energy along the MEP (local maxima). In practice, it is often a better idea to redefine these new meta-stable intermediates found during a preliminary calculation as the initial and final states of another CI-NEB calculation.

II.6.2. Dimer method

The dimer method, as developed by Henkelman et al.[74] and which is the one used in this work, can be used to find saddle points without the calculation of multiple replicas, and hence is computationally cheaper than the CI-NEB.

The dimer procedure requires as input a set of coordinates (which can be close or not of the TS) and the vibrational mode describing the reaction of interest. In practice, if no mode is provided at the beginning of the calculation, a random one will be generated. However, as the method does not ensure that the result will be the desired TS, the expectations to obtain the right saddle point are lowered. Hence in practice, it can be wiser to consider an initial system close to the TS whose vibrations are known. Such system can be obtained from a previous CI-NEB calculation or from a wise guess of what the TS could be for the investigated mechanism.

From the initial image, a pair of images (hence the name 'dimer') will be generated by moving the coordinates by a given distance ΔR in the two directions along the mode of interest N (obtained from a previous vibrational calculation) (**Figure II-6**). Notably, only the energies and forces acting on these two images are needed to describe the initial point. The energy of the dimer is defined as $E = E_1 + E_2$ with E_i the energy of the image i and the forces acting on the midpoint are obtained through $F_R = (F_1 + F_2)/2$with F_i the forces acting on the image i. The energy of the midpoint E_0 can be calculated from **Eq.146**.

$$E_0 = \frac{2E + \Delta R}{4}(F_1 - F_2) \cdot N \qquad \textbf{146}$$

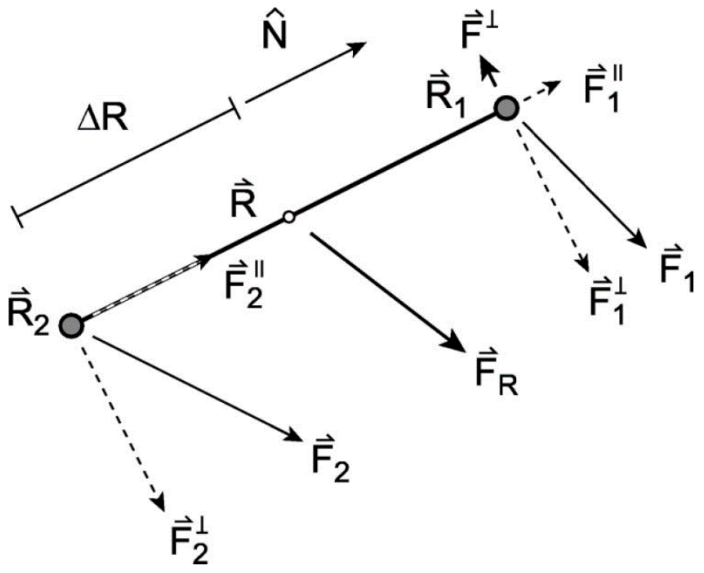

Figure II-6. Representation of the Dimer method and the various quantities (energies, forces, distances) used. Taken from ref.[74]

At each displacement of the dimer, these quantities need to be calculated. In addition to that, and at each new position, the dimer energy is minimized. As the midpoint is not allowed to move, this step is equivalent to finding the lowest curvature mode by rotating the dimer. Details on this step and their intrinsic difficulties can be found in the original paper of Henkelman et al.[74]. Once the dimer has been rotated and hence the lowest curvature mode has been found, the dimer system can be translated along it. According to the nature of the minimum curvature of the PES at the midpoint, two definitions of the forces acting on the midpoint ($F_R^{\ddagger}$ in **Eq.147**) can be defined. If the curvature is positive (C>0 in **Eq.147**), then only the forces along this mode are kept ($F^{||}$ in **Eq.147**), otherwise, and similarly to what is done for the CI-NEB in **Eq.145** the intensity of the forces parallels to the lowest curvature mode are modified (C<0 in **Eq.147**, with F_R being the forces acting on the midpoint) in order to translate the dimer upward the PES. Energy and forces for the new position of the midpoint are then recalculated to evaluate if the required convergence for the calculation is reached. If not, a new iteration must be done.

$$F_R^{\ddagger} = \begin{cases} -F^{||}\ if\ C > 0 \\ F_R - 2F^{||}\ if C < 0 \end{cases} \qquad \textbf{147}$$

Despite being able to follow the lowest curvature mode of the PES at a given position, no calculation of the Hessian matrix is required, which greatly lowers the computational cost of the search of a saddle point. In the end, at least 6 evaluations of the gradient of the PES are needed for one dimer iteration. It can be noted that an

improvement of the presented algorithm which requires less gradient's evaluation has been developed by Heyden et al.[75] and is currently implemented in VASP. However, in this work, the dimer from Henkelman et al.[74] was used.

II.6.3. IRC

The saddle points obtained from the two methods above are not assured to be those of interest. Hence it is necessary to verify that they connect the wanted reactant and product. One way to do it is by doing an Intrinsic Reaction Coordinate (IRC) analysis. The concept of IRC was defined by Fukui in 1981[76] but its formalism was first introduced in an previous paper of the same author.[77] IRC is defined as the particular solution curve of a set of differential equations. These equations are obtained from the movement of N nuclei during a chemical reaction, and are described in classical mechanics as follow:

$$d\left(m_\alpha \dot{X_\alpha}\right) = -\frac{\partial U}{\partial X_\alpha}dt;\ d\left(m_\alpha \dot{Y_\alpha}\right) = -\frac{\partial U}{\partial Y_\alpha}dt;\ d\left(m_\alpha \dot{Z_\alpha}\right) = -\frac{\partial U}{\partial Z_\alpha}dt \qquad \textbf{148}$$

Where m_α is the mass, $(X_\alpha, Y_\alpha, Z_\alpha)$ the coordinates of the αth atoms and U the potential. The assumption defined by Fukui is that the nuclei move with an infinitesimal velocity, thus the integration of **Eq.148** lead to **Eq.149**.

$$\frac{m_\alpha dX_\alpha}{\partial U/\partial X_\alpha} = \frac{m_\alpha dY_\alpha}{\partial U/\partial Y_\alpha} = \frac{m_\alpha dZ_\alpha}{\partial U/\partial Z_\alpha} = -tdt \qquad \textbf{149}$$

By considering the mass-weighted cartesian coordinates, such as:

$$m_\alpha^{1/2} X_\alpha = x_{3\alpha-2};\ m_\alpha^{1/2} Y_\alpha = x_{3\alpha-1};\ m_\alpha^{1/2} Z_\alpha = x_{3\alpha} \qquad \textbf{150}$$

Hence, the IRC equations in mass-weighted coordinates can be rewritten under a more concise vector form as:

$$dx = -g_x t dt \qquad \textbf{151}$$

With $x = (x_1, x_2, \dots, x_{3N})^T$ and $g_x = \left(\frac{\partial U}{\partial x_1}, \frac{\partial U}{\partial x_2}, \dots, \frac{\partial U}{\partial x_{3N}}\right)^T$. By finally introducing the infinitesimal distance ds such as $ds^2 = dx \cdot dx$ the IRC equations can be written under the form they are commonly found.

$$\frac{dx}{ds} = -\frac{g_x}{||g_x||} \qquad \textbf{152}$$

These equations admit an infinite number of solutions, and the IRC is defined as the one reaching both the reactant (or product) and the TS, otherwise the solutions are 'meta-IRC'. In practice the IRC can be obtain by starting from the TS and then following the steepest gradient's direction. Such procedure of plotting the IRC for a chemical reaction is called reaction ergodography.[76]

Analytical solutions to the IRC equations exist[78] but cannot be considered for ab initio calculations[79]. Hence, approximative scheme to integrate the IRC equations were developed. In this work, a damped velocity Verlet algorithm developed by Hratchian et al.[80] is used to approach the IRC solution.[80] This integration scheme based on the gradient determines the position and velocity after each step to propagate the trajectory. In the damped flavour of it, the velocity is adjusted after each step. In the work of Hratchian et al.[80] an adjustable time step is used to ensure that the propagated trajectory stays close enough to the real IRC curve.

During this PhD thesis, transition states were identified using both the CI-NEB and dimer methods. Although no universal protocol was followed, we could sum up the main steps of the research of TS as follows. First, a CI-NEB calculation was converged using the reactant and product of interest. The highest image(s) were then optimized with tighter convergence using a quasi-newton algorithm, and system frequencies were calculated using the finite difference method. Finally, an IRC analysis was performed. In case of unsuccessful IRC analysis, a dimer calculation was performed to refine the suspected "TS". Frequencies were recalculated, and a new IRC analysis was conducted on the refined TS. This procedure was repeated with tighter convergence criterion until a successful IRC analysis was obtained.

II.7. X-Ray Adsorption Near Edge Structure

II.7.1. Main principle

The absorption of electromagnetic radiation by a material is a rich phenomenon which reveals numerous information on the nature of the material. In the case of XAS (for X-ray absorption spectroscopy) the absorption process is related to the transition of core electrons up to empty states above the Fermi level or the Highest

Occupied Molecular Orbital. Spectra are recorded over an energy range covering selected "absorption edge" and covering typically 100 eV for the XANES (which stands for X-ray absorption near edge structure) or some thousands of eV for EXAFS (Extented X-ray Absorption Fine Structure). The intensity of absorption is given by the Beer-Lambert law which links the transmitted intensity (I) as a function of the intensity of the incident X-ray beam (I_0), the thickness of the material (x) and the linear absorption coefficient (μ) which depends on the X-ray energy:[81]

$$I = I_0 e^{-\mu(E)x} \qquad \textbf{153}$$

For a periodical material, the linear absorption coefficient is related to the volume of the unit cell, V, and the absorption cross sections σ_i of the atoms i in the unit cell through:

$$\mu(E) = \frac{1}{V}\sum_i \sigma_i \qquad \textbf{154}$$

At the edge energy, the absorption cross section suddenly increases showing often a so-called white line, that is a maximum. It is followed by different features characteristic of the local geometry in the material. The white line is sensitive to the electronic state of the probed atom. The more oxidized is the atom the more the white line is shifted toward higher energies. The intensity of the edge, that is the probability that the transition occurs is linked to the density of state (DOS). Thus, XANES informs on the projection of the DOS, onto the absorbing atom itself related to the geometric surrounding.[82] If the X-ray energy is more increased, photo-electrons probe with more kinetic energy the close environment of the adsorbing atom, and we are in the EXAFS range (**Figure II-7**).

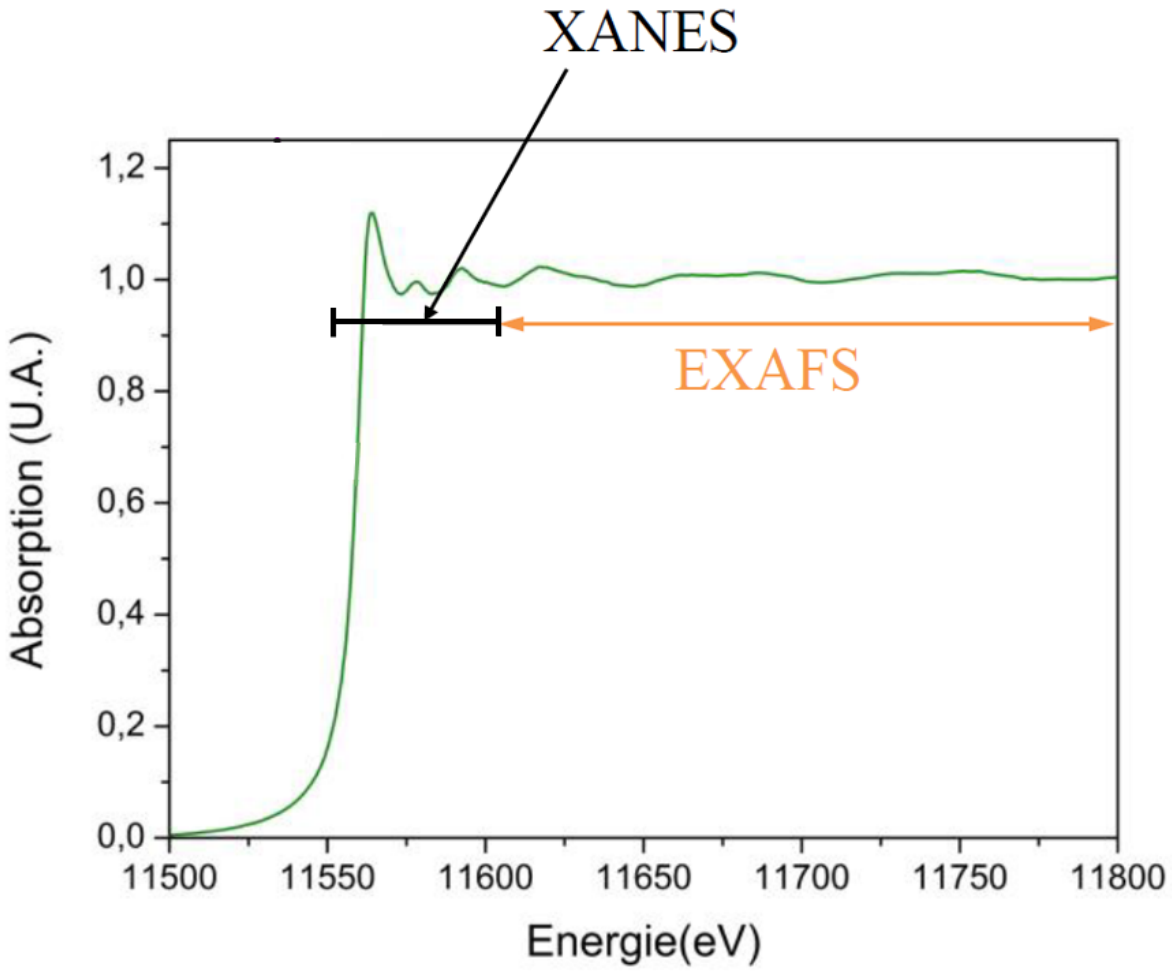

Figure II-7. Illustration of the different zones of the XAS spectrum of Pt powder at the L_3 edge. Adapted from ref.[83]

The interpretation of X-ray absorption spectra is usually done based on reference spectra. This can be an issue in case of new material or for a material whose exact nature remains unknown. In order to assist in the deciphering of the X-ray spectra, ab initio simulations can be done in parallel. In our case, the calculation of the XANES spectra was done using the FDMNES (standing for Finite Difference Method Near Edge Spectroscopy) software developed by Yves Joly.[84,85]

II.7.2. FDMNES

The nature of the XAS spectra is impacted by how the atom of interest will adsorb the incident beam. This quantity is related to the cross-section. The cross section $\sigma(\omega)$ can be expressed as:[81]

$$\sigma(\omega) = 4\pi^2\alpha\hbar\omega \sum_{fg} \left|\langle\Psi_f|\hat{o}|\Psi_g\rangle\right|^2 \delta(E_f - E_g - \hbar\omega) \qquad \textbf{155}$$

with α the fine structure constant, $\hbar\omega$ the photon energy, E_g the energy of the initial (core) state g associated to the wavefunction $|\Psi_g\rangle$, E_f the energy of the accessible state f associated to the wavefunction $|\Psi_f\rangle$ and $\hat{o}$ the transition operator that can be simplified in the X-ray regime as:

$$\hat{o} = \boldsymbol{\epsilon} \cdot \boldsymbol{r}\left(1 + \frac{i}{2}\boldsymbol{k} \cdot \boldsymbol{r}\right) \quad \textbf{156}$$

with $\boldsymbol{\epsilon}$ the polarization of the photon, $\boldsymbol{k}$ its wavevector and $\boldsymbol{r}$, the position of the absorbing atom. The first term is the dipolar transition (usually called E_1) and the second one is the quadrupolar contribution (usually called E_2). The contribution to E_2 to the cross section is smaller than for E_1. Both of this transition are subject to different selection rules according to the nature of the orbitals implied during the electron's excitation. In our case, we studied the L_3 edge of the platinum, and the transition was from the $2p_{3/2}$ to the 5d orbitals.

In order to evaluate the cross section $\sigma(\omega)$, the knowledge of the states $|\Psi_{f,g}\rangle$ is required. The calculation of the electronic structure is performed by the FDMNES[84,85] package within the DFT framework. This choice seems counter-intuitive as the calculations that we are describing are those of excited states. However, in practice, for the L_3 edge of heavy element ($Z > 31$) experimental spectra are relatively well reproduced.

The FDMNES code solves the Schrödinger equation in real space within the finite difference method (hence the name of the package) or the multiple scattering method in a cluster of a given radius around the atom(s) of interest. With a higher computational cost, the finite difference method allows to get rid of the spherical approximations on the potentials as done in the multiple scattering theory who relies on the muffin-tin approximation. The evaluation of the electronic structure is then done self-consistently using an LDA or GGA exchange-correlation potential. In our calculation, the LDA as parametrized by Hedin and Lundqvist[86] was used. Relativistic effects are handled by FDMNES through the resolution of a relativistic Schrödinger equation obtained from the Dirac equation but neglecting the small components. It includes the spin-orbit term, very important at the L_3 Pt edges. From there the state of interest are known and the cross section can be calculated to get the XANES spectra. Once the XANES spectrum is calculated, it can be broadened through its convolution by a Lorentzian function in order to be comparable to experimental spectra.

In practice, to be comparable to experimental spectra the calculated ones need to be normalized and shifted according to a reference and well-defined material for which the experimental XANES is known. More details on the parameters and practices used during the calculation of XANES spectra can be found in the **Chapter IV** Section **IV.2.6**.

II.8. Conclusions

The density functional theory is an ab initio method used to determine the electronic structure of an electronic system based on its electronic density. Because of its relatively good ratio cost/accuracy, it is widely used in the field of quantum chemistry domain. However, while DFT is in principle an exact theory, the exchange correlation term remains unknown and needs to be approximate. Currently, no perfect exchange correlation functional exists and ongoing research aims to develop more accurate and cost-effective approximation. Because of their local nature, most of the exchange correlation functional cannot accurately capture dispersive forces. To address this issue, corrective schemes have been developed. Another increasingly popular approach is to treat exactly the exchange part through the Hartree-Fock theory and to add the correlation energy. The exact expression of the correlation energy can be derived from the DFT framework through the ACFDT formalism, and its calculation is possible notably under the random phase approximation. While the RPA correlation energy is not exempt of defaults, it is fully non-local and includes long-range vdW interactions. Planewave basis sets are well suited for studying periodic systems. However, to reduce computational costs, it is preferable to use pseudopotentials to describe core electrons. Methods such as CI-NEB or dimer have been developed to find transition states for a given reaction and identify potential kinetic limitations. X-ray adsorption spectroscopy is a powerful method for accessing the electronic structure and geometry of a material. In the absence of reference spectra for comparison, DFT calculation of XANES spectra can be performed to help interpret experimental results.

In this work, we will use the PBE exchange correlation functional (GGA) corrected for dispersion forces through the dDsC scheme to calculate the optimized geometries of our systems. From the optimized geometry, the Hessian matrix will be calculated to consider entropic and enthalpic effects that are important in simulating preparation steps occurring at high temperature. We will use a high-level theory such as the ACFDT-RPA to evaluate the suitability of various exchange functional in describing the calcination and reduction preparation steps. Based on the benchmark results, energies might be recalculated at a higher level of theory for specific cases. The search for first order saddle point will be carried in the so-called static approach through the use of CI-NEB or dimer methods. An IRC analysis will be performed to ensure the validity of the TS obtained.

Details on the calculation parameters related to the methods presented in this chapter will be provided in the corresponding chapter, where specific information on the computational setup, basis sets, convergence criteria and other relevant parameters will be discussed in depth.

II.9. References

1. Dirac, P. A. M. Quantum mechanics of many-electron systems. *Proc. R. Soc. Lond. A* **123,** 714–733 (1929).
2. Szabó, A. & Ostlund, N. S. *Modern quantum chemistry. Introduction to advanced electronic structure theory* (Dover Publications, Mineola (N.Y.), 1996).
3. Kohn, W. Nobel Lecture: Electronic structure of matter—wave functions and density functionals. *Rev. Mod. Phys.* **71,** 1253–1266 (1999).
4. Thomas, L. H. The calculation of atomic fields. *Math. Proc. Camb. Phil. Soc.* **23,** 542–548 (1927).
5. Fermi, E. Eine statistische Methode zur Bestimmung einiger Eigenschaften des Atoms und ihre Anwendung auf die Theorie des periodischen Systems der Elemente. *Z. Physik* **48,** 73–79 (1928).
6. Hohenberg, P. & Kohn, W. Inhomogeneous Electron Gas. *Phys. Rev.* **136,** B864-B871 (1964).
7. Kohn, W. & Sham, L. J. Self-Consistent Equations Including Exchange and Correlation Effects. *Phys. Rev.* **140,** A1133-A1138 (1965).
8. Becke, A. D. Perspective: Fifty years of density-functional theory in chemical physics. *J. Chem. Phys.* **140,** 18A301 (2014).
9. Dreizler, R. M. & Engel, E. *Density Functional Theory. An Advanced Course* (Springer-Verlag, Berlin, Heidelberg, 2011).
10. Parr, R. G. *Density-Functional Theory of Atoms and Molecules* (Oxford University Press, Oxford, 2015).
11. Lieb, E. H. Density functionals for coulomb systems. *Int. J. Quantum Chem.* **24,** 243–277 (1983).
12. Levy, M. Universal variational functionals of electron densities, first-order density matrices, and natural spin-orbitals and solution of the v-representability problem. *Proc. Natl. Acad. Sci. U.S.A* **76,** 6062–6065 (1979).
13. Koch, W. & Holthausen, M. *A chemist's guide to density functional theory* (Wiley-VCH, Weinheim, New York, 2001).
14. Perdew, J. P. Jacob's ladder of density functional approximations for the exchange-correlation energy. *AIP. Conf. Proc.* **577,** 1–20 (2001).
15. Fiolhais, C., Nogueira, F. & Marques, M. A. *A primer in density functional theory* (Springer, New York, 2003).
16. Toulouse, J. Review of approximations for the exchange-correlation energy in density-functional theory. arxiv:2103.02645, (physics.chem-ph).
17. Henderson, T. M., Janesko, B. G. & Scuseria, G. E. Generalized gradient approximation model exchange holes for range-separated hybrids. *J. Chem. Phys.* **128,** 194105 (2008).
18. Kimball, J. C. Short-Range Correlations and Electron-Gas Response Functions. *Phys. Rev. A.* **7,** 1648–1652 (1973).
19. Ceperley, D. M. & Alder, B. J. Ground State of the Electron Gas by a Stochastic Method. *Phys. Rev. Lett.* **45,** 566–569 (1980).
20. Vosko, S. H., Wilk, L. & Nusair, M. Accurate spin-dependent electron liquid correlation energies for local spin density calculations: a critical analysis. *Can. J. Phys.* **58,** 1200–1211 (1980).
21. Perdew, J. P. & Wang, Y. Accurate and simple analytic representation of the electron-gas correlation energy. *Phys. Rev. B* **45,** 13244–13249 (1992).
22. Gunnarsson, O., Jonson, M. & Lundqvist, B. I. Descriptions of exchange and correlation effects in inhomogeneous electron systems. *Phys. Rev. B* **20,** 3136–3164 (1979).
23. Hood, R. Q., Chou, M. Y., Williamson, A. J., Rajagopal, G. & Needs, R. J. Exchange and correlation in silicon. *Phys. Rev. B* **57,** 8972–8982 (1998).
24. Perdew, J. P., Burke, K. & Ernzerhof, M. Generalized Gradient Approximation Made Simple. *Phys. Rev. Lett.* **77,** 3865–3868 (1996).
25. Perdew, J. P., Kurth, S., Zupan, A. & Blaha, P. Accurate Density Functional with Correct Formal Properties: A Step Beyond the Generalized Gradient Approximation. *Phys. Rev. Lett.* **82,** 2544–2547 (1999).
26. Perdew, J. P., Kurth, S., Zupan, A. & Blaha, P. Erratum: Accurate Density Functional with Correct Formal Properties: A Step Beyond the Generalized Gradient Approximation. *Phys. Rev. Lett.* **82,** 5179 (1999).

27. Tao, J., Perdew, J. P., Staroverov, V. N. & Scuseria, G. E. Climbing the density functional ladder: nonempirical meta-generalized gradient approximation designed for molecules and solids. *Phys. Rev. Lett.* **91,** 146401 (2003).
28. Becke, A. D. A new mixing of Hartree–Fock and local density-functional theories. *J. Chem. Phys.* **98,** 1372–1377 (1993).
29. Becke, A. D. Density-functional thermochemistry. IV. A new dynamical correlation functional and implications for exact-exchange mixing. *J. Chem. Phys.* **104,** 1040–1046 (1996).
30. Stephens, P. J., Devlin, F. J., Chabalowski, C. F. & Frisch, M. J. Ab Initio Calculation of Vibrational Absorption and Circular Dichroism Spectra Using Density Functional Force Fields. *J. Phys. Chem.* **98,** 11623–11627 (1994).
31. Becke, A. D. Density-functional exchange-energy approximation with correct asymptotic behavior. *Phys. Rev. A.* **38,** 3098–3100 (1988).
32. Lee C., Yang W. & Parr, R. G. Development of the Colle-Salvetti correlation-energy formula into a functional of the electron density. *Phys. Rev. B* **37,** 785–789 (1988).
33. Heyd, J., Scuseria, G. E. & Ernzerhof, M. Hybrid functionals based on a screened Coulomb potential. *J. Chem. Phys.* **118,** 8207–8215 (2003).
34. Klimeš, J. & Michaelides, A. Perspective: Advances and challenges in treating van der Waals dispersion forces in density functional theory. *J. Chem. Phys.* **137,** 120901 (2012).
35. Grimme, S. Accurate description of van der Waals complexes by density functional theory including empirical corrections. *J. Comput. Chem.* **25,** 1463–1473 (2004).
36. Grimme, S. Semiempirical GGA-type density functional constructed with a long-range dispersion correction. *J. Comput. Chem.* **27,** 1787–1799 (2006).
37. Grimme, S., Antony, J., Ehrlich, S. & Krieg, H. A consistent and accurate ab initio parametrization of density functional dispersion correction (DFT-D) for the 94 elements H-Pu. *J. Chem. Phys.* **132,** 154104 (2010).
38. Sato, T. & Nakai, H. Local response dispersion method. II. Generalized multicenter interactions. *J. Chem. Phys.* **133,** 194101 (2010).
39. Tkatchenko, A. & Scheffler, M. Accurate molecular van der Waals interactions from ground-state electron density and free-atom reference data. *Phys. Rev. Lett.* **102,** 73005 (2009).
40. Becke, A. D. & Johnson, E. R. Exchange-hole dipole moment and the dispersion interaction revisited. *J. Chem. Phys.* **127,** 154108 (2007).
41. Steinmann, S. N. & Corminboeuf, C. A generalized-gradient approximation exchange hole model for dispersion coefficients. *J. Chem. Phys.* **134,** 44117 (2011).
42. Steinmann, S. N. & Corminboeuf, C. Comprehensive Benchmarking of a Density-Dependent Dispersion Correction. *J. Chem. Theory. Comput.* **7,** 3567–3577 (2011).
43. Dion, M., Rydberg, H., Schröder, E., Langreth, D. C. & Lundqvist, B. I. van der Waals density functional for general geometries. *Phys. Rev. Lett.* **92,** 246401 (2004).
44. Vydrov, O. A. & van Voorhis, T. Improving the accuracy of the nonlocal van der Waals density functional with minimal empiricism. *J. Chem. Phys.* **130,** 104105 (2009).
45. Vydrov, O. A. & van Voorhis, T. Nonlocal van der Waals density functional made simple. *Phys. Rev. Lett.* **103,** 63004 (2009).
46. Vydrov, O. A. & van Voorhis, T. Nonlocal van der Waals density functional: the simpler the better. *J. Chem. Phys.* **133,** 244103 (2010).
47. Ángyán, J. G., Gerber, I. C., Savin, A. & Toulouse, J. van der Waals forces in density functional theory: Perturbational long-range electron-interaction corrections. *Phys. Rev. A* **72** (2005).
48. Ren, X., Rinke, P., Joas, C. & Scheffler, M. Random-phase approximation and its applications in computational chemistry and materials science. *J. Mater. Sci.* **47,** 7447–7471 (2012).
49. Pines, D. & Nozières, P. *Theory of quantum liquids* (Addison-Wesley Pub. Co. Advanced Book Program, Reading Mass., 1989).

50. Langreth, D. C. & Perdew, J. P. The exchange-correlation energy of a metallic surface. *Solid State Commun.* **17,** 1425–1429 (1975).
51. Niquet, Y. M., Fuchs, M. & Gonze, X. Exchange-correlation potentials in the adiabatic connection fluctuation-dissipation framework. *Phys. Rev. A* **68** (2003).
52. Chen, G. P., Voora, V. K., Agee, M. M., Balasubramani, S. G. & Furche, F. Random-Phase Approximation Methods. *Annu. Rev. Phys. Chem.* **68,** 421–445 (2017).
53. Kresse, G. & Hafner, J. Norm-conserving and ultrasoft pseudopotentials for first-row and transition elements. *J. Phys.: Condens. Matter* **6,** 8245–8257 (1994).
54. Kresse, G. & Furthmüller, J. Efficiency of ab-initio total energy calculations for metals and semiconductors using a plane-wave basis set. *Comput. Mater. Sci.* **6,** 15–50 (1996).
55. Payne, M. C., Teter, M. P., Allan, D. C., Arias, T. A. & Joannopoulos, J. D. Iterative minimization techniques for ab initio total-energy calculations: molecular dynamics and conjugate gradients. *Rev. Mod. Phys.* **64,** 1045–1097 (1992).
56. Fermi, E. Sopra lo Spostamento per Pressione delle Righe Elevate delle Serie Spettrali. *Nuovo Cim* **11,** 157–166 (1934).
57. Hellmann, H. A New Approximation Method in the Problem of Many Electrons. *J. Chem. Phys.* **3,** 61 (1935).
58. Kleinman, L. & Phillips, J. C. Crystal Potential and Energy Bands of Semiconductors. III. Self-Consistent Calculations for Silicon. *Phys. Rev.* **118,** 1153–1167 (1960).
59. Phillips, J. C. & Kleinman, L. New Method for Calculating Wave Functions in Crystals and Molecules. *Phys. Rev.* **116,** 287–294 (1959).
60. Topp, W. C. & Hopfield, J. J. Chemically Motivated Pseudopotential for Sodium. *Phys. Rev. B* **7,** 1295–1303 (1973).
61. Kresse, G. & Joubert, D. From ultrasoft pseudopotentials to the projector augmented-wave method. *Phys. Rev. B* **59,** 1758–1775 (1999).
62. Andersen, O. K. Linear methods in band theory. *Phys. Rev. B* **12,** 3060–3083 (1975).
63. Vanderbilt. Soft self-consistent pseudopotentials in a generalized eigenvalue formalism. *Phys. Rev. B* **41,** 7892–7895 (1990).
64. Blöchl. Projector augmented-wave method. *Phys. Rev. B* **50,** 17953–17979 (1994).
65. McDouall, J. J. *Computational quantum chemistry. Molecular structure and properties in silico* (RSC publishing, Cambridge, 2013).
66. Jensen, F. *Introduction to computational chemistry.* 2nd ed. (John Wiley & Sons, Chichester, England, Hoboken, NJ, 2007).
67. Atkins, P. W., Paula, J. d. & Keeler, J. *Atkins' physical chemistry.* 11th ed. (Oxford University Press, Oxford (GB), 2018).
68. Reuter, K., Stampf, C. & Scheffler, M. AB Initio Atomistic Thermodynamics and Statistical Mechanics of Surface Properties and Functions. In *Handbook of materials modeling,* edited by S. Yip (Springer, Dordrecht, 2005), pp. 149–194.
69. Reuter, K. & Scheffler, M. Composition, structure, and stability of RuO_2(110) as a function of oxygen pressure. *Phys. Rev. B* **65** (2001).
70. Henkelman, G., Uberuaga, B. P. & Jónsson, H. A climbing image nudged elastic band method for finding saddle points and minimum energy paths. *J. Chem. Phys.* **113,** 9901–9904 (2000).
71. Berne, B. J., Ciccotti, G. & Coker, D. F. *Classical and Quantum Dynamics in Condensed Phase Simulations* (WORLD SCIENTIFIC, 1998).
72. Sheppard, D., Terrell, R. & Henkelman, G. Optimization methods for finding minimum energy paths. *J. Chem. Phys.* **128,** 134106 (2008).
73. Henkelman, G. & Jónsson, H. Improved tangent estimate in the nudged elastic band method for finding minimum energy paths and saddle points. *J. Chem. Phys.* **113,** 9978–9985 (2000).
74. Henkelman, G. & Jónsson, H. A dimer method for finding saddle points on high dimensional potential surfaces using only first derivatives. *J. Chem. Phys.* **111,** 7010–7022 (1999).

75. Heyden, A., Bell, A. T. & Keil, F. J. Efficient methods for finding transition states in chemical reactions: comparison of improved dimer method and partitioned rational function optimization method. *J. Chem. Phys.* **123,** 224101 (2005).
76. Fukui, K. The path of chemical reactions - the IRC approach. *Acc. Chem. Res.* **14,** 363–368 (1981).
77. Fukui, K. Formulation of the reaction coordinate. *J. Phys. Chem.* **74,** 4161–4163 (1970).
78. Deng, L. & Ziegler, T. The determination of intrinsic reaction coordinates by density functional theory. *Int. J. Quantum Chem.* **52,** 731–765 (1994).
79. Page, M. & McIver, J. W. On evaluating the reaction path Hamiltonian. *J. Chem. Phys.* **88,** 922–935 (1988).
80. Hratchian, H. P. & Schlegel, H. B. Following Reaction Pathways Using a Damped Classical Trajectory Algorithm. *J. Phys. Chem. A* **106,** 165–169 (2002).
81. Joly, Y. & Grenier, S. Theory of X-Ray Absorption Near Edge Structure. In *X-Ray Absorption and X-Ray Emission Spectroscopy,* edited by J. A. van Bokhoven & C. Lamberti (John Wiley & Sons, Ltd, Chichester, UK, 2016), pp. 73–97.
82. J. van Bokhoven, C. Lamberti. *X-ray absorption and X-ray emission spectroscopy: Theory and applications* (John Wiley & Sons Ltd, Chichester, 2016).
83. Gorczyca, A. Caractérisation de catalyseurs métalliques supportés par spectroscopie XANES- Apport du calcul quantique dans l'interprétation des spectres expérimentaux. PhD thesis, 2011-2014.
84. Bunău, O. & Joly, Y. Self-consistent aspects of x-ray absorption calculations. *J. Phys.: Condens. Matter* **21,** 345501 (2009).
85. Guda, S. A., Guda, A. A., Soldatov, M. A., Lomachenko, K. A., Bugaev, A. L., Lamberti, C., Gawelda, W., Bressler, C., Smolentsev, G., Soldatov, A. & Joly, Y. Optimized Finite Difference Method for the Full-Potential XANES Simulations: Application to Molecular Adsorption Geometries in MOFs and Metal-Ligand Intersystem Crossing Transients. *J. Chem. Theory. Comput.* **11,** 4512–4521 (2015).
86. Hedin, L. & Lundqvist, B. I. Explicit local exchange-correlation potentials. *J. Phys. C: Solid State Phys.* **4,** 2064–2083 (1971).

Chapter III

$PtO_xCl_y(OH)_z(H_2O)_n$ Complexes under Oxidative and Reductive Conditions: Impact of the Level of Theory on Thermodynamic Stabilities

---

This chapter is dedicated to the study of platinum complexes in gas phase. It reproduces the text of a paper published in 2023 in ChemPhysChem: "Hellier, A.; Chizallet, C.; Raybaud, P. $PtO_xCl_y(OH)_x(H_2O)_n$ complexes under oxidative and reductive conditions: Impact of the level of theory on thermodynamic stabilities. *ChemPhysChem* **2023**, 24, e202200711." Supporting information is at the end of the chapter.

III.1. Introduction

Transition metal complexes are largely used in catalysis, either in solution (homogeneous and enzymatic catalysis), or supported on a solid (heterogeneous catalysis). Among these, platinum compounds are of paramount practical importance, besides being at the origin of organometallic chemistry with the Zeise's salt[1] $K[PtCl_3(C_2H_4)]\cdot H_2O$. For example, platinum complexes of various oxidation states and containing various ligands can be either solvated[2] or deposited on a support to be used as precursors of platinum nanoparticles, which are largely used in industry and academia to catalyze hydrogenation, dehydrogenation and oxidation reactions, inter alia.[3] Thus, gaining knowledge about the molecular structure, the energetics and the electronic properties of platinum species in oxidative and reductive media is important for future progress of platinum based catalyst. Moreover, the conventional preparation of supported platinum catalysts involves an impregnation step of oxidized platinum precursors followed by various possible thermal treatments such as drying (at mild temperature T~393 K), calcination (at higher T~800 K) under dry air and reduction (often at high T under H_2) into metallic nanoparticles.[4]

Platinum-chloride complexes in solution have shown to be efficient in homogeneous catalysis,[5] and are at the core of the synthesis procedure of many heterogeneous catalysts starting from hexachloroplatinic acid (H_2PtCl_6).[6,7] Moreover, in aqueous solution, chlorine exchanges with water or hydroxyls, in a pH dependent fashion as detailed by Shelimov et al..[8] On the alumina support, after calcination and release of the water solvent, platinum is also found to be still linked to hydroxyl, chlorine and oxo ligands according to EXAFS and temperature programmed desorption.[6,7] However, the relative thermodynamic stability and precise nature and number of ligands involved in these complexes after thermal treatment such as calcination and reduction remain challenging to decipher. Understanding the formation mechanisms of catalytic sites on a support is required to better control the resulting properties of the catalysts (selectivity, reactivity or lifetime) by optimizing the intrinsic properties of active sites (electronic and coordination properties) as well as by maximizing the number of active sites (dispersion). In such catalyst, the role of chlorine is also of primary importance. It has been shown recently that Cl content influence the concentration of Pt single atoms.[9] Moreover, it enables the redispersion of the used platinum active phase during a regeneration step involving an oxychloration treatment upon O_2 and a chlorinating agent such as HCl, CCl_4 or else.[10–12] In this experimental context, the nature of the $PtO_xCl_yH_z$ complex stabilized on the support may be key to control the size of the (re)formed Pt metallic nanoparticles.

Reaching this level of control requires a precise knowledge at the atomistic scale of the thermodynamic behavior of the systems and of the various mechanisms linking the precursors to the final product. Density functional theory[13] (DFT) is a tool of choice to quantify thermodynamic, structural and kinetic properties of complex catalysts.[14] However, it is still challenging for DFT simulations to decipher the chemical and structural evolution of the catalyst active phase from the oxidized metallic precursors to the final metallic active phase during the thermal and reduction treatments of the synthesis steps.[15] Moreover, in spite of being a famous and powerful method to describe relevant properties of chemical systems, DFT suffers from some weaknesses. The treatment of the exchange correlation energy is approximated through exchange correlation functionals whose validity is system dependent, as it can be deduced from many benchmarking works on bulk materials, surfaces or inorganic or organic metallic complexes.[16–24] The accurate description of van der Waals (vdW) interactions is one of the challenges to be addressed.[25] It is thus necessary to assess the validity of a chosen functional, either by comparison with accurate experimental data, or, when absent, by computing reference properties at a higher level of theory. According to Perdew, the Random Phase Approximation (RPA) method used in the framework of DFT via the Adiabatic Connection Fluctuation Dissipation Theorem (ACFDT),[26] lies on the fifth and last ring of the "Jacob's ladder", i.e. the highest level of chemical accuracy.[27] ACFDT-RPA allows the calculation of a fully non-local correlation energy able to grasp the long-range correlation effects such as van der Waals interactions (in particular, the London terms). The exchange correlation energies are exactly calculated, even if under some approximations (RPA),[28] so the validity of the results does not depend on some compensation errors, contrary to DFT. However, the ACFDT-RPA method in its simplest form (also called the direct RPA[29]) is not exempt of defaults. In particular, short-range correlation effects are not well described leading to underestimation of binding energies, and poorly accurate atomization energies,[30] whereas formation enthalpies of solids, reaction energies or adsorption energies are significantly improved by ACFDT-RPA with respect to generalized gradient approximation (GGA) with PBE[31] functionals as detailed in what follows.[32] To compensate for some deficiencies on cohesive energies, new RPA schemes have been developed.[30,33]

The ACFDT-RPA method was found to perform remarkably well for the quantification of lattice parameters,[32,34] of relative stability of polymorphs,[35] of adsorption energies and adsorption site preferences of various molecules on transition metal surfaces (including platinum)[36] and on zeolites.[37,38] In the work of Göltl et al.,[37] the use of Hartree-Fock (HF) orbitals was found to be an improvement compared to the more classically PBE orbitals used. However, for small metallic complexes, Burrow et al.[39] found that the use of Kohn Sham (KS) orbitals leads to better results.

Although only few benchmarks are available to assess the quality of the RPA on the transition metal compounds, the ability of this method to describe such multi-referential species is highlighted even for its

simplest form: the direct RPA. Energy barrier [40] for the HTBH38 and NHTBH38 test sets by Truhlar et al.,[41] which do not include metals, are particularly well reproduced at the direct RPA level, while more sophisticated RPA methods (such as RPA+, range separated-RPA, RPA+SOSEX, etc.) do not lead to better results because of a partial cancelation error due to the similitude of the involved species with direct RPA.[42] Bates et al.[43] highlight on three different test sets of reactions (Furhe-Perdew 18,[18] Johnson-Becke 32[44] and Steinmetz-Grimme 13[17]), containing transition metals but not Pt, the fact that RPA based on various KS orbitals provide more accurate results than GGA, hybrids or metaGGA functionals allowing a relatively good description of such multi determinant species using a single KS determinant. Waitt et al.[45] showed that the reaction energies obtained on the SG13[17] set are more than satisfactory compared to other tested functionals even though the chemical accuracy of less than 1 kcal/mol is still not achieved. Another benchmark done by Chedid et al.[46] on various test sets, which include transition metals, and mechanisms showed that the RPA method was the closest one among the tried functional to their numerical reference (DLPNO-CCSD(T)) while being generally close to experimental results too. ACFDT-RPA thus appears as a good alternative to the costly wavefunction methods such as coupled cluster. In any cases, the RPA method performed quite well and consistently for such systems while the most suited exchange-correlation functional performance changes with the considered set of reactions.[17–23]

As a consequence, the present work will serve a dual purpose. On the one hand, it aims at determining the evolution of $[PtO_xCl_y(OH)_z(H_2O)_n]^0$ complexes under various thermal and gas phase treatments as used during catalytic activation steps (thus, after the release of the aqueous solvent). On the other hand, since the previous state of the art has shown the reliability of ACFDT-RPA method to quantify reaction/formation energies, we will undertake a benchmark of reactions energies involving these Pt complexes. For that purpose, we will study the thermodynamic stability of $[PtO_xCl_y(OH)_z(H_2O)_n]^0$ complexes through the calculation of Gibbs free energy variation for relevant reactions at a high level of theory (ACFDT-RPA) in order to assess the validity of various affordable exchange correlation functionals. We will thus provide a reliable benchmark based on ACFDT-RPA method in order to discriminate among some of the well-known and less computational demanding functionals for studying platinum complexes. The impact of the functionals will be analyzed at 0 K, and the impact of the electronic energy deviations will be quantified on the elaboration of thermodynamic phase diagrams, depicting the evolution of stability and chemical composition of the $[PtO_xCl_y(OH)_z(H_2O)_n]^0$ complexes under various thermal and gas phase (O_2, H_2, HCl, H_2O) treatments, including calcination and reduction conditions applied during the synthesis and activation of catalysts. To the best of our knowledge, no theoretical works were devoted to such metallic complexes solving the coordination sphere of Pt in reaction conditions. We thus expect to provide an unambiguous determination of the coordination sphere of platinum under reaction conditions.

III.2. Computational methods

All the calculations were done using the VASP 5.4.1 software.[47] Geometries were optimized using the GGA PBE[31] exchange correlation functional corrected with the dDsC[48,49] scheme for the dispersion forces. A 400 eV cut-off was used for the kinetic energy of the plane wave basis set. 15x15x15 $Å^3$ cells were used, allowing to reach converged energies with deviation lower than 3 meV with respect to the cell volume. Core electrons were treated by using the Projector Augmented Wave (PAW) formalism.[50] All calculations were performed at the gamma point of the Brillouin zone, and spin polarization were considered to define the ground state of each structure. A Gaussian smearing of 0.05 eV was applied and charges were evaluated using the Hirshfeld[51] formalism. Convergence criteria were fixed to 10^{-7} eV for SCF cycles and to 10^{-2} eV.$Å^{-1}$ for forces.

Electronic energies are calculated by undertaking a single point calculation on the previously optimized geometries. Various classes of exchange correlation functionals were used: two GGAs (PBE[31] (dDsC[48,49]) and optPBE[52–55]); three meta-GGAs (TPSS,[56] RTPSS[57] and SCAN[58]); and three hybrids (HSE06,[59–61] B3LYP[62–64] and PBE0[65]). A higher cut-off energy of 800 eV combined with a smaller Gaussian smearing (0.001 eV) was used to ensure that no bands are partially occupied. Moreover, because VdW-DFT functional (optPBE-VdW) is used and as calculations involve a transition metal, aspherical contributions from the gradient correction inside the PAW spheres were considered.

ACFDT-RPA calculations were done on the geometries previously optimized at the PBE-dDsC level to calculate correlation energies. One can then obtain the total electronic energy by adding the exchange energy. The exchange energy was calculated using the Hartree Fock formalism for PAW pseudopotential as implemented in VASP. 15x15x15 $Å^3$ cells with 800 eV cut-off were used in addition to pseudo-potentials with smaller cut-off radii for O, Cl and H (**Table SIII-1**, **Table SIII-2**, while s, p and d electrons of Pt were treated as valence electrons. The correlation energy was calculated using smaller cells (10x10x10 $Å^3$) and smaller cut-off energy for the basis set (600 eV) as this calculation is considerably more expensive. As many unoccupied bands must be taken into account , *GW* pseudo potentials were used, as proposed by Harl et al.[66] For platinum, p and d electrons were considered as valence ones. The response function was integrated over 20 frequencies. Such a number can be considered as overkill for some of the considered systems, but as it did not lead to a sizable computational cost, this set up was applied independently of the system. The cut-off of the response function was set at 2/3 of the cut-off energy (tests showed no significant impact). GGA orbitals from PBE-dDsC calculation were used for both the exchange and correlation calculations.

The thermodynamic stability of platinum complexes under various reaction conditions was determined by calculating Gibbs free energies of a large set of relevant reactions (calcination and reduction processes, as described later) involving $[PtO_xCl_y(OH)_z(H_2O)_n]^0$ formed after the release of aqueous solution under thermal and gas treatments. Among these, $PtCl_4$ was found to be a key species, as mentioned by Lambert et al.[67] justifying that we will use $PtCl_4$ as a neutral formal reference to quantify all the reaction energies. However, the final thermodynamic diagrams are fully independent from this choice of the reference. Translational, rotational and vibrational contributions were calculated under the rigid-rotor and harmonic oscillator approximation and added to the electronic energy. Frequencies have been computed on the structures previously optimized at the PBE level by determining the hessian matrix using density functional perturbation theory. The Gibbs free energy of platinum single atom was calculated with the translational component only. Details on formula can be found in **Supporting Information 2 (Equations S1-S10)**. Gibbs free energies were calculated for temperatures ranging from 0 K to 1000 K and pressures from 10^{-12} bar to 1 bar. Calcination reactions are considered at a fixed $P(O_2)$ of 0.21 bar as it is usually chosen in experimental preparation, while reduction reactions are achieved under 1 bar of H_2.[68] The surrounding environment is treated as an ideal gas phase reservoir. The vapor/liquid water equilibrium is reported on all thermodynamic diagrams to recall the limit of stability of vapor water used in our thermodynamic model.

III.3. Results and discussion

III.3.1. Platinum complexes

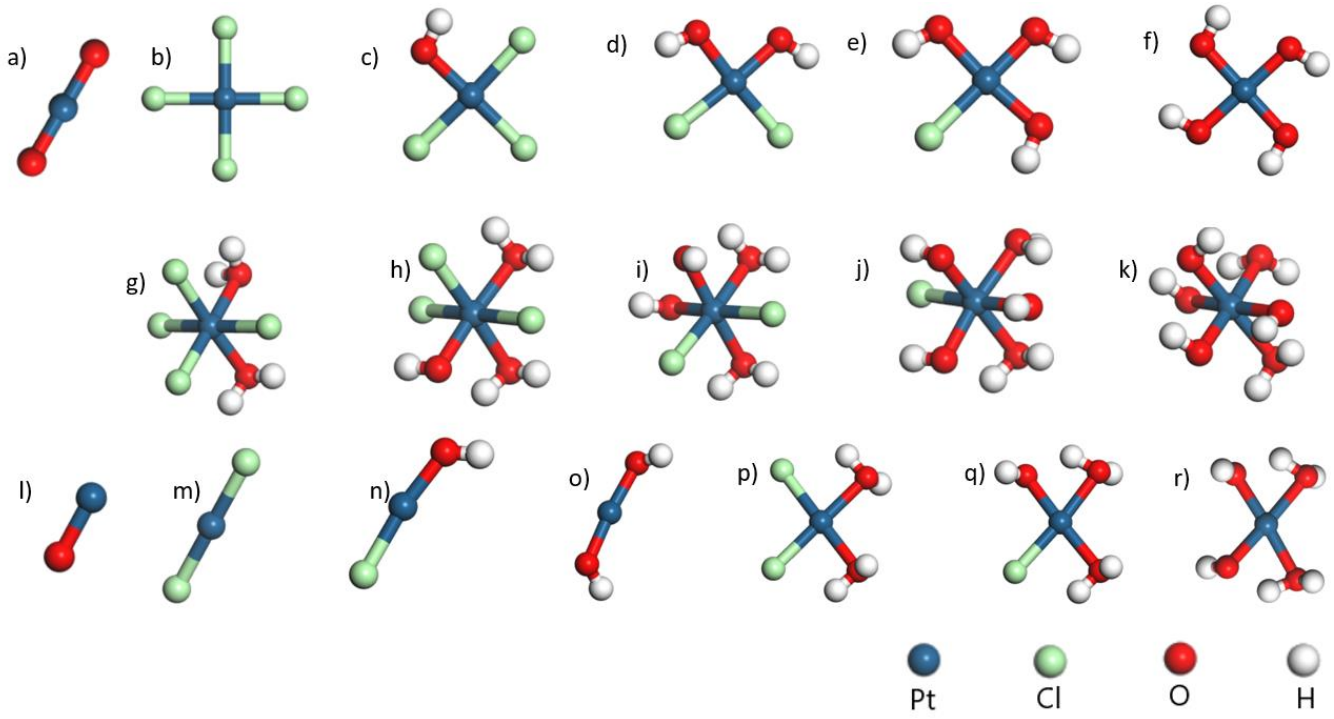

Figure III-1 – Optimized structures of a selection of the most stable considered platinum complexes ranked by their formal oxidation degree (Pt(IV): a-k and Pt(II): l-r) and hydration level.

Considering experimental observations,[6,7,69] $[Pt_1(O^{2-})_x(Cl^-)_y(HO^-)_z(H_2O)_n]^0$ complexes were simulated. Starting from $PtCl_4$, model reactions such as ligand exchange, hydration and reduction were considered to build a pool of 38 species (**Table SIII-3**). In cases where several isomers exist, only the most stable geometry at 0 K was kept for the given stoichiometry. These complexes are classified according to their formal oxidation degree (+IV, +III, +II, +I, 0), being calculated as a function of the nature of the surrounding ligands (Cl^- and OH^- being X ligands, O^{2-} of X_2 type, H_2O of L type). Some of the most stable complexes, with various geometries and ligands, found during the calcination and/or the reduction processes are exhibited in **Figure III-1**. Ground state geometries of the complexes are mainly impacted by the number of ligands in the coordinative shell, rather than by the nature of these ligands: octahedral geometries are obtained for hexa-coordinated complexes, square based pyramids for penta-coordinated complexes with little deviations due to the presence of H-bonds which introduce some internal constraints, square planar for tetra-coordinated complexes, trigonal planar for the tri-coordinated and linear for the bi and mono coordinated ones. The bond lengths reported in **Table SIII-3** reveal the following

classification: Pt-Cl > Pt-O (H_2O) > Pt-(OH) > Pt-O (oxo). Bond lengths for Pt(II) are shorter than for Pt(IV). Increasing the number of ligands in the coordination sphere of the platinum leads to longer bonds. The PtO distance in PtO_2 is calculated at 1.70 Å (close to 1.72 Å reported by Xu et al.[70]) while it is elongated to 1.75-1.76 Å for the $PtOCl_y(OH)_z$ systems. The same occurs for the Pt-Cl bond in $PtCl_y(OH)_z$ systems (both Pt(IV) and Pt(II)) upon addition of undissociated water molecules. For Pt(IV), Pt-Cl bonds increases from 2.24 Å without water to 2.22-2.34 Å as one water molecule is added, up to 2.26-2.35 Å for the octahedral complexes. This effect is also visible on the same complexes for the Pt-(OH) bonds which varies from 1.93-1.96 Å for the complexes without water to 1.96 Å-2.03 Å for the octahedral platinum. Pt-Cl and Pt-(OH) bond lengths of octahedral complexes are in good agreement with bond lengths of alumina supported complexes after calcination treatment, measured by extended X-ray absorption fine structure spectroscopy (EXAFS).[7,71–73] However none of the Pt-O bond length reported in these experimental studies is as short as the Pt-O of the oxo ligand calculated here (1.70-1.80 Å) which results from support effect, beyond the scope of the present study. The elongation of the bonds with the addition of water molecules is also observed for the Pt(II) with the Pt-Cl bond length going from 2.15 Å for the dehydrated complexes (which is slightly smaller than the one found by Xu et al.[74] who optimized their structures at a B3LYP level), to 2.18-2.23 Å for the tri-coordinated complexes and up to 2.25 Å for the square planar Pt(II). **Table SIII-3** illustrates that a simple correlation exists between the Pt-ligand distance elongation and the increasing number of ligands for a given ligand type.

The spin ground state **(Table SIII-3)** is more impacted by the number of ligands (and by the geometry) and the oxidation degree of platinum rather than by the nature of the ligand. Among Pt(IV) complexes, the tetracoordinated square planar complexes are all in triplet state, while the penta-coordinated and octacoordinated complexes (with H_2O ligands) exhibit a singlet ground state. This trend is expected from ligand field theory, whereas the behavior of $PtOCl_2$, PtOCl(OH) and $PtO(OH)_2$ is more complicated to anticipate. $PtOCl_2$ exhibits a triplet ground state while PtOCl(OH) and $PtO(OH)_2$ are stable with a singlet spin state. This change of spin state is accompanied by a deformation of the complexes, and $PtOCl_2$ exhibits an asymmetrical geometry while $PtO(OH)_2$ is symmetrical, details of the relation between the constrained spin state and geometry of $PtOCl_2$ and $PtO(OH)_2$ can be found in **Table SIII-4** and **Table SIII-5**. In the case of PtOCl(OH), the geometry is asymmetrical due to the 3 different types of ligands. Among Pt(II) complexes, PtO and $PtCl_xO_{(2-x)}$ exhibit a triplet spin state, while all the other ones involving more water ligands are singlet. The neutral Pt(0) atom is found to be more stable in a triplet configuration which is coherent with the d^9s^1 ground state observed experimentally[75]. By contrast, its hydrated forms $Pt(H_2O)$ or $Pt(H_2O)_2$ (involving water adsorption) exhibit a singlet state. Such spin state crossing of Pt(0) was also reported by Granatier et al.[76], using various level of

theory, during the adsorption of benzene on Pt. Finally, only Pt(III) and Pt(I) complexes are stable with a doublet state.

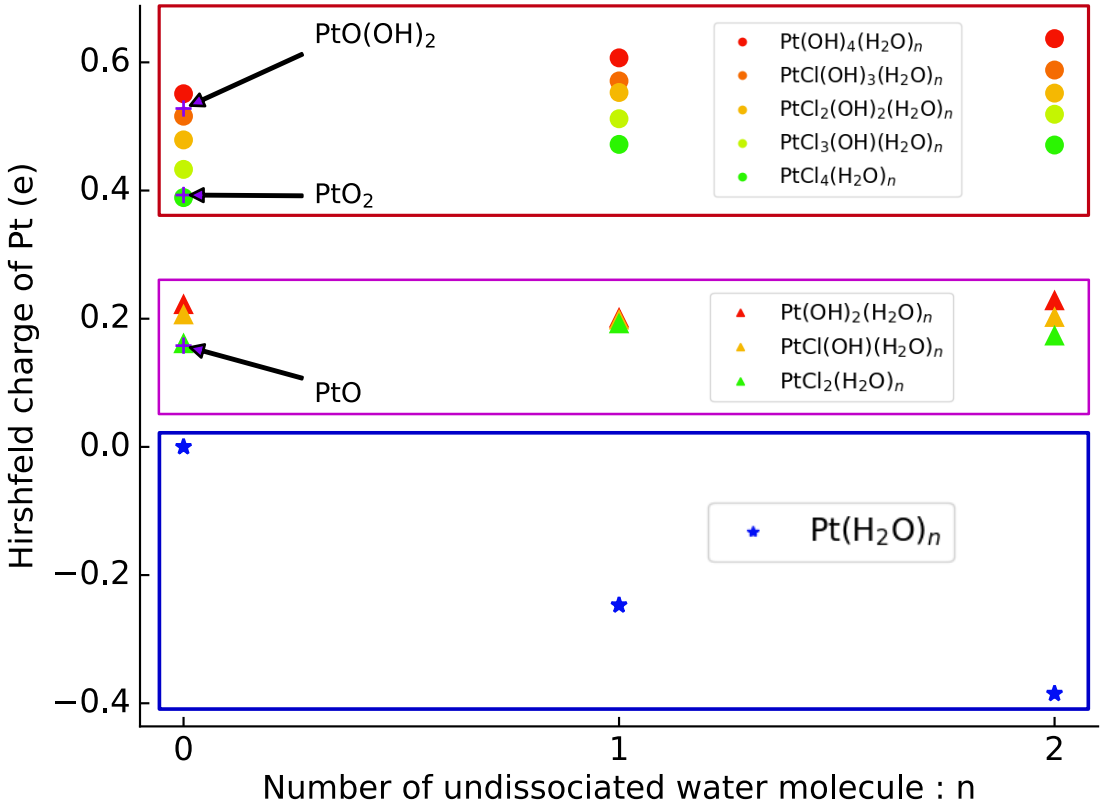

Figure III-2- Hirshfeld charges of the Pt(0), Pt(II) and Pt(IV) complexes according to their chlorination level and number of undissociated water molecule in their coordinative shell. Blue box is for Pt(0), purple one for Pt(II) and the red box for Pt(IV).

Platinum charges were evaluated using the Hirshfeld formalism[51] at the PBE-dDsC level **Figure III-2**). In every case, the distinction of the platinum according to their formal oxidation degree is consistent with the Hirshfeld charges showing that Pt(IV) is more positively charged (+0.39 to +0.64) than Pt(II) (+0.16 to +0.23). For $PtCl_y(OH)_z(H_2O)_n$ complexes, both Pt(II) and Pt(IV) are more oxidized as the number of hydroxyls in the coordinative shell increases (i.e. the number of chlorine decreases). This trend is particularly relevant for Pt(IV) whatever the number of undissociated water molecules. The impact of hydration is less systematic and depends on the oxidation level of the platinum and the relative hydration mechanism. For Pt(IV), whose hydration occurs without dissociation, a slight depletion of the electronic density is observed with additional water molecules. By contrast, this behavior is opposite for Pt(0) complexes for which adding water in the coordinative shell is accompanied by a significant augmentation of the negative Hirshfeld charge. For both Pt(IV) and Pt(II), if there is

neither OH group nor H_2O in the coordinative sphere, the oxidative power of an oxo ligand is very close to the one of two chlorine ligands. Indeed, PtO_2 and $PtCl_4$ have similar Hirshfeld charges, PtO and $PtCl_2$ also exhibit similar charges. However, this trend does not hold anymore as soon as other ligands are coordinated to the platinum, and for example, $PtO(OH)_2$ and $PtCl_2(OH)_2$ exhibit different Hirshfeld charges.

III.3.2. Impact of the level of theory on relevant reaction energies

To assess the validity of DFT calculations of the properties of these platinum complexes, different levels of exchange correlation functionals are compared: 2 GGAs which take into account dispersive forces with different methods (PBE[31]-dDsC[48,49] and optPBE-vDW[52–55]); 3 meta-GGAs (TPSS,[56] RTPSS[57] and SCAN[58]); and 3 hybrids (B3LYP,[62–64] HSE06[59–61] and PBE0[65]). Single point calculations with the different functionals are undertaken on geometries previously optimized at the PBE-dDsC level as described in the methods section. This choice is firstly justified by the fact that the highest level ACFDT-RPA does not allow to perform systematic geometry optimization. Secondly, for the reactions used in our benchmark, we tested the impact of geometry optimization at the HSE06 level and found that the energy difference between optimized systems and those frozen at PBE-dDsC level is lower than 6.5 kJ/mol with an absolute average difference over all the benchmark reactions of 1.2 kJ/mol (**Table SIII-6**). Such a good agreement between energies obtained from a fully self-consistent HSE06 calculations and those obtained after a single point evaluation done at the HSE06 level on a GGA optimized structures was also reported by Gouveia et al. for calculation on surfaces.[77]

To benchmark the exchange correlation functionals, 57 relevant model reactions are chosen which will be defined as ligand exchange, hydration and reduction. 35 reactions are considered for the Pt(IV) complexes, divided into 14 ligands exchanges, 14 hydrations and 7 reductions. 20 reactions (6 ligand exchanges, 7 hydrations and 7 reductions) are used for the Pt(II) complexes and two hydrations of Pt^0. The equations for the ligand (OH/Cl) exchange reactions (1), for hydrations (dissociative (2) or not (3)) and those for reductions ((4), (5) and (6)) are written as follows:

$$PtO_xCl_y(OH)_z(H_2O)_n + H_2O \rightleftarrows PtO_xCl_{y-1}(OH)_{z+1}(H_2O)_n + HCl \quad (1)$$

$$PtO_xCl_y(OH)_z(H_2O)_n + H_2O \rightleftarrows PtO_{x-1}Cl_y(OH)_{z+2}(H_2O)_n \quad (2)$$

$$PtCl_y(OH)_z(H_2O)_n + H_2O \rightleftarrows PtCl_y(OH)_z(H_2O)_{n+1} \quad (3)$$

$$PtCl_y(H_2O)_n + iH_2 \rightleftarrows PtCl_{y-2i}(H_2O)_n + 2iHCl \quad (4)$$

$$Pt(OH)_z(H_2O)_n + iH_2 \rightleftarrows Pt(OH)_{z-2i}(H_2O)_n + 2i(H_2O) \quad (5)$$

$$PtO_x + iH_2 \rightleftarrows PtO_{x-i} + i(H_2O) \quad (6)$$

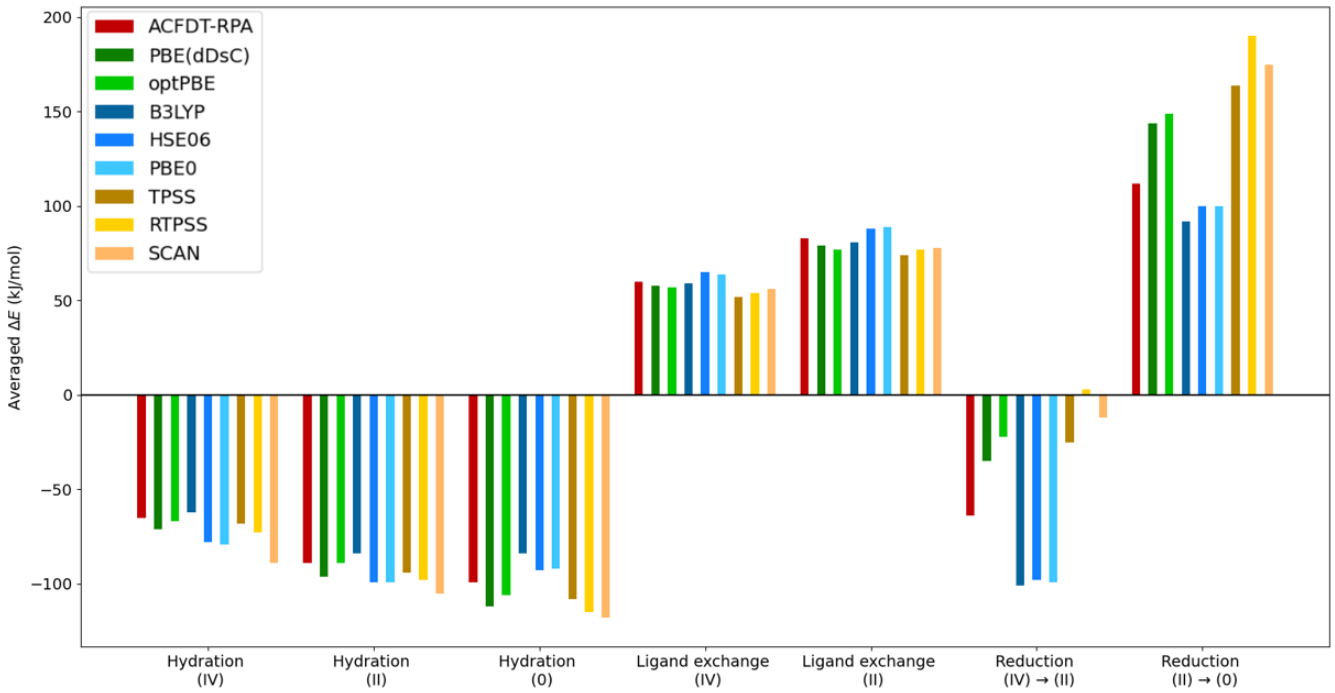

Figure III-3. Averaged reaction energies classified per class of reaction and ranked according to the oxidation level of the platinum. ACFDT-RPA (red) is taken as reference and compared to GGAs (green colors), hy-brids (blue colors) and metaGGAs (yellow-brown colors)

The exhaustive list of all the reactions and reaction energies calculated at each level of theory is reported in **Table SIII-7**, while values averaged for each level of theory are plotted in **Figure III-3**.

Before benchmarking the exchange correlation functionals with ACFDT-RPA, we will describe the reaction energetics of the Pt complexes at the ACFDT-RPA level in order to highlight the main factors impacting the reaction energies of the platinum complexes, such as the hydration level, the oxidation degree and the number of chlorine ligands.

Considering first hydration energies (2) and (3), they are predominantly exothermic at 0 K (excepting the hydration of $Pt(OH)_4$ and PtO_2) and cover a wide range from -145 kJ/mol for the hydration of PtO to +21 kJ/mol for the hydration of $Pt(OH)_4$ (**Table SIII-7**). The formation of either octahedral Pt(IV) complexes or square planar Pt(II) complexes is a stabilizing factor compared to the formation of penta-coordinated Pt(IV) or tri-coordinated Pt(II) complexes. Moreover, the presence of chlorine in the coordinative shell of Pt(IV), tends to facilitate hydration. For instance, the hydration energy of $PtCl_4$ is -57 kJ/mol, whereas that of $Pt(OH)_4$ is +21 kJ/mol. This

phenomenon is not observed for the hydration of Pt(II). In presence of oxo ligand in Pt complexes, the hydration always leads to the dissociation of the added water molecule with the formation of two hydroxyls.

The exchange of one chlorine for one hydroxyl (1) is always endothermic for both Pt(II) and Pt(IV), with reaction energies varying between 39 kJ/mol and 91 kJ/mol (**Table SIII-7**). The exchange becomes more and more endothermic with the number of undissociated water molecule in the coordinative sphere, especially for Pt(IV).

Reaction energies of reductions (4), (5) and (6) are highly impacted by the coordination shell of platinum. For both Pt(IV) and Pt(II), chlorinated platinum are harder to reduce than hydroxylated ones. Moreover, whereas the reduction of Pt(IV) into Pt(II) is found exothermic, the reduction of Pt(II) into Pt(0) is endothermic for almost all considered reactions but the reduction of PtO. Increasing the number of undissociated water molecules in the coordination shell impacts differently the reduction energetics depending on the oxidation state of Pt and the presence of Cl or OH ligands. Hence, the reduction of $Pt(OH)_4(H_2O)_n$, $Pt(OH)_2(H_2O)_n$ and $PtCl_2(H_2O)_n$ is easier for higher *n* values, whereas the reduction of $PtCl_4(H_2O)_n$ becomes more difficult increasing *n*.

To benchmark the exchange correlation functionals, we consider first the hydration reactions (2) and (3). **Figure III-3** shows that for all functionals the mean reaction energies are exothermic at 0 K and for GGAs and metaGGAs the exothermicity depends on the Pt oxidation states as follows: Pt(0) > Pt(II) > Pt(IV), as previously described for ACFDT-RPA. For hybrids the trends is different with the hydration of Pt(II), being slightly favored compared to the hydration of Pt(0). The energies obtained at the GGA level are close to the ACFDT-RPA values and their relative difference to the ACFDT-RPA reference do not depend on the functionals. The largest mean absolute error (MAE) with the RPA reference (+13 kJ/mol) being for the hydration of Pt(0) at PBE-dDsC level (**Table SIII-7**). The same trend is observed for the metaGGAs with the three functionals: TPSS, RTPSS and SCAN all lead to more negative hydration energies than the ACFDT-RPA reference. By contrast, the behavior of hybrids is not consistent. Indeed, B3LYP tends to favor the dehydrated form of Pt(IV) and Pt(II), while PBE0 and HSE06 overestimate the favorable nature of hydration compared to ACFDT-RPA. The hydration of Pt(0) is less favorable with all three hybrids than with ACFDT-RPA. For Pt(0), no disparity between exchange correlation functional of a given class is observed : GGAs and metaGGAs facilitate the hydration in contrast with hybrids.

Regarding ligand exchange (1), all functionals reveal an endothermic nature at 0 K with a higher endothermicity for Pt(II) than for Pt(IV). All functionals exhibit rather small MAE values (all inferior to 10 kJ/mol). This means that the replacement of chlorine atoms by hydroxyls is not intrinsically favored at 0 K. GGAs provide values very close to ACFDT-RPA (slight underestimation and MAE<5 kJ/mol). HSE06 and PBE0 tend to stabilize the chlorinated complexes compared to ACFDT-RPA while B3LYP does the opposite. Contrary to hybrids, the three

metaGGAs behave rather similarly by providing less endothermic values than ACFDT-RPA (MAE between + 5 kJ/mol and + 10 kJ/mol).

The results become, however, extremely functional dependent for the reduction reactions and high deviations to the ACFDT-RPA values are observed. Both GGAs and metaGGAs stabilize the oxidized state of Pt compared to ACFDT-RPA, while hybrids facilitate the reduction. In the case of the reduction of Pt(IV) into Pt(II), only RTPSS predicts slightly endothermic reactions. As a matter of fact, the largest differences are observed for the RTPSS functional with a MAE of +66 kJ/mol for the reduction of Pt(IV) into Pt(II) and of +78 kJ/mol for Pt(II) into Pt(0). GGA values are more consistent with each other and in all cases, the most oxidized form of the platinum being stabilized compared to ACFDT-RPA. The MAE values are still far from negligible even if PBE-dDsC exhibits slightly better performances with MAE values of 29 and 32 kJ/mol for Pt(IV) into Pt(II) and Pt(II) into Pt(0) reductions, respectively. Regarding hybrids, they exhibit comparable deviations comprised between 19 and 37 kJ/mol depending on the reduction reactions.

To summarize this analysis, we report in **Table III-1** the MAE averaged within each class of functional for the three main reactions. For the three reactions considered in our work, metaGGAs exhibit the largest MAE values among the three classes of functionals. In particular, for the reduction reactions, the MAE reaches its maximal value (58 kJ/mol) which makes TPSS, RTPSS or SCAN functionals not applicable for our further analyses. Hybrids seem to provide the best results with respect to ACFDT-RPA particularly for reduction (MAE=+28 kJ/mol) and ligand exchange (MAE=+5 kJ/mol). Interestingly, GGA functionals provide a good compromise since the discrepancy for reduction reactions is far smaller than metaGGA, while the MAEs for ligand exchange and hydration are the smallest of the three functionals. The benchmark provided by M. Steinmetz and S. Grimme on Pd and Ni complexes,[17] who compared reaction energies for similar classes of functionals with CCSD(T)/CBS methods, shows that hybrids and more particularly PBE0 functional perform the best. In our case, we saw that HSE06 and PBE0 may be considered also as the closest ones to RPA. Moreover, M. Steinmetz and S. Grimme also showed that metaGGAs do not provide any significant improvements with respect to GGAs, whereas we found that they be even worse.

XC functional / Reactions	GGA	Hybrid	metaGGA
Ligand Exchange	5	5	8
Hydration	8	15	14
Reduction	34	28	58

Table III-1. MAE (kJ/mol) calculated for each class of reaction and each family of exchange correlation functional.

To improve the accuracy for the reduction reaction energies (and also all other), it can also be suggested to combine energies obtained with PBE-dDsC and those with one hybrid functional such as HSE06. This observation may be in line with previous reports discussing the optimal amount of the Hartree-Fock exchange on the energetics of Pd complexes.[17,24]

III.3.3. Thermodynamic stability

The relative stability of the platinum species at 0 K was described in the previous section. In this part, we consider firstly the impact of temperature and reactant pressures (under calcination and reduction conditions) on the thermodynamic stability of the platinum complexes within the ACDFT-RPA approach. Then we assess the impact of the exchange-correlation functional on the thermodynamical diagrams. To build such diagrams, we linked the platinum complexes one to another through the reaction network illustrated in **Figure III-4**. This network contains most of the reactions or a linear combination of those analyzed in our previous benchmark.

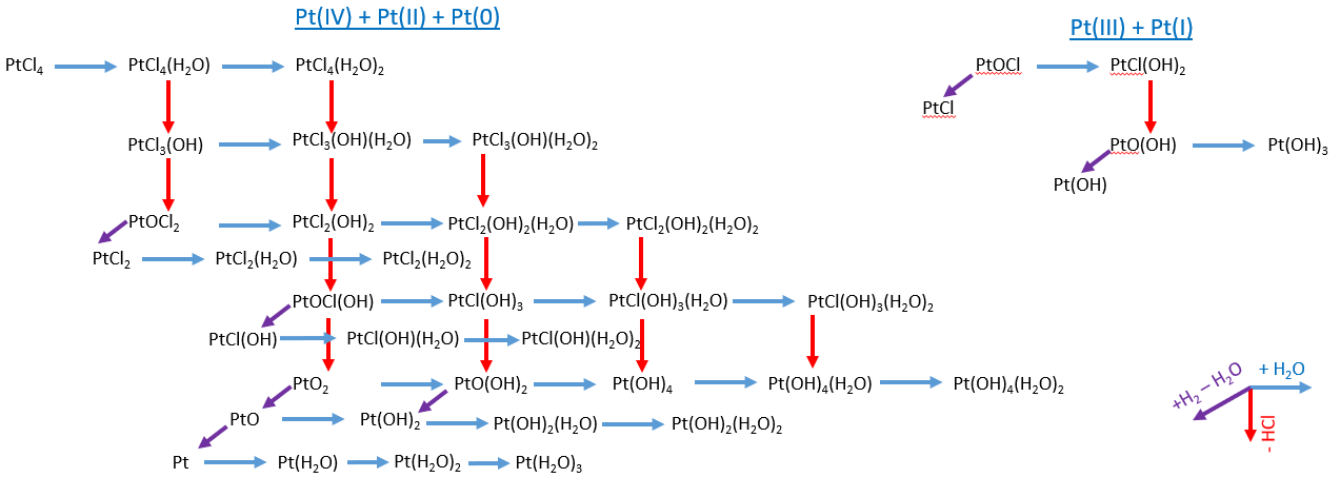

Figure III-4. Platinum complexes considered in the thermodynamic models and the interconnected reactions: hydration, ligand exchange and reduction. For the sake of clarity, Pt(III) and Pt(I) are put aside but are also linked to Pt(IV), Pt(II) and Pt(0) through a linear combination of these reactions.

In a preliminary analysis, we investigate the stability of Pt(IV) and Pt(II) complexes under water and HCl pressures and for various temperatures (T) in order to elucidate the nature of stable Pt species (**Figure SIII-1**). As it will be discussed in the forthcoming sections, these are important experimental parameters controlling the nature of species. Actually, under calcination and reduction conditions, P(HCl) is not directly controlled, hence

P(HCl) will be only used as an indicator of the amount of chlorine present in this case. However, chlorinating agent such as HCl may also be used for favoring the redispersion of the Pt active phase during the regeneration step of some catalysts.[10–12] Hence, it is relevant to firstly analyze the intrinsic impacts of HCl and H_2O in absence of any other gas phase reactants such as O_2 and H_2 used for calcination and reduction.

The evolution of the most stable Pt(IV) species are showed in **Figure SIII-1 (a)**. Considering the impact of a reactive atmosphere and temperature highlights the stabilization of dehydrated species such as $PtCl_4$ and PtO_2. Also, the stabilization of PtO_2 occurs as the temperature increases. As expected from the 0 K ligand exchange energy (discussed in section 3.2), the stability of chlorinated complexes over hydroxylated ones is confirmed at each temperature, while at room temperature the doubly hydrated $PtCl_4(H_2O)_2$ is stabilized for water pressure superior to 10^{-6} bar, and for HCl pressure greater than 10^{-10} bar. Even if a similar behavior is observed for Pt(II) complexes (**Figure SIII-1 (b)**), hydroxylated complexes exhibit a larger stability over temperature and HCl pressure. Moreover, the PtO complex shows a stability domain far narrower than its PtO_2 homologue, becoming stable only at 800 K.

III.3.3.a) Calcination

Calcination is a thermal treatment under oxidative atmosphere used during the activation step of supported platinum active phases. It is modelled here with O_2 as oxidative agent according to the reaction equations (7-10), with $PtCl_4$ as reference. As explained in the methods section, using $PtCl_4$ as the reference is purely formal as all the species are linked through the network of reaction (**Figure III-4**) during calcination (and reduction). Therefore, from a thermodynamical point of view, this choice of the reference has no impact on the nature of the most stable species in given thermodynamic conditions. No self-reduction is considered because this would involve the reaction between two monomeric Pt entities to form dimeric species. Our simulation will cover a large range of water pressures and temperatures to highlight general trends. Since calcination experimentally occurs at temperatures close to 800 K under dry air, we will focus on the pressure in O_2 at 0.21 bar. In addition, the presence of HCl pressure will be used as an external variable to probe the Cl content in the Pt complex.

$$PtCl_4 + a(H_2O) + c(O_2) \rightleftarrows PtO_xCl_y(OH)_z(H_2O)_n + b(HCl) \quad (7)$$

$$a = n + \frac{4 + z - y}{2} \quad (8)$$

$$b = 4 - y \quad (9)$$

$$c = \frac{2x + y + z - 4}{4} \quad (10)$$

As it was highlighted before, chlorine is impactful on many properties of the platinum complexes. Even if an oxidative agent such as O_2 is added, the Cl effect is still visible as showed in **Figure III-5, a) b) and c)** as a function of HCl pressure. Without chlorine (**Figure III-5, a**), only one species PtO_2 exhibits a stability domain under calcination conditions. Both $Pt(OH)_4$ and $Pt(OH)_4(H_2O)_2$ may become stable for (T, $P(H_2O)$) conditions where liquid water should be stable, ie. outside of the domain of strict validity of the chemical potential of water considered in this study.

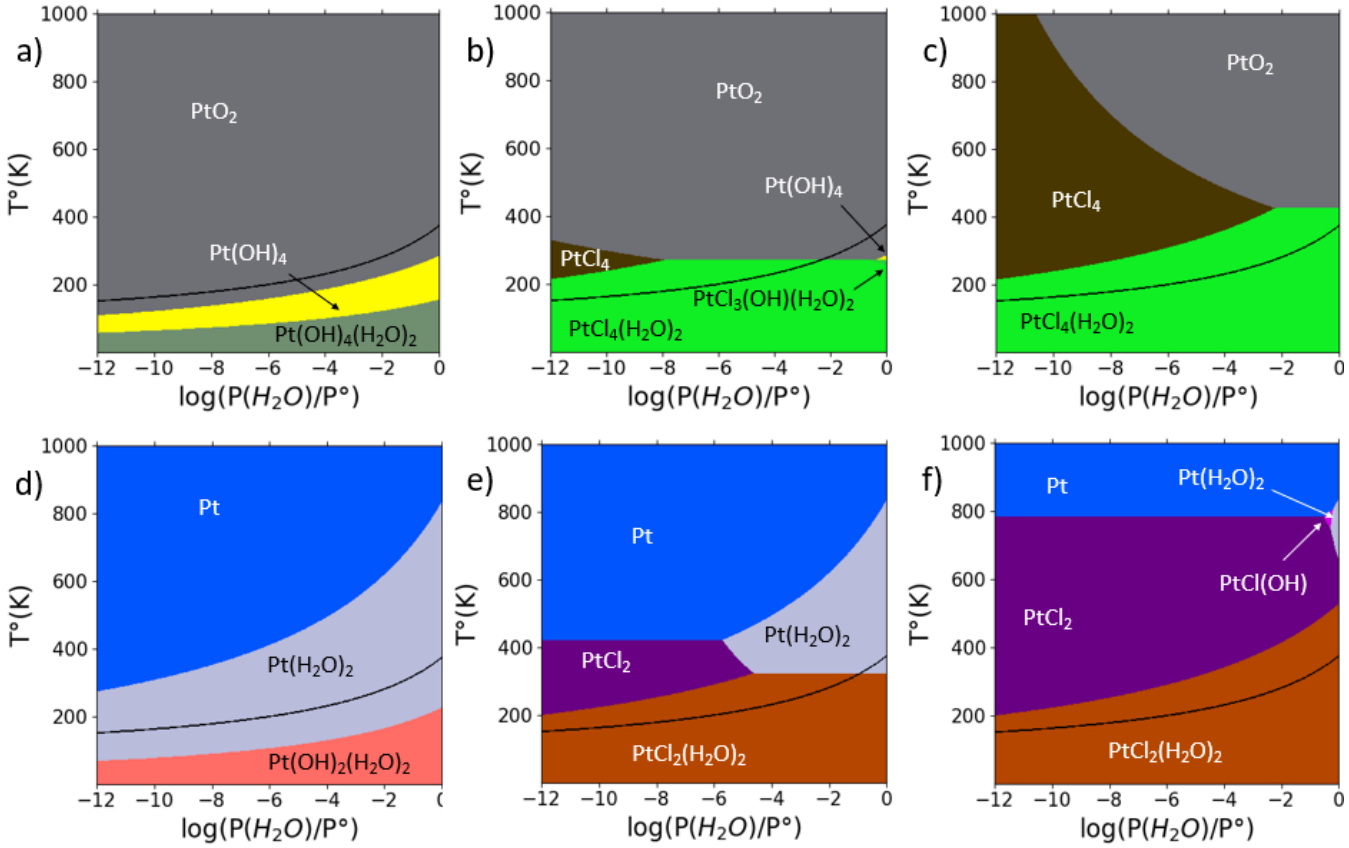

Figure III-5. ACFDT-RPA thermodynamic diagrams of the most stable species under oxidative conditions at $P(O_2)$ = 0.21 bar (a,b,c) and reductive conditions at $P(H_2$ = 1 bar) (d,e,f) for three chlorine loadings: a-d: without chlorine (P(HCl) = 0 bar); b-e: $P(HCl) = 10^{-12}$ bar and c-f: $P(HCl) = 10^{-5}$ bar. The gas phase domain of water is located above the black curved line.

The stabilization of chlorinated complexes appears for the very low pressure in HCl ($P(HCl) = 10^{-12}$ bar) but only for the low temperatures in **Figure III-5**, **b)**. Indeed, a small but existing domain of PtO_2 is starting to be replaced by $PtCl_4(H_2O)_2$ and $PtCl_4$ species. PtO_2 is occupying the majority of the thermodynamic domain even if the transition temperature is shifted to 350 K for $P(H_2O) = 10^{-12}$ bar. At 800 K, the classical calcination temperature, PtO_2 is the most stable species whatever the water pressure. Increasing the amount of chlorine ($P(HCl) = 10^{-5}$ bar, **Figure III-5**, **c)** drastically modifies the diagram and for T = 800 K, the most stable species depends on the

water pressure. For $P(H_2O) < 10^{-8}$ bar, $PtCl_4$ becomes more stable than PtO_2 which is the expected species for the higher water pressures.

However, the impact of chlorine is not limited to the high temperatures. For $P(HCl) = 10^{-5}$ bar, $PtCl_4$ is stable over a wide range of water pressure and temperatures, and it is even stable for temperature up to 1000 K for $P(H_20) < 10^{-9}$ bar. The stabilization of the doubly hydrated $PtCl_4(H_2O)_2$ is also more pronounced than for $P(HCl) = 10^{-12}$ bar with a stability domain up to 400 K at $P(H_20) > 10^{-2}$ bar. This is a consequence of the destabilization of the hydroxylated species with respect to the chlorinated one at such HCl/H_2O pressure ratio as no ligand exchange is possible. More generally, this analysis reveals the sensitivity of the relative stability of $PtCl_4$ and PtO_2 species to the ($P(H_2O)$, P(HCl), T) conditions which should be properly chosen during calcination conditions to control the nature of Pt species present. The transition between these two species according to the HCl pressure and temperature is illustrated in **Figure III-6, a)** for $P(H_2O) = 10^{-6}$ bar. $PtCl_4$ is favored by the increases of HCl pressure, while high temperatures stabilize PtO_2.

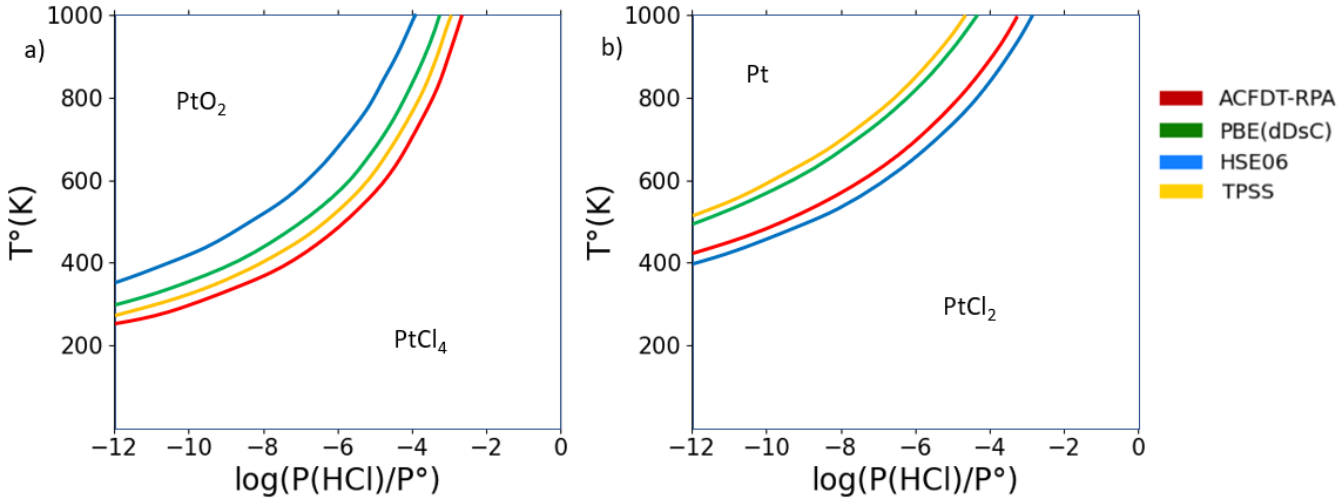

Figure III-6. Transition temperature according to the HCl pressure and temperature for the main stable species expected after calcination (a) and reduction (b).

Many EXAFS studies undertaken on alumina supported Pt systems, revealed the presence of Cl in the coordination sphere of Pt after calcination.[6,7,11,69,71,72] which is compatible with the stability of $PtCl_4$ species illustrated in **Figure III-5 and Figure III-6**. However, the thermodynamic diagrams do not reveal the stability of PtO_xCl_y species at high temperature as found by EXAFS on supported systems.[6,7,10–12,69,71,72] So, we suspect here an effect of the support stabilizing alternative species with the possible formation of Pt-O bond at the interface with the support. Moreover, we cannot exclude that the presence of oxychlorinated species after calcination could result from kinetic limitation effects not considered in our study.

III.3.3.b) Reduction

We will consider here that the reduction process is undertaken with H_2 gas used as reductive agent, usually at $P(H_2)$ = 1 bar and temperature around 825 K.[68] Keeping $PtCl_4$ as reference the reaction equations used to describe the reduction are written as in equation (11-14).

$$PtCl_4 + a(H_2O) + d(H_2) \rightleftarrows PtO_xCl_y(OH)_z(H_2O)_n + b(HCl) \quad (11)$$

$$a = n + x + z \quad (12)$$

$$b = 4 - y \quad (13)$$

$$d = 2 - \frac{2x + y + z}{2} \quad (14)$$

As shown in **Figure III-5**, **d)** the reduction of chlorine free complexes is thermodynamically feasible, since a major part of the diagram corresponds to Pt(0) species with two hydration levels, Pt and $Pt(H_2O)_2$. As for the calcination, chlorine impacts the stability of the species after the reduction. For the lowest amount of chlorine (**Figure III-5, e)** P(HCl) = 10^{-12} bar), the main changes occur for temperatures lower than 400 K. The Pt(0) domain shrinks in favor of Pt(II). $PtCl_2$ replaces a large part of the $Pt(H_2O)_2$ domain and a small portion of Pt(0) domain for $P(H_2O) < 10^{-6}$ bar. By increasing the HCl pressure to 10^{-5} bar (**Figure III-5, f**), the previous trends are enhanced and the reduction temperature leading to Pt(0) is shifted to about 800 K. For the highest water pressure (1 bar), PtCl(OH) has a very limited stability domain. Under reduction conditions (825 K and $P(H_2O) = 10^{-6}$ bar), the expected species depends on the chlorine loading (HCl pressure), being either Pt or $PtCl_2$. However, the destabilization of Pt(0) can be mitigated as the aggregation of the platinum single atom is not considered here, whereas in the gas phase it is expected to aggregate easily.[78,79] This aggregation process could be the reason why no Pt-Cl bond is observed with EXAFS after reduction[7] as reduced platinum single atom may form Pt clusters.[7,73,78,80] More generally, our analysis shows that the stabilization of oxidized species is limited to Pt(II) in $PtCl_2$ species and no Pt(IV) is found stable. So, the Cl content is directly correlated to the reduction temperature of the Pt species through the formation of such $PtCl_2$ species. The temperature of transition between the reduced $PtCl_2$ and Pt(0) according to the HCl pressure is illustrated in **Figure III-6, b)**. The reduction of $PtCl_2$ is favored by the high temperature while increasing HCl pressure will stabilize $PtCl_2$.

III.3.4. Impact of the exchange-correlation functional

The impact of the exchange correlation functional is now analyzed after considering temperature and pressure effects (**Figure SIII-2-Figure SIII-7**). The first general insight is that the main trends observed with ACFDT-RPA are not strongly modified. For calcination conditions, where only Pt(IV) are stable, only little changes were expected

according to the benchmark of section 3.2. The most significant change occurs for the higher HCl pressures, with the stabilization of the oxychlorinated $PtOCl_2$ as a transition domain between $PtCl_4$ and PtO_2 for the hybrids (**Figure SIII-4**). The metaGGAs stabilizes an intermediate hydroxylated species $PtCl_y(OH)_z$ with the increase of the water pressure for temperatures between 400 K and 600 K (**Figure SIII-3**). Interestingly, the GGAs diagram are the closest to the ACFDT-RPA calcination diagram, making such affordable exchange correlation functional a good compromise between accuracy and calculation time to simulate these platinum complexes. For typical calcination conditions, PtO_2 is predicted to be the thermodynamically most stable product by all functionals for the low chlorine amount (P(HCl) = 10^{-12} bar), while higher amount of chlorine in the system, chlorinated or oxychlorinated species such as $PtCl_4$ or $PtOCl_2$ may become dominant. The transitions between these two dominant species, PtO_2 and $PtCl_4$, during calcination for all functionals compared to ACFDT-RPA, according to the HCl pressure and temperature are represented in **Figure III-6, a)**. All functionals tend to over-stabilize $PtCl_4$ over PtO_2 compared to ACFDT-RPA. The largest overestimation is obtained for hybrids (ΔT~100 K for P(HCl)=10^{-6} bar), while TPSS and PBE-dDsC functionals provide transition rather close to the ACFDT-RPA one. Despite not being obvious from our benchmark, the good agreement between TPSS and ACFDT-PRA can be rationalized by subdividing the transition between $PtCl_4$ and PtO_2 into four successive ligand exchanges to form $Pt(OH)_4$ from $PtCl_4$ followed by two dehydrations of $Pt(OH)_4$ into PtO_2. In that case, due to error cancelations between ligand exchange and dehydration steps, TPSS provides results closer to the RPA reference.

Regarding the thermodynamic diagrams of reduction, hybrid functionals are the closest ones to the ACFDT-RPA (**Figure SIII-7**). They lead to the same stable species whose domains differ only by small differences on transition temperatures. GGAs and metaGGAs (to a greater extent) tend to stabilize Pt(II) species over Pt(0) while hybrids shift the reduction temperature to lower temperatures. As for the calcination diagrams, metaGGAs diagrams exhibit stability domain for the hydroxylated species PtCl(OH) and $Pt(OH)_2$ at the highest pressure in water. For P(HCl) = 10^{-12} bar, this trend is particularly enhanced and $Pt(OH)_2$ is found stable for temperatures starting around 500 K and water pressure superior to 10^{-5} bar.

Under reduction conditions, controlling the amount of chlorine in the system becomes crucial as a change in the oxidation degree of the product can be observed. For the low loading in Cl, all exchange correlation functionals predicted Pt(0) as the stable species, and differences are limited to other domains. However, for the highest amount in HCl, two behaviors are observed: hybrid and ACFDT-RPA predict Pt(0) as the most stable species, while $PtCl_2$ is expected with GGAs and metaGGAs. In a consistent way, the level of theory has thus a direct impact on the transition temperature between $PtCl_2$ and the reduced Pt(0) as reported **Figure III-6, b)**. Oxidized form of $PtCl_2$ is favored by the GGA and metaGGA exchange correlation functionals, while the transition obtained with hybrids is much closer to the ACFDT-RPA one. This trend is fully in line with observations made in

our benchmark. Hence, for further study of the reduction of such Pt complexes, it seems to be mandatory to go beyond PBE functionals by calculating the energetics at a hybrid functional level to determine the most appropriate reduction temperature.

III.4. Conclusion

By using DFT calculations, we studied the energetic and structural properties of the neutral $[PtO_xCl_y(OH)_z(H_2O)_n]$ complexes for formal oxidation degree going from +IV to 0. Three families of exchange correlation functionals (GGAs, hybrids, metaGGAs) were benchmarked against the high-level method ACFDT-RPA. The choice of the exchange correlation functional needs to be considered with care if changes of the oxidation state of Pt occurs, such as along the reduction processes of Pt(IV) $\rightarrow$ Pt(II) $\rightarrow$ Pt(0). For that, hybrid functionals are the ones that best predict the redox properties of the platinum complexes under consideration. On the other hand, if no change in the formal oxidation degree is expected as observed during calcination, cheaper functionals such as PBE-dDsC are well suited, whereas metaGGAs exhibit too large discrepancies.

The thermodynamic stability of these complexes under realistic (T, P) conditions was simulated and the impact of the chlorine was highlighted. For the calcination conditions, dehydrated species are expected, and chlorine was found to modify their coordination sphere, going from PtO_2 for the less chlorinated systems to $PtCl_4$ for higher loading in chlorine. The presence of Cl as ligand of Pt agrees with EXAFS experiments on supported system. However, for most of theoretical methods used, no oxychloride Pt species was found to be stable as suggested by EXAFS for alumina supported catalysts. This suggests a specific role of the support in the stabilization of greater variety of Pt species. Interestingly, we highlighted a thermodynamic correlation between HCl pressure and temperature which governs the $PtCl_4$ vs. PtO_2 transition, which is of crucial interest for controlling the conditions of calcination and of oxychlorination applied during the preparation or regeneration of Pt catalysts.

For the reduction step, the presence of chlorine stabilized $PtCl_2$ and shifted the reduction of Pt precursor into Pt(0) single atom to a higher temperature. This $PtCl_2$/Pt(0) transition depends also on HCl pressure which is correlated to the reduction temperature determined on thermodynamic criteria (in absence of any kinetic limitations). Under reduction conditions, where the largest impact could be expected, we found that the hybrid functional HSE06 is better suited to describe these platinum complexes.

We expect this study to be a milestone towards a future work devoted to the understanding of the formation of platinum active phase on supported catalysts. These insights are crucial to provide a more rational understanding of the genesis of metallic Pt active phase. In a near future, we thus propose to investigate how

the presence of an oxide support such as alumina (widely used in industrial catalysts) may impact the present results. In particular, we expect that the relative stability of the various chlorinated and non-chlorinated Pt complexes may be influenced as well as their coordination chemistry involving the surface alumina sites as additional ligands for Pt.

III.5. References

[1] W. C. Zeise, *Ann. Phys. Chem.* **1831**, *97*, 497–541.
[2] M. L. Clarke, *Polyhedron* **2001**, *20*, 151–164.
[3] a) *Handbook of heterogeneous catalysis*, VCH, Weinheim (Germany), **1997**; b) A. Chen, P. Holt-Hindle, *Chem. Rev.* **2010**, *110*, 3767–3804; c) R. J. Farrauto, R. M. Heck, *Catalysis Today* **1999**, *51*, 351–360; d) G. W. Huber, R. D. Cortright, J. A. Dumesic, *Angew. Chem. Int. Ed.* **2004**, *43*, 1549–1551;
[4] a) S. Soled in *Synthesis of solid catalysts* (Ed.: K. P. de Jong), Wiley-VCH, Weinheim, **2009**; b) E. Marceau, X. Carrier, M. Che in *Synthesis of solid catalysts* (Ed.: K. P. de Jong), Wiley-VCH, Weinheim, **2009**;
[5] a) R. D. Cramer, E. L. Jenner, R. V. Lindsey, U. G. Stolberg, *J. Am. Chem. Soc.* **1963**, *85*, 1691–1692; b) J. C. Bailar, H. Itatani, *J. Am. Chem. Soc.* **1967**, *89*, 1592–1599; c) F. Agbossou, J.-F. Carpentier, A. Mortreux, *Chem. Rev.* **1995**, *95*, 2485–2506; d) O. Zaitceva, V. Bénéteau, D. S. Ryabukhin, I. I. Eliseev, M. A. Kinzhalov, B. Louis, A. V. Vasilyev, P. Pale, *Tetrahedron* **2020**, *76*, 131029;
[6] H. Liekse, *J. Catal.* **1983**, *81*, 8–16.
[7] A. T. F. Batista et al., *ACS Catal.* **2020**, *10*, 4193–4204.
[8] B. Shelimov, J.-F. Lambert, M. Che, B. Didillon, *J. Mol. Catal. A. Chem.* **2000**, *158*, 91–99.
[9] A. T. F. Batista, C. Chizallet, F. Diehl, A.-L. Taleb, A.-S. Gay, O. Ersen, P. Raybaud, *Nanoscale* **2022**, *14*, 8753–8765.
[10] J. P. Franck, G. Martino in *Progress in Catalyst Deactivation* (Ed.: J. L. Figueiredo), Springer-Verlag, Dordrecht, **1982**.
[11] F. Le Normand, A. Borgna, T. F. Garetto, C. R. Apesteguia, B. Moraweck, *J. Phys. Chem.* **1996**, *100*, 9068–9076.
[12] K. Morgan, A. Goguet, Alexandre, C. Hardacre, *ACS Catal.* **2015**, *5*, 3430–3445.
[13] a) P. Hohenberg, W. Kohn, *Phys. Rev.* **1964**, *136*, B864-B871; b) W. Kohn, L. J. Sham, *Phys. Rev.* **1965**, *140*, A1133-A1138;
[14] a) C. Chizallet, P. Raybaud, *Catal. Sci. Technol.* **2014**, *4*, 2797–2813; b) V. Pershina, A. Borschevsky, M. Iliaš, *J. Chem. Phys.* **2014**, *141*, 64314;
[15] a) A. Sahu, S. N. Steinmann, P. Raybaud, *J. Catal.* **2022**, *408*, 303–315; b) M. C. Valero, P. Raybaud, *J. Catal.* **2020**, *391*, 539–547;
[16] S. Gautier, S. N. Steinmann, C. Michel, P. Fleurat-Lessard, P. Sautet, *PCCP.* **2015**, *17*, 28921–28930.
[17] M. Steinmetz, S. Grimme, *ChemistryOpen* **2013**, *2*, 115–124.
[18] F. Furche, J. P. Perdew, *J. Chem. Phys.* **2006**, *124*, 44103.
[19] J. G. Brandenburg, J. E. Bates, J. Sun, J. P. Perdew, *Phys. Rev. B* **2016**, *94*.
[20] W. Zhang, D. G. Truhlar, M. Tang, *J. Chem. Theory Comput.* **2013**, *9*, 3965–3977.
[21] T. Weymuth, E. P. A. Couzijn, P. Chen, M. Reiher, *J. Chem. Theory Comput.* **2014**, *10*, 3092–3103.
[22] L. R. Maurer, M. Bursch, S. Grimme, A. Hansen, *J. Chem. Theory Comput.* **2021**, *17*, 6134–6151.
[23] L. Goerigk, A. Hansen, C. Bauer, S. Ehrlich, A. Najibi, S. Grimme, *PCCP.* **2017**, *19*, 32184–32215.
[24] M. M. Quintal, A. Karton, M. A. Iron, A. D. Boese, J. M. L. Martin, *J. Phys. Chem. A* **2006**, *110*, 709–716.
[25] J. Klimeš, A. Michaelides, *J. Chem. Phys.* **2012**, *137*, 120901.
[26] a) D. C. Langreth, J. P. Perdew, *Solid State Commun.* **1975**, *17*, 1425–1429; b) D. C. Langreth, J. P. Perdew, *Phys. Rev. B* **1977**, *15*, 2884–2901; c) O. Gunnarsson, B. I. Lundqvist, *Phys. Rev. B* **1976**, *13*, 4274–4298;
[27] J. P. Perdew, *AIP. Conf. Proc.* **2001**, *577*, 1–20.
[28] P. Nozières, D. Pines, *Phys. Rev.* **1958**, *111*, 442–454.
[29] J. Toulouse, *arxiv:2103.02645 [physics.chem-ph]*, **2021**.
[30] T. Olsen, C. E. Patrick, J. E. Bates, A. Ruzsinszky, K. S. Thygesen, *npj Comput. Mater.* **2019**, *5*.
[31] J. P. Perdew, K. Burke, M. Ernzerhof, *Phys. Rev. Lett.* **1996**, *77*, 3865–3868.
[32] J. Harl, G. Kresse, *Phys. Rev. Lett.* **2009**, *103*, 56401.
[33] a) H. Jiang, E. Engel, *J. Chem. Phys.* **2007**, *127*, 184108; b) J. Paier, B. G. Janesko, T. M. Henderson, G. E. Scuseria, A. Grüneis, G. Kresse, *J. Chem. Phys.* **2010**, *132*, 94103; c) X. Ren, P. Rinke, C. Joas, M. Scheffler, *J.*

Mater. Sci. **2012**, *47*, 7447–7471; d) A. Ruzsinszky, J. P. Perdew, G. I. Csonka, *J. Chem. Theory Comput.* **2010**, *6*, 127–134; e) J. G. Ángyán, R.-F. Liu, J. Toulouse, G. Jansen, *J. Chem. Theory Comput.* **2011**, *7*, 3116–3130;
[34] J. Harl, L. Schimka, G. Kresse, *Phys. Rev. B* **2010**, *81*.
[35] Z.-H. Cui, F. Wu, H. Jiang, *PCCP.* **2016**, *18*, 29914–29922.
[36] a) X. Ren, P. Rinke, M. Scheffler, *Phys. Rev. B* **2009**, *80*; b) Z. Wei, F. Göltl, P. Sautet, *J. Chem. Theory Comput.* **2021**, *17*, 7862–7872; c) L. Schimka, J. Harl, A. Stroppa, A. Grüneis, M. Marsman, F. Mittendorfer, G. Kresse, *Nat. Mater.* **2010**, *9*, 741–744; d) P. S. Schmidt, K. S. Thygesen, *J. Phys. Chem. C* **2018**, *122*, 4381–4390; e) M. Rohlfing, T. Bredow, *Phys. Rev. Lett.* **2008**, *101*, 266106; f) C. Sheldon, J. Paier, J. Sauer, *J. Chem. Phys.* **2021**, *155*, 174702;
[37] F. Göltl, A. Grüneis, T. Bučko, J. Hafner, *J. Chem. Phys.* **2012**, *137*, 114111.
[38] a) F. Göltl, J. Hafner, *Micropor. Mesopor. Mat.* **2013**, *166*, 176–184; b) F. Göltl, J. Hafner, *J. Chem. Phys.* **2011**, *134*, 64102; c) D. Rocca, A. Dixit, M. Badawi, S. Lebègue, T. Gould, T. Bučko, *Phys. Rev. Mater.* **2019**, *3*;
[39] A. M. Burow, J. E. Bates, F. Furche, H. Eshuis, *J. Chem. Theory Comput.* **2014**, *10*, 180–194.
[40] J. Paier, X. Ren, P. Rinke, G. E. Scuseria, A. Grüneis, G. Kresse, M. Scheffler, *New J. Phys.* **2012**, *14*, 43002.
[41] a) Y. Zhao, B. J. Lynch, D. G. Truhlar, *J. Phys. Chem. A* **2004**, *108*, 2715–2719; b) Y. Zhao, N. González-García, D. G. Truhlar, *J. Phys. Chem. A* **2005**, *109*, 2012–2018;
[42] X. Ren, P. Rinke, G. E. Scuseria, M. Scheffler, *Phys. Rev. B* **2013**, *88*.
[43] J. E. Bates, P. D. Mezei, G. I. Csonka, J. Sun, A. Ruzsinszky, *J. Chem. Theory Comput.* **2017**, *13*, 100–109.
[44] E. R. Johnson, A. D. Becke, *Can. J. Chem.* **2009**, *87*, 1369–1373.
[45] C. Waitt, N. M. Ferrara, H. Eshuis, *J. Chem. Theory Comput.* **2016**, *12*, 5350–5360.
[46] J. Chedid, N. M. Ferrara, H. Eshuis, *Theor. Chem. Acc.* **2018**, *137*.
[47] a) G. Kresse, J. Hafner, *J. Phys.: Condens. Matter* **1994**, *6*, 8245–8257; b) G. Kresse, J. Furthmüller, *Comput. Mater. Sci.* **1996**, *6*, 15–50;
[48] S. N. Steinmann, C. Corminboeuf, *J. Chem. Phys.* **2011**, *134*, 44117.
[49] S. N. Steinmann, C. Corminboeuf, *J. Chem. Theory Comput.* **2011**, *7*, 3567–3577.
[50] G. Kresse, D. Joubert, *Phys. Rev. B* **1999**, *59*, 1758–1775.
[51] F. L. Hirshfeld, *Theor. Chim. Acta.* **1977**, *44*, 129–138.
[52] G. Román-Pérez, J. M. Soler, *Phys. Rev. Lett.* **2009**, *103*, 96102.
[53] M. Dion, H. Rydberg, E. Schröder, D. C. Langreth, B. I. Lundqvist, *Phys. Rev. Lett.* **2004**, *92*, 246401.
[54] J. Klimeš, D. R. Bowler, A. Michaelides, *J. Phys. Condens. Matter* **2010**, *22*, 22201.
[55] J. Klimeš, D. R. Bowler, A. Michaelides, *Phys. Rev. B* **2011**, *83*.
[56] J. Tao, J. P. Perdew, V. N. Staroverov, G. E. Scuseria, *Phys. Rev. Lett.* **2003**, *91*, 146401.
[57] J. P. Perdew, A. Ruzsinszky, G. I. Csonka, L. A. Constantin, J. Sun, *Phys. Rev. Lett.* **2009**, *103*, 26403.
[58] J. Sun, A. Ruzsinszky, J. P. Perdew, *Phys. Rev. Lett.* **2015**, *115*, 36402.
[59] J. Heyd, G. E. Scuseria, *J. Chem. Phys.* **2004**, *121*, 1187–1192.
[60] J. Heyd, G. E. Scuseria, M. Ernzerhof, *J. Chem. Phys.* **2003**, *118*, 8207–8215.
[61] A. V. Krukau, O. A. Vydrov, A. F. Izmaylov, G. E. Scuseria, *J. Chem. Phys.* **2006**, *125*, 224106.
[62] C. Lee, W.T. Yang, R.G. Parr, *Phys. Rev. B* **1988**, *37*, 785–789.
[63] S. H. Vosko, L. Wilk, M. Nusair, *Can. J. Phys.* **1980**, *58*, 1200–1211.
[64] A. D. Becke, *J. Chem. Phys.* **1993**, *98*, 1372–1377.
[65] J. P. Perdew, M. Ernzerhof, K. Burke, *J. Chem. Phys.* **1996**, *105*, 9982–9985.
[66] J. Harl, G. Kresse, *Phys. Rev. B* **2008**, *77*.
[67] J. F. Lambert, E. Marceau, B. Shelimov, J. Lehman, V. Le Bel de Penguilly, X. Carrier, S. Boujday, H. Pernot, M. Che, *Stud. Sci. Surf. Catal.* **2000**, *130*, 1043–1048.
[68] G. J. Antos, A. M. Aitani (Eds.) *Chemical industries*, *Vol. 100,* 2nd ed., rev. and expanded. ed., Marcel Dekker, New York, **2004**, *Vol. 100*.
[69] P. Lagarde, *J. Catal.* **1983**, *84*, 333–343.
[70] Y. Xu, W. A. Shelton, W. F. Schneider, *J. Phys. Chem. A* **2006**, *110*, 5839–5846.
[71] J. Berdala, E. Freund, J.P. Lynch., *J. Phys. Colloques* **1986**, *47*, C8-265-C8-268.
[72] F. J. Gracia, J. T. Miller, A. J. Kropf, E. E. Wolf, *J. Catal.* **2002**, *209*, 341–354.
[73] C. Dessal, A. Sangnier, C. Chizallet, C. Dujardin, F. Morfin, J.-L. Rousset, M. Aouine, M. Bugnet, P. Afanasiev, L. Piccolo, *Nanoscale* **2019**, *11*, 6897–6904.
[74] X. Xu, J. Kua, R. A. Periana, W. A. Goddard, *Organometallics* **2003**, *22*, 2057–2068.

[75] a) J. Blaise, J. Vergès, J.-F. Wyart, R. Engleman, *J. Res. Natl. Inst. Stand. Technol.* **1992**, *97*, 213–216; b) J. E. Sansonetti, W. C. Martin, *J. Phys. Chem. Ref. Data* **2005**, *34*, 1559–2259;
[76] J. Granatier, M. Dubecký, P. Lazar, M. Otyepka, P. Hobza, *J. Chem. Theory Comput.* **2013**, *9*, 1461–1468.
[77] J. D. Gouveia, J. Coutinho, *Electron. Struct.* **2019**, *1*, 15008.
[78] C. Mager-Maury, C. Chizallet, P. Sautet, P. Raybaud, *ACS Catal.* **2012**, *2*, 1346–1357.
[79] C.H. Hu, C. Chizallet, H. Toulhoat, P. Raybaud, *Phys. Rev. B* **2009**, *79*.
[80] C. Dessal, T. Len, F. Morfin, J.-L. Rousset, M. Aouine, P. Afanasiev, L. Piccolo, *ACS Catal.* **2019**, *9*, 5752–5759.

III.6. Supporting information

SI 1. Pseudopotentials used for the calculations

Atom	Valence	R_c [a.u.]	E_{cut} [eV]
Pt	5d6s	2.5_{sp}	800
O	2s2p	1.2_s 1.52_p	800
Cl	3s3p	1.9_{sp}	800
H	1s	1.1_s	800

Table SIII-1. Valence, core radii (R_c) for the PAW potentials used for the DFT calculation in this work.

Atom	Valence	R_c [a.u.] (PBE HF)	E_{cut} [eV] (PBE HF)	R_c [a.u.] (ACFDT-corr)	E_{cut} [eV] (ACFDT-corr)
Pt	5p5d6s (HF) 5d6s (ACFDT-corr)	2.2_{spd}	800	1.5_s 1.8_d	600
O	2s2p	1.1_{sp}	800	1.2_s 1.52_p	600
Cl	3s3p	1.5_{sp}	800	1.7_s 1.9_p	600
H	1s	0.8_s	800	0.95_s	600

Table SIII-2. Valence, core radii (R_c) for the PAW potentials used for the HF and correlation energies in this work.

SI 2. Thermochemical equations

Internal energy, entropy and enthalpy can be decomposed as following:

$$U_{tot} = U_{trans} + U_{rot} + U_{elec} + U_{vib} \quad \text{S1}$$

$$S_{tot} = S_{trans} + S_{rot} + S_{vib} \quad \text{S2}$$

$$H_{tot} = H_{trans} + H_{rot} + H_{elec} + H_{vib} \quad \text{S3}$$

With

$$U_{vib}(T) = N_A \sum_{i=1}^{N_{vib}} h\nu_i \left(\frac{1}{2} + \frac{e^{-h\nu_i/k_BT}}{1 - e^{-h\nu_i/k_BT}}\right) \quad \text{S4}$$

$$U_{trans}(T) = U_{rot} = \frac{3}{2}RT \quad \text{S5}$$

$$S_{vib}(T) = R \sum_{i=1}^{N_{vib}} \left[\frac{h\nu_i}{k_BT} \frac{e^{-h\nu_i/k_BT}}{1 - e^{-h\nu_i/k_BT}} - \ln\left(1 - e^{-h\nu_i/k_BT}\right)\right] \quad \text{S6}$$

$$S_{Trans}(T) = R\left[\frac{5}{2} + ln\left(\frac{RT}{P^\circ}\left(\frac{2\pi m k_b T}{h^2}\right)^{3/2}\right)\right] \quad \text{S7}$$

$$S_{Rot}(T) = R\left[\frac{3}{2} + ln\left(\frac{\sqrt{\pi}}{\sigma}\left(\frac{8\pi^{2k_B}T}{h^2}\right)^{3/2}(I_A I_B I_c)^{1/2}\right)\right] \quad \text{S8}$$

N_{vib} is taken as 3N-5 for linear molecules and 3N-6 otherwise.

The chemical potential of atmosphere is calculated as:

$$\mu(T,p) = \mu^0(T,p^\circ) + nRTln\left(\frac{p}{p^\circ}\right) \quad \text{S9}$$

The Gibbs free energy is calculated as:

$$G = H - TS \quad \text{S10}$$

SI 3. Bond lengths calculated at the PBE(dDsC) level

Complex	OD	d(Pt-Cl) [Å]	d(Pt-O) (OH) [Å]	d(Pt-O) (H_2O) [Å]	d(Pt-O) (O) [Å]	Spin State
$PtCl_4$	+ IV	2.24 2.24 2.24 2.24				Triplet
$PtCl_3(OH)$	+ IV	2.24 2.24 2.24	1.93			Triplet
$PtCl_2(OH)_2$	+ IV	2.24 2.24	1.93 1.93			Triplet
$PtCl(OH)_3$	+ IV	2.24	1.93 1.93 1.93			Triplet
$Pt(OH)_4$	+ IV		1.93 1.93 1.93 1.93			Triplet
$PtCl_4(H_2O)$	+ IV	2.31 2.29 2.24 2.22		2.15		Singlet
$PtCl_3(OH)(H_2O)$	+ IV	2.32 2.30 2.26	1.90	2.13		Singlet
$PtCl_2(OH)_2(H_2O)$	+ IV	2.32 2.30	1.98 1.88	2.12		Singlet
$PtCl(OH)_3(H_2O)$	+ IV	2.31	2.00 1.95 1.91	2.14		Singlet
$Pt(OH)_4(H_2O)$	+ IV		2.02 1.97 1.96 1.91	2.14		Singlet
$PtCl_4(H_2O)_2$	+ IV	2.32 2.32 2.26 2.26	1.97	2.14 2.14		Singlet
$PtCl_3(OH)(H_2O)_2$	+ IV	2.34 2.30 2.27	1.97	2.14 2.13		Singlet
$PtCl_2(OH)_2(H_2O)_2$	+ IV	2.35 2.26	1.99 1.97	2.13 2.13		Singlet
$PtCl(OH)_3(H_2O)_2$	+ IV	2.30	2.03 1.96 1.96	2.16 2.15		Singlet
$Pt(OH)_4(H_2O)_2$	+ IV		2.03 2.02 1.97 1.96	2.13 2.13		Singlet
PtO_2	+ IV				1.70 1.70	Singlet
$PtOCl_2$	+ IV	2.22 2.20			1.76	Triplet
PtOCl(OH)	+ IV	2.18	1.87		1.75	Singlet
$PtO(OH)_2$	+ IV		1.87 1.87		1.76	Singlet
PtOCl	+ III	2.15			1.74	Doublet
PtO(OH)	+ III		1.85		1.73	Doublet
$PtCl(OH)_2$	+ III	2.22	1.91 1.91			Doublet
$Pt(OH)_3$	+ III		1.91 1.91 1.90			Doublet
$PtCl_2$	+ II	2.15 2.15				Triplet
PtCl(OH)	+ II	2.15	1.87			Triplet
$Pt(OH)_2$	+ II		1.87 1.87			Triplet
$PtCl_2(H_2O)$	+ II	2.22 2.18		2.13		Singlet
$PtCl(OH)(H_2O)$	+ II	2.23	1.90	2.13		Singlet
$Pt(OH)_2(H_2O)$	+ II		1.89 1.99	2.11		Singlet
$PtCl_2(H_2O)_2$	+ II	2.25 2.25		2.13 2.13		Singlet
$PtCl(OH)(H_2O)_2$	+ II	2.25	1.98	2.12 2.12		Singlet
$Pt(OH)_2(H_2O)_2$	+ II		1.99 1.99	2.11 2.11		Singlet
PtO	+ II				1.74	Triplet
Pt(OH)	+ I		1.86			Doublet
PtCl	+ I	2.13				Doublet
$Pt(H_2O)$	0			2.01		Singlet
$Pt(H_2O)_2$	0			2.06 2.06		Singlet

Table SIII-3. Bond lengths calculated at the PBE(dDsC) level for the considered complexes, as a function of their oxidation degree (OD).

SI 4. Impact of the PBE(dDsC) geometries on the energetics of HSE(06) functional

Spin state and xc functional	d(Pt-O) [Å]	d(Pt-Cl) [Å]		$\widehat{OPtCl}$ [°]		$\widehat{ClPtCl}$ [°]	Energy [eV]
Singlet (PBE-dDsC)	1.75	2.18	2.18	118°	118°	124°	0.16
Singlet (HSE06)	1.72	2.17	2.17	113°	112°	135°	0.27
Doublet (PBE-dDsC)	1.75	2.22	2.22	133°	132°	94°	0.20
Doublet (HSE06)	1.74	2.20	2.19	138°	127°	95°	0.68
Triplet (PBE-dDsC)	1.76	2.21	2.20	139°	126°	95°	0.00
Triplet (HSE06)	1.76	2.20	2.19	156°	98°	106°	0.00

Table SIII-4. Energies (referenced to the most stable spin state) and geometries of $PtOCl_2$ calculated with two exchange correlation functionals (PBE-dDsC and HSE06) for various spin states. The energy represented is the difference between the energy of the corresponding setup (geometry, exchange correlation functional and spin state) and the most stable state for the same exchange correlation functional.

Spin state and xc functional	d(Pt-O) [Å]	d(Pt-(OH)) [Å]		$O\widehat{Pt(OH)}$[°]		$(OH)\widehat{Pt(OH)}$[°]	Energy [eV]
Singlet (PBE-dDsC)	1.76	1.88	1.88	116°	116°	128°	0.00
Singlet (HSE06)	1.73	1.86	1.86	117°	117°	126°	0.00
Doublet (PBE-dDsC)	1.77	1.91	1.91	112°	111°	137°	0.33
Doublet (HSE06)	1.74	1.89	1.89	111°	111°	138°	0.76
Triplet (PBE-dDsC)	1.78	1.94	1.91	134°	94°	132°	0.40
Triplet (HSE06)	1.76	1.91	1.89	139°	94°	127°	0.24

Table SIII-5. Energies (referenced to the most stable spin state) and geometries of $PtO(OH)_2$ calculated with two exchange correlation functionals (PBE-dDsC and HSE06) for various spin states. The energy represented is the difference between the energy of the corresponding setup (geometry, exchange correlation functional and spin state) and the most stable state for the same exchange correlation functional.

SI 5. Impact of the PBE(dDsC) geometries on the energetics of HSE(06) functional

Pt(IV)	ΔE	Pt(II)	ΔE	Pt(0)	ΔE
Ligand exchange	[kJ/mol]	Ligand exchange	[kJ/mol]	Hydration	[kJ/mol]
$PtCl_4 + H_2O \rightarrow PtCl_3(OH) + HCl$	0.4	$PtCl_2 + H_2O \rightarrow PtCl(OH) + HCl$	0.1	$Pt + H_2O \rightarrow Pt(H_2O)$	0.8
$PtCl_3(OH) + H_2O \rightarrow PtCl_2(OH)_2 + HCl$	0.1	$PtCl(OH) + H_2O \rightarrow Pt(OH)_2 + HCl$	0.2	$Pt(H_2O) + H_2O \rightarrow Pt(H_2O)_2$	0.1
$PtCl_2(OH)_2 + H_2O \rightarrow PtCl(OH)_3 + HCl$	0.7	$PtCl_2(H_2O) + H_2O \rightarrow PtCl(OH)(H_2O) + HCl$	1.0		
$PtCl(OH)_3 + H_2O \rightarrow Pt(OH)_4 + HCl$	0.4	$PtCl(OH)(H_2O) + H_2O \rightarrow Pt(OH)_2(H_2O) + HCl$	1.3		
$PtCl_4(H_2O) + H_2O \rightarrow PtCl_3(OH)(H_2O) + HCl$	1.1	$PtCl_2(H_2O)_2 + H_2O \rightarrow PtCl(OH)(H_2O)_2 + HCl$	0.7		
$PtCl_3(OH)(H_2O) + H_2O \rightarrow PtCl_2(OH)_2(H_2O) + HCl$	0.9	$PtCl(OH)(H_2O)_2 + H_2O \rightarrow Pt(OH)_2(H_2O)_2 + HCl$	0.5		
$PtCl_2(OH)_2(H_2O) + H_2O \rightarrow PtCl(OH)_3(H_2O) + HCl$	0.1	Hydration			
$PtCl(OH)_3(H_2O) + H_2O \rightarrow Pt(OH)_4(H_2O) + HCl$	0.6	$PtCl_2 + H_2O \rightarrow PtCl_2(H_2O)$	1.1		
$PtCl_4(H_2O)_2 + H_2O \rightarrow PtCl_3(OH)(H_2O)_2 + HCl$	0.9	$PtCl(OH) + H_2O \rightarrow PtCl(OH)(H_2O)$	2.0		
$PtCl_3(OH)(H_2O)_2 + H_2O \rightarrow PtCl_2(OH)_2(H_2O)_2 + HCl$	0.5	$Pt(OH)_2 + H_2O \rightarrow Pt(OH)_2(H_2O)$	3.1		
$PtCl_2(OH)_2(H_2O)_2 + H_2O \rightarrow PtCl(OH)_3(H_2O)_2 + HCl$	0.7	$PtCl_2(H_2O) + H_2O \rightarrow PtCl_2(H2O)_2$	0.5		
$PtCl(OH)_3(H_2O)_2 + H_2O \rightarrow Pt(OH)_4(H_2O)_2 + HCl$	1.4	$PtCl(OH)(H_2O) + H_2O \rightarrow PtCl(OH)(H_2O)_2$	0.1		
$PtOCl_2 + H_2O \rightarrow PtOCl(OH) + HCl$	-6.4	$Pt(OH)_2(H_2O) + H_2O \rightarrow Pt(OH)_2(H_2O)_2$	-0.6		
$PtCl_4 + H_2O \rightarrow PtCl_3(OH) + HCl$	0.5	$PtO + H_2O \rightarrow Pt(OH)_2$	0.4		
Hydration		Reduction			
$PtCl_4 + H_2O \rightarrow PtCl_4(H_2O)$	2.0	$PtCl_2 + H_2 \rightarrow Pt + 2HCl$	0.1		
$PtCl_3(OH) + H_2O \rightarrow PtCl_3(OH)(H_2O)$	2.7	$Pt(OH)_2 + H_2 \rightarrow Pt + 2H_2O$	-0.2		
$PtCl_2(OH)_2 + H_2O \rightarrow PtCl_2(OH)_2(H_2O)$	3.6	$PtO + H_2 \rightarrow Pt + H_2O$	0.2		
$PtCl(OH)_3 + H_2O \rightarrow PtCl(OH)_3(H_2O)$	2.9	$PtCl_2(H_2O) + H_2 \rightarrow Pt(H_2O) + 2HCl$	-0.2		
$Pt(OH)_4 + H_2O \rightarrow Pt(OH)_4(H_2O)$	3.1	$Pt(OH)_2(H_2O) + H_2 \rightarrow Pt(H_2O) + 2H_2O$	-2.5		
$PtCl_4(H_2O) + H_2O \rightarrow PtCl_4(H_2O)_2$	0.0	$PtCl_2(H_2O)_2 + H_2 \rightarrow Pt(H_2O)_2 + 2HCl$	-0.6		
$PtCl_3(OH)(H_2O) + H_2O \rightarrow PtCl_3(OH)(H_2O)_2$	-0.2	$Pt(OH)_2(H_2O)_2 + H_2 \rightarrow Pt(H_2O)_2 + 2H_2O$	-1.8		
$PtCl_2(OH)_2(H_2O) + H_2O \rightarrow PtCl_2(OH)_2(H_2O)_2$	-0.7				
$PtCl(OH)_3(H_2O) + H_2O \rightarrow PtCl(OH)_3(H_2O)_2$	-0.1				
$Pt(OH)_4(H_2O) + H_2O \rightarrow Pt(OH)_4(H_2O)_2$	0.8				
$PtOCl_2 + H_2O \rightarrow PtCl_2(OH)_2$	-6.5				
$PtOCl(OH) + H_2O \rightarrow PtCl(OH)_3$	0.7				
$PtO(OH)_2 + H_2O \rightarrow Pt(OH)_4$	0.6				
$PtO_2 + H_2O \rightarrow PtO(OH)_2$	-0.1				
Reduction					
$PtCl_4 + H_2 \rightarrow PtCl_2 + 2HCl$	0.0				
$Pt(OH)_4 + H_2 \rightarrow Pt(OH)_2 + 2H_2O$	-1.3				
$PtO_2 + H_2 \rightarrow PtO + H_2O$	-2.5				
$PtCl_4(H_20) + H_2 \rightarrow PtCl_2(H2O) + 2HCl$	-2.5				
$Pt(OH)_4(H_2O) + H_2 \rightarrow Pt(OH)_2(H_2O) + 2H_2O$	-2.1				
$PtCl_4(H_20)_2 + H_2 \rightarrow PtCl_2(H_2O)_2 + 2H_20$	-2.5				
$Pt(OH)_4(H_2O)_2 + H_2 \rightarrow Pt(OH)_2(H_2O)_2 + 2H_2O$	-1.7				

Table SIII-6. Differences for the reaction energies considered calculated with two different set-ups. One is calculated using PBE-dDsC optimized geometries at the HSE06 level and the other one is calculated at the HSE06 level using geometries also optimized at the HSE06 level. The small differences observed are used to justify the use of PBE-dDsC in the study. $\Delta E = E_{HSE06}^{PBE-dDsC} - E_{HSE06}^{HSE06}$ with: $E_{Energy}^{Geometry}$

SI 6. Reaction and energies used for the benchmark

Reactions	ACFDT-RPA	PBE(dDsC)	opt-PBE	B3LYP	HSE06	PBE0	TPSS	RTPSS	SCAN
Pt(IV)									
Ligand exchange									
$PtCl_4 + H_2O \rightarrow PtCl_3(OH) + HCl$	39	41	41	42	46	46	34	36	36
$PtCl_3(OH) + H_2O \rightarrow PtCl_2(OH)_2 + HCl$	41	40	39	39	42	42	31	33	33
$PtCl_2(OH)_2 + H_2O \rightarrow PtCl(OH)_3 + HCl$	49	47	45	45	52	52	42	44	44
$PtCl(OH)_3 + H_2O \rightarrow Pt(OH)_4 + HCl$	52	48	45	46	53	53	44	46	44
$PtCl_4(H_2O) + H_2O \rightarrow PtCl_3(OH)(H_2O) + HCl$	49	46	47	52	57	57	39	41	45
$PtCl_3(OH)(H_2O) + H_2O \rightarrow PtCl_2(OH)_2(H_2O) + HCl$	57	57	57	59	64	64	50	51	54
$PtCl_2(OH)_2(H_2O) + H_2O \rightarrow PtCl(OH)_3(H_2O) + HCl$	77	72	69	71	80	79	67	69	73
$PtCl(OH)_3(H_2O) + H_2O \rightarrow Pt(OH)_4(H_2O) + HCl$	77	70	69	68	75	75	65	68	67
$PtCl_4(H_2O)_2 + H_2O \rightarrow PtCl_3(OH)(H_2O)_2 + HCl$	63	60	60	59	65	65	53	55	57
$PtCl_3(OH)(H_2O)_2 + H_2O \rightarrow PtCl_2(OH)_2(H_2O)_2 + HCl$	72	77	72	70	77	77	71	72	71
$PtCl_2(OH)_2(H_2O)_2 + H_2O \rightarrow PtCl(OH)_3(H_2O)_2 + HCl$	77	69	69	68	76	76	63	66	69
$PtCl(OH)_3(H_2O)_2 + H_2O \rightarrow Pt(OH)_4(H_2O)_2 + HCl$	89	76	79	82	86	86	72	77	78
$PtOCl_2 + H_2O \rightarrow PtOCl(OH) + HCl$	44	62	59	67	75	74	58	57	70
$PtOCl(OH) + H_2O \rightarrow PtO(OH)_2 + HCl$	54	49	48	53	59	58	45	47	49
Mean value	60	58	57	59	65	64	52	54	56
MAE		5	5	6	6	5	10	7	7
Hydration									
$PtCl_4 + H_2O \rightarrow PtCl_4(H_2O)$	-57	-55	-54	-50	-68	-69	-52	-58	-72
$PtCl_3(OH) + H_2O \rightarrow PtCl_3(OH)(H_2O)$	-48	-51	-47	-40	-57	-58	-47	-52	-63
$PtCl_2(OH)_2 + H_2O \rightarrow PtCl_2(OH)_2(H_2O)$	-32	-34	-30	-20	-35	-36	-28	-34	-43
$PtCl(OH)_3 + H_2O \rightarrow PtCl(OH)_3(H_2O)$	-3	-9	-6	5	-8	-8	-3	-9	-14
$Pt(OH)_4 + H_2O \rightarrow Pt(OH)_4(H_2O)$	21	13	18	28	14	14	19	12	9
$PtCl_4(H_2O) + H_2O \rightarrow PtCl_4(H_2O)_2$	-120	-119	-114	-102	-120	-121	-114	-120	-136
$PtCl_3(OH)(H_2O) + H_2O \rightarrow PtCl_3(OH)(H_2O)_2$	-106	-105	-101	-94	-112	-113	-100	-106	-124
$PtCl_2(OH)_2(H_2O) + H_2O \rightarrow PtCl_2(OH)_2(H_2O)_2$	-91	-85	-86	-83	-99	-99	-80	-86	-107
$PtCl(OH)_3(H_2O) + H_2O \rightarrow PtCl(OH)_3(H_2O)_2$	-91	-87	-85	-86	-103	-103	-84	-89	-111
$Pt(OH)_4(H_2O) + H_2O \rightarrow Pt(OH)_4(H_2O)_2$	-78	-82	-75	-72	-91	-91	-77	-79	-100

Reactions	ACFDT-RPA	PBE(dDsC)	opt-PBE	B3LYP	HSE06	PBE0	TPSS	RTPSS	SCAN
$PtOCl_2 + H_2O \rightarrow PtCl_2(OH)_2$	-108	-110	-106	-92	-107	-107	-111	-115	-137
$PtOCl(OH) + H_2O \rightarrow PtCl(OH)_3$	-104	-125	-120	-114	-129	-130	-127	-129	-163
$PtO(OH)_2 + H_2O \rightarrow Pt(OH)_4$	-106	-126	-123	-121	-135	-135	-129	-129	-168
$PtO_2 + H_2O \rightarrow PtO(OH)_2$	13	-17	-11	-24	-45	-45	-14	-21	-22
Mean value	-65	-71	-67	-62	-78	-79	-68	-73	-89
MAE		8	7	12	13	14	9	9	24
Reduction									
$PtCl_4 + H_2 \rightarrow PtCl_2 + 2HCl$	-41	-10	0	-80	-72	-74	-6	22	0
$Pt(OH)_4 + H_2 \rightarrow Pt(OH)_2 + 2H_2O$	-57	-27	-16	-93	-91	-92	-7	20	-2
$PtO_2 + H_2 \rightarrow PtO + H_2O$	-4	10	23	-63	-84	-83	26	48	8
$PtCl_4(H_2O) + H_2 \rightarrow PtCl_2(H_2O) + 2HCl$	-34	-1	11	-66	-55	-56	0	30	25
$Pt(OH)_4(H_2O) + H_2 \rightarrow Pt(OH)_2(H_2O) + 2H_2O$	-133	-95	-83	-155	-153	-153	-78	-51	-62
$PtCl_4(H_2O)_2 + H_2 \rightarrow PtCl_2(H_2O)_2 + 2HCl$	-25	0	15	-68	-55	-55	-2	29	28
$Pt(OH)_4(H_2O)_2 + H_2 \rightarrow Pt(OH)_2(H_2O)_2 + 2H_2O$	-151	-119	-105	-180	-178	-178	-107	-80	-84
Mean value	-64	-35	-22	-101	-98	-99	-25	3	-12
MAE		29	42	37	34	35	39	66	51
Pt(II)									
Ligand exchange									
$PtCl_2 + H_2O \rightarrow PtCl(OH) + HCl$	85	81	79	81	88	87	77	80	80
$PtCl(OH) + H_2O \rightarrow Pt(OH)_2 + HCl$	80	78	76	78	86	86	74	77	76
$PtCl_2(H_2O) + H2O \rightarrow PtCl(OH)(H_2O) + HCl$	77	73	71	78	87	86	70	72	75
$PtCl(OH)(H_2O) + H_2O \rightarrow Pt(OH)_2(H_2O) + HCl$	83	77	77	83	91	91	73	76	76
$PtCl_2(H_2O)_2 + H_2O \rightarrow PtCl(OH)(H_2O)_2 + HCl$	85	79	79	80	88	88	74	78	79
$PtCl(OH)(H_2O)_2 + H_2O \rightarrow Pt(OH)_2(H_2O)_2 + HCl$	91	83	83	87	94	94	79	83	84
Mean value	83	79	77	81	89	89	74	77	78
MAE		5	6	3	5	5	9	6	5
Hydration									
$PtCl_2 + H_2O \rightarrow PtCl_2(H_2O)$	-51	-46	-43	-36	-51	-51	-45	-50	-47
$PtCl(OH) + H_2O \rightarrow PtCl(OH)(H_2O)$	-59	-54	-50	-38	-52	-52	-52	-58	-52
$Pt(OH)_2 + H_2O \rightarrow Pt(OH)_2(H_2O)$	-55	-55	-50	-34	-47	-47	-53	-58	-51
$PtCl_2(H_2O) + H_2O \rightarrow PtCl_2(H_2O)_2$	-111	-118	-110	-103	-120	-120	-116	-120	-133
$PtCl(OH)(H_2O) + H_2O \rightarrow PtCl(OH)(H_2O)_2$	-103	-112	-103	-101	-119	-119	-111	-115	-129
$Pt(OH)_2(H_2O) + H_2O \rightarrow Pt(OH)_2(H_2O)_2$	-95	-105	-97	-97	-116	-116	-105	-108	-122
$PtO + H_2O \rightarrow Pt(OH)_2$	-145	-180	-173	-175	-188	-189	-176	-178	-199
Mean value	-89	-96	-89	-84	-99	-99	-94	-98	-105
MAE		10	7	14	15	15	10	10	20
Reduction									
$PtCl_2 + H_2 \rightarrow Pt + 2\ HCl$	244	286	287	217	229	229	298	330	313

Reactions	ACFDT-RPA	PBE-dDsC	opt-PBE	B3LYP	HSE06	PBE0	TPSS	RTPSS	SCAN
$Pt(OH)_2 + H_2 \rightarrow Pt + 2\ H_2O$	80	127	132	58	55	56	148	173	158
$PtO + H_2 \rightarrow Pt + H_2O$	-66	-53	-41	-117	-132	-133	-28	-5	-42
$PtCl_2(H_2O) + H_2 \rightarrow Pt(H_2O) + 2HCl$	218	255	258	217	237	237	271	300	295
$Pt(OH)_2(H_2O) + H_2 \rightarrow Pt(H_2O) + 2H_2O$	62	105	110	56	59	60	128	152	144
$PtCl_2(H_2O)_2 + H_2 \rightarrow Pt(H_2O)_2 + 2HCl$	209	226	229	189	216	216	243	271	258
$Pt(OH)_2(H_2O)_2 + H_2 \rightarrow Pt(H_2O)_2 + 2H_2O$	37	63	67	22	34	35	89	111	95
Mean value	112	144	149	92	100	100	164	190	175
MAE		32	37	20	19	19	52	78	63
Pt(0)									
Hydration									
$Pt + H_2O \rightarrow Pt(H_2O)$	-77	-77	-72	-37	-44	-44	-73	-80	-65
$Pt(H_2O) + H_2O \rightarrow Pt(H_2O)_2$	-122	-147	-140	-131	-141	-141	-144	-149	-171
Mean value	-99	-112	-106	-84	-92	-92	-108	-115	-118
MAE		13	11	24	26	26	13	15	30
$H_2 + 0.5\ O_2 \rightarrow H_2O$	-233	-243	-230	-248	-257	-257	-220	-200	-243
MAE Global		13	14	14	15	15	18	24	26

Table SIII-7. Exhaustive list of the various considered reactions used for the benchmark and their relative reaction energies (in kJ mol^{-1}) for the ACFDT-RPA method and the various XC functionals considered. MV stands for the Mean Value, and MAE for the Mean Average Error compared to the reference (ACFDT-RPA) value. The last line (MAE Global) is the Mean Average Error calculated over all the considered reactions.

SI 7. Evolution of the Pt(II) complexes at three temperatures as a function of the water and HCl pressures.

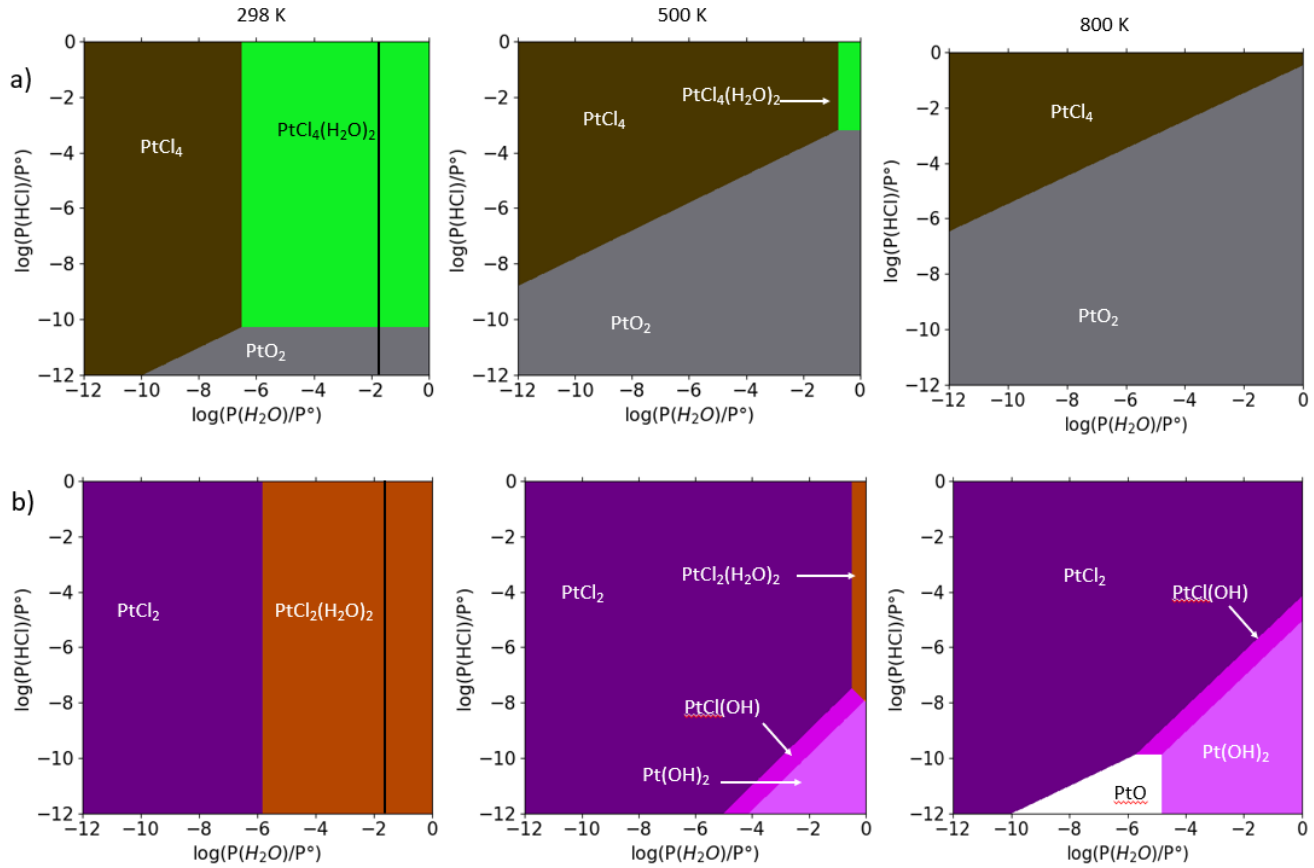

Figure SIII-1. Evolution of the most stable Pt(IV) (a) and Pt(II) (b) complexes at various temperatures (298 K, 500 K and 800 K) according to the partial pressure in H_2O and HCl. At room temperature, the gas phase domain of water is only valid for pressures located on the left of the black line.

SI 8. Thermodynamic diagrams calculated for the calcination and reduction process using various XC functionals.

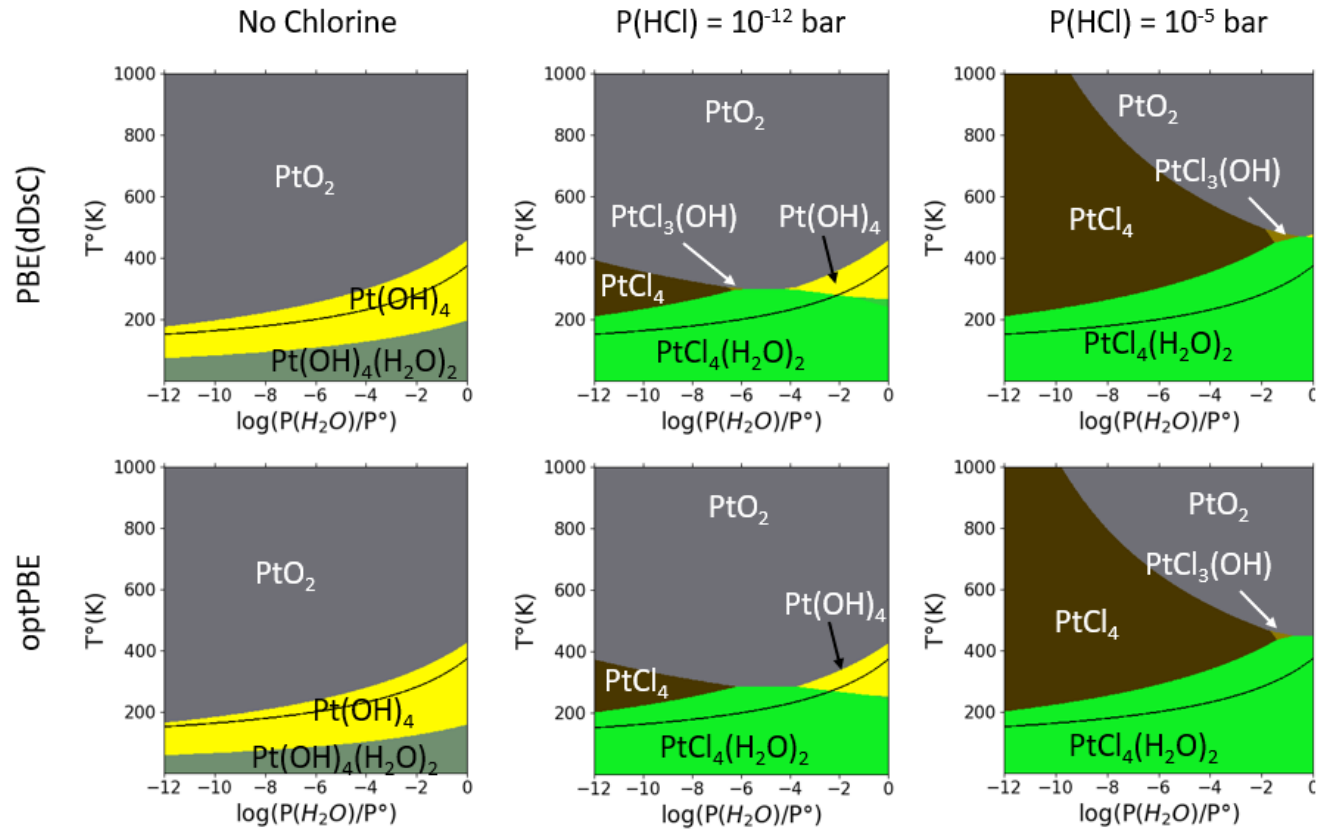

Figure SIII-2. PBE(dDsC) and optPBE GGA calculated thermodynamic diagrams of the most stable species under oxidative ($P(O_2)$ = 0.21 bar) atmosphere for three loading in chlorine: without chlorinated species, P(HCl) = 0 bar (left); P(HCl) = 10^{-12} bar (center) and P(HCl) = 10^{-5} bar (right). The gas phase domain of water is above the black line

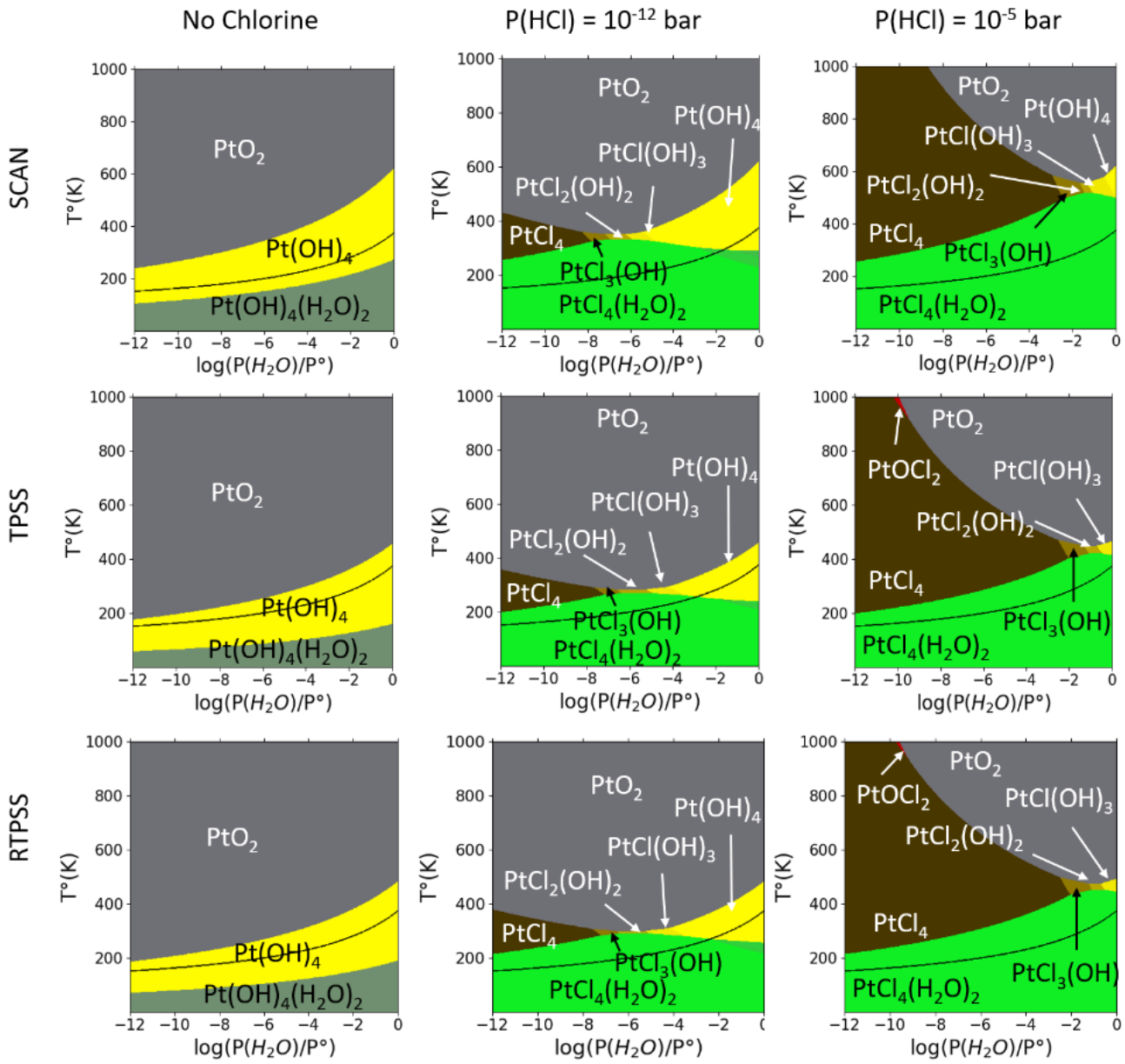

Figure SIII-3. Most stable species under oxidative ($P(O_2)$ = 0.21 bar) atmosphere for three loading in chlorine: No chlorinated species (left); P(HCl) = 10^{-12} bar (center) and P(HCl) = 10^{-5} bar (right). The gas phase domain of water is above the black line. The corresponding XC metaGGA is written on the left.

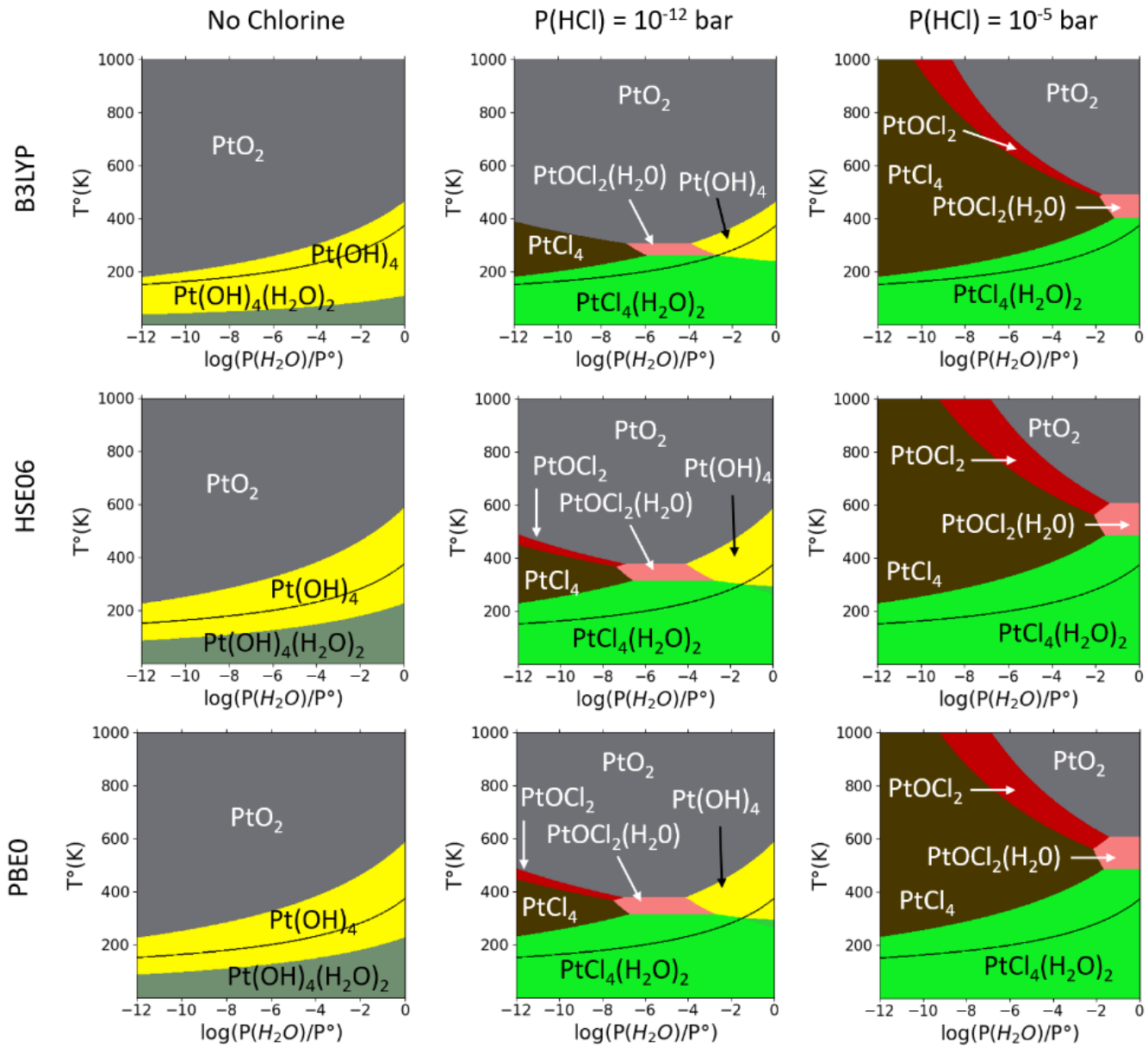

Figure SIII-4. Most stable species under oxidative ($P(O_2)$ = 0.21 bar) atmosphere for three loading in chlorine: No chlorinated species (left); P(HCl) = 10^{-12} bar (center) and P(HCl) = 10^{-5} bar (right). The gas phase domain of water is above the black line. The corresponding XC hybrid is written on the left.

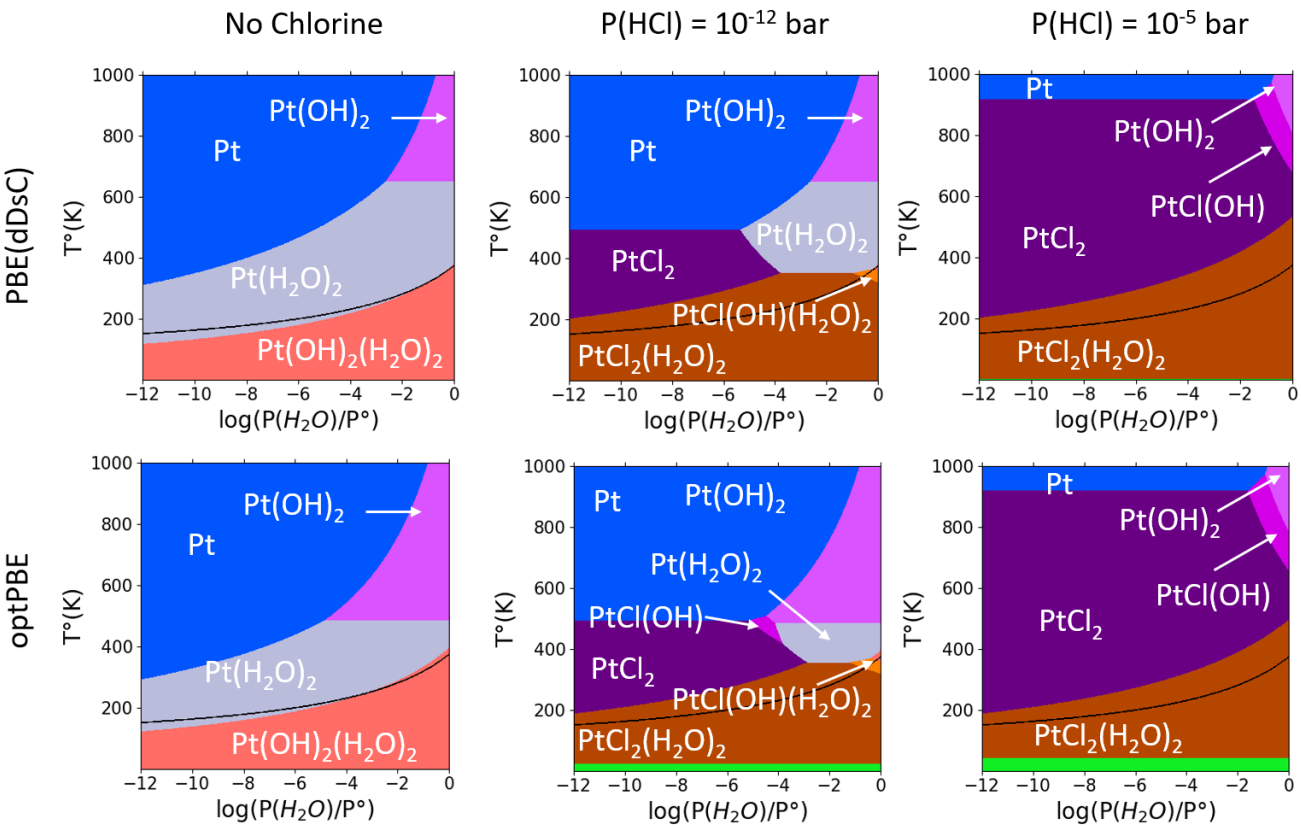

Figure SIII-5. Most stable species under reducing ($P(H_2)$ = 1 bar) atmosphere for three loading in chlorine: No chlorinated species (left); P(HCl) = 10^{-12} bar (center) and P(HCl) = 10^{-5} bar (right). The gas phase domain of water is above the black line. The corresponding XC GGA is written on the left.

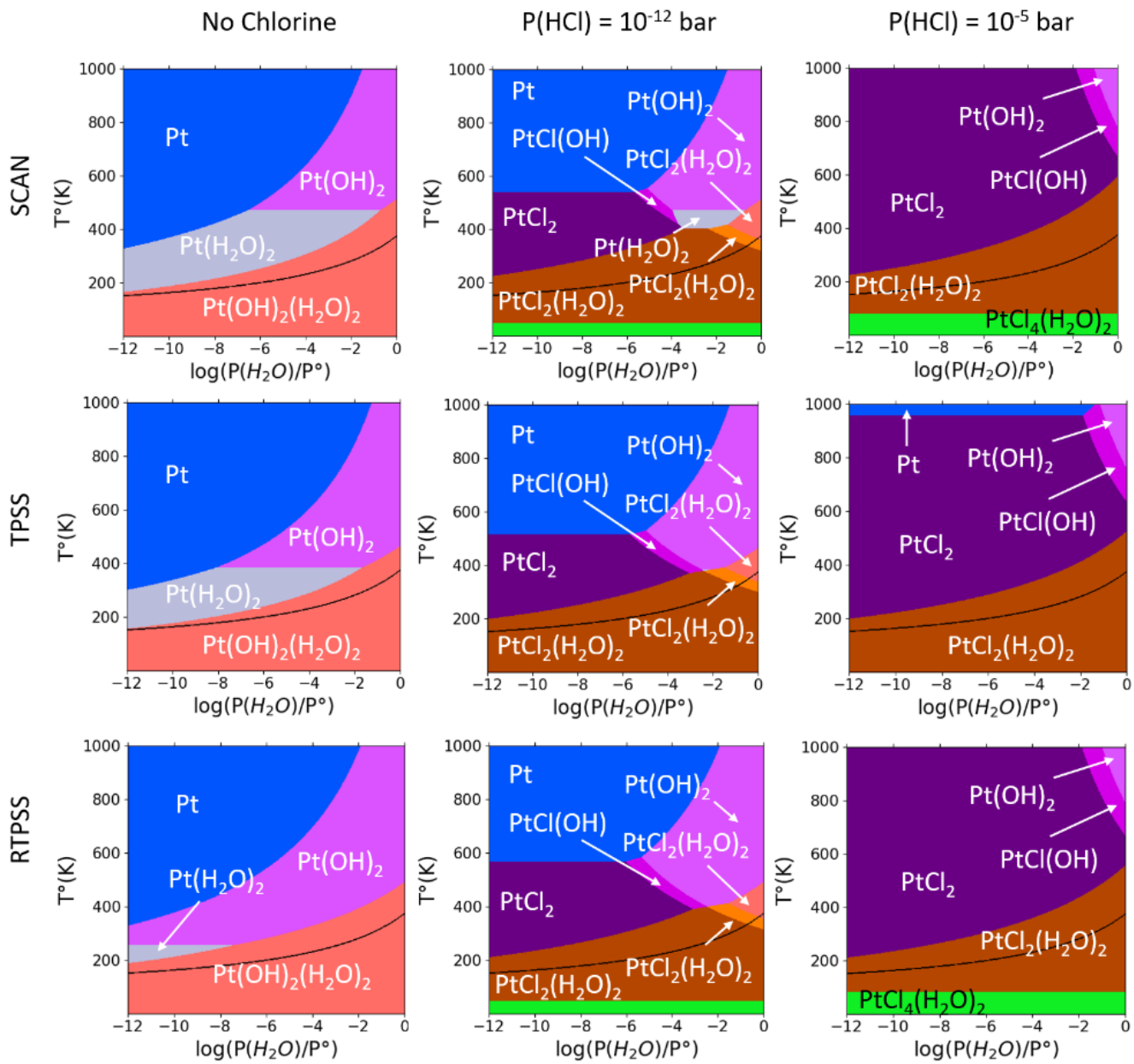

Figure SIII-6. Most stable species under reducing ($P(H_2)$ = 1 bar) atmosphere for three loading in chlorine: No chlorinated species (left); $P(HCl) = 10^{-12}$ bar (center) and $P(HCl) = 10^{-5}$ bar (right). The gas phase domain of water is above the black line. The corresponding XC metaGGA is written on the left.

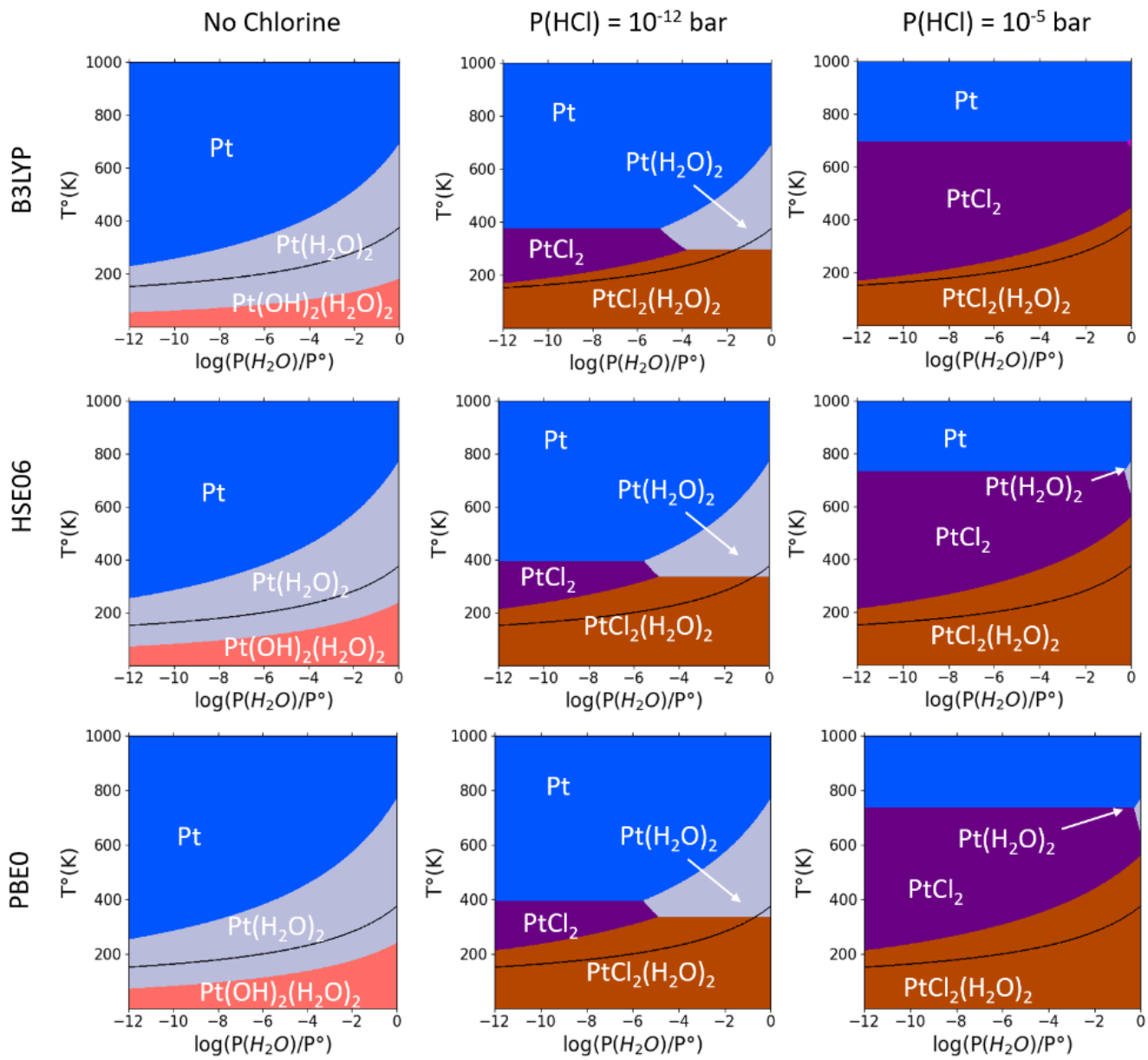

Figure SIII-7. Most stable species under reducing ($P(H_2)$ = 1 bar) atmosphere for three loading in chlorine: No chlorinated species (left); $P(HCl) = 10^{-12}$ bar (center) and $P(HCl) = 10^{-5}$ bar (right). The gas phase domain of water is above the black line. The corresponding XC hybrid is written on the left.

Chapter IV

Identification of Platinum Single Atoms on Chlorinated γ–Alumina Support by Density Functional Theory Calculations and X-Ray Absorption Spectroscopy

---

This chapter is dedicated to the study of supported platinum complexes during the calcination through a combined approach of DFT and XAS. The chapter represents the draft of a forthcoming publication with the following co-authors: Ana T. F. Batista, Christèle Legens, Antonio Aguilar-Tapia, Olivier Proux, Jean-Louis Hazemann, Fabrice Diehl, Anne-Sophie Gay, Yves Joly, Céline Chizallet and Pascal Raybaud. The experimental part was performed in the framework of the previous thesis of Ana Teresa Fialho Batista. I have performed the DFT study as well as the part related to the calculation of XAS spectra. The supporting information is presented at the end of the chapter.

IV.1. Introduction

Single atom catalysts (or SACs) are more than ever in the scope of the scientific community[1–5] not only due to their adequation with today needs for energetic and resources' use sobriety[1] but also because of their interesting catalytic properties that differ from nanoparticles (NPs) or bulk metal.[3] Indeed, while they offer an elegant solution in line with the atom economy concept to the use of scarce resource such as the transition metals usually used in catalysis, they also allow new reactivities. This is due to, among other reasons, the exacerbated impact of the support which can tune active site properties similarly to ligands in homogeneous catalysis.[1] However, because of thermodynamic reasons single atoms tend to sinter, making their stabilization everything but straightforward. Cluster and nanoparticles have been known for decades to be attractive metallic catalysts, but it is now known that they sometimes co-exist with single atoms.[6,7] Thus, understanding how to control the genesis of the active phase is at the heart of many research works among the scientific community,[8,9] with several challenges to overcome, in particular that of the observation of single atoms, and of the definition of the metallic coordination sphere. As an example, a recent study points out the difficulty for characterization techniques such as XAS to quantitatively and accurately determine the proportion of single atom in catalysts.[10]

In 1949, Haensel et al.[11] proposed the use of a very low loading of Pt supported on alumina for catalytic reforming reactions and showed that using a small quantity of an expensive noble metal such as Pt could make it an economically attractive catalyst. Even if we might deviate from the SAC definition, the control of the final state of the active phase was already primordial to optimize the activity of the catalyst. Next developments then made Pt/γ-Al_2O_3 a major actor among model and industrial heterogeneous catalysts with numerous applications in refining, petrochemistry, pollution abatement, biomass conversion, plastic recycling, inter alia.[9,12–16] Since the earliest work on Pt/γ-Al_2O_3 by Haensel et al.[11] numerous works have set to optimize this system, exploring the modification of the support[17–19] or the use of multimetallic catalysts[20–22] to increase the selectivity, resistance, or lifetime of the catalyst.[16,23] But despite the tremendous advances done during these decades, key questions regarding the evolution of the platinum species (dispersion, local structure, interaction with the support) during the catalyst preparation remain unanswered.

Controlling the state of the Pt/γ-Al_2O_3's active phase is usually done during its preparation. In the case of Pt/γ-Al_2O_3 used in catalytic reforming units, preparation usually involves several steps.[16,24–26] The impregnation of oxidized platinum precursors[27] (usually chlorinated for naphta reforming applications) is followed by various possible thermal treatments such as drying, calcination and

reduction under H_2 to finally obtain a metallic Pt. The presence of chlorine in the precursor serves a dual interest. While it increases the acidity of the support,[28] and by consequence the activity of the bi-functional Pt/γ-Al_2O_3 catalyst, chlorine is also responsible for a higher platinum dispersion[6,7,29] this comes in play in the synthesis but also in regeneration steps such as oxychlorination.[30–32] Recently it was observed that the SA/NP ratio after reduction was increasing with the amount of chlorine in the system.[6,33] However, to the best of our knowledge, chlorine promoted 'dispersive' mechanisms remain unknown. In the other hand, the role of chlorine is not always beneficial, and in case of oxidation reactions, the presence of chlorine in the system lead to poorer performance of the catalyst.[33–36]

The calcination step is of primordial interest as it dictates the state of platinum that will undergo further activation processes such as reduction. Thus, a refined understanding of platinum state after calcination could enhance our capacity to tune efficiently the catalyst. After calcination, Pt is expected to be mainly under the form of oxidized single atom, or eventually of oxidized oligomers (small clusters)[7,37–41] depending on the Pt loading. Despite the role of chlorine during the reduction step, no impact of the chlorine loading on the clustering of oxidized Pt after calcination was observed.[42] As it could be expected from the mono atomic nature of the platinum, the support is of primordial importance. Its impact on the highly dispersed phase of the platinum was reported by Bradley et al.[40] and Lee et al.[41] who observed that aggregation of Pt was refrained by the strength of the Pt-support interaction. Lambert et al.[43] proposed that the support was not only able to impact the aggregation level of the Pt, but also its coordination sphere with an hypothesis made on self-reduction of $Pt(IV)Cl_4$ into Pt^0 being possible on SiO_2 but not on Al_2O_3 due to the nature of $PtCl_x$ interaction with the support. Other authors[44,45] found results in line with Lambert's proposal in presence of chlorine in the system during calcination. By using Temperature Programmed Reduction (TPR) combined with UV analysis, Liekse et al.[46] and Liezt et al.[47] suggested that the nature of Pt species was either $PtCl_x(OH)_y$ or $PtCl_xO_y$ when chlorinated precursors or HCl post-treatment were used or α, β-PtO_2 otherwise. More recently, various works,[7,29,36] despite using different Pt loadings, Cl loadings, or calcination temperature, confirm the presence of $PtCl_x\{O(H)\}_y$ on γ-Al_2O_3 by EXAFS after calcination . This impact of chlorine on Pt under O_2 atmosphere is profitably used for oxychlorination processes applied to regenerate naphta reforming catalysts. Indeed, in these treatments, a synergetic behaviour of chlorine and oxygen to redisperse the platinum species can be suspected as the presence of both is required to successfully regenerate the catalyst.[30–32,36,44,46,48]

In the present contribution, we aim at elucidating the precise nature of oxidized platinum species supported on γ-Al_2O_3 after calcination, including the role of chlorine, due to the relevance of this catalytic system, and to the lack of precise knowledge in that respect.

Density functional theory[49,50] (DFT) is an efficient tool to provide an atomic scale description[51,52] of such Pt species by combining energetic, electronic and structural insights. Hence, numerous DFT studies have been devoted to oxide supported platinum systems, in particular on γ-Al_2O_3 in oxidizing atmosphere. Generally speaking, a strong size effect was observed in terms of interaction strength between platinum species and oxygen,[39,53,54] the smaller entities interacting more strongly with O_2. Sangnier et al.[54] studied the absorption of O_2 on Pt_{13}/γ-Al_2O_3 clusters and demonstrated the key role of bridging interfacial oxygen atoms to anchor the cluster to the surface aluminum atoms. Dessal et al.[39] predicted that the formation of oxidized cluster such as $Pt_{13}O_{22}$ from PtO_4 was unlikely to happen during calcination. Similarly to Sangnier et al.[54], they attributed to O_2 a stabilizing role on SA through the formation of strong Pt-O-Al bonds. However, no chlorine was considered in these studies. Our previous work[55] was dedicated to a theoretical study of isolated unsupported $PtO_xCl_y(OH)_z(H_2O)_n$ expected to form during calcination, under oxidative and reductive atmosphere. Through the undertaken benchmark considering DFT-GGA functionals and beyond (hybrids and RPA), the use of GGA functionals such as PBE-dDsC was justified for reactions involved in calcination conditions. During calcination, through first principles thermodynamics, we assessed the combined role of water and chlorine on the most stable species according to experimental conditions and revealed the stability of $PtCl_4$ or PtO_2 species, only. Hence, no PtO_xCl_y species was found to be stable as expected experimentally. Hence, it will be important to investigate how the presence of the support (not previously considered) impacts this important aspect. Zhou et al.[56] considered the role of chlorine during the redispersion of platinum supported on γ-Al_2O_3 by using DFT. They argue that chlorine facilitates the redispersion of Pt through the formation of an oxychlorinated complex ($PtCl_2(OH)_2$) easier to evaporate from Pt_{bulk} than PtO_2 and that will interact more strongly with Al_2O_3 facilitating the followed step of re-adsorption of these SA onto the surface.

To the best of our knowledge, no theoretical work has been dedicated to the description and the evolution of the experimentally observed oxychlorinated Pt SA during calcination. The aim of this work is thus to investigate by a combined XAS and DFT approach the nature of γ-Al_2O_3 supported single atom platinum under calcination conditions in order to assess the impact of chlorine used in the preparation. Such symbiotic approach resonates with the recent work of Finzel et al.[10] highlighting the limitation of XAS techniques to characterize SA. In the present work, the catalysts are prepared by using a H_2PtCl_6 precursor deposited on a γ-Al_2O_3 support (Pural SB3) and submitted to calcination at 520°C. To enhance the formation of Pt SA, the Pt content is as low as 0.3 %wt Pt. To explore the effect of chlorine, two Cl contents (0.1 wt% and 1.4 wt%) are considered. The two samples are characterized by both XANES and EXAFS techniques. For the DFT study, a large set of $[Pt_1O_xCl_y(OH)_z(H_2O)_n]^0$ complexes are simulated on various sites of the (100) surface of γ-Al_2O_3 where

their Cl and O coordination sphere, and oxidation degree are tested through Gibbs free energy calculations as a function of the external conditions (T, $P(O_2)$, $P(H_2O)$, P(HCl)). The comparison of DFT results with XAS experiments is undertaken through the analysis of coordination number and bond lengths of DFT models to make the bridge with EXAFS data and through the explicit simulation of the XANES spectrum. Thanks to this multi-technique approach, we propose a mapping of the species present at an unequalled level of precision in terms of definition of nature of coordination sphere of platinum.

IV.2. Methods

IV.2.1. Catalyst preparation

The two catalysts samples were prepared using the same protocol as described in ref.[6] by diffusional impregnation of γ-Al_2O_3 extrudates (S_{BET}=183 m^2/g by N_2 physisorption) prepared from PuralSB3™ commercial boehmite powder from Sasol with a H_2PtCl_6 and HCl solution, followed by drying overnight and finally calcination at 520°C for 2h under dry air (heating 5°Cmin^{-1}, 1 L$min^{-1}g_{cat}^{-1}$). The platinum loading was 0.3 %w/w. For the 1.4% w/w Cl samples, the chlorine loading was increased by thermal treatment at 520°C by adding dichloropropane ($C_3H_6Cl_2$) to the air flow in the proportion of 1%wt per gram of catalyst, which decomposes into HCl, H_2O and CO_2, creating a HCl partial pressure that allows for the exchange of surface hydroxyls with HCl. For the 0.1% w/w Cl samples, the chlorine loading was decreased by dechlorination, by injecting 8000 ppm of water into a dry air flow (1 L/min/g_{cata}.) at 520°C. The H_2O partial pressure shifts the surface species equilibria to form surface hydroxyls and gaseous HCl.[28]

IV.2.2. XAS characterization

EXAFS and High Energy Resolved Fluorescence Detection (HERDF)-XANES spectra were acquired at the FAME-UHD beamline[57] at the ESRF (Grenoble, France). Experiments were performed at the Pt L_3 edge in fluorescence mode using a multi-crystal analyzer composed of Ge (110) crystals and a mono-element silicon drift detector. A Helium bag was placed between the sample, the crystals and the detector to prevent signal intensity loss by absorption of the (fluorescence emitted) X-rays by air molecules. The beam energy was calibrated with Pt foil (first maximum of the first derivative XANES spectrum of the Pt metallic foil was set to 11564 eV). The grinded oxide catalyst samples were packed in quartz Mark-tubes (10 µm wall thickness) for acquisition Reference compounds were

platinum oxide PtO_2 (Sigma-Aldrich, purity >99.9%, CAS Number 52785-06-5) and metallic platinum powder (Strem Chemicals, purity >99.9%, CAS Number 7440-06-4) (**SI 1**). Data were processed and EXAFS spectra were fitted using Athena and Artemis, respectively, from the Demeter 0.9.26 software package.[58] The EXAFS spectra of references PtO_2 and Pt powder were used to obtain S_0^2. Simulated EXAFS spectra were obtained from crystalline structural cif files created from DFT calculations considering different Pt supported systems. FEFF6 module in Demeter package was used to generate the paths files further considered in the simulation. Only single scattering up to 3.7 Å with sufficient ranking (>5%) were taken into account to model the O, Cl, Al and Pt summed paths. For the reconstructed paths, S_0^2 was set to 0.88 as obtained when fitting the PtO_2 reference, while □r was set to 0. Debye Waller factors were taken at 0.002 Å² for all scatterers on the ΔR range.

IV.2.3. DFT calculations

All the calculations were performed by using the VASP 5.4.1 software.[59,60] Geometries were optimized using the GGA PBE[61] exchange correlation functional corrected with the dDsC[62,63] scheme for the dispersion forces. A 400 eV cut-off was used for the kinetic energy of the plane wave basis set. Calculations were done at the Γ-point of the Brillouin zone due to the large supercell used: 16.71 x 16.79 x 21.80 $Å^3$. Core electrons were treated by using the Projector Augmented Wave (PAW) formalism.[64] Spin polarization was considered to define the ground state of each structure. Energies were recalculated after applicating a dipolar correction along the z axis (perpendicular to the slab). A Gaussian smearing of 0.05 eV was applied and charges were evaluated using the Hirshfeld[65] formalism. Convergence criteria were fixed to 10^{-7} eV for SCF cycles and to 10^{-2} eV $Å^{-1}$ for forces. If several isomers exist, the most stable geometry at 0 K was kept for the given stoichiometry. Frequencies have been computed at the PBE[61]-dDsC[62,63] level on the previously optimized structures using the finite difference method as implemented in VASP using the central difference scheme with a 0.01 Å step to ensure the stable, or meta-stable nature of the models and for calculating the vibrational component of the Gibbs free energies. The same convergence criterion of the wavefunction than for the energy calculations (10^{-7} eV) was used.

The impact of the functional on these supported systems is assessed by computing electronic energies using an HSE06[66–68] exchange correlation functional. Due to the computational cost of such calculation, a single point evaluation was done on the geometry and spin state previously optimized at PBE-dDsC level. Because of the minimal impact of the dipolar correction along the z-axis observed at the PBE-dDsC level, they were not considered for HSE06 calculations.

The (100) surface of γ-Al_2O_3 as proposed by Digne et al.[69,70] according to the bulk model of Krokidis et al.[71] was used. Four layers were considered to build the (100) slab and the first two layers were relaxed (**SI. 2**). A vacuum thickness of around 15 Å was used to avoid spurious interactions. The surface was considered dehydrated at the PBE[61]-dDsC[62,63] level as calculated by Pigeon et al.[72] which is consistent with the calculations of Digne et al.[69] at the PW91 level.

IV.2.4. Pt complex hydration and OH/Cl exchange reactions under consideration

In the same spirit as proposed in our previous study,[55] we considered that the exchange of a Cl by a OH ligand occurs according to the general equations involving H_2O/HCl in the medium (**Eq. 1**). Hydrations were modelled through three different equations (**Eq. 2-4**). **Eq.2** represents a water molecule added to the coordination sphere of the platinum without dissociation, while **Eq.3** represents a water molecule dissociatively adsorbed on Pt and forming two new hydroxyls on the Pt complex (one involving an oxo ligand). Finally, **Eq.4** stands for water dissociative adsorption leading to two hydroxyls: one on the Pt complex and the other one on the alumina surface, coming from the transfer of a proton to a surface O site (labelled as H*). These equations were also used to link all the considered species in the thermodynamic diagrams presented in the next section.

$$PtO_xCl_y(OH)_z(H_2O)_n + H_2O \rightleftarrows PtO_xCl_{y-1}(OH)_{z+1}(H_2O)_n + HCl \quad \textbf{Eq.1}$$

$$PtCl_y(OH)_z(H_2O)_n + H_2O \rightleftarrows PtCl_y(OH)_z(H_2O)_{n+1} \quad \textbf{Eq.2}$$

$$PtO_xCl_y(OH)_z(H_2O)_n + H_2O \rightleftarrows PtO_{x-1}Cl_y(OH)_{z+2}(H_2O)_n \quad \textbf{Eq.3}$$

$$PtCl_y(OH)_z(H_2O)_n + H_2O \rightleftarrows PtCl_y(OH)_{z+1}(H_2O)_n + H^* \quad \textbf{Eq.4}$$

IV.2.5. Thermodynamic stability evaluation

The thermodynamic stability of supported platinum complexes under various calcination conditions was determined by calculating Gibbs free energies. Translational, rotational and vibrational contributions were calculated under the rigid-rotor and harmonic oscillator approximation and added to the electronic energy for the gas phase molecule while only the vibrational contributions were considered for the supported systems. For every system, zero-point energy was added. Gibbs free energies were calculated for temperatures ranging from 0 K to 1000 K and external pressures from 10^{-12} bar to 1 bar. (as detailed in section **II.5**) The surrounding environment is treated as an ideal gas phase reservoir. The vapor/liquid water equilibrium is reported on all thermodynamic diagrams to recall the limit of stability of water vapor used in our thermodynamic model. Both PBE-dDsC and

HSE06 electronic energies are used to compute stability of platinum complexes during calcination, but independently of the exchange correlation functional used for energies, frequencies calculations are done at the PBE-dDsC level.

IV.2.6. XANES simulations

The ab-initio XANES simulation at platinum's L_3 edge was undertaken using the FDMNES package developed by Joly et al.[73,74] The package calculates self-consistently the electronic structure of a given structure in real space using DFT. The calculation of XANES spectra required the knowledge of all the final states up to a certain energy. In this part, the LDA exchange correlation functional parametrized by Hedin and Lundqvist[75] was used and final states were calculated by solving the Schrödinger equation with finite difference method (FDM).[76] Despite being more computationally expensive than the multiple scattering theory that relies on the Muffin-tin approximation,[76] using the finite difference method allows to get rid of any approximation on the shape of the potential and is thus more accurate. Considering Pt as a heavy atom, fully relativistic calculations were undertaken, and spin orbit coupling was accounted for. Better agreement with experimental spectra was obtained after considering that the absorbing atom was excited, that is with a core-hole in the 2p3/2. Convolution parameters were chosen to get best agreement with experimental spectra. Most parameters were let as default while core level width was fixed at 1.1 eV (Γ_{hole}) and the maximum width of the final state fixed at 8 eV (Γ_{max}). Pt-L_3 edges calculations were performed first for the reference Pt_{bulk} spectrum using the fcc structure (bulk parameter of a = b = c = 3.9239 Å and $\alpha = \beta = \gamma = 90°$) and within a 7 Å radius sphere centered on one Pt atom. A slightly lower 6 Å radius was used for the supported Pt of the previously optimized structures. The core hole effect makes that LUMO are shifted down by a constant value of -1 eV compared to the Fermi level calculated during the SCF procedure.

For Pt bulk the shift was up to -4 eV to get a better agreement with experimental Pt's L_3 spectra. Then, both white lines (WL) of experiment and simulation of Pt bulk were aligned, and the shift needed to achieve it was applied to all calculated spectra. Finally, the intensity of all calculated spectra is multiplied by a constant factor such that the post-edge regions of both Pt_{bulk} spectra are equals. In order to quantitatively compare the XANES simulations with the experimental spectra of calcinated catalysts, linear combination of calculated spectra was calculated using the CVXPY[77,78] library after discretizing the calculated spectra over the same energies than the experimental ones.

IV.3. Results

IV.3.1. XANES experiments

Figure IV-1 reports the XANES spectra of the two samples under consideration. The two XANES spectra are rather similar considering the white line position (11568 eV) and intensity. This confirms the oxidized state of platinum, being comparable to that of Pt(IV) in PtO_2 (**Figure IV-1**). However, a slight difference between the three spectra at ~15580 eV where a bump is observed on the chlorinated alumina supported platinum sample. This bump is not present for the reference PtO_2 while its intensity is slightly more pronounced in the case of the 1.4%Cl sample than for the 0.1 %Cl. However, a deeper understanding of this phenomenon requires to simulate the XANES spectra on the basis of relevant DFT molecular models of the catalyst as it will be proposed latter.

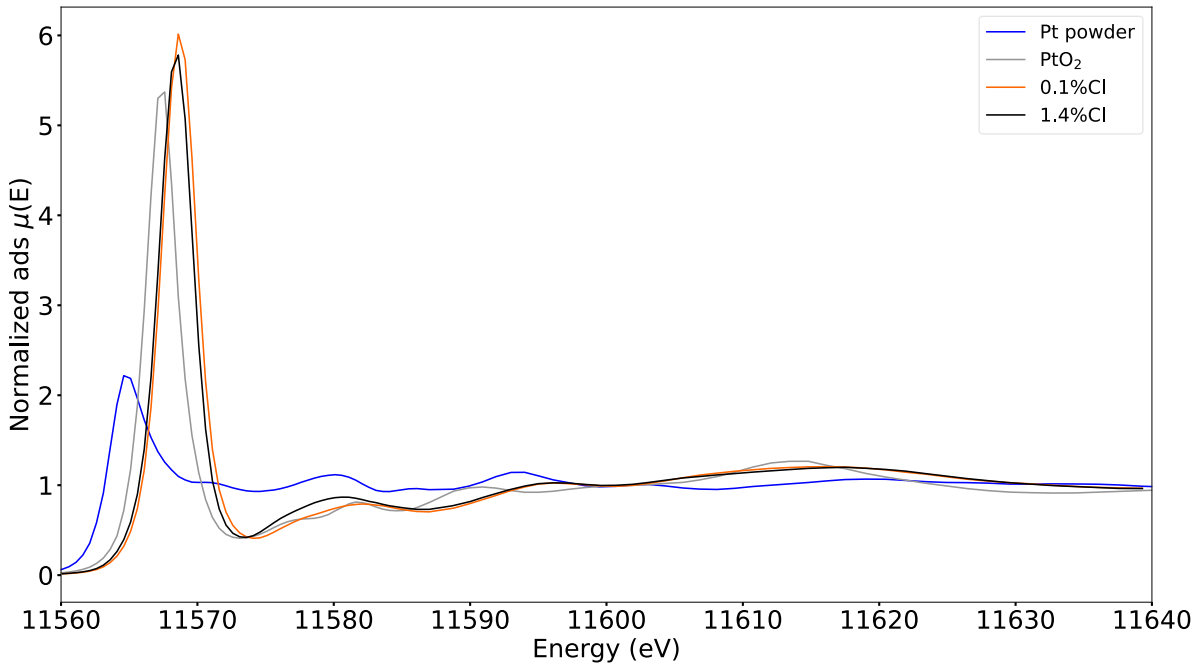

Figure IV-1. Pt L_3 edge HERDF-XANES of reference PtO_2 and metallic Pt powder in addition of Pt L_3 edge HERDF-XANES of calcinated samples: 0.3 %Pt supported on γ-alumina with 0.1 %Cl and 1.4 %Cl.

IV.3.2. EXAFS experiments

The EXAFS spectra and the wavelet transform analysis are presented in **Figure IV-2, a-c)** for the sample with low chlorine content (0.1 %Cl). The parameters used for the fit shown in **Figure IV-2** are reported in **Table IV-1**. Two main regions can be distinguished in the |χ(R)| spectra **(Figure IV-2**): one

from 1.3 to 2.3 Å and another from 2.3 to 3.3 Å. The Continuous Cauchy Wavelet Transform[79] (CCWT) analysis suggests that the first region should correspond to one main light scatterer with possible contribution of a second one. The position of the second region could be compatible with the signal from a Pt-Pt distance (at around 2.7 Å). Nevertheless, the wavelet analysis does not indicate a heavy scatterer in this region (even when k^3 weighted data is used) and indeed such a path could not be successfully fitted. The 2.3-3.3 Å signal was thus treated as a 2nd shell light scatterer. The fitted parameters for the fits in **Figure IV-2** are detailed in **Table IV-1**.

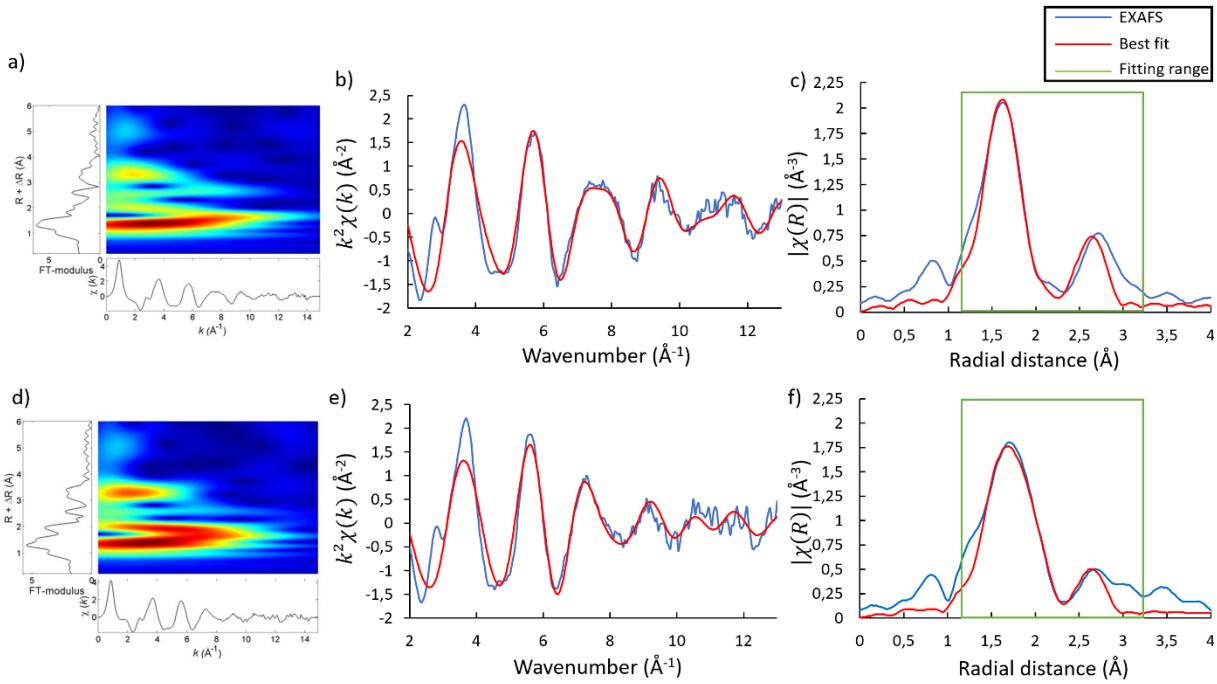

Figure IV-2. EXAFS results for 0.3 %Pt supported on γ-Al_2O_3 at 0.1 %Cl (a-c) and 1.4 %Cl (d-f). a) and d) CCWT analysis,[79] b) and e) EXAFS χ(k), c) and f) magnitude of the Fourier transform \|χ(R)\| (no phase correction), all weighted by k². In b), c), e) and f), the red line represents the best fit. In c) and f), the fitting range is represented by the green frame. The fits are done using Pt-Al as a second shell.

The 1.3-2.3 Å region can thus be fitted with a Pt-O path and a Pt-Cl path, with oxygen being the main neighbor in the 1st shell. Indeed, the dechlorination process removes the chlorine and substitutes the attached Cl with O resulting in an oxygen rich $PtCl_xO_y$ oxide complex. However, the contribution of the Pt-Cl path cannot be ignored. Even with a lengthy dechlorination protocol, the remaining chlorine stays in the oxide complex; leading to a neighboring environment distinct from the one found in Pt/Al_2O_3 samples prepared from non-chlorinated precursors.[36,39,80,81]

Fitting the 2-3 Å region is less straight forward. However, not considering this region, the fit would not correctly reproduce all the main features of χ(k). Pt-Pt paths from various reference structures were tried but none improved the fit, in agreement with the wavelet analysis. This indicates again that oxide platinum complexes are atomically dispersed.

0.3%Pt supported on γ-alumina with Cl contents	k-range ($Å^{-1}$)	Path	Coordination number	R (Å)	σ^2 ($Å^2$)	ΔE_0 (eV)	R-factor
0.1%Cl 2nd shell : Pt-O_{long}	4.0 – 11.7	Pt-O	5.2±0.6	1.98±0.01	0.002±0.001	9.6±1.9	0.04
		Pt-Cl#	0.8±0.6	2.29±0.03			
		Pt-O_{long}	5.5±3.4	3.05±0.04	0.002±-0.007		
0.1%Cl 2nd shell : Pt-Al	4.0 – 11.7	Pt-O	5.6 ±0.5	1.98±0.02	0.002±0.001	11.6±1.2	0.04
		Pt-Cl#	0.4±0.5	2.26±0.04			
		Pt-Al	3.1±1.8	2.91±0.03	0.002±0.006		
1.4%Cl 2nd shell : Pt-O_{long}	3.6 – 11.8	Pt-O	3.9±0.5	2.00±0.02	0.003±0.001	10.7±1.0	0.04
		Pt-Cl#	2.1±0.5	2.28±0.02			
		Pt-O_{long}	3.9±2.5	3.09±0.05	0.003±0.008		
1.4%Cl 2nd shell : Pt-Al	3.6 – 11.8	Pt-O	4.1±0.5	2.01±0.02	0.002±0.001	11.4±0.8	0.04
		Pt-Cl#	1.9±0.5	2.29±0.02			
		Pt-Al	1.9±1.6	2.95±0.03	0.002±0.008		

Table IV-1. EXAFS fitting results for oxide catalysts at 0.1%Cl considering either a 2nd shell Pt-O_{long} or a 2nd shell Pt-Al coordination. E0=11566.1 eV; 1.15 < R < 3.2 Å; N_{ind}=12; N_{var}=8. #Pt-Cl coordination number is evaluated imposing N_{PtCl} + N_{PtO} = 6 after verifying that smaller values for the total coordination number of Pt are not appropriate.

As already mentioned, this region was fitted as a 2nd shell. Indeed, a second shell Pt-O contribution with a distance of 3.3 Å is reported in the literature[82] for 1%Pt and 10%Pt/γ-Al_2O_3 catalysts calcined at 300°C. It was found that using paths obtained through the Quick First Shell (QFS) tool of Artemis, setting a path distance of 3.0 Å, here called Pt-O_{long} or Pt-Al, resulted in fits of a reasonable quality as shown in **Table IV-1**. The fit shown in **Figure IV-2** was done by using Pt-Al. It was not possible to establish categorically which of these scatterers, O or Al originates this signal. Also, using both did not improve the fit. The 2nd shell parameters vary depending on the scattering atom: CN of Pt-O_{long} is higher and Pt-Al atomic distance is slightly shorter. As we will discuss it by considering DFT results, the 2nd shell scatterer, be it O or Al, is due to the alumina support and it reveals Pt precursor-alumina interactions.

For the higher Cl content (1.4 wt%, **Figure IV-2, d-f)**) the wavelet analysis indicates clearly that there are two 1st shell light scatterers. Accordingly, in the magnitude spectra of the Fourier transform, the signal between 1.3 and 2.3 Å is broad. Indeed, the χ(k) is distinct from what was obtained for the catalysts with 0.1%Cl, particularly after 6 $Å^{-1}$. At 1.4%Cl, the coordination number for the Pt-Cl path is enclosed between 1.9 and 2.1, indicating that the surface oxide complex $PtCl_xO_y$ is enriched in chlorine with respect to the sample at 0.1%Cl. Regarding the Pt-Cl distance, it remains rather similar (around 2.28 Å) for the two samples at 0.1%Cl and 1.4%Cl. The signal in the 2.3 – 3.3 Å region was treated as a 2nd shell with a light scatterer, considering either Pt-O_{long} or Pt-Al (**Figure IV-2**) as in the

previous case (**Table IV-1**). As in the previous case, any attempt to use Pt-Pt contribution (initiated from PtO_2 reference phase) was unsuccessful.

In summary, the fitting of EXAFS data for the oxide samples at 0.1 %Cl and 1.4 %Cl suggests that platinum should be mostly atomically dispersed in the form of an oxygen rich $PtCl_xO_y$ complex. Pt is coordinated to 6 ligands with CN(Pt-O)≈5 and CN(Pt-Cl)≈1 for 0.1%Cl and CN(Pt-O)≈4 and CN(Pt-Cl)≈2 for 1.4 %Cl. No Pt-Pt or Pt-O-Pt contributions are found for the first or second shells. This finding is further confirmed by high resolution scanning transmission electron microscopy, as illustrated in the case of 0.3 %wt Pt over γ-alumina with 1.4%Cl in **Figure SIV-3,** revealing that platinum is well dispersed and well distributed over the support. Predominantly Pt single atoms are found, while some dimers and trimers are observed, clusters of more than 5 atoms are scarce, in agreement with previous reports.[7,40] Such samples have been described as single atom catalysts in the literature. [39,40,83] These Pt species are in interaction with the alumina support, as evidenced by the contribution of a long-distance 2nd shell EXAFS signal assigned to either O or Al. This analysis will be further refined with DFT models determined in what follows.

IV.3.3. DFT calculations: structural, electronic and energetic trends

In this first part we describe the structural (including adsorption sites) and electronic properties of the $[Pt^{IV}(O^{2-})_x(Cl^-)_y(HO^-)_z(H_2O)_n]^0$ complexes that are used to model the calcination process by DFT calculations.

Structural features

Adsorption of $[Pt^{IV}(O^{2-})_x(Cl^-)_y(HO^-)_z(H_2O)_n]^0$ (with 2x + y + z = 4) complexes have been simulated on the (100) surface of the γ-Al_2O_3 to assign the experimental features. The dehydrated (100) γ-Al_2O_3 surface developed by Digne et al.[69,70] exhibits various anchoring sites (**Figure IV-3**, **a**). Using the same nomenclature as Digne et al.[69,84], three different oxygens (A, B, C) and three aluminum sites (I, II, III) allow multiple configurations for the adsorption of platinum complexes. A rigorous screening was done for all complexes to determine the most stable anchoring sites. During this exploration, we found a simple relation between the number of ligands in the coordination of the platinum and the most favorable adsorption site. Complexes with three or more ligands adsorb more favorably on top of oxygen B (O_B) (**Figure IV-3**, **b**). For the PtO_2 complex (with two ligands), an anchoring mode involving two oxygens A (O_A) and C (O_C) is preferred (**Figure IV-3**, **c**).

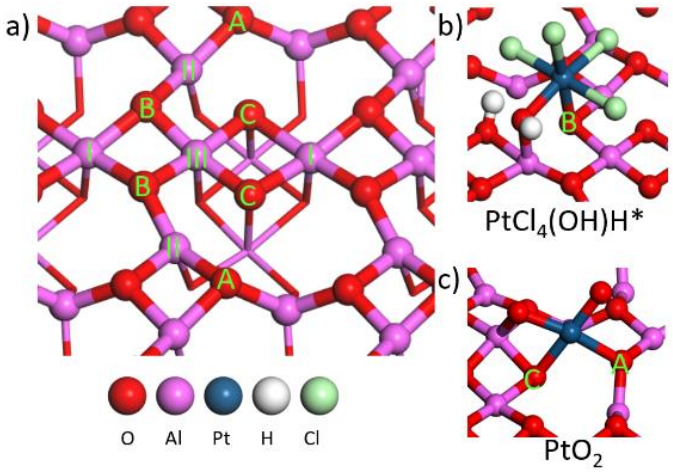

Figure IV-3. a) Non-equivalent Al and O sites on the (100) g-Al_2O_3 surface. Illustration of the most stable adsorption sites according to the coordination sphere of the Pt complexes: b) $PtCl_4(OH)H^*$ with a Pt-O_b bond, b) PtO_2 with two Pt-$O_{A,C}$ bonds. $PtCl_4(OH)H^*$ means that the water ligand is dissociated into on OH group as ligand and one proton adsorbed on the alumina surface.

As it could be expected from the single atom nature of the platinum, both the coordination sphere and the surface interplay in the resulting properties of the catalyst and need to be considered carefully. **Table SIV-2** reports the complete list and description of supported complexes under consideration. Upon adsorption, Pt complexes undergo structural changes with respect to their gas phase analogues, and an elongation of the Pt-X bonds (X being a ligand in the coordination sphere) is observed. The norm of the observed elongation with the nature of the ligand follows the trend: Cl < OH < O < H2O. The mean Pt-Cl bond length is actually unchanged with 2.27 Å in both supported and gas state[55] respectively, while the average Pt-OH bond elongates from 1.94 Å in gas phase to 2.02 Å for the supported system. Pt-O_{oxo} are more impacted and an elongation of 0.11 Å is calculated between the gas phase (1.74 Å) and the adsorbed species (1.85 Å). Finally, the platinum-water mean distance exhibits a significant contraction (0.18 Å) with 2.05 Å for the adsorbed complexes against 2.23 Å for the gas phase. This is also the only bond being longer before adsorption. Moreover, in some cases, the dissociation of H_2O occurs, leading to the formation of two hydroxyls, one on the complex and the second on the alumina surface. The two concerned species are $PtCl_4(H_2O)$ and $PtCl_3(OH)(H_2O)$ that will be named $PtCl_4(OH)H^*$ and $PtCl_3(OH)_2H^*$ respectively (* highlighting the dissociation of the proton on the surface). The geometry (square planar, pentahedral or octahedral) of the complex strongly impacts the distance between the platinum and the surface, but for a given geometry the Pt-O_{surf} distance is almost always elongated with the number of chlorine ligands. Among complexes coordinated to the surface by only one Pt-O bond the distances range between 1.97 Å for $Pt(OH)_4$ and 2.11 Å for both $PtCl_4$ and $PtCl_4(H_2O)$. During the hydration of the pentahedral

$PtCl_y(OH)_{4-y}$ leading to octahedral complexes an average elongation of the Pt-O_{surf} bond of 0.044 Å is calculated and the biggest difference is observed between $PtCl_3(OH)_2H$* and $PtCl_3(OH)$ with 0.1 Å. This big difference is due to $PtCl_3(OH)$ being of the trends and exhibiting a short Pt-O_{surf} distance of 1.99 Å. The square planar complexes, despite having oxo ligands, have rather long Pt-O_{surf} distance with 2.05 Å for both $PtO(OH)_2$ and PtOCl(OH), and slightly longer for $PtOCl_2$ with 2.08 Å. While PtO_2 is the closer to the surface due to its double anchoring site, its two Pt-O_{surf} bonds are calculated at 2.07 and 2.15 Å with the last bond being the longest out of all the considered species (**Table SIV-2**).

Charge analysis

Although the formal oxidation degree is +IV for all the complexes in gas phase, the charge of platinum is impacted by various factors (**Figure IV-4**), such as the nature of the ligands including the surface. Independently of the adsorption mode of the complexes, oxo ligands are more oxidizing than hydroxyls, being themselves more oxidizing than chlorines (for a fixed number of ligands). This trend was already observed in gas phase.[55] Thus, substituting Cl ligands for OH induces a systematic increase of the platinum Hirshfeld charge. One oxo ligand has a similar impact as two chlorine ligands on the platinum charge without change of the anchoring site of the Pt. For example, a small difference of 0.008 e was calculated between $PtCl_4$ and $PtOCl_2$, the difference slightly increases to 0.017 e between $PtCl_2(OH)_2$ and $PtO(OH)_2$, while $PtCl_3(OH)$ and PtOCl(OH) have the same Pt Hirshfeld charge with 0.543 e (**Table SIV-2**). The formation of an octahedral complex through the hydration of a pentahedral complex impacts only slightly the charge of platinum. During the hydration of the $PtCl_y(OH)_{4-y}$ (with y<3) no transfer of electrons is calculated and thus similar Pt's charges are obtained with the addition the addition of water into the platinum coordination sphere. Surprisingly, this is still true for the two dissociative hydrations ($PtCl_4 + H_2O \rightarrow PtCl_3(OH)H$* and $PtCl_3(OH) + H_2O \rightarrow PtCl_3(OH)_2H$*) despite the addition of a hydroxyl in the coordination sphere instead of a water molecule. For these two cases, we found in the one hand an increase of the oxidative power of the coordination sphere of the platinum but in the other hand we also calculated that the surface was less oxidated (**Table SIV-2**). Overall, these two phenomena compensate each other, leading as for the other hydrations to only small changes to the Pt's charge.

The surface impacts the platinum electronic density through the grafting mode of the complexes with a stronger depletion with increasing number of anchoring sites. This effect of the support is particularly well highlighted by comparing the Hirshfeld charges of the complexes supported or in gas phase (**Figure IV-4).** An average difference of + 0.071 e is calculated between the supported and gas phase species, which is due to the supplementary impact of the additional ligand effect of the O_{surf} site which further depletes Pt atom from electrons. The largest difference is for PtO_2 with 0.58 e for

Pt if supported, compared to 0.39 e in gas phase. This may be explained by the fact that PtO_2 is grafted on the support through two Pt-O_{surf} bonds.

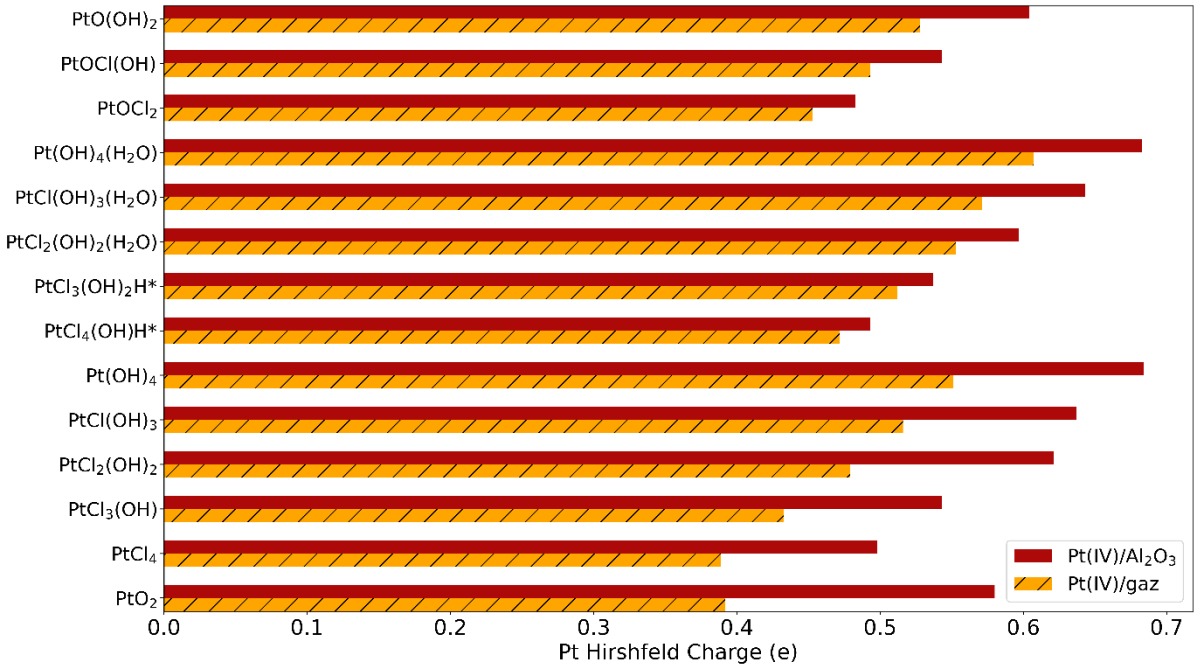

Figure IV-4. Analysis of the Hirshfeld charges of platinum within complexes for a given stoichiometry. Gas phase model are taken from our previous work.[55] As described in the method, the water is dissociated into a bridging hydroxyl and proton for $PtCl_4(OH)H^*$ and $PtCl_3(OH)_2H^*$. Numerical values for supported complexes are reported in Table SIV-2, gas phase values are from ref.[55]

Adsorption energies and deformations

The difference between the charge of the supported and gas phase complexes gathers many contributions into one quantity. During the adsorption, the surface plays a direct role on the platinum atom that was obviously not present on the gas phase, but it also modulates the impact of the ligands on platinum. On the other hand, the adsorption energy expresses the strength of a complex's adsorption by accounting for the destabilization induced by the deformations of both the complex and the surface. Interestingly, by comparing these two quantities, relevant trends are identified related to: the adsorption energy, the coordination sphere of platinum, its geometry, and the total transfer of electron during the adsorption of the complex. Four groups of systems, as depicted in **Figure IV-5**, appear. These four groups are in fact complexes sharing a similar geometry. The isolated point is PtO_2, which is the sole bi-grafted complex, it exhibits the lowest adsorption energy in absolute value and the highest charge transfer during adsorption. Another group is constituted by the pentahedral complexes (after adsorption where the fifth ligand is an oxygen from the surface). The two remaining groups gather complexes undergoing small electronic transfers during adsorption, namely square planar and octahedral complexes. The former exhibits similar

adsorption energies than those of the pentahedral complexes while the octahedral complexes exhibit the strongest adsorption energies among the three categories. By focusing on each sub-category delimited by dotted lines in **Figure IV-5**, we can analyze tendencies by getting rid of interferences coming from the geometry. As an almost general rule, for a given geometry, hydroxyls induce a stronger charge's transfer which is also linked to a stronger adsorption energy than in presence of chlorine ligands. The only exception being $PtCl_2(OH)_2$ (yellow triangle in **Figure IV-5**) which exhibits an adsorption energy off the trend of the pentahedral complexes but due to an unexpectedly high Pt charge in the supported state maybe because of a different spatial arrangement (**Figure IV-7**, **c)**) as described next.

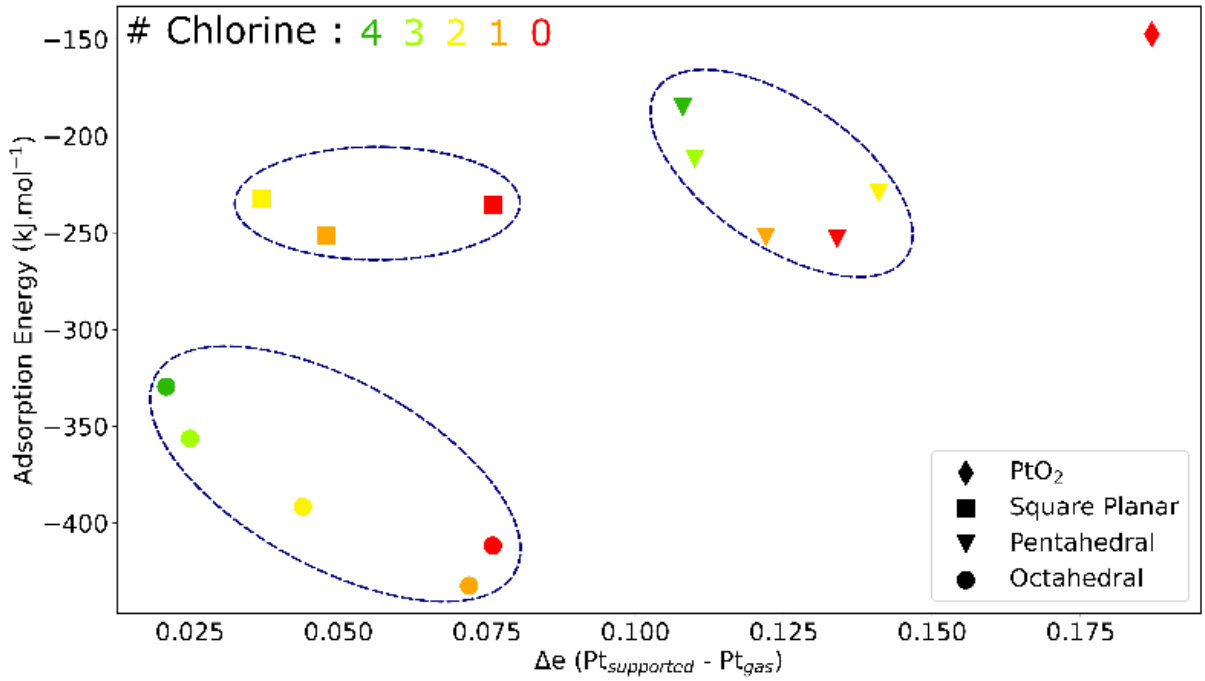

Figure IV-5. Adsorption energies (in kJ/mol) of the Pt(IV) complexes against the difference of the platinum's charge after adsorption (Hirshfeld charges in e). Number of chlorine in the coordination sphere of the Pt is represented by a color code: dark green : 4 Cl, green : 3 Cl, yellow : 2 Cl, orange : 1 Cl and red no Cl. The geometry of the complexes (square planar, pentahedral, octahedral) refers to the one observed in the supported state.

After the adsorption of the complexes, constraints from the interaction between ligands and the surface induce a destabilization of the complexes compared to their reference geometries in gas phase (**Figure SIV-6**). Other than the two spurious deformation energies of the complexes which undergo a dissociation ($PtCl_4(OH)H^*$ and $PtCl_3(OH)_2H^*$) the deformation energies are between 23.3 kJ/mol ($PtOCl_2$) and 234.1 kJ/mol (PtO_2). As for the adsorption energies represented in **Figure IV-5**, the deformation of the complex is related to both the geometry of the complex and the nature of the ligand. After adsorption, the three square planar complexes ($PtOCl_2$, PtOCl(OH) and $PtO(OH)_2$) are the

among the less impacted, with small deformation energies increasing from 23.3 kJ/mol for two chlorines ($PtOCl_2$) to 79 kJ/mol for two hydroxyls ($PtO(OH)_2$). This increase of the deformation energy with the exchange of chlorine by hydroxyl is well respected for these three complexes as they share similar geometries before and after adsorption. Indeed, the same trend is observed (after adsorption) for the three octahedral $PtCl_y(OH)_{4-y,\ y<3}(H_2O)$ (75 kJ/mol for $PtCl_2(OH)_2(H_2O)$, 87 kJ/mol for $PtCl(OH)_3(H_2O)$ and 122 kJ/mol for $Pt(OH)_4(H_2O)$). Again, for these complexes, their adsorbed geometries are unique because of the five ligands already in the coordination sphere. However, the case of the pentahedral $PtCl_y(OH)_{4-y}$ is less straightforward as different geometries and changes from the gas phase reference are observed. The deformation energies obtained are as follows: $PtCl_4$ with 69 kJ/mol; $PtCl_3(OH)$ with 85 kJ/mol; $PtCl(OH)_3$ with 89 kJ/mol $Pt(OH)_4$ with 110 kJ/mol and finally $PtCl_2(OH)_2$ with 136 kJ/mol. This last unexpectedly high deformation energy is related to the geometry of $PtCl_2(OH)_2$ after adsorption (**Figure IV-7**, **c)**), which has a chlorine atom in an apical position while all of the other $PtCl_y(OH)_{4-y}$ are square planar in gas phase.[55] While all of them go from a square planar geometry to a pentahedral one, only $PtCl_4$ and $PtCl_2(OH)_2$ exhibit an apical ligand. The reason why $PtCl_4$ is less impacted despite its similar behavior remains unclear. Perhaps this atypical ligand effect persists but is compensated by the fully chlorinated coordination sphere limiting further deformation.

In a similar way the surface is also destabilized during the adsorption of the complexes (**Figure SIV-6**). This quantity is mostly driven by the number of bridging ligands, their nature and the adsorption site. As for the deformation of the complexes, chlorines tend to be less constraining for the surface than hydroxyls with again some subtilities coming from the geometries of the complexes after adsorption. The relative impact of oxo ligand is hard to evaluate as it is only present on complexes with specific geometries limiting the analysis of trends. Indeed, oxo ligands are encountered in PtO_2 which exhibits the highest surface deformation energy (+ 221 kJ/mol) but it is also the only complex in the O(A)-O(C) adsorption site (**Figure IV-3**, **c)**. In this specific adsorption site, the complex is closer to the surface, hence constraining it in bigger proportions. They are also present in the $PtOCl_y(OH)_{2-y}$ series which are again the only complexes bonded to the support by two bridging ligands in addition to the platinum which is adsorbed in O(B) site. This low number of bonds with the surface allows small deformation of the surface with only 79 kJ/mol for $PtOCl_2$, 87 kJ/mol for PtOCl(OH) and 85 kJ/mol for $PtO(OH)_2$. As the oxo ligand is always bridging, both PtOCl(OH) (**Figure IV-8**, **c)**) and $PtO(OH)_2$ have the same bridging ligands, explaining their similar impact on the surface. Beside these four complexes, all the remaining ($PtCl_y(OH)_{4-y}$ and $PtCl_y(OH)_{4-y}(H_2O)$) are bonded to the surface by one Pt-O bond and three Pt-X-Al (X being a ligand) and the relative impact of Cl and OH is, quite, well-illustrated. The less constraining complex to the surface (77 kJ/mol) is the $PtCl_4$ which is the only

complex with three Pt-Cl-Al bonds, followed by $PtCl_2(OH)_2$ at 89 kJ/mol. Both $Pt(OH)_4$ and $PtCl(OH)_3$ share similar anchoring ligands (3 Pt-O(H)-Al) and thus they distorted the surface in similar proportion with 143 kJ/mol and 147 kJ/mol respectively. The surface is quite insensitive to the addition of a water molecule to these two complexes, with 141 kJ/mol for $PtCl(OH)_3(H_2O)$ and 151 kJ/mol for $Pt(OH)_4(H_2O)$. However, in the case of $PtCl_2(OH)_2(H_2O)$, despite sharing geometric similarities with the last two octahedral complexes, the addition of H_2O results in a stronger surface deformation (+120 kJ/mol) compared to the pentahedral $PtCl_2(OH)_2$. The formation of a surface hydroxyl for both $PtCl_4(OH)H^*$ and $PtCl_3(OH)_2H^*$ is responsible for a bigger impact on the surface with deformations calculated at 151 kJ/mol and 168 kJ/mol respectively. Unexpectedly and totally off the trends lies $PtCl_3(OH)$ (**Figure IV-7**, **b)**) with 174 kJ/mol. In its case, the presence of only one Pt-O(H)-Al bond is responsible for strong elongation of an Al-O bond of the surface that cannot be compensated by the presence of a symmetric Pt-O(H)-Al as in all other complexes.

Energetic trends at 0 K

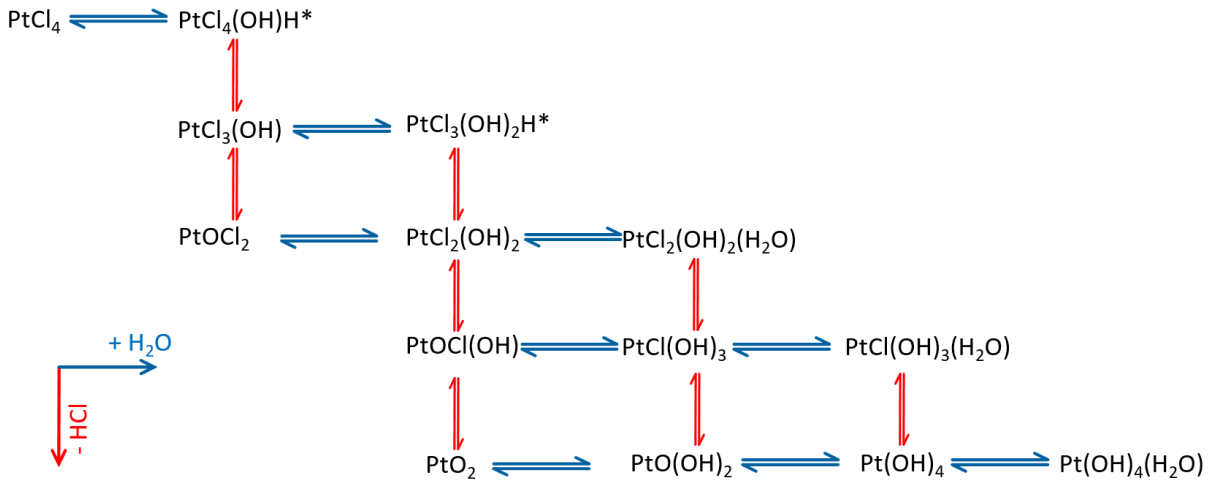

Figure IV-6. Platinum complexes considered in the thermodynamic model and the interconnected reactions: hydrations and ligand exchange. The ligand exchange reaction discussed in this section can be considered as a combination of a red and blue arrows.

During the calcination process, changes on the coordination sphere of the platinum species are expected. Here we consider that such changes occur through hydration reactions (blue arrows in **Figure IV-6**) and ligand exchange (combination of 1 blue and 1 red arrow in **Figure IV-6**). In this part we describe the energetics of these reactions. A graphical illustration of these reactions and how they link the considered species is displayed in **Figure IV-6**.

Hydration reactions are always exothermic at 0 K and the average hydration energy is -156 kJ mol^{-1} (**Table SIV-3**). The exothermicity is impacted by different factor such as the coordination sphere, the geometry, or the grafting mode of the complexes. In the absence of oxo ligand in the coordination

sphere of the platinum, hydrations are easier in presence of chlorine with hydration energies of -196 kJ.mol^{-1}for $PtCl_4$, -188.4 kJ mol^{-1} for $PtCl(OH)_3$ and -144.7 kJ/mol for $Pt(OH)_4$. No notable difference between the reaction energies described by **Eq.2** and **Eq.3** (undissociated water molecule, and formation of a surface hydroxyl) has been noticed. Interestingly, the trend is reversed in presence of oxo ligand (**Eq.4**) and hydration becomes harder with the number of chlorines in the coordination sphere of the platinum. In these cases, chlorine hardens the hydration by around 20 kJ/mol. The hydration of $PtOCl_2$ into $PtCl_2(OH)_2$ and PtOCl(OH) into $PtCl(OH)_3$ are calculated at -108.4 kJ/mol and -126.9 kJ/mol respectively while the hydration of $PtO(OH)_2$ into $Pt(OH)_4$ is at -145.6 kJ/mol. The geometries of the hydrated complexes are an important factor. In particular, the formation of octahedral complexes from penta-coordinated ones result in highly exothermic hydration reactions (between -144.7 kJ/mol and -196.0 kJ/mol for the hydration of the $PtCl_y(OH)_z$). The grafting of the complexes can also modulate the hydration energies, and the hydration of PtO_2 (which is bounded to the surface through two Pt-O_{surf} bonds as exhibited in **Figure IV-8**) is more resistant to hydration with only -106.6 kJ/mol calculated for its hydration into $PtO(OH)_2$. As in this case, both the reactant and product exhibit a square planar geometry, the grafting mode rather than the geometry is suspected to be responsible for this high stabilization of PtO_2, probably due, as it will be described later, to the high interaction energies (**Figure SIV-6**) of the bi-grafted complex (**Figure IV-3, c**).

By considering the hydration values calculated for these Pt(IV) complexes in gas phase, we conclude that the support is responsible for easier hydrations with an overall gain of -85 kJ/mol compared to what was calculated for similar reactions in gas phase (averaged reaction energies for Pt(IV) calculated in PBE-dDsC: -71 kJ mol^{-1}).[55] However, others factors have to be considered. Indeed, the geometry being an important factor of stabilisation, it is not straightforward to compare the $PtCl_y(OH)_{4-y}$ supported or in gas phase, as they go from an unstable pentahedral geometries to octahedral ones if supported, while during the hydration in gas phase the stable square planar are transformed into pentahedral. The mean hydration energies of the gas phase square planar $PtCl_y(OH)_{4-y}$ into pentahedral $PtCl_y(OH)_{4-y}(H_2O)$ and then octahedral $PtCl_y(OH)_{4-y}(H_2O)_2$ were calculated at -27.2 kJ/mol and -96.5 kJ/mol.[55] While once supported, the mean hydration of the $PtCl_y(OH)_{4-y}$ is 183.3 kJ/mol. In a similar spirit, the comparison of the hydration of $PtOCl_y(OH)_{2-y}$ also supports the stabilizing impact of the support. Indeed, similar energies are calculated in gas phase where a square planar is formed (120.3 kJ/mol) and on the support where pentahedral complexes are formed (127.0 kJ/mol). Thus, while this consideration on the geometries of reactant and product during hydration has to be considered to evaluate the intrinsic contribution of the support onto the hydration of these complexes, there is an undeniable role of the support in the stabilization of the hydrated $PtCl_y(OH)_{4-y}(H_2O)$ complexes. This is probably due to the fact that water is able to interact with the support,

either through chemical bonding after its dissociation, and/or through dispersion forces, and/or finally due to the stronger charge of platinum once supported.

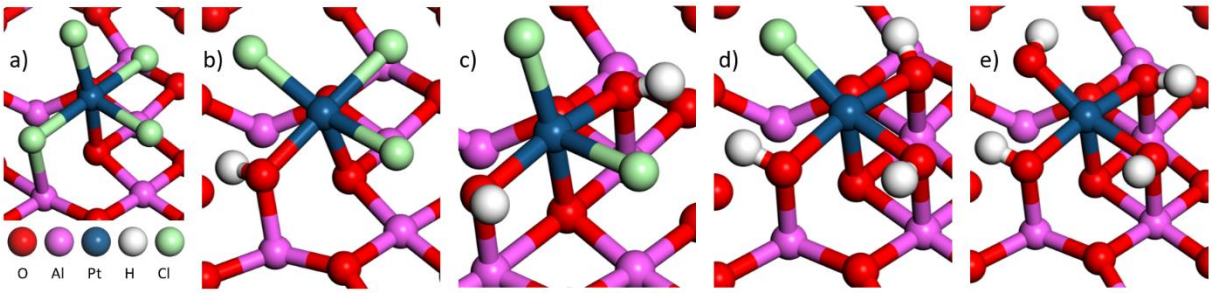

Figure IV-7. Supported pentahedral $PtCl_y(OH)_{4-y}$ complexes. a: $PtCl_4$, b: $PtCl_3(OH)$, c: $PtCl_2(OH)_2$, d: $PtCl(OH)_3$, e: $Pt(OH)_4$.

Ligand exchange energies are calculated by considering the exchange of a chlorine ligand by a hydroxyl (**Eq.1** and **Figure IV-6**). As exhibited by the positive reaction energies (average value of 37 kJ mol^{-1}), chlorinated species are intrinsically more stable than their hydroxylated counterpart (**Table SIV-3**). A similar but stronger trend was also predicted for gas phase complexes, with an average energy of reaction calculated at 53.2 kJ/mol for the same reactions.[55] By comparing the supported reaction energies to the ones obtained in gas phase helps to reveal the considerable role of the surface in the platinum complexes chemistry. Indeed, in a number of cases, the hydroxyl formed upon H_2O/HCl exchange becomes a bridging ligand between the Pt center and one Al site (**Figure IV-8**) leading to stronger interaction energies (**Figure SIV-6**) with the support. This replacement of bonding ligands is possible up to 3 hydroxyls in the coordination sphere of the $PtCl_y(OH)_{4-y}(H_2O)_n$ complexes, which corresponds to the number of available aluminum sites around an Oxygen (B) (site where the Pt complex is coordinated (**Figure IV-8**)). By computing the adsorption energies (**Eq.S4**) of $PtCl_y(OH)_{4-y}$, we found out that they increase with the number of hydroxyls in the coordination sphere (**Figure IV-7**) and reach a plateau for 3 hydroxyls, with the adsorption energies of $PtCl(OH)_3$ (-252.0 kJ/mol) and $Pt(OH)_4$ (-253.2 kJ/mol) being almost equal. Similar trend is calculated for the $PtCl_y(OH)_{4-y}(H_2O)$ octahedral complexes. However, in that case, the replacement of the last chlorine by an hydroxyl is calculated 19.9 kJ/mol higher on the support with + 89.9 kJ/mol (**Table SIV-3**) against 70 kJ/mol in gas phase.[55] In the presence of oxo ligands, the first exchange which allows the replacement of bridging chlorine into a bridging hydroxyl is also easier than in gas phase with + 42.3 kJ/mol on the support and + 62 kJ/mol in gas phase.[55] During the last exchange, as the hydroxyl cannot interact with the support (exchanging it in place of the oxo ligand led to an highly unstable conformer) the exchange is harder than in gas phase with 64.9 kJ/mol (**Table SIV-3**) against 49 kJ/mol.[55] The fact that no exchange reaction energy for the $PtCl_y(OH)_{4-y}$ pentahedral complexes exceeds the gas phase ones even in the case of the 4th hydroxyl is probably due to H-bonds between

the last added hydroxyl and the support. Indeed, the distances between the hydrogen of the added hydroxyl and the two closest oxygens of the support are 3.09 Å and 3.39 Å, allowing the existence of H-bonds (**Figure IV-7, e)**). In the cases of octahedral and square planar complexes, the last hydroxyls are in apical position, therefore no stabilizing interaction with the support is possible. Thus, the support facilitates the replacement of chlorines by hydroxyls as long as these new hydroxyls can form Pt-O(H)-Al bonds, once this limit is reached, similar or higher reaction energies are calculated for supported complexes.

IV.3.4. Thermodynamics of calcination

In this part we present the evolution of the stable species under oxidizing conditions to mimic the calcination step of the catalyst preparation through thermodynamic diagrams. All the calculated $[PtO_xCl_y(OH)_z(H_2O)_n]^0$ complexes are linked through a network of reactions such as ligand exchange and hydrations (**Eq. 1-4**) as graphically illustrated in **Figure IV-6**, similarly to our previous study in gas phase.[55]

Calcination is modelled here with O_2 as oxidative agent, as it is usually done under air flow,[7,39] with O_2 pressure fixed at 0.21 bar. During the calcination step, various reactions such as dehydration or ligand exchange are experimentally expected.[7,47] These reactions will be simulated by considering variable pressures of H_2O and HCl. Due to experimental protocols, the HCl pressure is rarely measured during calcination processes while the water pressure is known. The HCl pressure will be used here as a variable adjusting the chlorine contents in the system.[28] Thus, we used a set of HCl pressure values (0 – chlorine free case-, 10^{-12} and 10^{-6} bar) and letting $P(H_2O)$ ranges between 10^{-12} and 1 bar. Temperatures are allowed to range from 0 K to 1000 K. Such values allow us to describe both precise transitions and major trends.

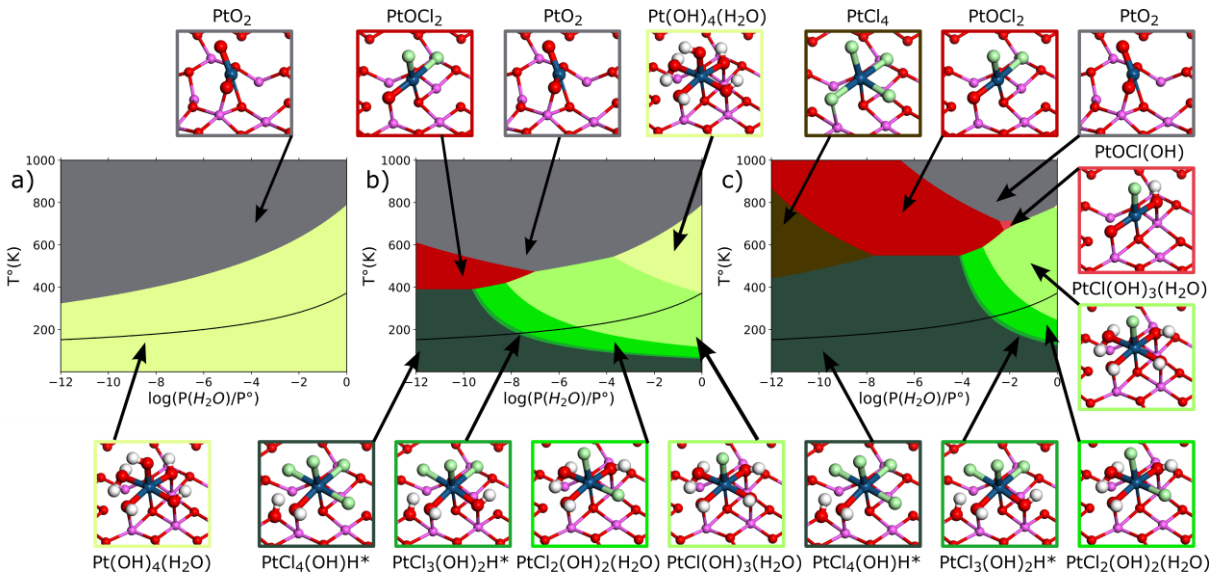

Figure IV-8. Thermodynamic diagrams of the most stable species under oxidative conditions at $P(O_2)$ = 0.21 bar for three chlorine pressures: a) Without chlorine; b) P(HCl) = 1.10^{-12} bar; c) P(HCl) = 1.10^{-6} bar. The gas phase domain of water is located above the black curved line representing the liquid/vapor equilibrium.

Figure IV-8 represents the most stable species (lowest Gibbs free energy of all simulated species) expected in calcination conditions according to the water pressure and temperature for three levels of Cl pressure. In the absence of chlorine only two Pt species are expected, PtO_2 and its hydrated counterpart $Pt(OH)_4(H_2O)$. PtO_2 is a particular species among the Pt(IV) as it is the only one being bonded to two oxygens of the support (A and C) as described previously. The dehydrated form is expected above 400 K for 1.10^{-6} bar of water (**Figure IV-8**, **a)**) which is a water pressure usually considered experimentally. As it could be expected from the nature of the reaction linking these two species, higher water pressure stabilizes $Pt(OH)_4(H_2O)$. Despite the simple nature of the reaction linking these two species (**Figure IV-6**) the Pt complex has to migrate from an oxygen (B) to oxygens (A) and (C) (**Figure IV-3**) during dehydration.

Adding chlorine drastically changes the thermodynamic landscape as exchanging hydroxyls for chlorine ligands was found to be favored (**Table SIV-3**) from an electronic energy point of view. Thus, a great variety of $PtCl_y(OH)_z(H_2O)$ complexes are stable at low temperatures, with Cl/OH ratio decreasing as the water pressure increases. Chlorine stabilizes the hydration state of the Pt(IV) complexes with a dehydration temperature being slightly higher for the hydroxychlorinated complexes (~500 K at 1.10^{-6} bar of water) than for the totally hydroxylated case (~400 K at 1.10^{-6} bar of H_2O) (**Figure IV-8, a), b) and c)**). However, at a low amount of HCl (P(HCl) = 1.10^{-12} bar), the role of chlorine is not significant enough to impact the high temperatures part of the diagram where PtO_2 is still expected to be the most stable specie, especially for typical calcination conditions (T~800 K and $P(H_2O)$ = 1.10^{-6} bar). At low water pressure and intermediate temperature (~400-600 K), a square

planar platinum is stabilized ($PtOCl_2$) and it can be seen as possible intermediate species between the hydrated octahedral Pt complexes and PtO_2.

Increasing the HCl pressure to 10^{-6} bar (**Figure IV-8, c)**) strongly modifies the diagram at both low and high temperatures. On the low temperature domain the $PtCl_y(OH)_z(H_2O)$ complexes (already present at P(HCl) = 1.10^{-12} bar) are strongly stabilized. In particular, the fully chlorinated $PtCl_4(H_2O)$ is stable on a larger domain: up to 550 K for $P(H_2O)$ between 10^{-8} and 10^{-4} bar. The other hydroxychlorinated complexes are still found at higher water pressure but on a smaller domain and the fully hydroxylated $Pt(OH)_4(H_2O)$ vanishes. At higher temperature, the PtO_2 domain is shrunk in favor of $PtCl_4$, $PtOCl_2$ and marginally PtOCl(OH). $PtCl_4$ is stable for the lowest water pressure and up to $P(H_2O)$ = 10^{-11} bar at T = 800 K. Then $PtOCl_2$, a square planar platinum complex, is expected until $P(H_2O)$ reaches 10^{-4} bar at 825 K. Finally, the stabilization of PtO_2 should occur for $P(H_2O) > 10^{-4}$ bar. These diagrams show the importance of controlling the amount of chlorine in the system as it drastically changes the expected species after calcination. In summary, for typical calcination conditions (T = 800 K and $P(H_2O) = 1.10^{-6}$ bar), three species PtO_2, $PtOCl_2$ and $PtCl_4$ appear to be stable depending on the amount of chlorine (P(HCl)) present in the system (**Figure SIV-4**).

The role of the support in the stabilization of the platinum complexes is far from being negligeable. Indeed, by comparing these calcination diagrams to the ones involving similar species in gas phase,[55] it is shown that the stabilization of $PtOCl_2$ is possible only in the presence of the support which stabilizes it by forming a square planar platinum. Moreover, at the low temperature, the support stabilizes various $PtCl_y(OH)_{4-y}(H_2O)$ hydroxy-chlorinated platinum complexes by facilitating successive exchanges of chlorine for hydroxyl through the formation of bridging Al-O(H)-Pt bonds. In gas phase, only $PtCl_4(H_2O)$ was expected. Finally, the transition temperature between the $PtCl_y(OH)_{4-y}(H_2O)$ and the dehydrated species is around 200 K higher than in gas phase as it could be expected from the reaction energies values of the hydrations. We will come back to this difference between gas phase and supported system in the section devoted to the comparison with EXAFS.

To check the sensitivity of our results with the functional, we report in **Figure SIV-5** the calcination thermodynamic diagram calculated at the HSE06[66–68] level. As it was observed for the gas phase complexes,[55] both PBE[61]-dDsC[62,63] and HSE06 provide similar results as long as no changes of the oxidative degree are expected as it is the case for the calcination models. Without chlorine no change is observed, PtO_2 and $Pt(OH)_4(H_2O)$ are still expected and the transition is calculated at similar ($T,P(H_2O)$). Small changes are revealed for chlorinated species and the square planar $PtOCl_2$ is expected with PBE-dDsC at low HCl pressure (P(HCl) = 10^{-12} bar) at temperature between 400 K and 600 K for water pressure below 10^{-8} bar, whereas its domain is strongly shrunken in HSE06. The

stabilization domain of $PtOCl_2$ increases at higher HCl pressure for water pressure ranging from 10^{-12} bar to 10^{-4} bar at 800 K for PBE-dDsC but only up to 10^{-6} bar in HSE06. Moreover, the very small domain of stability which was found with PBE-dDsC for another square planar specie, PtOCl(OH), is not visible in HSE06. Overall, both functional are in good agreement as it was predicted from similar models in gas phase.[55]

IV.4. Discussion

IV.4.1. Comparison of DFT structures with EXAFS results

The impact of chlorine on the coordination shell of platinum has been observed through EXAFS experiments as shown before for the two samples containing 0.1 and 1.4 wt% Cl. It is composed of one Cl atom and five O atoms are found close to the platinum for $0.1\%_{w/w}$ Cl against two Cl atoms and four O atoms at $1.4\%_{w/w}$ Cl. For similar Pt loading (0.3% wt) and in the absence of chlorine, Dessal et al.[39] observed a coordination number of 5.5 ± 0.8 oxygens in the platinum first shell. Thus, the Pt species could be suspected to correspond to the octahedral complexes as predicted by DFT at low temperature.

In order to compare the previous XAS experiments, it has to be noticed that our samples as well as those by Dessal et al.[39] were cooled down at room temperature before analysis. We model this cooling down from a thermodynamic point of view in **Figure IV-9**, **a)**. The water pressure is fixed at 1.10^{-6} bar (as during experiences) and as HCl pressure remains unknown during calcination, we allow it to range from 10^{-12} bar and 1 bar, thus we can describe the evolution of these complexes before analysis. Independently of the HCl content, below 500 K octahedral complexes $PtCl_y(OH)_{4-y}(H_2O)$ (with $y \geq 1$) are expected to be formed in place of PtO_2, $PtOCl_2$ or $PtCl_4$. As we observed here and in previous work[7] dedicated to similar species but on different type of γ-Al_2O_3 support, even at the lowest chlorine amount considered, at least one Cl neighbor is expected. This observation is in agreement with the absence of the octahedral $Pt(OH)_4(H_2O)$ that could be expected from successive hydration of PtO_2. However, from **Figure IV-8, a)** in absence of chlorine in the system, $Pt(OH)_4(H_2O)$ is expected if calcinated catalysts are cooled down. Thus, from a thermodynamical point of view, cooling down the sample before analysis is expected to change the supported species by stabilizing the five octahedral $PtCl_y(OH)_{4-y}(H_2O)$ species depending on the chlorine content in the system: $PtCl_4(OH)H^*$, $PtCl_3(OH)_2H^*$, $PtCl_2(OH)_2(H_2O)$, $PtCl(OH)_3(H_2O)$ and $Pt(OH)_4(H_2O)$.

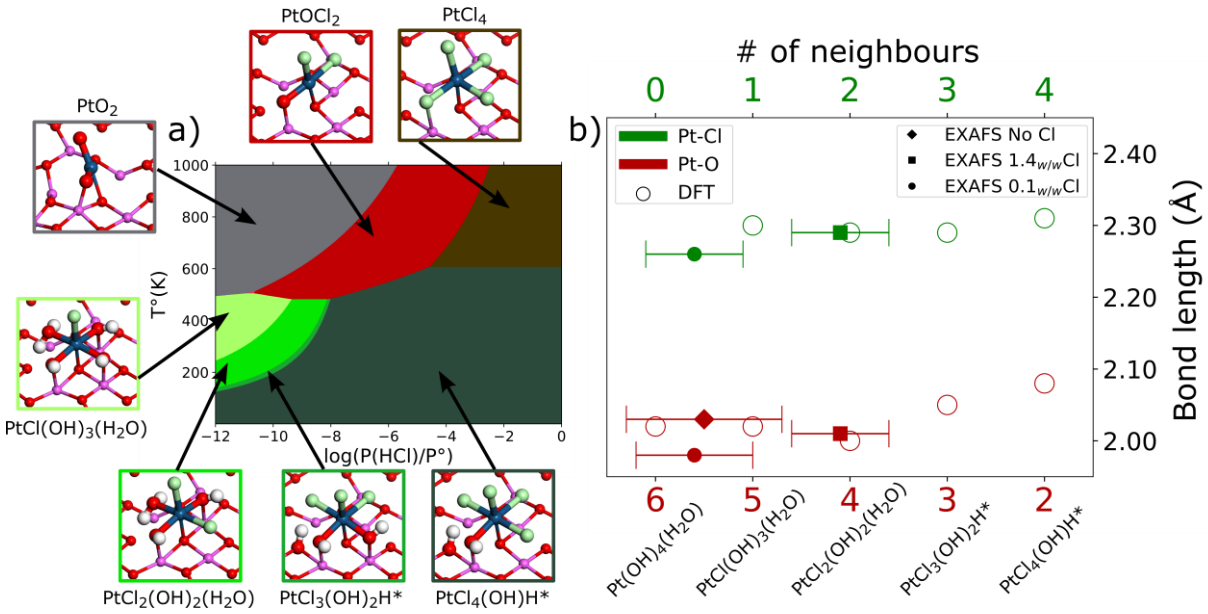

Figure IV-9. a) Thermodynamic diagram modelling the cooling down of calcined samples before analysis. Most stable species according to HCl pressure e and temperature are depicted. Water pressure is fixed at 1.10^{-6} bar. b) Comparison of structural data obtained by EXAFS on 0.3%Pt calcinated samples with various loading in chlorine, with DFT models. The unchlorinated case (diamond symbol) was characterized by Dessal et al.[39] Plain symbols represent experimental values while empty ones represent DFT models. Bond lengths are plotted against the number and type of bonds in the Pt coordinative sphere with the top x-axis in green representing the #Pt-Cl bonds, and in red on the bottom x-axis the #Pt-O. EXAFS values for chlorinated samples are taken from the fit done with aluminum in the second shell of the Pt (SI.9).

The structural parameters of these five octahedral complexes are reported and compared to EXAFS results in **Figure IV-9**, **b).** Data corresponding to the chlorinated samples are reported in **Table IV-1**, while unchlorinated data are from Dessal et al.[39] For the highest experimental amount of chlorine (1.4 wt%), $PtCl_2(OH)_2(H_2O)$ matches the best with both Pt-Cl and Pt-O coordination numbers and bond lengths. Experimentally, the coordination sphere of the platinum was fitted to be $N_{Pt\text{-}O}$ = 3.9 ± 0.5 and $N_{Pt\text{-}Cl}$ = 2.1 ± 0.5 with Pt-Cl and Pt-O distances fitted at 2.28 Å and 2.00 Å while average distances Pt-Cl and Pt-O bond lengths are calculated to be 2.29 Å and 2.04 Å respectively in the DFT models (**Table IV-1** and **Table SIV-2**). For a lower loading of chlorine (0.1 wt%), the simulated $PtCl(OH)_3(H_2O)$ species agrees well with EXAFS observations: the unique Pt-Cl bond is calculated at 2.30 Å and the mean Pt-O at 2.03 Å from DFT while EXAFS reports $N_{Pt\text{-}Cl}$ = 0.8 ± 0.6 with Pt-Cl at 2.29 Å and $N_{Pt\text{-}O}$ = 5.2 ± 0.6 with Pt-O at 1.98 Å. The number of Cl atoms founds as ligands of Pt is compatible with the chlorine contents of the two catalysts, the theoretical maximal Cl/Pt atomic ratio being of ~1.9 and 26 for 0.1 wt% and 1.4 wt% respectively with the possibility for chlorine atoms to be located on the alumina surface. Finally, without chlorine, $N_{Pt\text{-}O}$ is estimated at 5.5 ± 0.8 and the mean Pt-O distance is 2.03 ± 0.03 Å, similarly as those calculated for $Pt(OH)_4(H_2O)$ (2.02 Å). By mimicking the

experimental calcination and XAS acquisition protocols, we are thus able to identify 3 species of supported platinum complexes which are in good agreement with experimental observations.

Considering now the second coordination sphere, the comparison of the distance between the platinum and the atoms of the second shell reveal that DFT Pt-O_{long} values are about 0.4 Å larger than EXAFS (**Table IV-1** and **Table SIV-4**). By contrast, DFT Pt-Al distances are much closer to EXAFS estimations: 2.99-3.16 Å and 2.91-2.95 Å, respectively (**Table SIV-4**). Pt-Al coordination numbers (computed at 3) are also consistent. Thus, it can be deduced that the relevant EXAFS values are those obtained from the fit done with aluminum considered in the second shell.

To further compare the DFT models with EXAFS observations, we report in **Figure IV-10, a)**, the FEFF simulation of the k^2 weighted magnitude of the Fourier transform (FT) of three different octahedral Pt complexes supported on the (100) γ-alumina surface (the fully chlorinated $PtCl_4(OH)H^*$, the fully hydroxylated $Pt(OH)_4(H_2O)$ and the intermediate case $PtCl_2(OH)_2(H_2O)$). The remaining octahedral species as the analyses of the various path are displayed in **SI.10**. In line with the previous analysis, we observe a reasonable agreement (both intensities and peak positions) with the FT spectra reported in **Figure IV-1 c** and **f**. We also notice a shift to higher radial distances for the first peak in the case of the $PtCl_3(OH)_2H^*$ (**Figure SIV-7, c**) and $PtCl_4(OH)H^*$ complexes in line with the increase of Cl neighbors.

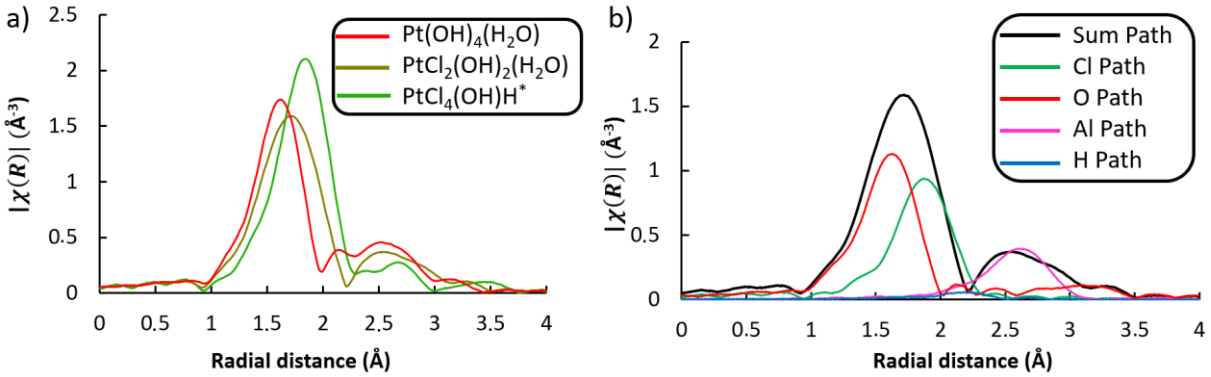

Figure IV-10. FEFF simulation of the k^2 weighted magnitude of the Fourier transform (FT). a) The sum of all paths is represented for the considered species, b) Decomposition of the paths for the $PtCl_2(OH)_2(H_2O)$ species. Fits were performed over Δk = 4-12Å^{-1} and ΔR = 1.15- 3.7Å.

The analysis of the various paths (**Figure IV-10, b**) in the case of $PtCl_2(OH)_2(H_2O)$ clearly reveals the distinct contributions of O and Cl atoms to the first peak of the sum while the second low intensity peak is mainly constituted from Pt-Al paths. By contrast Pt-O paths at large distances are more diffuse and may only contribute to the smaller peaks observed at larger radial distances (beyond 3 Å in **Figure IV-1**). Similar paths analysis for the other complexes are reported in **SI 10**. This confirms

that the best EXAFS fit proposed in **Table IV-1** should be the one based on Pt-Al which contributes to the second peak and not on Pt-O_{long} which contributes to larger distances, according to DFT models.

Moreover, as discussed in our previous DFT work,[55] no Pt-O bond and only Pt-Cl bonds were found in isolated Pt complexes for similar conditions (room temperature, $P(H_2O) = 1.10^{-6}$ bar). The stabilizing effect of the bridging Al-O(H)-Pt bonds revealed herein on the supported system explains reasonably well why numerous EXAFS studies (including the present one) undertaken on alumina supported platinum materials report the existence of Pt-Cl and Pt-O bonds.[7,29,32,36,46,85,86]

IV.4.2. Comparison of DFT structures with HERDF-XANES

XANES spectra have been simulated at the Pt L_3 edge for all platinum complexes identified on the thermodynamic diagram. However, we only report here the computed features of the octahedral species identified from the first principle thermodynamic study reported above, in line with the EXAFS results. Consistently, the XANES spectra calculated from the octahedral platinum species are the closest to the experimental XANES spectra, with respect to the computed XANES spectra of all other species (not shown).

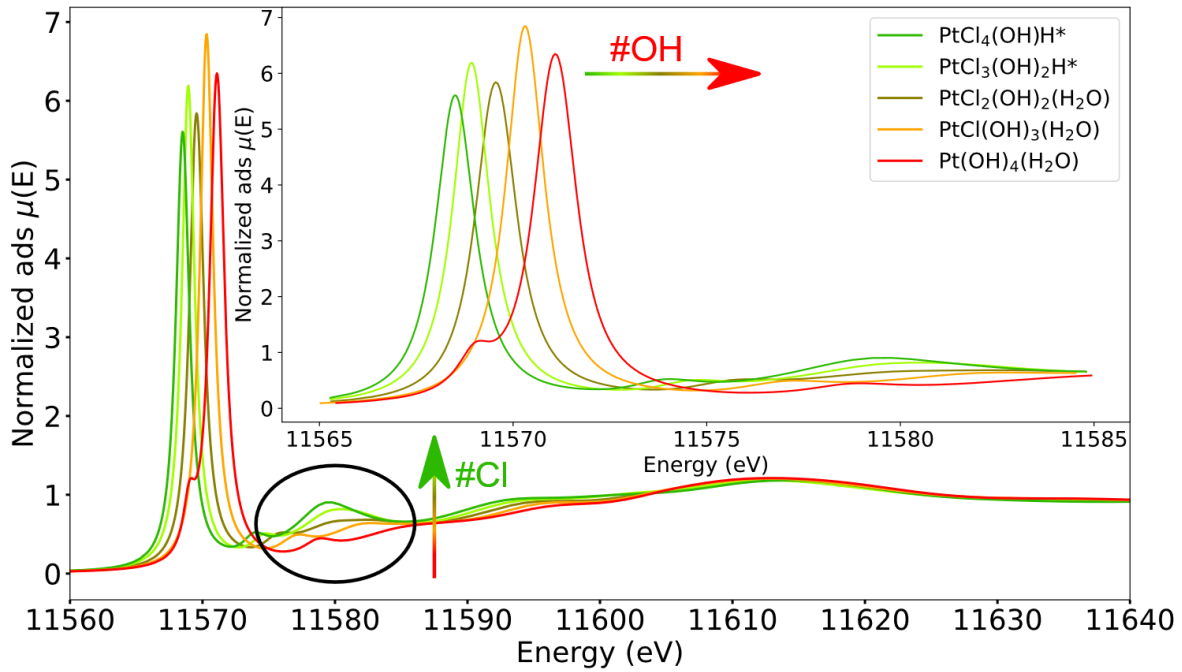

Figure IV-11. Calculated Pt L_3 XANES spectra for various relevant octahedral $PtCl_y(OH)_{4-y}(H_2O)$ complexes. The two arrows represent the increasement of a ligand in the coordination sphere of the Pt. From red to green colors correspond to a change from a purely hydroxylated Pt complex to a fully chlorinated one.

Figure IV-11 reveals that as chlorine ligands are replaced by hydroxyls, a gradual shift of the WL toward the high energies is calculated (with the maximum of the WL calculated at 11568.52 eV for $PtCl_4(OH)H^*$ and at 11571.10 eV for $Pt(OH)_4(H_2O)$ (**Table SIV-5**)) in coherence with the increase of the positive charge of the platinum atom (**Figure IV-4**). Simultaneously, the WL intensity is non-monotonously increased upon OH/Cl exchange. Overall, the WL intensities of these five species in are good agreement with the WL of the experimental spectra (**Figure IV-11** and **Figure IV-12**). More importantly, the spectral feature between 11575 eV and 11585 eV is obviously linked to the number of Cl atoms present in the coordination sphere of the Pt. Indeed, we observe a gradual increase of the bump in this region as the number of chlorine ligands (y) increases in $PtCl_y(OH)_{4-y}(H_2O)$ (**Figure IV-11**).

In order to compare the simulated XANES more quantitatively to the experimental measurements of calcinated $Pt/\gamma\text{-}Al_2O_3$ for the two chlorine loadings (0.1% and 1.4%), we fitted the experimental spectra with a linear combination of all the octahedral $PtCl_y(OH)_{4-y}(H_2O)$ computed spectra by solving a least square problem using the CVXPY library.[77,78] From these best fits, we aim at determining a quantified proportion of the species recovering the experimental XANES spectra. However, due to the ground state nature of the DFT, that is used during the XANES calculation, the wight line (WL) area of the spectrum is not expected to be perfectly described. Reasonable agreements are obtained for heavy elements,[73] although DFT is still a strong approximation. For this reason, we have attempted to fit calculated spectra for various interval of energies, including or excluding the WL to probe the sensitivity of the proportion of the identified species (**Table SIV-6**).

The corresponding fitted spectra over the range of energies corresponding to the 11575 eV – 11585 eV bump is reported in **Figure IV-12.** Even if **Table SIV-6** reveals that this quantification depends on the choice of the energy interval used (see **SI. 11** for more details), we are able to propose a rather coherent trend for the proportion of each platinum complex after calcination. The fitted spectra (**Figure IV-12**) reproduce nicely the positions and intensity of the WL as well as post WL features compared to experimental spectra. However, despite the combination of various spectra, the width of the WL remains underestimated compared to the experimental one. From the evolution of the composition of the fitted spectra according to the two samples, the role of the chlorine on the feature between 11575 eV and 11585 eV seems undeniable. While exact compositions are reported in **Table SIV-6**, the average number of Cl in the coordination sphere of platinum is evaluated at 2.7 Cl in the 0.1% Cl sample and 3.9 Cl for the reference at 1.4% Cl. Independently of the domain of energies used for the fits, the trend remain similar and more chlorinated platinum complexes are calculated during the fit of the 1.4%Cl than for the 0.1%Cl (**SI.11**). This confirms the EXAFS observation that the amount of chlorine in the platinum coordination sphere after calcination is

impacted by the loading of chlorine used during the preparation. However, as the composition of the fitted spectra are highly sensitive to the domain used for the fit, we emphasize that these values coming from the composition of the fitted spectra to quantify the speciation of the $PtCl_y(OH)_{4-y}(H_2O)$ have to be considered with care. We finally notice that the XANES and EXAFS interpretations do not lead rigorously to the same species. While EXAFS reveals the presence of $PtCl(OH)_3(H_2O)$ and $PtCl_2(OH)_2(H_2O)$ respectively for 0.1 wt% and 1.4 wt% Cl content, XANES suggests slightly higher Cl coordination with a combination of $PtCl_2(OH)_2(H_2O)$ and $PtCl_3(OH)_2(H_2O)$ in the first case and a majority of $PtCl_4(OH)(H_2O)$ in the more chlorinated sample. This discrepancy reveals the fact that the two experimental techniques do not exactly probe in the same way the Pt environment and have also their own margin of errors. For instance, the fit of EXAFS coordination number is typically estimated within 20% of accuracy,[87] while we have seen that the XANES fit is also subject to uncertainty due to some DFT limitations in the treatment of excited states.

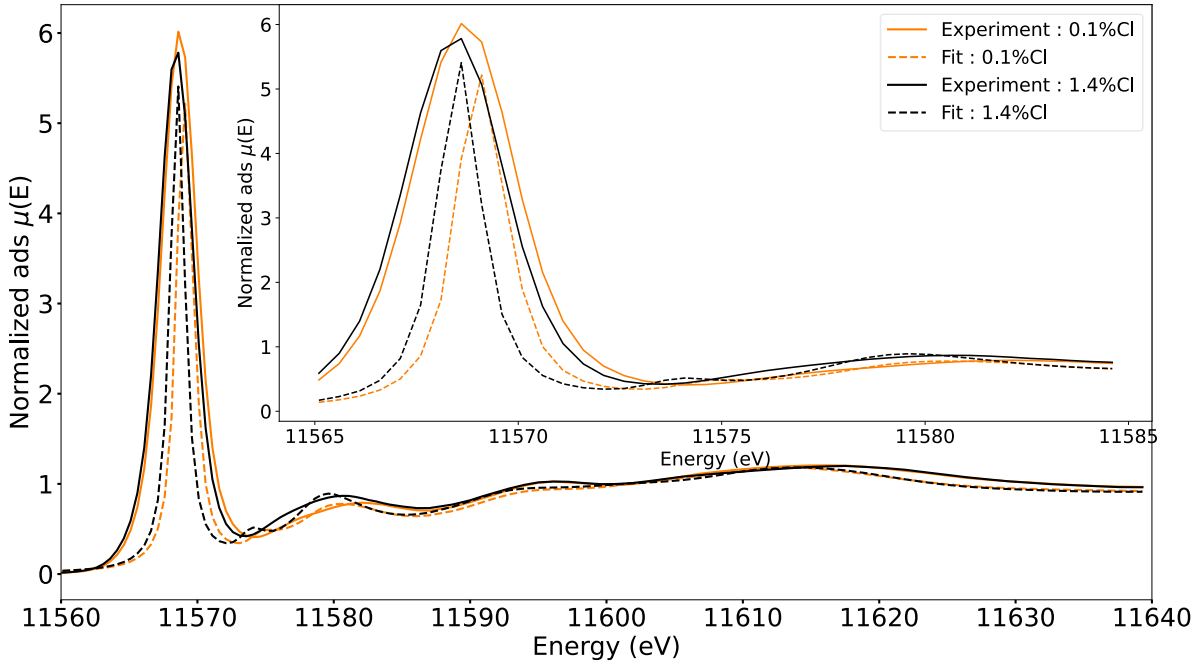

Figure IV-12. Pt's L3 XANES spectra for the two calcinated sample with 0.1%Cl and 1.4%Cl (plain lines). The two simulated spectra obtained from the fitting of the PtCly(OH)4-y(H2O) on the two references are in dashed lines. The fit was done for energies between 11575 eV and 11585 eV. $PtCl_y(OH)_z(H_2O)$ compositions corresponding to the fitted spectra are given in Table SIV-6.

IV.5. Conclusion

The preparation from H_2PtCl_6 precursor of two samples of γ-Al_2O_3 supported Pt catalysts (0.3 wt% Pt) with two optimized chlorine contents (0.1 and 1.4 wt%) and calcined (520°C) allowed to generate

mostly Pt single atom species, with local environments depending on the chlorine content as identified by EXAFS and HERDF-XANES.

Structural and energetic properties of $PtO_xCl_y(OH)_z(H_2O)_n$ supported on the (100) γ-Al_2O_3 surface have been studied by periodic DFT simulations. While most of the Pt SA complexes are grafted to the same surface site of the γ-Al_2O_3 surface through one Pt-O_{surf} bond and ligands (OH or Cl)-Al bonds, the PtO_2 species is adsorbed on a different site by two Pt-O_{surf} bonds. The support highly impacts the chemistry of the $PtO_xCl_y(OH)_z(H_2O)_n$, and while a stronger oxidization of the platinum was calculated with the increase of grafting bonds made, the support is also responsible for facilitating the replacement of chlorine in the coordination sphere of Pt (with respect to gas phase complexes) by making stronger bonds with hydroxyls ligands than with chlorine.

First principles thermodynamic diagrams have been calculated to evaluate the relative stability of these supported complexes during calcination. Realistic conditions (T, $P(H_2O)$, P(HCl)) were accounted for and their impact on the platinum coordination sphere was highlighted. While in the absence of chlorine PtO_2 is expected at calcination temperature, we observed the stabilization of chlorinated species such as $PtOCl_2$ and $PtCl_4$ with increasing amounts of HCl imposed on the system. At conditions corresponding to XAS analysis (room temperature), the impact of chlorine is stronger, and very low Cl amounts transform $Pt(OH)_4(H_2O)$ (expected in absence of chlorine) into the hydroxy chlorinated $PtCl_y(OH)_z(H_2O)$ complex.

According to EXAFS, the number (x) of Cl neighbors to Pt is about 1 or 2 ($\pm$10%) and the number of O atoms (y) is about 5 or 4, respectively, while the total number of O and Cl atoms (x+y) is about 6. These octahedral $PtCl_y(OH)_{4-y}(H_2O)$ species lead to a very good correspondence with EXAFS fitting results: for the weakly chlorinated catalysts, EXAFS is consistent with the $PtCl(OH)_3(H_2O)$ while for the highly chlorinated, $PtCl_2(OH)_2(H_2O)$ is expected. XANES characterization reveals a bump feature above the whiteline (between 11575 eV and 11585 eV) which is sensitive to the chlorine content. By using the FDMNES code, the simulation of the XANES spectra of the $PtCl_y(OH)_{4-y}(H_2O)$ complexes for the platinum L_3 edge highlighted a remarkable bump feature observed between 11575 eV and 11585 eV in the experimental spectra. This feature is related to the amount of chlorine in the coordination sphere of the Pt. Fitting this region with the various possible $PtCl_y(OH)_{4-y}(H_2O)$ spectra revealed that the most probable species would be mainly $PtCl_3(OH)_2(H_2O)$ and $PtCl_4(OH)_2(H_2O)$.

Thus, thanks to a symbiotic DFT-EXAFS-XANES approach, we go far beyond the previous state-of-art in terms of definition of the environment of the coordination sphere of platinum. Through pertinent DFT modelling of Pt complexes it is possible to better interpret XANES spectra and to better comfort

EXAFS fitting results. We expect this study to provide a better understanding of the calcination step and thus a better control over the genesis of the Pt SA on γ-Al_2O_3.

IV.6. References

(1) Serp, P.; Minh, D. P. *Supported Metal Single Atom Catalysis*; Wiley, 2022.

(2) Liu, L.; Corma, A. Metal Catalysts for Heterogeneous Catalysis: From Single Atoms to Nanoclusters and Nanoparticles. *Chem. Rev.* **2018**, *118* (10), 4981–5079.

(3) Wang, A.; Li, J.; Zhang, T. Heterogeneous single-atom catalysis. *Nat. Rev. Chem.* **2018**, *2* (6), 65–81.

(4) Kaiser, S. K.; Chen, Z.; Faust Akl, D.; Mitchell, S.; Pérez-Ramírez, J. Single-Atom Catalysts across the Periodic Table. *Chem. Rev.* **2020**, *120* (21), 11703–11809.

(5) Piccolo, L. Restructuring effects of the chemical environment in metal nanocatalysis and single-atom catalysis. *Catal. Today* **2021**, *373*, 80–97.

(6) Batista, A. T. F.; Chizallet, C.; Diehl, F.; Taleb, A.-L.; Gay, A.-S.; Ersen, O.; Raybaud, P. Evaluating acid and metallic site proximity in Pt/γ-Al2O3-Cl bifunctional catalysts through an atomic scale geometrical model. *Nanoscale* **2022**, *14* (24), 8753–8765.

(7) Batista, A. T. F.; Baaziz, W.; Taleb, A.-L.; Chaniot, J.; Moreaud, M.; Legens, C.; Aguilar-Tapia, A.; Proux, O.; Hazemann, J.-L.; Diehl, F.; Chizallet, C.; Gay, A.-S.; Ersen, O.; Raybaud, P. Atomic Scale Insight into the Formation, Size, and Location of Platinum Nanoparticles Supported on γ-Alumina. *ACS Catal.* **2020**, *10* (7), 4193–4204.

(8) Munnik, P.; Jongh, P. E. de; Jong, K. P. de. Recent developments in the synthesis of supported catalysts. *Chem. Rev.* **2015**, *115* (14), 6687–6718.

(9) Chen, A.; Holt-Hindle, P. Platinum-based nanostructured materials: synthesis, properties, and applications. *Chem. Rev.* **2010**, *110* (6), 3767–3804.

(10) Finzel, J.; Sanroman Gutierrez, K. M.; Hoffman, A. S.; Resasco, J.; Christopher, P.; Bare, S. R. Limits of Detection for EXAFS Characterization of Heterogeneous Single-Atom Catalysts. *ACS Catal.* **2023**, 6462–6473.

(11) V. Haensel. Alumina-Platinum-Halogen Catalyst And Preparation Thereof. U.S. Patent 2,479,109. 788,672.

(12) Farrauto, R. J.; Heck, R. M. Catalytic converters: state of the art and perspectives. *Catal. Today* **1999**, *51* (3-4), 351–360.

(13) Huber, G. W.; Cortright, R. D.; Dumesic, J. A. Renewable alkanes by aqueous-phase reforming of biomass-derived oxygenates. *Angew. Chem. Int. Ed.* **2004**, *43* (12), 1549–1551.

(14) Sattler, J. J. H. B.; Ruiz-Martinez, J.; Santillan-Jimenez, E.; Weckhuysen, B. M. Catalytic dehydrogenation of light alkanes on metals and metal oxides. *Chem. Rev.* **2014**, *114* (20), 10613–10653.

(15) Zhang, F.; Zeng, M.; Yappert, R. D.; Sun, J.; Lee, Y.-H.; LaPointe, A. M.; Peters, B.; Abu-Omar, M. M.; Scott, S. L. Polyethylene upcycling to long-chain alkylaromatics by tandem hydrogenolysis/aromatization. *Science* **2020**, *370* (6515), 437–441.

(16) Ertl, G.; Knözinger, H.; Schüth, F.; Weitkamp, J. *Handbook of Heterogeneous Catalysis, 2nd ed.,*; Wiley-VCH; Weinhei, 2008.

(17) Jahel, A. N.; Moizan-Baslé, V.; Chizallet, C.; Raybaud, P.; Olivier-Fourcade, J.; Jumas, J.-C.; Avenier, P.; Lacombe, S. Effect of Indium Doping of γ-Alumina on the Stabilization of PtSn Alloyed Clusters Prepared by Surface Organostannic Chemistry. *J. Phys. Chem. C* **2012**, *116* (18), 10073–10083.

(18) Jang, E. J.; Lee, J.; Jeong, H. Y.; Kwak, J. H. Controlling the acid-base properties of alumina for stable PtSn-based propane dehydrogenation catalysts. *Appl. Catal. A* **2019**, *572*, 1–8.

(19) Karim, W.; Spreafico, C.; Kleibert, A.; Gobrecht, J.; VandeVondele, J.; Ekinci, Y.; van Bokhoven, J. A. Catalyst support effects on hydrogen spillover. *Nature* **2017**, *541* (7635), 68–71.

(20) Sinfelt, J. H. Catalysis by alloys and bimetallic clusters. *Acc. Chem. Res.* **1977**, *10* (1), 15–20.

(21) Yu, W.; Porosoff, M. D.; Chen, J. G. Review of Pt-based bimetallic catalysis: from model surfaces to supported catalysts. *Chem. Rev.* **2012**, *112* (11), 5780–5817.

(22) Burch; R. Platinum-tin reforming catalysts I. The oxidation state of tin and the interaction between platinum and tin. *J. Catal.* **1981**, *71* (2), 348–359.

(23) Rocherfort, A. Particle size effect in supported platinum: Methylcyclohexane dehydrogenation. *J. Catal.* **1992**, *138* (2), 482–490.
(24) Antos, G. J.; Aitani, A. M., Eds. *Catalytic naphtha reforming*, 2nd ed., rev. and expanded.; Chemical industries, Vol. 100; Marcel Dekker, 2004.
(25) Marceau, E.; Carrier, X.; Che, M. Impregnation and Drying. In *Synthesis of solid catalysts*; Jong, K. P. de, Ed.; Wiley-VCH, 2009; pp 59–82.
(26) García-Sánchez, J. T.; Baldovino-Medrano, V. G. Elements of the Manufacture and Properties of Technical Catalysts. *Ind. Eng. Chem. Res.* **2023**.
(27) Shelimov, B.; Lambert, J. F.; Che, M.; Didillon, B. Initial Steps of the Alumina-Supported Platinum Catalyst Preparation: A Molecular Study by 195Pt NMR, UV–Visible, EXAFS, and Raman Spectroscopy. *J. Catal.* **1999**, *185* (2), 462–478.
(28) Digne, M.; Raybaud, P.; Sautet, P.; Guillaume, D.; Toulhoat, H. Atomic scale insights on chlorinated gamma-alumina surfaces. *J. Am. Chem. Soc.* **2008**, *130* (33), 11030–11039.
(29) Berdala, J., Freund, E., Lynch J. P. Environment of platinum atoms in a H2 PtCl6/Al2O3 catalyst : Influence of metal loading and chlorine content. *J. Phys. Colloques* **1986**, *47* (C8), C8-269-C8-272.
(30) Franck, J. P.; Martino, G. Deactivation and Regeneration of Catalytic-Reforming Catalysts. In *Figueiredo (Ed.) – Progress in Catalyst Deactivation*; pp 355–397.
(31) Le Normand, F.; Borgna, A.; Garetto, T. F.; Apesteguia, C. R.; Moraweck, B. Redispersion of Sintered Pt/Al 2 O 3 Naphtha Reforming Catalysts: An in Situ Study Monitored by X-ray Absorption Spectroscopy. *J. Phys. Chem.* **1996**, *100* (21), 9068–9076.
(32) Morgan, K.; Goguet, A.; Hardacre, C. Metal Redispersion Strategies for Recycling of Supported Metal Catalysts: A Perspective. *ACS Catal.* **2015**, *5* (6), 3430–3445.
(33) Svintsitskiy, D. A.; Kibis, L. S.; Stadnichenko, A. I.; Slavinskaya, E. M.; Romanenko, A. V.; Fedorova, E. A.; Stonkus, O. A.; Doronkin, D. E.; Marchuk, V.; Zimina, A.; Casapu, M.; Grunwaldt, J. D.; Boronin, A. I. Insight into the Nature of Active Species of Pt/Al 2 O 3 Catalysts for low Temperature NH 3 Oxidation. *ChemCatChem* **2020**, *12* (3), 867–880.
(34) Marceau, E.; Lauron-Pernot, H.; Che, M. Influence of the Metallic Precursor and of the Catalytic Reaction on the Activity and Evolution of Pt(Cl)/δ-Al2O3 Catalysts in the Total Oxidation of Methane. *J. Catal.* **2001**, *197* (2), 394–405.
(35) Marceau, E.; Che, M.; Saint-Just, J.; Tatibouët, J. M. Influence of chlorine ions in Pt/A12O3 catalysts for methane total oxidation. *Catal. Today* **1996**, *29* (1-4), 415–419.
(36) Gracia, F. J.; Miller, J. T.; Kropf, A. J.; Wolf, E. E. Kinetics, FTIR, and Controlled Atmosphere EXAFS Study of the Effect of Chlorine on Pt-Supported Catalysts during Oxidation Reactions. *J. Catal.* **2002**, *209* (2), 341–354.
(37) Yao, H.; Sieg, M.; Plummerjr, H. Surface interactions in the Pt/-AlO system. *J. Catal.* **1979**, *59* (3), 365–374.
(38) Dessal, C.; Len, T.; Morfin, F.; Rousset, J. L.; Aouine, M.; Afanasiev, P.; Piccolo, L. Dynamics of Single Pt Atoms on Alumina during CO Oxidation Monitored by Operando X-ray and Infrared Spectroscopies. *ACS Catal.* **2019**, *9* (6), 5752–5759.
(39) Dessal, C.; Sangnier, A.; Chizallet, C.; Dujardin, C.; Morfin, F.; Rousset, J. L.; Aouine, M. Bugnet, M.; Afanasiev, P.; Piccolo, L. Atmosphere-dependent stability and mobility of catalytic Pt single atoms and clusters on γ-Al2O3. *Nanoscale* **2019**, *11* (14), 6897–6904.
(40) Bradley, S. A.; Sinkler, W.; Blom, D. A.; Bigelow, W.; Voyles, P. M.; Allard, L. F. Behavior of Pt Atoms on Oxide Supports During Reduction Treatments at Elevated Temperatures, Characterized by Aberration Corrected Stem Imaging. *Catal. Lett.* **2012**, *142* (2), 176–182.
(41) Lee, J.; Jang, E. J.; Oh, D. G.; Szanyi, J.; Kwak, J. H. Morphology and size of Pt on Al2O3: The role of specific metal-support interactions between Pt and Al2O3. *J. Catal.* **2020**, *385*, 204–212.
(42) Fialho Batista, A. T. Atomic scale insight into platinum based catalysts supported on chlorinated gamma-alumina. Ph.D., IFP Energies nouvelles, 2016-2019.
(43) Lambert, J. F.; Marceau, E.; Shelimov, B.; Lehman, J.; Le Bel de Penguilly, V.; Carrier, X.; Boujday, S.; Pernot, H.; Che, M. Thermal chemistry of oxide-supported platinum catalysts: A comparative study. *Stud. Sci. Surf. Catal.* **2000**, *130*, 1043–1048.

(44) Mordente, M. G. V.; Rochester, C. H. Infrared study of the effects of oxychlorination on Pt dispersion in Pt/Al2O3 catalysts. *J. Chem. Soc., Faraday Trans. 1* **1989**, *85* (10), 3495.
(45) Zhou, Y.; Wood, M.; Winograd, N. A time-of-flight SIMS study of the chemical nature of highly dispersed Pt on alumina. *J. Catal.* **1994**, *146* (1), 82–86.
(46) Lieske, H. Reactions of platinum in oxygen- and hydrogen-treated Pt/gamma;-Al2O3 catalysts I. Temperature-programmed reduction, adsorption, and redispersion of platinum. *J. Catal.* **1983**, *81* (1), 8–16.
(47) Lietz, G. Reactions of platinum in oxygen- and hydrogen-treated Pt/gamma;-Al2O3 catalysts II. Ultraviolet-visible studies, sintering of platinum, and soluble platinum. *J. Catal.* **1983**, *81* (1), 17–25.
(48) Cholley, T. Etude de la redispersion de phase bimétallique à base de platine supportées sur alumine chlorée ou neutralisée. PhD, IFP Energies nouvelles, 1997.
(49) Kohn, W.; Sham, L. J. Self-Consistent Equations Including Exchange and Correlation Effects. *Phys. Rev.* **1965**, *140* (4A), A1133-A1138.
(50) Hohenberg, P.; Kohn, W. Inhomogeneous Electron Gas. *Phys. Rev.* **1964**, *136* (3B), B864-B871.
(51) Chizallet, C.; Raybaud, P. Density functional theory simulations of complex catalytic materials in reactive environments: beyond the ideal surface at low coverage. *Catal. Sci. Technol.* **2014**, *4* (9), 2797–2813.
(52) Chizallet, C. Achievements and Expectations in the Field of Computational Heterogeneous Catalysis in an Innovation Context. *Top. Catal.* **2022**, *65* (1-4), 69–81.
(53) Shahrokhi, M.; Chizallet, C.; Loffreda, D.; Raybaud, P. Stability of Pt 10 Sn 3 Clusters Supported on γ-Al 2 O 3 in Oxidizing Environment: a DFT Comparison of Alloying and Size Effects. *ChemCatChem* **2022**, *14* (23).
(54) Sangnier, A.; Matrat, M.; Nicolle, A.; Dujardin, C.; Chizallet, C. Multiscale Approach to the Dissociative Adsorption of Oxygen on a Highly Dispersed Platinum Supported on γ-Al 2 O 3. *J. Phys. Chem. C* **2018**, *122* (47), 26974–26986.
(55) Hellier, A.; Chizallet, C.; Raybaud, P. PtOxCly(OH)z(H2O)n Complexes under Oxidative and Reductive Conditions: Impact of the Level of Theory on Thermodynamic Stabilities. *ChemphysChem* **2023**, 24, e202200711. Published Online: Oct. 10, 2022.
(56) Zhou, X.; Zhang, Y.; Wang, J. DFT study on the regeneration of Pt/γ-Al2O3 catalyst: The effect of chlorine on the redispersion of metal species. *Appl. Surf. Sci.* **2021**, *545*, 148988.
(57) Proux, O.; Lahera, E.; Del Net, W.; Kieffer, I.; Rovezzi, M.; Testemale, D.; Irar, M.; Thomas, S.; Aguilar-Tapia, A.; Bazarkina, E. F.; Prat, A.; Tella, M.; Auffan, M.; Rose, J.; Hazemann, J. L. High-Energy Resolution Fluorescence Detected X-Ray Absorption Spectroscopy: A Powerful New Structural Tool in Environmental Biogeochemistry Sciences. *J. Environ. Qual.* **2017**, *46* (6), 1146–1157.
(58) Ravel, B.; Newville, M. ATHENA, ARTEMIS, HEPHAESTUS: data analysis for X-ray absorption spectroscopy using IFEFFIT. *J. Synchrotron Radiat.* **2005**, *12* (Pt 4), 537–541. Published Online: Jun. 15, 2005.
(59) Kresse, G.; Hafner, J. Ab initio molecular-dynamics simulation of the liquid-metal-amorphous-semiconductor transition in germanium. *Phys. Rev. B* **1994**, *49* (20), 14251–14269.
(60) Kresse, G.; Furthmüller, J. Efficiency of ab-initio total energy calculations for metals and semiconductors using a plane-wave basis set. *Comput. Mater. Sci.* **1996**, *6* (1), 15–50.
(61) Perdew, J. P.; Burke, K.; Ernzerhof, M. Generalized Gradient Approximation Made Simple. *Phys. Rev. Lett.* **1996**, *77* (18), 3865–3868. DOI: 10.1103/PhysRevLett.77.3865.
(62) Steinmann, S. N.; Corminboeuf, C. A generalized-gradient approximation exchange hole model for dispersion coefficients. *J. Chem. Phys.* **2011**, *134* (4), 44117.
(63) Steinmann, S. N.; Corminboeuf, C. Comprehensive Benchmarking of a Density-Dependent Dispersion Correction. *J. Chem. Theory Comput.* **2011**, *7* (11), 3567–3577. Published Online: Oct. 18, 2011.
(64) Kresse, G.; Joubert, D. From ultrasoft pseudopotentials to the projector augmented-wave method. *Phys. Rev. B* **1999**, *59* (3), 1758–1775.

(65) Hirshfeld, F. L. Bonded-atom fragments for describing molecular charge densities. *Theoret. Chim. Acta* **1977**, *44* (2), 129–138.
(66) Heyd, J.; Scuseria, G. E. Efficient hybrid density functional calculations in solids: assessment of the Heyd-Scuseria-Ernzerhof screened Coulomb hybrid functional. *J. Chem. Phys.* **2004**, *121* (3), 1187–1192.
(67) Heyd, J.; Scuseria, G. E.; Ernzerhof, M. Hybrid functionals based on a screened Coulomb potential. *J. Chem. Phys.* **2003**, *118* (18), 8207–8215.
(68) Krukau, A. V.; Vydrov, O. A.; Izmaylov, A. F.; Scuseria, G. E. Influence of the exchange screening parameter on the performance of screened hybrid functionals. *J. Chem. Phys.* **2006**, *125* (22), 224106.
(69) Digne, M.; Sautet, P.; Raybaud, P.; Euzen, P.; Toulhoat, H. Hydroxyl Groups on γ-Alumina Surfaces: A DFT Study. *J. Catal.* **2002**, *211* (1), 1–5.
(70) Digne, M. Use of DFT to achieve a rational understanding of acid basic properties of gamma-alumina surfaces. *J. Catal.* **2004**, *226* (1), 54–68.
(71) Krokidis, X.; Raybaud, P.; Gobichon, A. E.; Rebours, B.; Euzen, P.; Toulhoat, H. Theoretical Study of the Dehydration Process of Boehmite to γ-Alumina. *J. Phys. Chem. B* **2001**, *105* (22), 5121–5130.
(72) Pigeon, T.; Chizallet, C.; Raybaud, P. Revisiting γ-alumina surface models through the topotactic transformation of boehmite surfaces. *J. Catal.* **2022**, *405*, 140–151.
(73) Bunău, O.; Joly, Y. Self-consistent aspects of x-ray absorption calculations. *J. Phys.: Condens. Matter* **2009**, *21* (34), 345501. Published Online: Aug. 5, 2009.
(74) Bunău, O.; Ramos, A. Y.; Joly, Y. The FDMNES code. *International tables for crystallography - X-ray Absorption* **2021**, *I*.
(75) Hedin, L.; Lundqvist, B. I. Explicit local exchange-correlation potentials. *J. Phys. C: Solid State Phys.* **1971**, *4* (14), 2064–2083. DOI: 10.1088/0022-3719/4/14/022.
(76) Joly, Y. X-ray absorption near-edge structure calculations beyond the muffin-tin approximation. *Phys. Rev. B* **2001**, *63* (12).
(77) Diamond, S.; Boyd, S. CVXPY: A Python-Embedded Modeling Language for Convex Optimization. *JMLR* **2016**, *17*.
(78) Agrawal, A.; Verschueren, R.; Diamond, S.; Boyd, S. A rewriting system for convex optimization problems. *JCD* **2018**, *5* (1), 42–60.
(79) Muñoz, M.; Argoul, P.; Farges, F. Continuous Cauchy wavelet transform analyses of EXAFS spectra: A qualitative approach. *Am. Min.* **2003**, *88* (4), 694–700.
(80) Oudenhuijzen, M. K.; Bitter, J. H.; Koningsberger, D. C. The Nature of the Pt−H Bonding for Strongly and Weakly Bonded Hydrogen on Platinum. A XAFS Spectroscopy Study of the Pt−H Antibonding Shaperesonance and Pt−H EXAFS. *J. Phys. Chem. B* **2001**, *105* (20), 4616–4622.
(81) Munoz-Paez, A.; Koningsberger, D. C. Decomposition of the Precursor [Pt(NH3)4](OH)2, Genesis and Structure of the Metal-Support Interface of Alumina Supported Platinum Particles: A Structural Study Using TPR, MS, and XAFS Spectroscopy. *J. Phys. Chem.* **1995**, *99* (12), 4193–4204.
(82) Mei, D.; Kwak, J. H.; Hu, J.; Cho, S. J.; Szanyi, J.; Allard, L. F.; Peden, C. H. F. Unique Role of Anchoring Penta-Coordinated Al 3+ Sites in the Sintering of γ-Al 2 O 3 -Supported Pt Catalysts. *J. Phys. Chem. Lett.* **2010**, *1* (18), 2688–2691.
(83) Cui, X.; Junge, K.; Dai, X.; Kreyenschulte, C.; Pohl, M. M.; Wohlrab, S.; Shi, F.; Brückner, A.; Beller, M. Synthesis of Single Atom Based Heterogeneous Platinum Catalysts: High Selectivity and Activity for Hydrosilylation Reactions. *ACS central science* **2017**, *3* (6), 580–585.
(84) Raybaud, P.; Digne, M.; Iftimie, R.; Wellens, W.; Euzen, P.; Toulhoat, H. Morphology and Surface Properties of Boehmite (γ-AlOOH): A Density Functional Theory Study. *J. Catal* **2001**, *201* (2), 236–246.
(85) Borgna, A.; Le Normand, F.; Garetto, T.; Apesteguia, C. R.; Moraweck, B. Sintering of Pt/Al2O3 reforming catalysts: EXAFS study of the behavior of metal particles under oxidizing atmosphere. *Catal. Lett.* **1992**, *13* (3), 175–188.
(86) Lagarde, P. EXAFS studies of Pt/Al2O3 catalysts. *J. Catal.* **1983**, *84* (2), 333–343.

(87) Li, G. G.; Bridges, F.; Booth, C. H. X-ray-absorption fine-structure standards: A comparison of experiment and theory. *Phys. Rev. B* **1995**, *52* (9), 6332–6348.

IV.7. Supporting Information

SI 1. Pt powder and PtO_2 references. EXAFS.

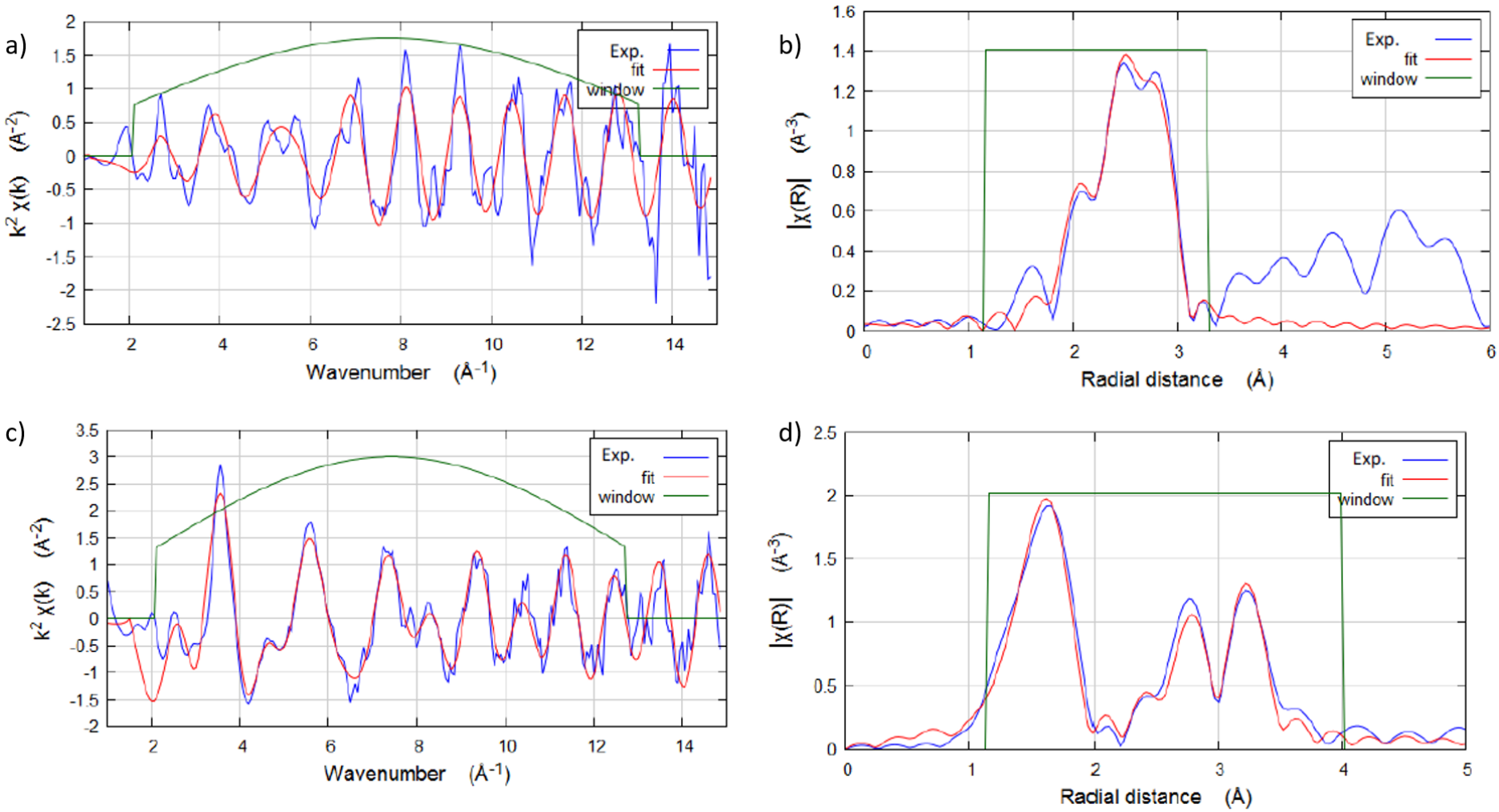

Figure SIV-1. EXAFS and magnitude of the Fourier Transform weighted by k^2 of the references Pt powder (a, b) and PtO2 (c, d) (acquired in 2018 at BM16).

	Path origin*	Path	Coordination number**	R (Å)	σ^2 (Å^2)	S_0^2	ΔE_0	R-factor	N_{ind}	N_{par}
PtO_2 (2017)	PtO_2 (1530633)	P-O (1)	6	2.013±0.006	0.002±0.002	0.89±0.04	9.93±0.76	0.02	18	10
	PtO_2 (1537410)	Pt-Pt	6	3.102±0.006	0.002±0.001					
		Pt-O (2)	6	3.66±0.03	0.004±0.006					
		Pt-O (3)	6	4.04±0.04	0.01±0.01					
PtO_2 (2018)	PtO_2 (1530633)	P-O (1)	6	2.009±0.008	0.003±0.002	0.86±0.05	8.65±0.94	0.02	18	12
	PtO_2 (1537410)	Pt-Pt	6	3.100±0.010	0.002±0.001					
		Pt-O (2)	6	3.67±0.05	0.003±0.007					
		Pt-O (3)	6	3.6±0.1	0.01±0.02					
		Pt-O (4)	6	4.05±0.08	0.02±0.02					

Table SIV-1. EXAFS fitting of reference corresponding to the red line on the figure above. *Crystallographic structure ID in parenthesis; **Coordination number is fixed

SI 2. (100) surface

We considered a 2x3 supercells with respect to the Digne's unit cell[1] (**Figure SIV-2**). The slab considered is made of four alumina layers and the first two layers were relaxed during geometry optimizations (**Figure SIV-2**).

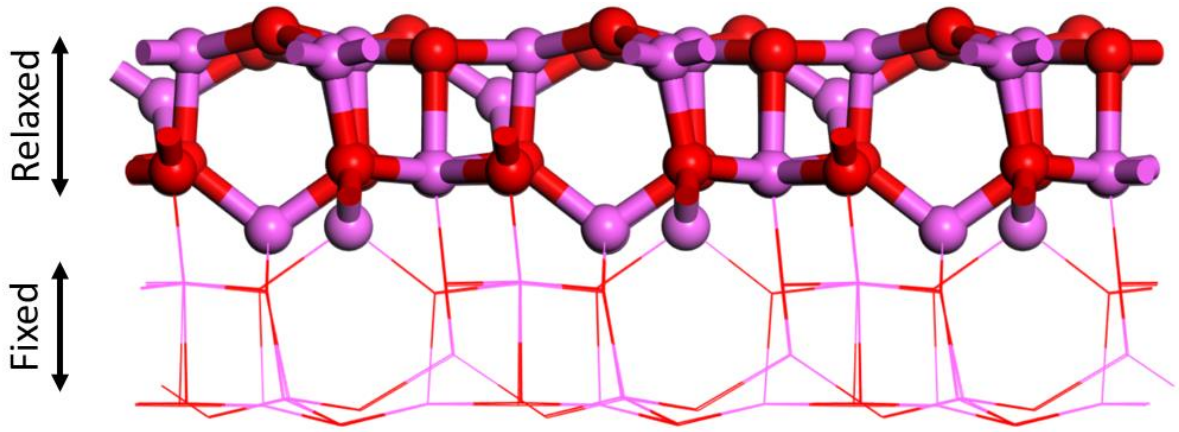

Figure SIV-2. Side view of the molecular model of the (100) surface of γ-Al_2O_3. [‡]). Color code for atomic structures: O: red; Al: pink.

SI 3. Scanning transmission electron microscopy.

High resolution high angle annular dark field in scanning transmission electron microscopy (HR-HAADF-STEM) imaging, HAADF-STEM *in situ* reduction experiments and HAADF-STEM electron tomography analyses were carried out on a Cs-corrected JEOL JEM 2100F microscope, operated at 200kV, equipped with a JEOL HAADF detector. For the HR-STEM images, the camera length used in the HAADF mode was 10 cm, corresponding to inner and outer diameters of the annular detector of 60 and 160 mrad, respectively. The size of the electron probe in STEM mode is 0.11 nm. Before the STEM analyses, the powdered samples were deposited without solvent on a 300 mesh holey carbon copper grid.

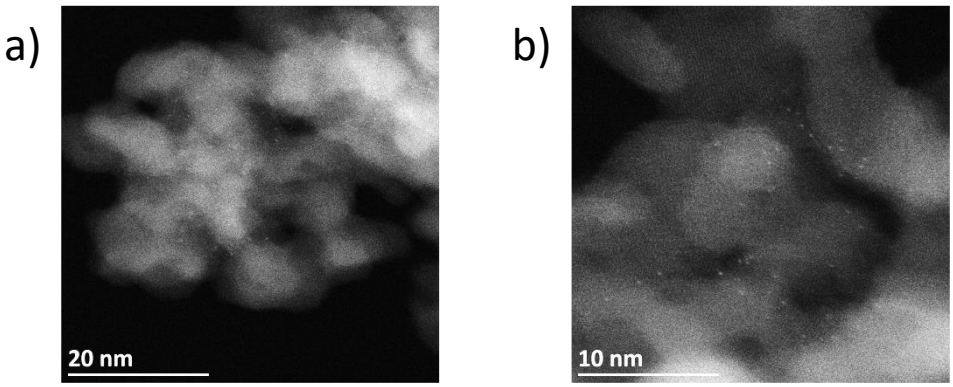

Figure SIV-3. HR-HAADF-STEM images of Pt oxychloride supported on γ-alumina 0.3 (Pt wt% over PuralSB3-1.4 wt%Cl).

SI 4. Structural and electronic properties of the various Pt complexes.

Stoichiometry	d(Pt-O_{surf}) (Å)	d(Pt-Cl) (Å)	d(Pt-OH) (Å)	d(Pt-O) (Å)	d(Pt-OH_2) (Å)	Pt charge (e)	Ligands charge (e)	Surface charge (e)	Grafting mode
PtO_2	2.07 2.15			1.79 1.94		0.580	-0.656	0.075	2
$PtOCl_2$	2.08	2.24 2.26		1.86		0.490	-0489	0.002	1
PtOCl(OH)	2.05	2.24	1.96	1.85		0.543	-0.515	-0.026	1
$PtO(OH)_2$	2.05		1.91 1.98	1.84		0.604	-0.458	-0.148	1
$PtCl_4$	2.11	2.26 2.28 2.29 2.32				0.498	-0.285	-0.216	1
$PtCl_3(OH)$	2.00	2.23 2.28 2.34	2.05			0.543	-0.488	-0.05	1
$PtCl_2(OH)_2$	2.04	2.27 2.27	2.01 2.04			0.621	-0.387	-0.234	1
$PtCl(OH)_3$	1.98	2.23	2.00 2.04 2.04			0.637	-0.372	-0.266	1
$Pt(OH)_4$	1.97		1.90 2.00 2.03 2.05			0.684	-0.355	-0.331	1
$PtCl_4(OH)H$*	2.11	1.90 2.00 2.03 2.05	2.07			0.493	-0.466	-0.039	1
$PtCl_3(OH)_2H$*	2.09	2.28 2.29 2.30	2.05 2.06			0.537	-0.508	-0.035	1
$PtCl_2(OH)_2(H_2O)$	2.05	2.29 2.30	2.01 2.04		2.05	0.597	-0.368	-0.228	1
$PtCl(OH)_3(H_2O)$	2.02	2.30	2.00 2.01 2.03		2.05	0.643	-0.356	-0.283	1
$Pt(OH)_4(H_2O)$	2.04	1.99 2.00 2.02 2.03			2.05	0.683	-0.382	-0.299	1

Table SIV-2. Geometric description and platinum charge of supported complexes. Ligands charge is the sum of the Hirshfeld charges of all ligands. Surface charge is the sum of all the Hirshfeld charges of aluminum and oxygen of the surface. Grafting refers to the number of bonds between Pt and the O of the alumina support. The choice was made to keep for a given stoichiometry only the most stable isomer. This means that for systems containing H_2O sometimes the formation of hydrides or hydroxyls in place of a previously oxygen atom could be observed. Due to the acidic nature of the Al_2O_3 surface, protons could also be adsorbed on the surface oxygen atoms to form surface hydroxyls. Exponent will be used to differentiate these structures.

SI 5. Thermodynamic diagram for calcination. Impact of H_2O and HCl at fixed calcination temperature. Calculated at the PBE-dDsC level.

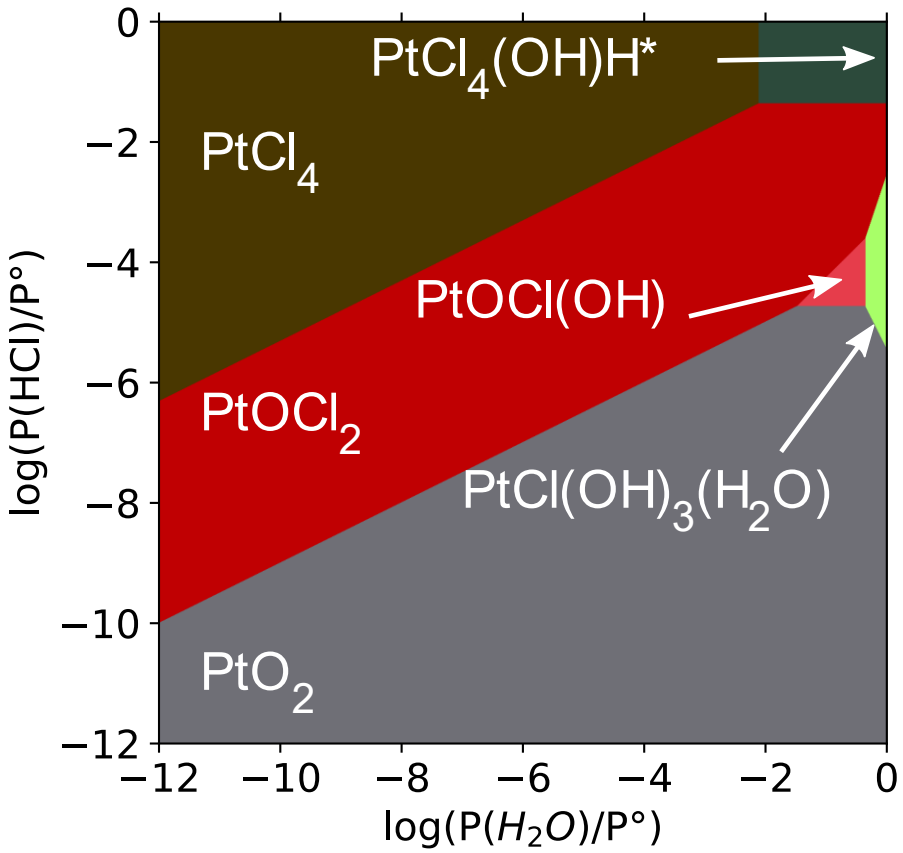

Figure SIV-4. Thermodynamic diagrams of the most stable species under oxidative conditions at T = 800 K.

SI 6. Calcination and reduction thermodynamic diagrams calculated at the HSE06 level.

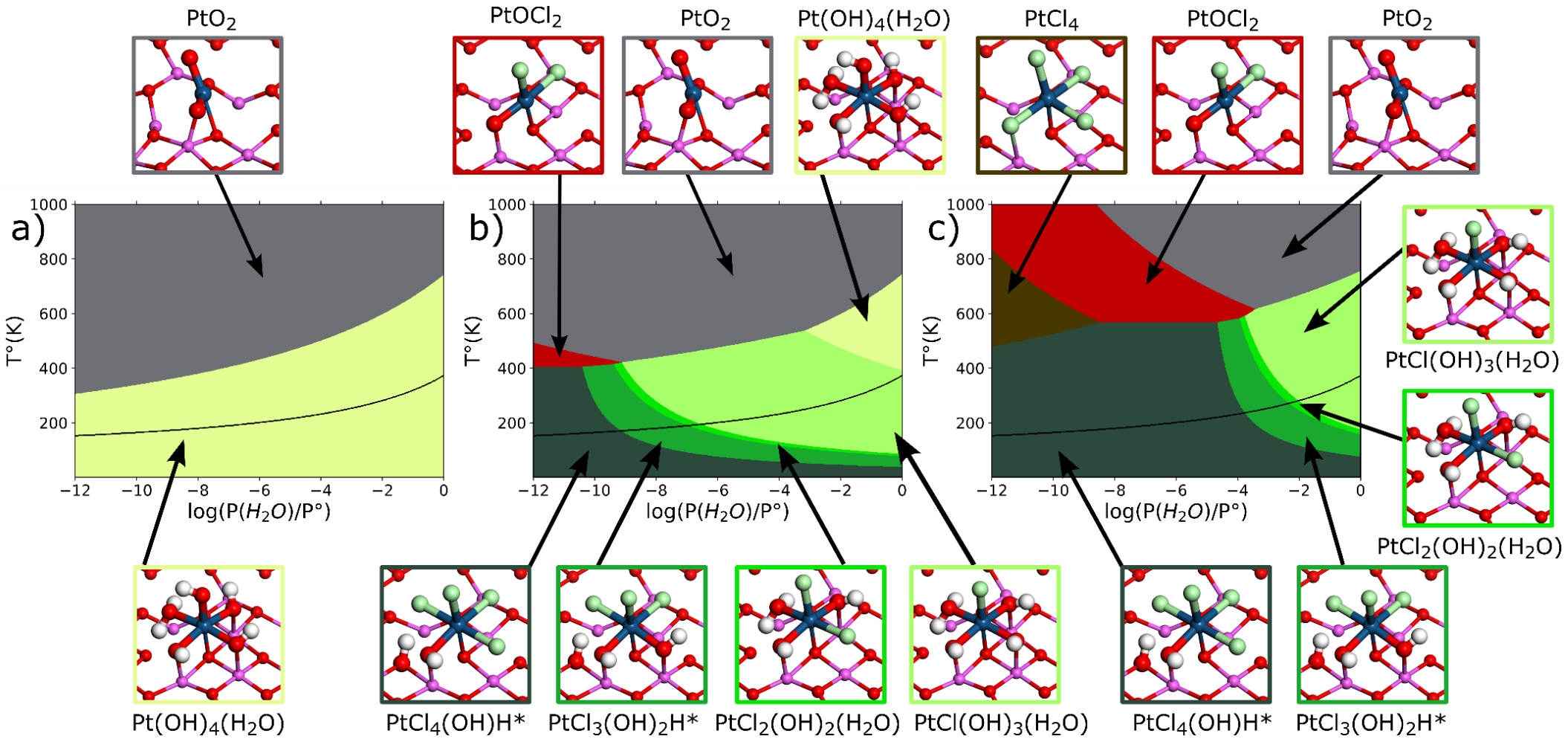

Figure SIV-5. Thermodynamic diagrams calculated at the HSE06 level of the most stable species under oxidative conditions at $P(O_2)$ = 0.21 bar for three chlorine loadings: a) Without chlorine; b) P(HCl) = 1.10^{-12} bar; c) P(HCl) = 1.10^{-6} bar. The gas phase domain of water is located above the black curved line, representing the liquid/vapor equilibrium. Atoms' colours are blue for Platinum, red for oxygen, green for chlorine, pink for aluminum and white for hydrogen.

SI 7. Energetics

Pt^{IV}	ΔE (kJ/mol)
Ligand Exchange	
$PtCl_4 + H_2O \rightarrow PtCl_3(OH) + HCl$	13.7
$PtCl_3(OH) + H_2O \rightarrow PtCl_2(OH)_2 + HCl$	21.4
$PtCl_2(OH)_2 + H_2O \rightarrow PtCl(OH)_3 + HCl$	23.9
$PtCl(OH)_3 + H_2O \rightarrow Pt(OH)_4 + HCl$	46.1
$PtCl_4(OH)H^* + H_2O \rightarrow PtCl_3(OH)_2H^* + HCl$	17.0
$PtCl_3(OH)_2H^* + H_2O \rightarrow PtCl_2(OH)_2(H_2O) + HCl$	20.0
$PtCl_2(OH)_2(H_2O) + H_2O \rightarrow PtCl(OH)_3(H_2O) + HCl$	29.8
$PtCl(OH)_3(H_2O) + H_2O \rightarrow Pt(OH)_4(H_2O) + HCl$	89.9
$PtOCl_2 + H_2O \rightarrow PtOCl(OH) + HCl$	42.3
$PtOCl(OH) + H_2O \rightarrow PtO(OH)_2 + HCl$	64.9
MAV	**36.9**
Hydration	
$PtCl_4 + H_2O \rightarrow PtCl_4(OH)H^*$	-196.0
$PtCl_3(OH) + H_2O \rightarrow PtCl_3(OH)_2H^*$	-193.1
$PtCl_2(OH)_2 + H_2O \rightarrow PtCl_2(OH)_2(H_2O)$	-194.3
$PtCl(OH)_3 + H_2O \rightarrow PtCl(OH)_3(H_2O)$	-188.4
$Pt(OH)_4 + H_2O \rightarrow Pt(OH)_4(H_2O)$	-144.7
$PtOCl_2 + H_2O \rightarrow PtCl_2(OH)_2$	-108.4
$PtOCl(OH) + H_2O \rightarrow PtCl(OH)_3$	-126.9
$PtO(OH)_2 + H_2O \rightarrow Pt(OH)_4$	-145.6
$PtO_2 + H_2O \rightarrow PtO(OH)_2$	-106.6
MAV	**-156.0**

Table SIV-3. Reaction energies for various type of reaction calculated at 0 K and ranked according to an increasing charge on Pt.

SI 8. Interaction Energies

Various quantities such as the interaction energy, adsorption energy, complex deformation energy and surface deformation energy were determined at 0 K (without zero-point energy correction). Interaction energy describes how strongly complexes interact with the support and were calculated according to **Eq.(1)**. The complex deformation energy is the destabilization resulting of the adsorption of the complex, it was calculated according to **Eq.(2)**. Similarly, the deformation of the surface was calculated according to **Eq.(3)**. Finally, the adsorption energy which describes the adsorption of a complex on the support by accounting of the interaction energy but also of the deformations induced by the adsorption was calculated according to **Eq.(4)**.

$$E^{int} = E_{system} - E'_{complex} - E'_{surface} \quad \textbf{Eq.S1}$$

$$E^{def}_{complex} = E'_{complex} - E_{complex} \quad \textbf{Eq.S2}$$

$$E^{def}_{surface} = E'_{surface} - E_{surface} \quad \textbf{Eq.S3}$$

$$E^{ads} = E^{int} - E^{def}_{complex} - E^{def}_{system} \quad \textbf{Eq.S4}$$

With E_{system} being the energy of the system (adsorbed complex + support), $E'_{complex}$ is the energy of the complex in gas phase with the same geometry and spin state as in the absorbed state. $E_{complex}$ is the energy of the complex after geometry and spin state optimization in gas phase. Similarly, $E'_{surface}$ is the energy of the surface without the complex adsorbed and for the geometry optimized after adsorption and $E_{surface}$ is the energy of the naked optimized surface. The spin state of the surface was considered to be a singlet.

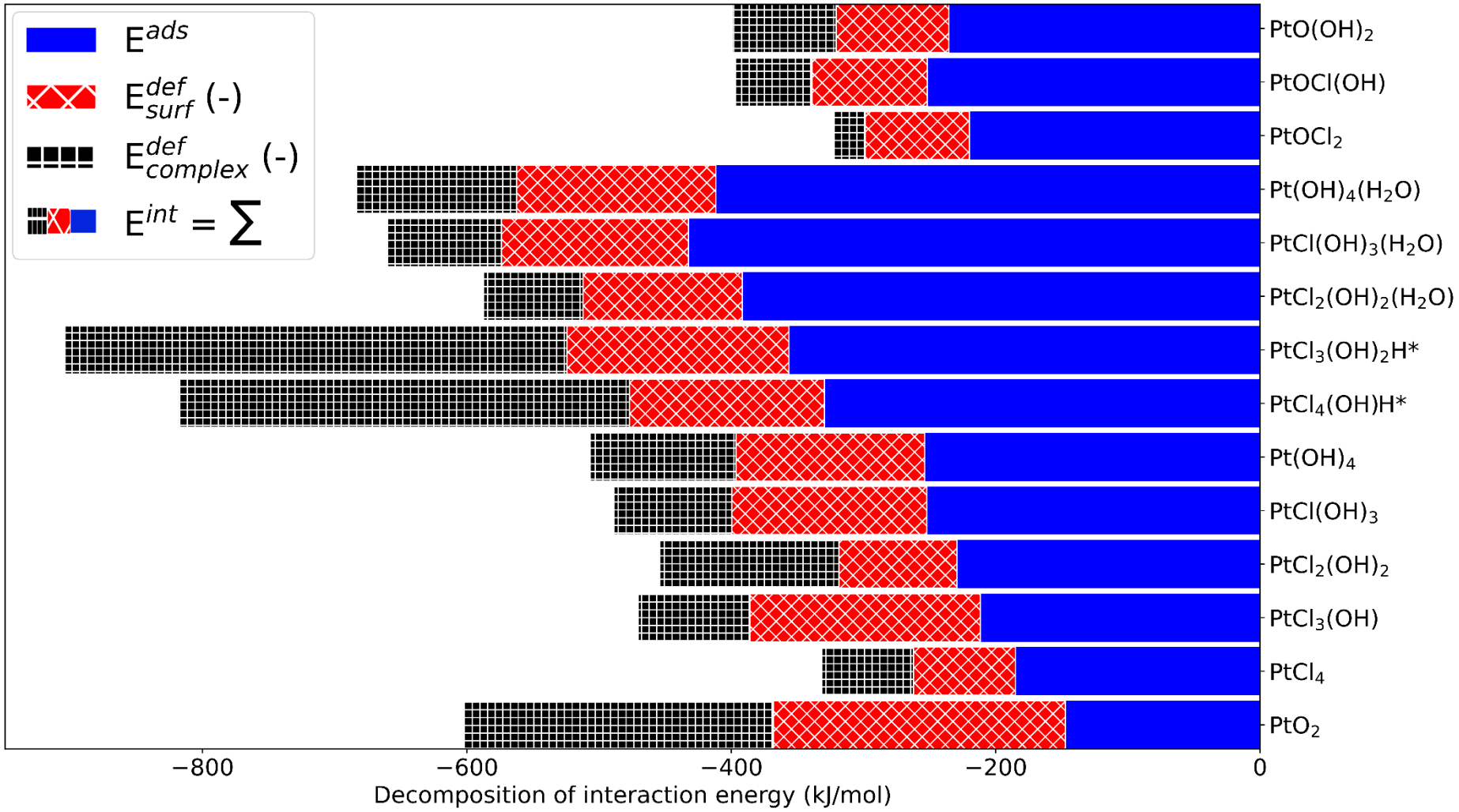

Figure SIV-6. Decomposition of the interaction energy for supported complexes. Both deformations are reported as negative value for the sake of clarity. The interaction energy is the sum of the three quantities: E^{ads} + E^{def} (surf) + E^{def}(complex) as described by Eq.1-3

SI 9. DFT calculated Pt-Al and Pt-O_{long} distances in octahedral platinum complexes

Pt complex	CN(Pt-Al)	Mean d(Pt-Al) (Å)	CN(Pt-O_{long})	Mean d(Pt- O_{long}) (Å)
$PtCl_4(OH)H$*	3	3.16	4	3.70
$PtCl_3(OH)_2H$*	3	3.10	4	3.64
$PtCl_2(OH)_2(H_2O)$	3	3.07	4	3.61
$PtCl(OH)_3(H_2O)$	3	3.00	4	3.56
$Pt(OH)_4(H_2O)$	3	2.99	4	3.55

Table SIV-4. Averaged second shell distances and coordination number (CN) for the octahedral $PtCl_y(OH)_{4-y}(H_2O)$ species

SI 10. FEFF simulation of octahedral $PtCl_y(OH)(H_2O)$.

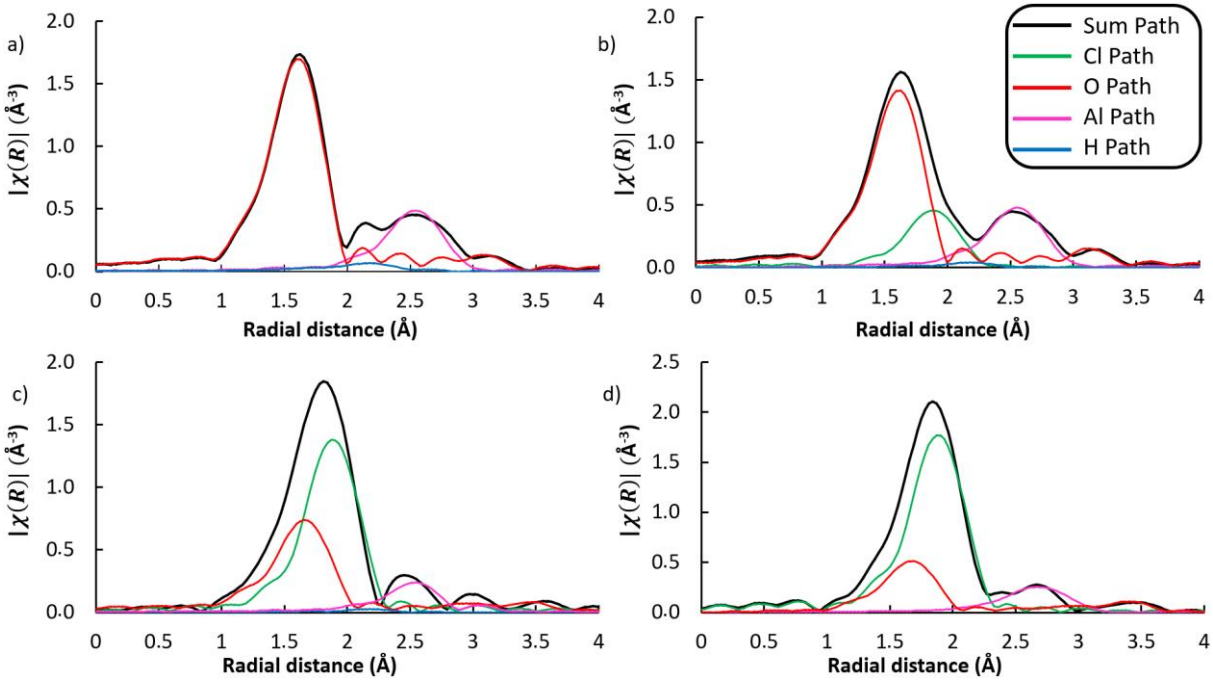

Figure SIV-7. FEFF simulation of the k² weighted magnitude of the Fourier transform (FT). a) $Pt(OH)_4(H_2O)$, b) $PtCl(OH)_3(H_2O)$, c) $PtCl_3(OH)_2H^*$, d) $PtCl_4(OH)H^*$.

SI 11. Details on the XANES analysis of $PtCl_y(OH)_{4-y}(H_2O)$ models

Species	While Line pic (eV)
Reference 0.1% Cl	11568.60
Reference 1.4 %Cl	11568.60
$PtCl_4(OH)H^*$	11568.52
$PtCl_3(OH)_2H^*$	11568.96
$PtCl_2(OH)_2(H_2O)$	11569.57
$PtCl(OH)_3(H_2O)$	11570.35
$Pt(OH)_4(H_2O)$	11571.10

Table SIV-5. Measured and computed energies of the whitelines in XANES.

Energy range	0.1%Cl reference	1.4%Cl reference
Full	17 % $PtCl_2(OH)_2(H_2O)$ 31 % $PtCl_3(OH)_2H^*$ 52 % $PtCl_4(OH)H^*$	9 % $PtCl_2(OH)_2(H_2O)$ 13 % $PtCl_3(OH)_2H^*$ 78 % $PtCl_4(OH)H^*$
11575-11640	39 % $PtCl_2(OH)_2(H_2O)$ 32 % $PtCl_3(OH)_2H^*$ 29 % $PtCl_4(H_2O)$	1% $PtCl_3(OH)_2H^*$ 99 % $PtCl_4(OH)H^*$
11575-11585	27 % $PtCl_2(OH)_2(H_2O)$ 73 % $PtCl_3(OH)_2H^*$	10 % $PtCl_3(OH)_2(H_2O)$ 90 % $PtCl_4(OH)H^*$

Table SIV-6. Contributions of the individual computed spectra in the fit of the two experimental spectra. Three range of energies are used to produce three different fitted spectra.

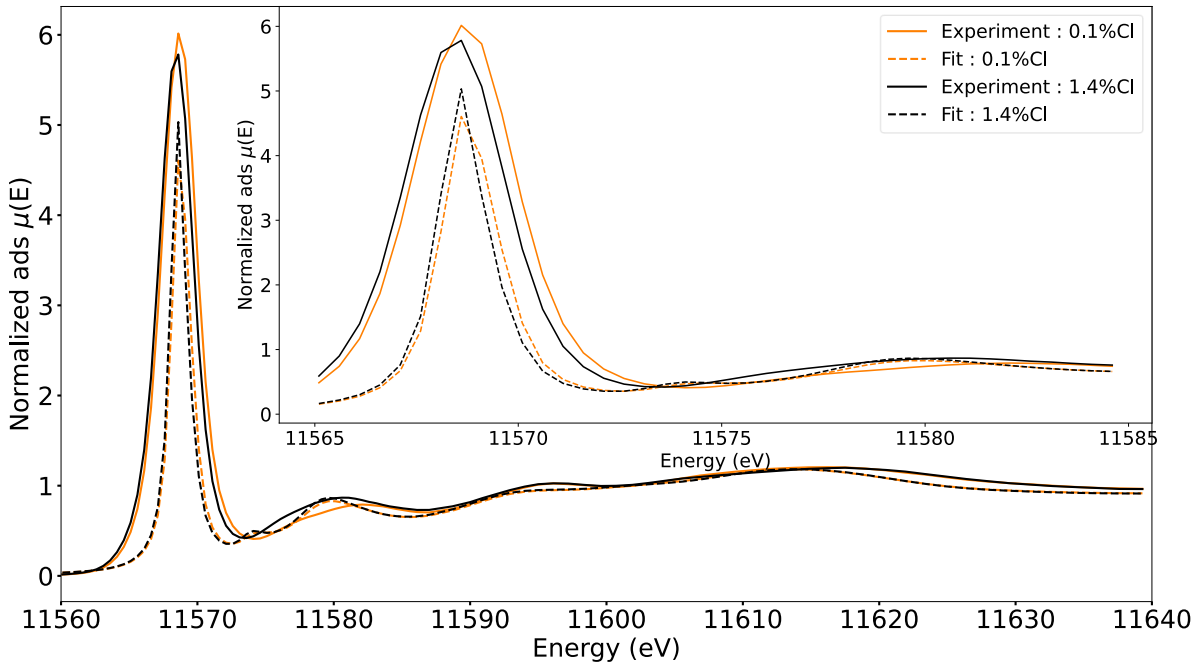

Figure SIV-8. Pt L_3 XANES fitted spectra obtained from the $PtCl_y(OH)_{4-y}(H_2O)$. Reference are the calcinated catalysts obtained for 0.1% Cl loading (pink) and 1.4% Cl loading (black). The full range of energies was used to fit the spectra. Composition of the fitted spectra are Table SIV-6.

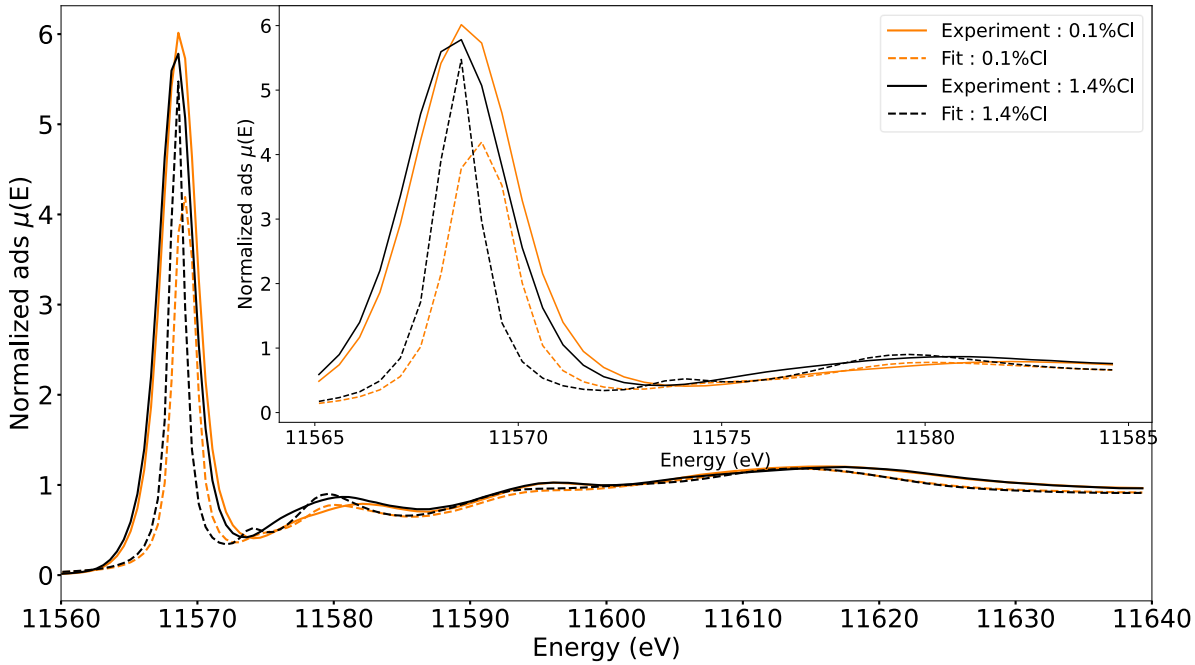

Figure SIV-9. Pt L₃ XANES fitted spectra obtained from the $PtCl_y(OH)_{4-y}(H_2O)$. Reference are the calcinated catalysts obtained for 0.1% Cl loading (pink) and 1.4% Cl loading (black). Only energies superior to 11575 eV were used to fit the spectra, excluding the WL. Composition of the fitted spectra are Table SIV-6.

Through the fit over the full range of energies (**Figure SIV-8**), we estimate that the 0.1%Cl loading reference is composed of 17% of $PtCl_2(OH)_2(H_2O)$, 31% of $PtCl_3(OH)_2H$* and 52% of $PtCl_4(OH)H$*, while the composition of the spectra become 10% of $PtCl_2(OH)_2(H_2O)$, 13 % of $PtCl_3(OH)_2H$* with 78 % of $PtCl_4(OH)H$* for the 1.4%Cl loading catalysts. Despite not being in perfect agreement with EXAFS values, the increases of the quantity of Cl is well reproduced going from an average of 3.3 Pt-Cl for the 0.1%Cl reference to 3.7 Pt-Cl for the 1.4%Cl catalyst. Compared to the fit reported in the main text in **Figure IV-11**, the intensity of the WL is slightly worse.

By avoiding the WL area and starting the fit at 11575 eV (**Figure SIV-9**), a new composition is expected with an average of 2.9 Pt-Cl for the 0.1%Cl reference and 4 Pt-Cl for the 1.4%Cl. While less chlorinated platinum complexes are now calculated to be in the fit of the low chlorine reference with 39 % of $PtCl_2(OH)_2(H_2O)$ and only 29 % of $PtCl_4(OH)H$*, only $PtCl_4(OH)$*H is expected in the description of the highly chlorinated spectra.

SI Reference

1. Digne, M., Sautet, P., Raybaud, P., Euzen, P. & Toulhoat, H. Hydroxyl Groups on γ-Alumina Surfaces: A DFT Study. *J. Catal.* **211,** 1–5 (2002).

Chapter V

Genesis of alumina supported platinum catalytic active phase: Chlorine-induced stabilization of platinum single atoms during reduction

---

This chapter focuses on the reduction of supported platinum complexes from a thermodynamic and kinetic perspective. The supporting information of this study can be found at the end of the chapter.

V.1. Introduction

Catalysts are at the center of our chemical industry, by being used in approximatively 72% of all the chemical processes.[1] By allowing new reactivities and by being in line with a more appropriate use of expensive, scarce and limited resources such as the noble metal frequently used in heterogeneous catalysts, single atom catalysts (SAC) appear as an appealing evolution in this area.[1–3] Despite these advantages, SAC often exhibit low stability. Indeed, for thermodynamic reasons SACs tend to sinter especially at high temperature and under H_2 pressure. Such operating conditions are encountered during the preparation steps of catalysts, or in catalytic reaction media.[3] Understanding how one can stabilize supported such single atoms on an oxide support is thus a priority, and one way to achieve it is through a better control of the preparation of these catalysts.

Pt dispersed on gamma-alumina (γ–Al_2O_3) is among the most important supported catalytic systems with numerous applications in refining, petrochemistry, pollution abatement, biomass conversion, plastic recycling, inter alia.[4–10] Most often, platinum clusters are considered, but platinum is also one of the most studied element in the area of SACs[1]. Pt/Al_2O_3 is also a great example on how the control of the genesis of the active phase can lead to better use of resources. Indeed, in 1949, Haensel et al.[11] showed that using a small amount of a noble metal such as Pt in presence of chlorine on Al_2O_3 led to more efficient and cheaper catalysts with respect to noble metal-free catalysts developed at that time for catalytic reforming. Since the seminal report of Haensel et al.[11] many research works have been carried out to improve the efficiency of Pt/Al_2O_3 through use of additional metals[12–15] or support modification.[15–18] But despite the numerous achievements in that regard, the understanding of the evolution of the nature and structure of the platinum species involved in the preparation steps remain incomplete. As a matter of fact, the role of the chlorine usually added in case of naphtha reforming[8,15] and which is of fundamental importance for these systems remains poorly understood.

It is known that the use of chlorine on Pt/Al_2O_3 serves multiple interests such as increasing the acidity of the support,[15,19,20] or enhancing the dispersion of Pt.[21–23] In the end this impacts the catalytic performances.[23–29] However, this impact on the catalytic properties can be either positive, as in the case of catalytic reforming,[28,29] or negative, such as during oxidation reactions[23–26] or reduction of NO[27] where platinum-based catalysts supported over various oxides were found to be less active as long as chlorine was present on the catalyst. The dispersive role of chlorine on the platinum active phase during both the synthesis and regeneration of the catalyst have been highlighted by numerous experimental studies dedicated to the role of Cl on the state of the platinum after its preparation,[21–23,30,31] or regeneration through oxychlorination treatments, which lead to more dispersed Pt.[21,22,30]

Recently it was observed that during the preparation of Pt/γ-Al_2O_3 the increase of the chlorine loading used during preparation was correlated to an augmentation of the number of SA.[21,30] However, and as for many others heterogenous catalysts,[32] the evolution of the supported platinum during its preparation on γ-Al_2O_3 in presence of chlorine is not well understood and the role of chlorine on the dispersion on Pt remain unknown.

In the case of Pt/γ-Al_2O_3-Cl, preparation usually involves several steps[8,33,34] that will impact the state of the active phase of the catalyst. Oxidized platinum complexes are first contacted with the support during the impregnation step. Thermal treatments follow, such as drying to remove water and calcination during which oxidized Pt(IV) are anchored to the surface and changes in its coordination sphere are observed[21,22,35,36]. Finally, the oxidized Pt(IV) species are reduced under H_2 during the reduction step. The high temperature (typically, 773 K) and reductive atmosphere (H_2) favor the aggregation of platinum into clusters of various forms and diameters according to the loading of Pt, the type of surface and the presence of additives. For low Pt loading (≤1 wt.%), it was observed by HR-HAADF-STEM that clustering occurs from 620 K to 970 K[37] and the majority of the observed clusters have diameters comprised between 0.6 and 1.2 nm.[21,37,38] Increasing the Pt loading results in the formation of bigger clusters.[21,38,39] These clusters coexist with smaller entities such as trimers, dimers and single atoms.[21,40] In the absence of chlorine, the presence of single atoms is still debated, some studies reported their presence[40], others their absence[39] which may be due also to the limitations of the characterization techniques.[41] The presence of Pt-Cl bonds after reduction is also debated. While some authors such as Batista et al.[21] or Gracia et al.[26] did not find Pt-Cl bonds by EXAFS after reduction of chlorinated sample, Svinsitsikiy et al.[23] reported the existence of 1.5 Pt-Cl after reduction of chlorinated catalysts and Smolikov et al.[42] proposed the existence of oxidized platinum (+II) with Pt-Cl bonds based on XPS. However, many authors agree that chlorine increases the resistance of Pt against sintering and reduction.[21–23,31] It has been advanced that an electronic depletion of the oxygen from the support due to chlorines lead to stronger Pt-$O_{support}$ which could limit the sintering.[43]

In order to rationalize these observations at the atomic scale, ab initio methods such as the density functional theory[44,45] (DFT) are efficient tools.[46,47] However, while some efforts have been devoted to the proposal of surface models representative of supported platinum species after reduction[39,48–56], almost no ab initio study deals with the mechanism of their formation from supported single atom precursor species. Indeed, investigating the genesis of such supported metallic catalysts at an atomic scale represents a great challenge for DFT methods because it requires to address complex phase transformation mechanisms involving change in chemical composition and oxidation states.[57] One recent example was provided by the DFT study of sulfo-reduction mechanisms of Mo_nO_{3n} oligomers

into Mo_nS_{2n} involving various $Mo_nO_{3n-x}S_x$ or Mo_nS_{3n} intermediates resulting from S/O exchange steps.[58]

However, the study of oxychlorinated Pt species is extremely scarce and to the best of our knowledge only, Zhou et al.[59] considered one oxychlorinated species ($PtCl_2(OH)_2$) supported on γ-Al_2O_3 to exhibit how chlorine could help redispersing platinum through the formation of oxychlorinated Pt species. In **Chapter III** we described the thermodynamic evolution of $PtO_xCl_y(OH)_z(H_2O)_n$ (with $2x+y+z \leq 4$ and $0 \leq n \leq 2$) during calcination and reduction but in the absence of the support. We evaluated the relevance of widely used exchange-correlation functionals for the quantification of reaction energies during these two preparation steps.[60] We showed that the use of hybrids such as HSE06 could be necessary in case of strong change of the oxidative degree of the platinum. Moreover, we showed the role of chlorine on the stabilization of an oxidized species ($PtCl_2$) under H_2. In **Chapter IV**, dedicated to the supported complexes during the calcination step, we showed that according to the conditions used three species could be expected after calcination: $PtCl_4$, $PtOCl_2$ and PtO_2. Hence the existence of chlorinated species with gradual amount of chlorine (from 0 to 4 per Pt) in the coordination sphere of the platinum must be considered in the modelling of the reduction step of species obtained from chlorinated precursors.

In the present contribution, we aim at deciphering the transformation of supported $PtO_xCl_y(OH)_z(H_2O)_n$ complexes during their reduction into Pt(0) in presence of H_2. Based on our previous gas phase study,[60] we first highlight the role of the support on the electronic properties of the platinum as a function of its coordination sphere and oxidation number. We found out a relation between the favored adsorption site on the (100) γ-Al_2O_3 surface and the platinum coordination number. The thermodynamic evolution of oxychlorinated Pt species under H_2 reveals the stabilizing role of chlorine on the oxidized Pt(+II) species, $PtCl_2$. Finally, by determining the reduction mechanisms starting from the expected calcined species (**Chapter V**), we highlight how the Gibbs free energy profiles depend on the ligand nature (OH, Cl, O). In particular, we show the role of chlorine on the stabilization of $PtCl_2$ through its diffusion to a specific adsorption site which highly increases its resistance against the reduction by H_2.

V.2. Computational methods

V.2.1. Total energy calculation at 0 K

All the calculations were performed using the VASP 5.4.1 software.[61,62] Geometries were optimized using the GGA PBE[63] exchange correlation functional corrected with the dDsC[64,65] scheme for the dispersion forces. A 400 eV cut-off was used for the kinetic energy of the plane wave basis set. Calculations were done at the Γ-point of the Brillouin zone due to the large supercell used: 16.71 x 16.79 x 21.80 $Å^3$. Core electrons were treated by using the Projector Augmented Wave (PAW) formalism.[66] Spin polarization was considered to define the ground state of each structure. Energies were recalculated after applicating a dipolar correction along the z axis (perpendicular to the slab). A Gaussian smearing of 0.05 eV was applied and charges were evaluated using the Hirshfeld[67] formalism. Convergence criteria were fixed to 10^{-7} eV for SCF cycles and to 10^{-2} eV $Å^{-1}$ for forces.

Following the conclusions of our previous analysis on similar unsupported systems[60], the impact of the functional has been carefully considered and the electronic energies have been also calculated using an HSE06[68–70] exchange correlation functional. No dipolar correction along the z-axis was considered in calculations at the HSE06 level. But due to the minimal impact that these corrections had on the PBE[63]-dDsC[64,65] energies, we believe that it won't change the drawn conclusion. Due to the computational cost of such calculation, a single point evaluation was done on the previously optimized geometry. No changes in the spin state were considered. Various energetic descriptors derived from the total energy are also calculated at 0 K such as interaction energy, adsorption energy, complex (more details are available in **SI.6)**

V.2.2. Supercell model and platinum species and reactions considered.

(100) surface

The (100) surface of γ-Al_2O_3 used has been developed by Digne et al.[71,72] following the work of Krokidis et al.[73]. We considered a 2x3 supercells with respect to the Digne's unit cell[71] (**Figure V-1**). The slab considered is made of four alumina layers and the first two layers were relaxed during geometry optimizations (**Figure V-1**). Because of the temperature used in the reduction step, the surface was considered dehydrated in line with results obtained at the PBE[63]-dDsC[64,65] level by Pigeon et al.[74] and with Digne et al.'s calculations at a PW91 level.

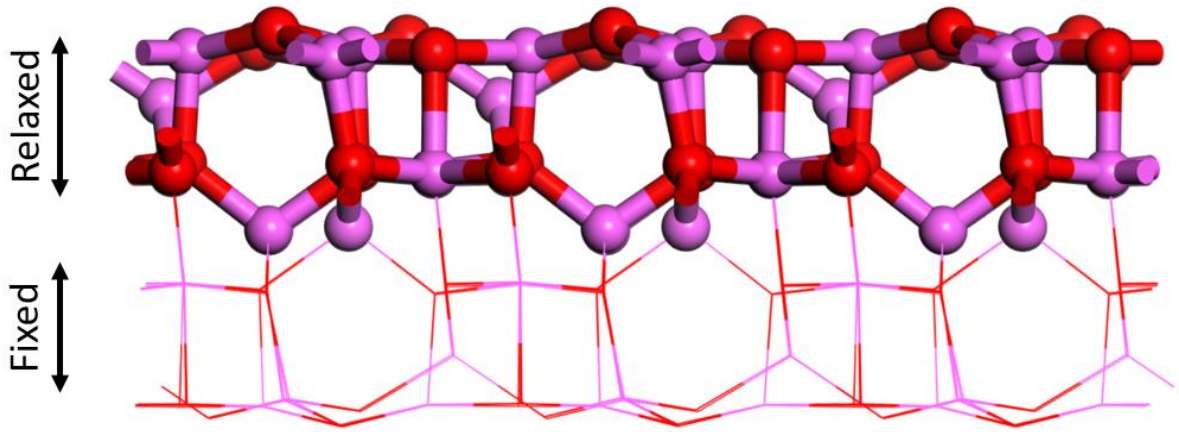

Figure V-1. Side view of the molecular model of the (100) surface of γ-Al_2O_3. [‡]). Color code for atomic structures: O: red; Al: pink.

Platinum species

To study the reduction step, we will consider the study of platinum species with oxidation degree ranging from +IV to 0. Similarly to what we did for the study of the calcination step in **Chapter IV** we consider that for a given oxidation degree, the complexes can be hydrated and we model these reactions with four equations (**Eq.1-4**). **Eq.1** represents the simplest case where a water molecule is added to the coordination sphere of the platinum without dissociation. **Eq.2** describes the formation of two hydroxyls from the dissociation of the adsorbed water molecule. In that case, one of the hydroxyls is formed from an oxo ligand. **Eq.3** describes a dissociative hydration leading to the formation of two hydroxyls but only one in the coordination sphere of the platinum, the second one is on the surface (these cases will be explicitly described by H* in the complex name). Finally, **Eq.4** models a dissociative adsorption of water but only one hydroxyl is formed, and the remaining hydrogen is coordinated to the platinum. This last reaction was found only for some specific hydration reactions of Pt(II) complexes.

In addition to the hydrations, we considered the possibility to exchange ligands. As described in **Eq.5** we consider the exchange of a Cl by a OH ligand through the adsorption of H_2O and desorption of HCl.

$$PtCl_y(OH)_z(H_2O)_n + H_2O \rightleftarrows PtCl_y(OH)_z(H_2O)_{n+1} \quad \textbf{Eq.1}$$

$$PtO_xCl_y(OH)_z(H_2O)_n + H_2O \rightleftarrows PtO_{x-1}Cl_y(OH)_{z+2}(H_2O)_n \quad \textbf{Eq.2}$$

$$PtCl_y(OH)_z(H_2O)_n + H_2O \rightleftarrows PtCl_y(OH)_{z+1}(H_2O)_n + H^* \quad \textbf{Eq.3}$$

$$PtCl_y(OH)_z(H_2O)_n + H_2O \rightleftarrows PtHCl_y(OH)_{z+1}(H_2O)_n \quad \textbf{Eq.4}$$

$$PtO_xCl_y(OH)_z(H_2O)_n + H_2O \rightleftarrows PtO_xCl_{y-1}(OH)_{z+1}(H_2O)_n + HCl \quad \textbf{Eq.5}$$

In addition to these five reactions that are used to describe the changes in the coordination sphere of the platinum without modifying the oxidation degree, we will consider H_2 as a reducing agent to link the complexes of various oxidation degree from +IV to 0. Numerous products can be obtained from the simple addition of H_2 and we will sum up all the encountered cases in three equation **Eq.6-8**. **Eq.6** describes the cases where H_2 interacts only with the platinum, in that case three scenario have to be considered: first, H_2 is adsorbed as it, this is represented by the variable i, second H_2 is adsorbed on Pt but dissociated, this is described by the variable j, last H_2 is dissociated but only one hydrogen remains on the Pt and the other forms a hydroxyl on the surface, in that case this is the variable k. **Eq.7** models the cases where hydrogens interact with an oxo ligand. In that case hydroxyls can be formed (i, k and l cases) and water can also be obtained if the two hydrogens are adsorbed on the oxygen (j). Finally, **Eq.8** describes the formation of water from a hydroxyl with the remaining hydrogen forming a hydroxyl on the surface. For all these equations we restricted the number of added H_2 molecules to one or two. ($i + j + k \leq 2$ for **Eq.6**; $i + j + k + l \leq 2$ for **Eq.7** and $i \leq 2$ for **Eq.8**.)

Following up the molecular and dissociative adsorption of H_2, the global reactions of reduction are modelled with **Eq.9** and **Eq.10**. The first equation (**Eq.9**) describes the reduction where H_2 is only used to form the molecule (HCl or H_2O) that will be desorbed. **Eq.10** is slightly more complex as it considers both possibilities to keep a hydrogen on the system through the transformation of an oxo ligand into a hydroxyl or water and the transformation of a hydroxyl into a water ligand. As for the reaction of H_2 adsorption, the number of H_2 molecules that can be added does not exceed two i.e. in **Eq.9** $i + j + k \leq 2$ and in **Eq.10** $i + j + k + l + m + n \leq 2$.

$$PtO_xCl_y(OH)_z(H_2O)_n(H_2)_a + (i+j+k)H_2 \rightleftarrows PtH_{(2j+k)}O_xCl_y(OH)_z(H_2O)_n(H_2)_{a+i} + kH^* \quad \textbf{Eq.6}$$

$$PtO_xCl_y(OH)_z(H_2O)_n(H_2)_a + (i+j+k+l)H_2 \rightleftarrows PtH_lO_{x-2i-j-k-l}Cl_y(OH)_{z+2i+l}(H_2O)_{n+j}(H_2)_a + kH^* \quad \textbf{Eq.7}$$

$$PtO_xCl_y(OH)_z(H_2O)_n(H_2)_a + (i)H_2 \rightleftarrows PtO_xCl_y(OH)_{z-i}(H_2O)_{n+i}(H_2)_a + iH^* \quad \textbf{Eq.8}$$

$$PtO_xCl_y(OH)_z(H_2O)_n + (i+j+k)H_2 \rightleftarrows PtO_{x-i}Cl_{y-2j}(OH)_{z-2k}(H_2O)_n + (i+2k)(H_2O) + 2j(HCl) \quad \textbf{Eq.9}$$

$$PtO_xCl_y(OH)_z(H_2O)_n + (i+j+k+l+m+n)H_2 \rightleftarrows PtO_{x-i-j-k}Cl_{y-i-l}(OH)_{z+i-j-l-m-n}(H_2O)_{n+k+l+m+2n} + (j+m)(H_2O) + (i+l)(HCl) \quad \textbf{Eq.10}$$

A simplified representation of the interconnection of the considered platinum species is shown in **Figure V-2**.

As we saw in the description of the reaction for systems containing H_2O and H_2 molecules could be observed through the formation of hydrides on Pt or protons on O atoms. Moreover, due to the acid/basic character of the Al_2O_3 surface, protons could also be adsorbed on its surface oxygen atoms to form hydroxyls, leading in fine to numerous isomers for a given stoichiometry. In these cases, the choice was made to keep only the most stable isomer for a given stoichiometry of an intermediate species.

To ease the description of systems a specific nomenclature will be used. The dissociation of H_2 or H_2O leading to the formation of such surface hydroxyls surface will be indicated with an asterisk (*). For example, various configurations can be obtained from H_2 adsorption on $PtCl_2$. The adsorption product will be named $PtHCl_2H^*$ when one H is on Pt while the other one is on the alumina surface. If the H_2 molecule is dissociated into two H on Pt, this will be indicated as PtH_2Cl_2. If the H_2 does not dissociate, it remains written $PtCl_2(H_2)$. All the detailed reactions are reported in **Table SV-3.** Reaction energies for various types of reactions calculated at 0 K and ranked according to the oxidation degree of the reactants.

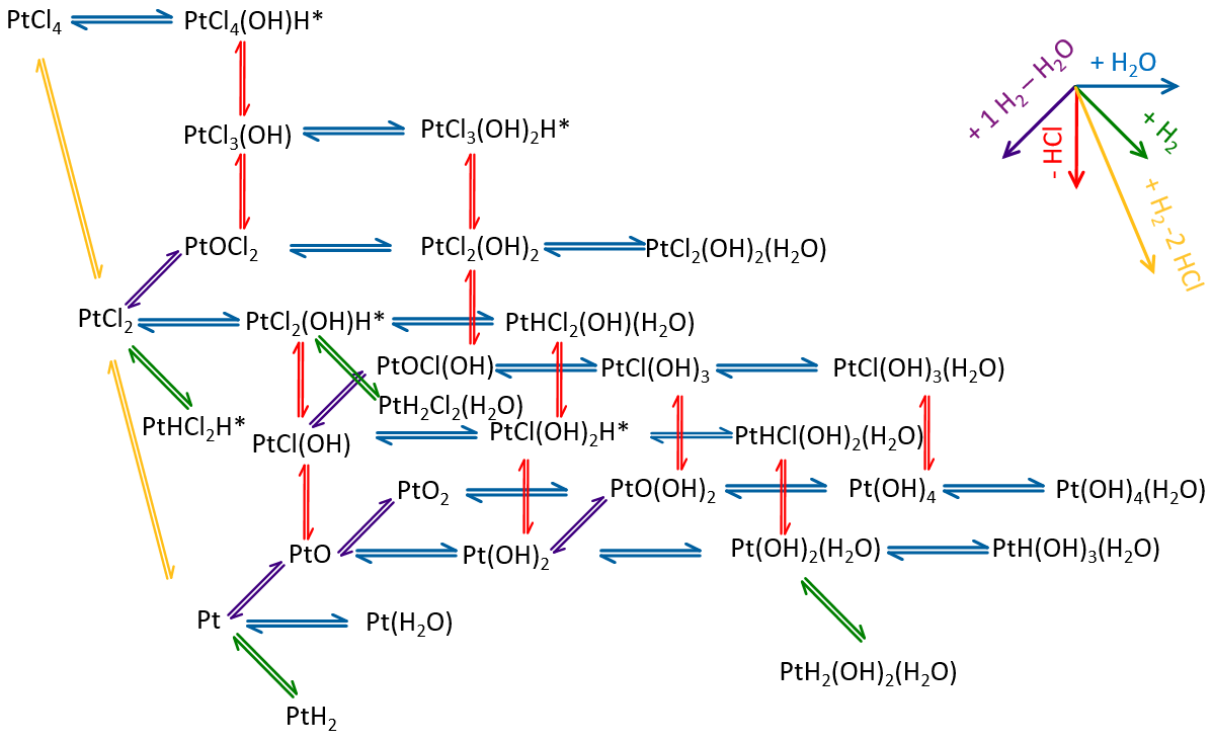

Figure V-2. Partial representation of the reactions network used to link the considered species. The focus is done on the Pt(IV), Pt(II), Pt(0) species and four relevant hydrogenated intermediates because of their higher relative stability. The list of all the considered reactions is reported in Table SV-3. For the sake of clarity, Pt(III) and Pt(I) are excluded of the representation.

V.2.3. Thermodynamic corrections

The thermodynamic stability of supported platinum complexes under various reaction conditions was determined by calculating Gibbs free energies.

Frequencies have been computed at the PBE[63]-dDsC[64,65] level on the previously optimized structures using the finite difference method as implemented in VASP using the central difference scheme with a 0.01 Å step to ensure the stable, or at least meta-stable, nature of our models and for calculating the vibrational component of the Gibbs free energies. Finite difference scheme was applied to all the atoms that were relaxed during the geometry optimization. The same convergence criterion of the wavefunction than for the energy calculations (10^{-7} eV) was used.

Translational, rotational and vibrational (including the zero-point energy term) contributions were calculated under the rigid-rotor and harmonic oscillator approximation and added to the electronic energy for the gas phase molecule while only the vibrational contributions were considered for the supported systems. (as detailed in **section II.5**) Gibbs free energies were calculated for temperatures ranging from 0 K to 1000 K and external pressures from 10^{-12} bar to 1 bar. The surrounding environment is treated as an ideal gas phase reservoir. The vapor/liquid water equilibrium is reported on all thermodynamic diagrams to recall the limit of stability of vapor water used in our thermodynamic model.

V.2.4. Determination of transition states

The transformation of the relevant intermediates according to the experimental condition was investigated by searching and calculating Transition State (TS) free energies to highlight the presence of limiting steps. A mix of Climbing Image Nudged Elastic Band method (CI-NEB)[75,76] followed by a Quasi-Newton (QN) optimization, and/or dimer[77] calculations were used in order to determine the TS. All TS were confirmed through frequencies calculations (with same threshold as described before) and the presence of only one imaginary mode which corresponds to the reactive mode. Confirmation that the imaginary mode was rightfully linking the reactant and the product, was done by calculation of the potential energy profiles along the Intrinsic Reaction Coordinate[78,79] (IRC) using a damped velocity Verlet algorithm as proposed by Hratchian et Schlegel[80] which is implemented in VASP. This step requires highly relaxed TS, thus some TS were optimized with tighter criterion to get reactant and product along the IRC. Due to highly time-consuming nature of these verifications, they were fully undertaken on every TS of the most relevant pathways, while on the less critical pathways the

IRC analysis was limited to some specific cases. All TS were optimized with at least 10^{-2} eV $Å^{-1}$ for forces and 10^{-7} eV for the wavefunction. No dipolar correction has been applied to the intermediates and TS considered in the kinetic part. Gibbs free energies of intermediate and TS are calculated at temperature and pressure describing experimental conditions: T = 775 K, $P(H_2O) = 1.10^{-6}$ bar, $P(H_2) =$ 1 bar and $P(HCl) = 1.10^{-6}$ bar. The generation of the intermediate images was done using either the Opt'n Path[81] open-source code or by using the scripts from Henkelman's group[82]. Plots of the reaction pathways are made by using an open-source code[83].

V.3. Results

V.3.1. Electronic and Energetic properties of relevant reduction intermediates

In this first part, we analyze the structural, electronical and energetical properties of relevant complexes involved in the thermodynamics and kinetics of reduction studied in the following sections.

V.3.1.a) Structures

Adsorption of $[Pt(O^{2-})_x(Cl^-)_y(HO^-)_z(H_2O)_n]^0$ complexes with oxidation degree ranging from +IV to 0 have been simulated on γ-Al_2O_3(100) due to experimental evidence of their existence during the calcination and reduction processes.[21,26,35] The dehydrated (100) γ-Al_2O_3 surface model developed by Digne et al.[71,72] exhibits various anchoring sites. Three different oxygens and three aluminum sites allow multiple possibilities for the adsorption of platinum complexes (**Figure V-3**). In the same spirit as in our previous analysis of the calcination thermodynamics (**Chapter IV**), a systematic screening was done for all complexes to determine the most stable anchoring site. Hence, we found a straightforward correlation between the number of ligands coordinated to Pt and the most favorable adsorption site, as illustrated in **Figure V-3 b), c)** and **d)** for some relevant species. The number of ligands depend themselves on the oxidation state of Pt as this will be analyzed latter. For complexes with three or more ligands, the oxygen B (O_B) provides the most stable anchored systems (**Figure V-3**, **c)**), these complexes with only one Pt-$O_{surface}$ bond will be referred as mono-grafted in the text. For complexes with two ligands (**Figure V-3**, **b)**), another anchoring mode implicating two oxygens A (O_A) and C (O_C) is preferred, such complexes will be referred as bi-grafted. For complexes with 1 or less ligand, an anchoring site maximizing the number of bonds with the surface oxygens and surface

aluminum is preferred (**Figure V-3**, **d)**). These complexes will be referred as tri-grafted. This adsorption site of the SA Pt(0) is the same found in a previous theoretical study.[52]

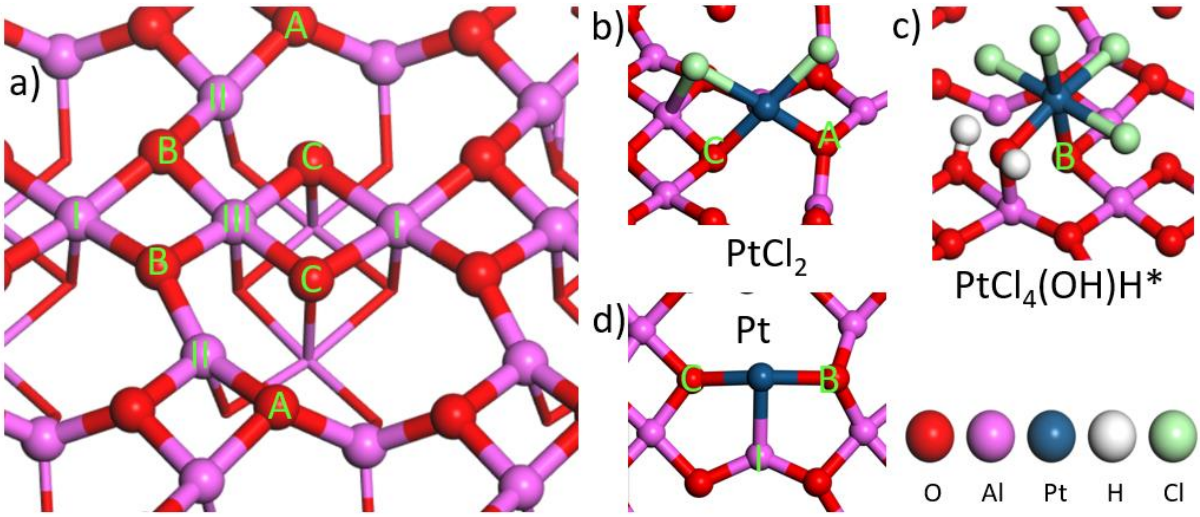

Figure V-3. a) Top view of the (100) γ–Al_2O_3 surface. b) bi-grafted $PtCl_2$ with the adsorption site represented O_A-O_C c) mono-grafted $PtCl_4(OH)H^*$ anchored to an O_B d) tri-grafted Pt(0) anchored to O_B-O_C-Al_I.

As it could be expected from the single atom nature of platinum, both the coordination sphere and the surface play a crucial role. Upon adsorption, $[Pt(O^{2-})_x(Cl^-)_y(HO^-)_z(H_2O)_n]^0$ complexes undergo structural changes, with an elongation of the Pt-X bonds (X being a ligand in the coordination sphere) compared to their gas phase equivalent (**Table V-1**). By averaging over all the oxidation degree, the observed elongation as a function the nature of the ligand follows the trend: Cl < H_2O < OH < O as reported in the **Table V-1** where mean distances are reported and detailed in the **Table SV-1**. The average Pt-Cl distance is very similar with 2.28 Å and 2.24 Å in supported and gas state respectively, while the average d(Pt-$O_{(H2O)}$) varies from 2.07 Å for the adsorbed complexes to 2.12 Å for gas phase complexes. The platinum-water distance is the only one being longer in gas phase than in the supported state. Pt-OH bonds are more impacted and a mean difference of 0.10 Å is calculated with 2.03 Å for supported Pt and 1.93 Å in gas phase. Finally, the elongation goes up to 0.15 Å for Pt-O with an average distance of 1.89 Å if supported against 1.74 Å in gas phase (**Table V-1**). The anchoring mode, and by extension the number of Pt-support bonds are responsible for small changes in the Pt-X bond length. Pt-OH are the more impacted bonds with an average Pt-OH distance calculated at 2.03 Å for the mono anchored complexes against 2.11 Å for the complexes bonded to the support through 3 bonds and 2.12 Å for the bi-grafted (are bi-grafted complexes whose Pt is bonded to the support by two bonds). Pt-Cl are less subject to such changes and both the bi-grafted and mono-grafted exhibit average Pt-Cl distance calculated at 2.34 Å and 2.29 Å respectively while a very small elongation is measured for the tri-grafted with 2.33 Å. Interestingly, the distance between

platinum and the bonding oxygens of the surface is independent of the anchoring mode, and we observe d(Pt-O_{surf}) varying between 2.10 Å and 2.13 Å (**Table** V-1). The impact of the support on Pt-O bonds depends on the number of anchoring sites for Pt. For the mono and bi grafted complexes, small differences are calculated with 1.88 Å and 1.91 Å respectively, but 1.98 Å is observed for PtO which is the sole tri grafted platinum with an oxo ligand. No clear correlation between the oxidation degree of platinum and the bond length variations was found. Adding H_2, independently of its possible dissociation after adsorption, results in an elongation of almost all the types of bonds but the Pt-O bonds which are 0.07 Å shorter after adsorption of H_2 on Pt(II) and 0.01 Å shorter for the Pt(III) (**Table V-1**). For the sake of simplicity, the hydrogenated species will be referred as their formal oxidation degree without H_2 adsorption plus a mention indicating that H_2 is adsorbed.

Systems	d(Pt-O_{surf})	d(Pt-Cl)	d(Pt-OH)	d(Pt-O)	d(Pt-H_2O)	d(Pt-H)
Pt(0,I,II,II,III,IV)/+H_2/gas	2.06/2.20/nc	2.28/2.32/2.24	2.03/2.05/1.93	1.89/1.90/1.74	2.07/2.17/2.12	1.55/1.57/nc
Pt(IV)/+H_2/gas	2.05/2.20/nc	2.27/2.32/2.27	2.02/2.04/1.94	1.85/nc/1.74	2.05/2.05/2.14	nc/1.55/nc
Pt(III)/+H_2/gas	2.02/2.16/nc	2.26/2.36/2.18	2.02/2.03/1.89	1.93/1.92/1.73	nc/nc/nc	nc/1.55/nc
Pt(II)/+H_2/gas	2.07/2.21/nc	2.28/2.29/2.20	2.05/2.05/1.92	1.98/1.91/1.74	2.10/2.21/2.12	1.56/1.59/nc
Pt(I)/+H_2/gas	2.15/2.33/nc	2.33/2.50/2.13	2.11/2.22/1.86	nc/nc/nc	nc/nc/nc	nc/1.55/nc
Pt(0)/+H_2/gas	2.02/2.24/nc	nc/nc/nc	nc/nc/nc	nc/nc/nc	2.09/-/2.04	nc/1.55/nc
Anchoring modes: 1/2/3	2.12/2.13/2.10	2.29/2.34/2.33	2.03/2.12/2.11	1.88/1.91/1.98	2.11/-/2.09	1.57/1.55/1.55

Table V-1. Average bond length (in Å) according to the formal oxidation degree of Pt for the supported Pt complexes without adsorption of H_2 (Pt(X)), hydrogenated supported complexes (+H_2) and gas phase complexes (without H_2 adsorbed) from previous study[60]. The anchoring modes refer to the number of bonds formed between Pt and atoms from the support after adsorption (1: mono grafted, 2: bi-grafted and 3: tri-grafted). Nc indicates that such systems have not been modelled. Details of each supported system is reported in Table SV-1.

V.3.1.b) Electronic properties

In the same spirit that what was calculated for the Pt(IV) systems considered in the chapter IV dedicated to the calcination step, the platinum charges calculated by Hirschfeld partitioning is impacted by various factors (**Figure V-4**). As it was calculated for the gas phase complexes and independently of the adsorption mode of the complexes or the formal oxidation degree of the complexes, oxo ligands were found to be more oxidizing than hydroxyls, themselves more oxidizing than chlorines (for the same number of ligand). The average Pt Hirshfeld charges (calculated for all complexes with a given formal oxidation number as reported in **Table SV-1**), follows qualitatively the same trend as the formal oxidation number as long as no addition of H_2 is considered. Without considering Pt complexes with adsorbed H_2 species, the average positive charges of platinum are 0.034 e, 0.291 e, 0.392 e, 0.493 e and 0.582 e for the complexes reported as Pt(0) , Pt(I), Pt(II), Pt(III), Pt(IV) in the **Table SV-1** respectively.

Effect of the support

It must be underlined that the formal oxidative degree of the platinum is often chosen to remain unaffected by its interaction with the alumina surface, being considered as an innocent ligand.[84] However, this behavior is not entirely justified since the Hirshfeld charge of Pt may be significantly impacted by the alumina surface, as illustrated in **Figure SV-1** where a consistent comparison with gas phase complexes is made. The surface impacts the electronic density of the platinum through the grafting mode of the complexes: the higher the number of anchoring sites, the stronger is the depletion. The average difference between the Pt charge in gas phase and on the support is 0.14 e but this difference increases with the number of anchoring sites: 0.10 e, 0.15 e and 0.20 e for mono-, bi- and tri-grafted complexes respectively (**Table SV-1**). Pt in $Pt(H_2O)$ only is slightly negatively charged species (**Table SV-1**) despite the support. This reducing effect of water on Pt was also observed in gas phase,[60] but in this case it is partially counterbalanced by the surface. Finally, the reduction is often accompanied by a reduction of the number of ligands in the coordination sphere. This implies a change of the adsorption sites which is accompanied by an increase of the number of bond Pt-support as the number of ligands in the coordination sphere decreases (**Figure V-3**). Hence, a levelling of the platinum charges during reduction is observed in comparison to the gas phase. While in gas phase[60] the Pt charge differences between Pt(IV)/Pt(II) and Pt(II)/Pt(0) were calculated at 0.315 e and 0.407 e, once supported these differences are smoother to 0.190 e and 0.358 e.

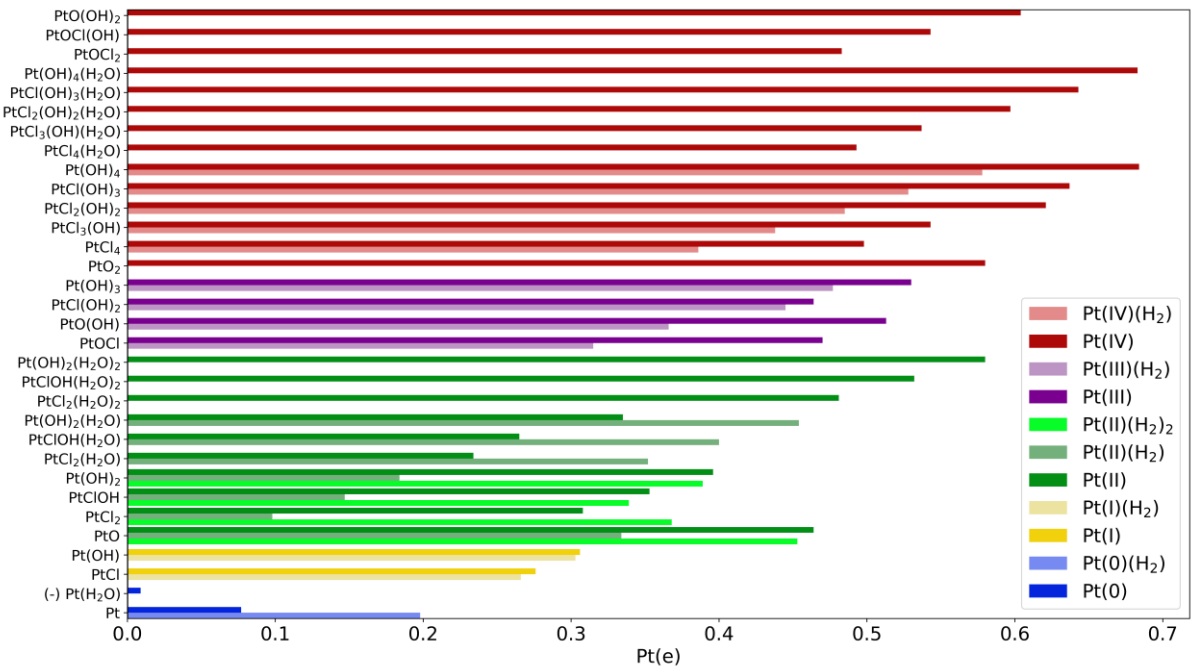

Figure V-4. Hirshfeld platinum charges for the various complexes classified by colors according to their oxidation degree. Lighter colors indicate that H_2 was absorbed on the complexes. For the sake of clarity, the (-) indicates a positive value of the Pt charge in $Pt(H_2O)$. More detailed results on the Pt complexes are reported in Table SV-1.

Effect of H_2 adsorption

Most of the H_2 adsorption reactions occur through dissociative mechanisms (**Eq.6-8**), leading to the adsorption of hydrogens on Pt or hydroxyls, either on the alumina surface or on Pt (from oxo ligands) (**Figure V-5**). Only two systems kept an H_2 almost undissociated: the doubly hydrogenated $PtH_2O(H_2)$ (**Figure V-5, i)**, and $PtHCl_2(H_2)H^*$ (**Figure V-5, d)**) on both of them the first absorbed H_2 was dissociated.

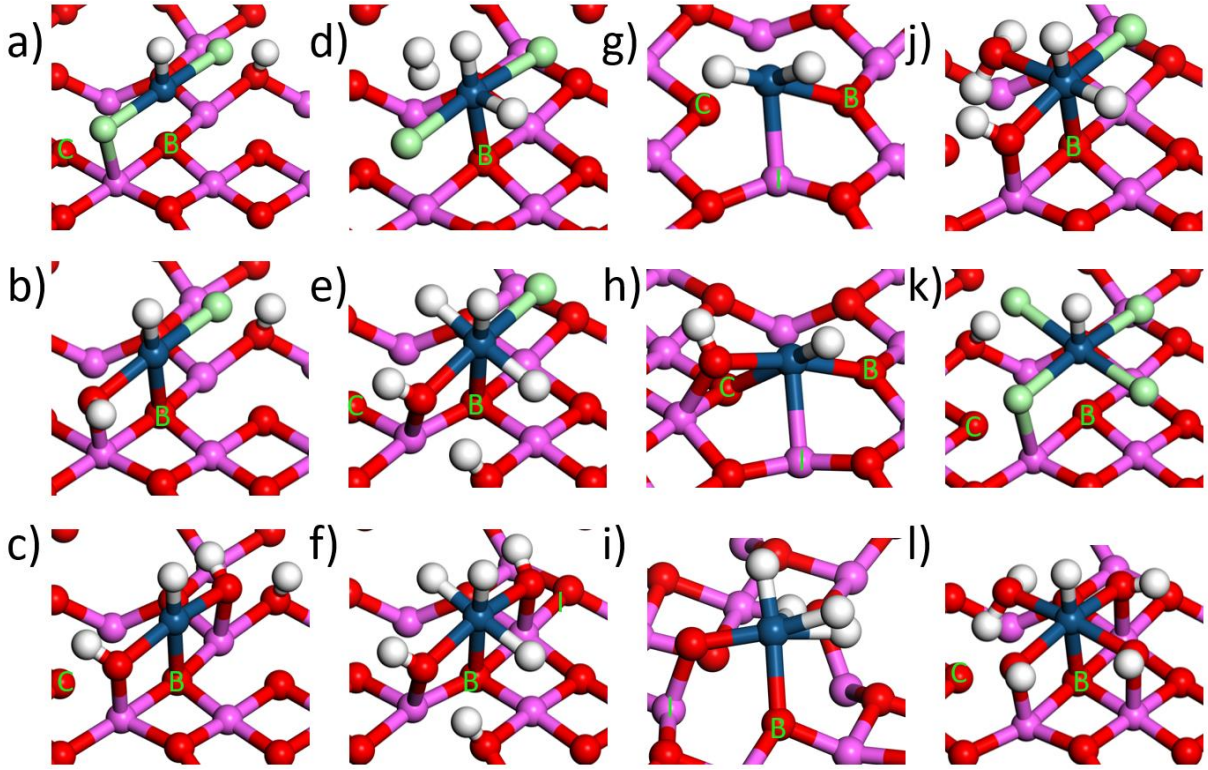

Figure V-5. Supported complexes after H_2 adsorption. a) $PtHCl_2H^*$, b) $PtHCl(OH)H^*$, c) $PtH(OH)_2H^*$, d) $PtH_2Cl_2(H_2)$, e) $PtH_3Cl(OH)H^*$, f) $PtH_3(OH)_2H^*$, g) PtH_2, h) $PtH(OH)$, i) $PtH_2O(H_2)$, j) $PtH_2Cl(OH)(H_2O)$, k) $PtHCl_4H^*$, l) $PtH(OH)_3(H_2O)$. Oxygen and aluminum are indicated with the same nomenclature as in Figure V-3. Color code for atomic structures: Pt: blue; Cl: green; O: red; Al: pink, H: white.

As in **Table SV-1**, hydrogenated species in **Figure V-4** will be referred as their formal oxidation degree without H_2 adsorption plus a mention indicating that H_2 is adsorbed. Although adding H_2 species may significantly change Pt charges. The adsorption of H_2 often induces a reduction of platinum (**Figure V-4**), with some exceptions. However, the impact of H_2 on the mean Hirshfeld charges of Pt depends on the oxidation degree of the Pt before adsorption. While Pt(IV), Pt(III) and Pt(II) are similarly reduced with a net decrease of 0.10 to 0.07 e, almost no impact is observed for Pt(I). By contrast, Pt(0) is oxidized upon H_2 adsorption (**Figure V-5, g)**) with net increase of 0.12 e. The oxidation of platinum after H_2 adsorption was also calculated for three hydrated Pt(II) species (**Table SV-1**):

$PtH_2Cl_2(H_2O)$, $PtH_2Cl(OH)(H_2O)$ (**Figure V-5, j)**) and $PtH_2(OH)_2(H_2O)$ and to a smaller extent for $PtH_2Cl_2(H_2)$ (**Figure V-5, d)**) compared to $PtCl_2$.

Trying to saturate Pt with H_2 as it is done in the case of these two successive adsorptions of H_2 on some Pt(II) result in a strong increase of the Pt charges compared to the cases where only one H_2 is added (**Table SV-1**). Among them $PtH_2Cl_2(H_2)$ is slightly different than $PtH_3Cl(OH)H^*$ and $PtH_3(OH)_2H^*$ (**Figure V-5, f)**) which dissociated all the adsorbed H_2 with three H on the platinum and one on the surface (**Figure SV-2**). For $PtH_2Cl_2(H_2)$, the presence of chlorine and absence of hydroxyls seems to be linked to the capacity to keep the second adsorbed H_2 undissociated (**SI.3**). The oxidative power of the surface is highlighted upon H_2 adsorption as among the largest Pt charge differences calculated after H_2 adsorption we retrieve fives complexes which change their adsorption mode after the addition of H_2 moving from the bi-grafted mode on two oxygens O_A and O_C to mono-grafted mode on O_B ($PtHCl_2H^*$, $PtHCl(OH)H^*$, $PtH(OH)_2H^*$ (**Figure V-5 a-c)**), PtHOClH* and PtHO(OH)H*).

Effect of H_2O ligand

H_2 is not the only species subject to dissociation during the adsorption, and as mentioned previously, and as described by the **Eq.1-4** some hydration reactions occur through a dissociative mechanism leading to the formation of a hydroxyl and a proton which can be located either on platinum or on the alumina surface to form a hydroxyl not coordinated to the platinum (**Figure SV-3, b)**). Most of the time, the proton goes on the surface due to the basic character of oxygen atoms, however for the double hydration of $PtCl_2$, PtCl(OH) and $Pt(OH)_2$ lead respectively to the formation of $PtHCl_2(OH)(H_2O)$ (**Figure SV-3, c)**), $PtHCl(OH)_2(H_2O)$ and $PtH(OH)_3(H_2O)$ where the proton from the dissociation of H_2O is found adsorbed on the Pt. These modifications in the coordination sphere of platinum are responsible for the drastic oxidation changes observed during this second hydration (**Figure V-4**). These systems must be taken carefully during the comparison of their Hirshfeld charges as the nature of the ligands is not the same for a given stoichiometry (**Table SV-1**). However, after water dissociation where the dissociated proton ends on the surface, the change on the platinum charge is similar than for a simple adsorption of H_2O, details on the hydration of Pt(IV)s are provided in **Chapter IV**.

Adding a ligand in the coordination sphere of the platinum can result in a change on its adsorption site which can impact the platinum charge. This is the case for the bi-grafted complexes: $PtCl_2$, PtCl(OH), $Pt(OH)_2$, PtOCl, PtO(OH) and PtO_2, whose adsorption sites is modified upon hydration as the number of ligand in the coordination sphere of the platinum exceeds two. In presence of an oxo ligand (PtOCl, PtO(OH) and PtO_2), two hydroxyls are formed upon hydration similarly as in **Figure SV-3 g, h, i, j)** where $PtOCl + H_2O \rightarrow PtCl(OH)_2$ (**g, h**) and $PtO_2 + H_2O \rightarrow PtO(OH)_2$ (**i, j**). The overall

process is slightly oxidizing in absence of chlorine (~+0.02 e) or almost neutral for $PtOCl_2$ in term of the Pt charges (**Table SV-1**). In absence of an oxo ligand, two phenomena are observed depending on the presence of chlorine coordinated to the Pt. If at least one chlorine is coordinated to the Pt, a similar phenomenon than for the hydration of Pt(IV) (**section IV.3.3**) is observed. For $PtCl_2$ and PtCl(OH), the added OH from the dissociation of H_2O can be used as a bridging ligand between the platinum and the surface by replacing the chlorine which becomes a daggling ligand (**Figure SV-3 a, b)** for $PtCl_2$ case). In the case of $Pt(OH)_2$, such replacement is not possible, and the most stable geometry is obtained with a daggling H_2O (**Figure SV-3 e, f)** where $Pt(OH)_2 + H_2O \rightarrow Pt(OH)_2(H_2O)$). In every case, trying to use the dangling ligand as a bridging one result in a strong destabilization of the system as the square planar nature of the complex would be lost. Despite these two different adsorption mode of water for the bi-grafted Pt(II), the platinum are all reduced upon hydration. (**Table SV-1**) Similarly, the hydration of H_2O onto Pt(0) (**Figure SV-3 k, l)**) results in a slight reduction of the platinum (**Table SV-1**), this result was also observed, albeit in a larger proportion, in gas phase.[60]

In presence of oxo ligands the dissociative hydration is preferred. Otherwise, hydrations have to be considered case by case as the dissociation of the water molecule will be impacted by the geometry of the complex, the number of available aluminum sites close to the platinum and the nature of the ligands already bonded to the platinum.

V.3.1.c) Energetic trend at 0 K

Hydration reactions

As discussed, hydration reactions are modelled by five different equations (**Eq.1-4**) for the different scenario described previously. These reactions are always exothermic at 0 K (**Table SV-3**) and favored by high oxidation level (**Table V-2**). Generally, hydration reactions are easier in presence of hydroxyls than chlorine ligands. Only the $PtCl_y(OH)_{4-y}$ (Pt(IV)) series is not in line with this trend and exhibits similar hydration energies for complexes with at least one chlorine, and a lower hydration energy for $Pt(OH)_4$ (cf **Chapter IV** for details). However, other factors impacting the exothermicity of the reaction must be considered. Indeed, a change of the adsorption site may occur during the adsorption and modulates hydration energies. For example, the loss of the bi-grafted nature upon hydration lowers the reaction energies. As previously discussed, the bi-grafted Pt(II) complexes $PtCl_2$, PtCl(OH) and $Pt(OH)_2$ undergo a change in their grafting mode as their number of ligands exceeds 2 after hydration (the case for $PtCl_2$ is illustrated in **Figure SV-3, a, b**) and this lead to hydration energies among the smallest calculated in spite of the formation of square planar complexes upon

hydration ($PtCl_2$: -27.9 kJ/mol; PtCl(OH): -21.8 kJ/mol and $Pt(OH)_2$: -50.6 kJ/mol (**Table SV-3**)). On the other hand, the formation of a bi-grafted complex highly favor the reaction, and the hydration of PtO into $Pt(OH)_2$ (a bi-grafted and square planar complex: **Figure SV-3 d, e)** is the most exothermic hydration (-208.9 kJ/mol). This highlight not only how the surface may interfere with the platinum chemistry, but also how the O_A-O_C adsorption site (**Figure V-3**) highly stabilizes platinum complexes. Among the Pt(IV), the lowest hydration energy (-106.6 kJ/mol, **Table SV-3**) is calculated for PtO_2 which is the only complex in the series undergoing this change of adsorption site upon hydration (**Figure SV-3 i, j**).

The geometries of the hydrated complexes are also an important factor of stability. For the same oxidation level (+IV), the formation of octahedral complexes from penta-coordinated ones result in highly exothermic hydration reactions (between -144.7 kJ/mol and -196.0 kJ/mol for the hydration of the $PtCl_y(OH)_z$ (**Table SV-3**)), while the formation of pentahedral complexes from square planar results in less exothermic reactions (-108.4 kJ/mol, -126.9 kJ/mol and -145.6 kJ/mol for the hydration of $PtOCl_2$, PtOCl(OH) and $PtO(OH)_2$). The structures of the square planar $PtOCl_2$ and its hydration products: $PtCl_2(OH)_2$ (+1 H_2O, pentahedral) and $PtCl_2(OH)_2(H_2O)$ (+2 H_2O, octahedral) are reported in **Figure SV-3 m,n,o)**. The high stability of octahedral and square planar geometries highlighted in this section seems to be an intrinsic property of these complexes as it was also reported in the gas phase.[60] Overall, the hydration of hydrogenated complexes is less favorable than for their dehydrogenated counterpart which is consistent with the fact that hydration energies increase (in absolute value) alongside the oxidation level of the Pt.

Ligand Exchange

Ligand exchange energies are calculated as described in **Eq.5** by considering the exchange of one hydroxyl ligand by one chlorine. Average values according to the oxidation degree are reported in **Table V-2** with details reported in **Table SV-3**. No clear trend is observed with the oxidation degree. In any case, the chlorinated species are intrinsically more stable at 0 K than their hydroxylated counterpart as shown by the endothermic reaction energies for all the considered exchange reactions. While this was also observed for gas phase complexes[60], the comparison of reaction energies for supported and gas phase complexes reveals a considerable impact of the surface in the platinum complexes chemistry. Indeed, for some exchange ligand (or hydration) reactions, the added hydroxyl becomes a bridging ligand with Al of the support leading to stronger interaction energies (**Figure SV-4**) than the former chlorine, which facilitates the exchange. As discussed in **Chapter IV,** this impact is well illustrated within the $PtCl_y(OH)_z(H_2O)_n$ series where for the last exchange ($PtCl_3(OH)(H_2O)_n + H_2O \rightarrow Pt(OH)_4(H_2O)_n + HCl$) the added hydroxyls cannot be a bridging ligand

between the platinum and the surface and reaction energies are at least twice larger than for the previous exchanges. Adsorption energies of the Pt complexes were computed, using gas phase complexes as a reference (**Eq. S1**) and we found out that the adsorption energy increases with the number of hydroxyl in the coordination sphere but reaches a plateau at 3 hydroxyls (which corresponds to the number of available aluminum for a Pt coordinated to an oxygen B (**Figure V-3**)). Thus, the adsorption energies of $PtCl(OH)_3$ (-252.0 kJ/mol) and $Pt(OH)_4$ (-253.2 kJ/mol) are almost equal while $PtCl(OH)_3(H_2O)$ (432.4 kJ/mol) exhibit an even stronger adsorption energy than $Pt(OH)_4(H_2O)$ (-411.7 kJ/mol) (**Figure SV-4**). In these cases where hydroxyls cannot participate to the anchoring of platinum, exchange energies are close to the ones calculated in gas phase.[60] By contrast, the bi-grafted Pt(II) series ($PtCl_2$, PtCl(OH) and $Pt(OH)_2$) reveals that even if the added hydroxyl can be used to anchor the platinum to the surface, this does not always favor the exchange. The $PtCl_2 + H_2O \rightarrow PtCl(OH) + HCl$ exchange verifies the previous trend with a reaction energy almost twice lower than in gas phase, and an decrease of the adsorption energy (going from -289.9 kJ/mol for $PtCl_2$ to -328.9 kJ/mol for PtCl(OH)). However, the $PtCl(OH) + H_2O \rightarrow Pt(OH)_2 + HCl$ exchange is harder and close to gas phase value despite the bridging nature of the added hydroxyl. In $Pt(OH)_2$, due to the stronger nature of the Pt-OH bonds and the particular geometries of these bi-grafted complexes, both the complex and the surface are deformed in such proportion that the gain from the new Pt-OH-Al bond is not enough to compensate the deformations. Thus, while the interaction energy (**Eq. S2**) increases from -619.6 kJ/mol for PtCl(OH) to -706.6 kJ/mol for $Pt(OH)_2$, the adsorption energy decreases from -328.9 kJ/mol to -313.7 kJ/mol due to increasing deformations (**Figure SV-4**) leading to a higher ligand exchange energy than calculated in gas phase for the same unsupported reaction.

H_2 adsorption

H_2 adsorption reactions are described by the **Eq.6-8**. The product of the adsorption of H_2 is highly dependent on the nature of the reactive. Here we detail these reactions from an energetic point of view. The adsorption of H_2 is almost always favorable (**Table SV-3**) with only some exceptions such as the adsorption of a second H_2 on $PtHCl_2H$*, PtHCl(OH)H*, or PtHO(OH) (**Figure V-5, a-c)**) which lead to $PtH_2Cl_2(H_2)$, $PtH_3Cl(OH)H$* and $PtH_3(OH)_2H$* respectively (**Figure V-5**, **d-f)**). Generally, it seems that the more oxidized Pt, the more favored the H_2 adsorption is, as it is reported in **Table V-2.** Some exceptions have to be noticed such as Pt(0) (**Figure V-5, g)**) exhibiting a H_2 adsorption energy of -148.9 kJ/mol (stronger adsorption than on Pt(I), Pt(II), Pt(III), considering average values), or the formation of PtH(OH) (**Figure V-5, h)**) from PtO which is isoenergetic with Pt(IV) with -278.5 kJ/mol. In this case, the PtH(OH) is adsorbed on the O_A-O_C oxygens sites with a similar geometry as the highly stable $PtCl_2$ (**Figure V-3, b)**), suggesting the highly stabilizing nature of these sites for complexes with two ligands. However, complexes adsorbed in these stables sites with already two ligands are

reluctant to the adsorption of H_2. Despite many attempts, it is impossible to adsorb H_2 (either dissociatively or non dissociatively) on $PtCl_2$, $PtCl(OH)$, $Pt(OH)_2$, $PtOCl$, $PtO(OH)$ while they are coordinated to these two O_A-O_C oxygens. In the end, the adsorption of H_2 on these species was only possible after migration of Pt and the most stable systems were calculated with Pt bonded to an oxygen B (**Figure V-5, a-c)**). Interestingly, the same trend related to the nature of the ligand as for hydration reactions is observed: in almost every case, the adsorption of H_2 is easier in presence of hydroxyls rather than in presence of chlorine. The only exceptions are the pentahedral Pt(IV) $PtCl_y(OH)_{4-y}$ complexes with their H_2 adsorption energies increasing from -271 kJ/mol for $PtCl_4 + H_2 \rightarrow PtHCl_4H^*$ to -237 kJ/mol for $Pt(OH)_4 + H_2 \rightarrow PtH(OH)_3(H_2O)$ (**Figure V-5 k, l)**).

Reduction

Reduction reactions are modelled according to **Eq.9-10**. As highlighted by the equation describing the reduction reactions, many products can be potentially expected, in **Table SV-3,** only the reactions leading to the most stable product at 0 K are reported. As we could deduce from the superior intrinsic stability of the chlorinated complexes compared to their hydroxylated counterpart, in case of reductions with potentially several products, the most stable product is obtained by maximizing the number of Cl in the coordination sphere of Pt.

The reduction energies are impacted by the oxidation level of the Pt. The difficulty to reduce platinum follows the trend: (Pt(II) → Pt(0)) > (Pt(III) → Pt(I)) > (Pt(IV) → Pt(II)). The reduction of Pt(IV) into Pt(II) is in average highly favored even at 0 K with an average of -96.8 kJ/mol. However, disparities exist according to the geometries of both the reactants and products, and the reduction of the hydrated $PtCl_y(OH)_{4-y}(H_2O)$ into $PtCl_y(OH)_{2-y}(H_2O)$ are endothermic (**Table SV-3**). This higher resistance of hydrated species to reduction is also calculated for the Pt(III). Despite an average reduction energy of -65.7 kJ/mol, Pt(III) exhibits two distinct behaviors: the reductions of PtOCl and PtO(OH) into PtCl and Pt(OH) are calculated at -103.4 kJ/mol and -147.1 kJ/mol respectively, while the reductions of their hydrated equivalent ($PtCl(OH)_2$ and $Pt(OH)_3$) are calculated at 3.7 and -16.1 kJ/mol. Pt(II) complexes are the most difficult to reduce, especially in presence of chlorine, and the only negative reduction energy is for the reduction of PtO into Pt with -132.9 kJ/mol.

Interestingly, we observe an opposite effect of the chlorine on the reduction of Pt(IV) into Pt(II) on one hand, and Pt(II) into Pt(0) on the other hand. While it is easier to reduce $PtCl_4$ than $Pt(OH)_4$ into their Pt(II) equivalent with -114.5 kJ/mol and -87.0 kJ/mol respectively, the order of the reductions of $PtCl_2$ and $Pt(OH)_2$ into Pt(0) is reversed with +208.7 kJ/mol and 76.0 kJ/mol respectively (**Table SV-3**). We believe that this opposite effect on the electronic energies is the result of the very high stability of the supported $PtCl_2$ as it is detailed in **SI. 7**.

Species	Hydration	Ligand Exchange	H_2 Adsorption	Reduction
Pt(IV)/Pt(IV)(H_2)	-156 / nc	36.9 / 34.9	-273.2 / nc -	-96.8 / nc
Pt(III)/Pt(III)(H_2)	-119.1 / -29.0	80.7 / 38.3	-95.2 / nc	-65.7 / nc
Pt(II)/Pt(II)(H_2)	-78.8 / -69.0	54.7 / 40.0	-128.5 / 59.75	116.5 / nc
Pt(I)/Pt^{I}(H_2)	nc / nc	48.5 / 38.9	-30.0 / nc	48.5 / nc
Pt(0) /Pt(0) (H_2)	-6.6 / nc	nc / nc	-148.9 / nc	nc / nc

Table V-2. Average reaction energies (kJ/mol) calculated at 0 K for various chemical reactions. nc indicates that these reactions have not been calculated. Details of considered reactions are reported in Table SV-3.

V.3.2. Thermodynamic aspects of reduction

In the same spirit as we proposed for the calcination process, we determine here through ab initio thermodynamic diagrams the nature of the stable Pt complexes under reducing conditions to mimic the activation step of the catalyst. Gibbs free energies are calculated to evaluate the most stable species by taking into account the reactive atmosphere. The considered species are reported in **Table SV-1** and a simplified representation of the network of reaction linking these species is reported in **Figure V-2**.

As described previously, the reduction is modelled here with H_2 as reducing agent as it is usually done for the preparation of Pt/Al_2O_3. The pressure of H_2 is allowed to range between 1.10^{-12} bar and 1 bar. While reductions are usually carried out at high temperature, we will consider a wide range of temperature between 0 K and 1000 K to highlight the role of the temperature during the reduction. Chlorine is expected to play a role on the state of the active phase of platinum after reduction.[24,25] The HCl pressure will be used here as a variable for adjusting the chlorine contents in the system[19] and three cases are considered: one unchlorinated sample (P(HCl) = 0 bar), and two chlorinated samples in various proportions (P(HCl) = 10^{-12} bar and P(HCl) = 10^{-6} bar). The H_2O pressure has little impact on the oxidation state of the platinum during the reduction step, thus $P(H_2O)$ will be fixed at the usual water pressure used for reduction: $P(H_2O) = 10^{-6}$ bar.

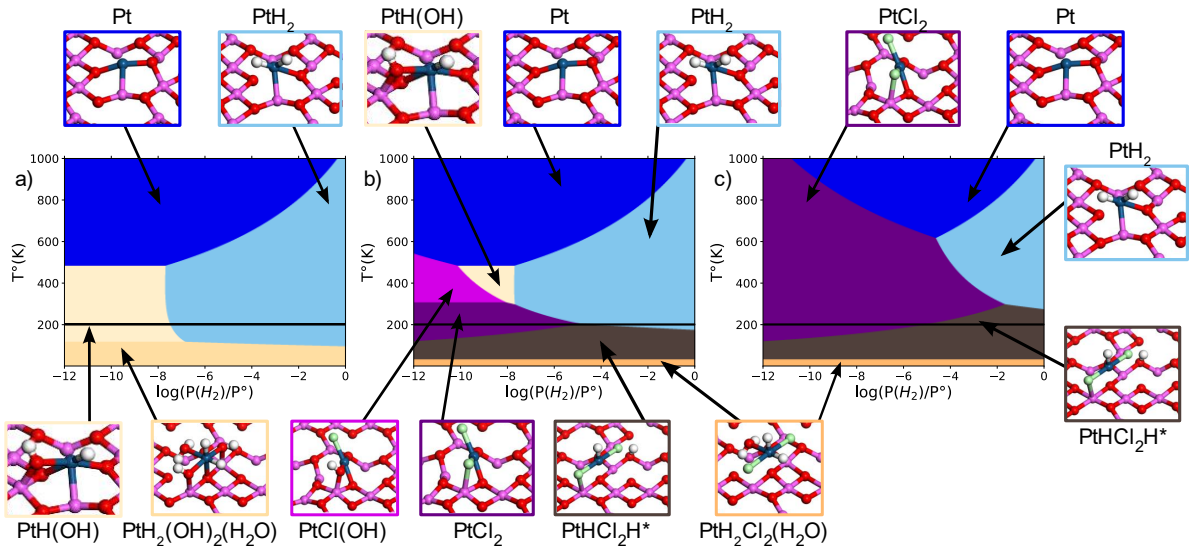

Figure V-6. Thermodynamic diagrams of the most stable species under reductive conditions at $P(H_2O) = 10^{-6}$ bar for three chlorine loadings: a) Without chlorine; b) $P(HCl) = 10^{-12}$ bar; c) $P(HCl) = 10^{-6}$ bar. Color code for atomic structures: Pt: blue; Cl: green; O: red; Al: pink, H: white. The gas phase domain of water is located above the black straight line.

The absence of Pt(IV) and the possible presence of Pt(II) in the thermodynamic diagrams of the reduction step echoes with the negative reaction energies found to reduce Pt(IV) into Pt(II) while reduction of Pt(II) into Pt(0) was less favorable at 0 K (**Table SV-3**). Without chlorine (**Figure V-6, a**) the reduction is strongly favored and only ($Pt^{II}H(OH)$) is found stable for temperature lower than 500 K and $P(H_2)$ below 10^{-7} bar. The competition between Pt and PtH_2 is driven by the high temperatures and low H_2 pressure (typically, the transition appears at 775 K for $P(H_2)$ around 1.10^{-2} bar), favoring the departure of H_2 for entropic reasons. Adding chlorine leads to the stabilization of more diverse species, as shown by the diagrams on **Figure V-6 b) and c)**.

In the less chlorinated case, the stability domain of Pt(II) is similar than in in the unchlorinated case, but chlorinated Pt(II) species are stabilized in place of PtH(OH). As for the calcination step (**cf Chapter IV**), for the low chlorination level, the impact of chlorine is mostly visible at low temperatures. Increasing the temperature leads to the recombination and desorption of the ligands of the complexes and thus to the formation of Pt for entropic and enthalpic reasons. The increase of H_2 pressure favors the release of HCl which reduces the platinum to Pt or PtH_2. The stabilization of PtCl(OH) over $PtCl_2$ at very low H_2 pressures with the increases of temperature is due to the high difference between the chemical potential of water (whose pressure is fixed at 1 ppm) *versus* HCl (with $P(HCl) = 10^{-12}$ bar here). From an electronic point of view the OH → Cl exchange is not favorable (**Table SV-3)** and indeed, the product of this ligand exchange from $PtCl_2$ is not expected anymore as the HCl pressure is increased to similar level than the H_2O pressure (**Figure V-6**, **c)**). The impact of chlorine on the stabilization of Pt(II) species such as $PtCl_2$ is highly visible with the increase of P(HCl)

up to 10^{-6} bar as the chlorinated Pt(II) is stable for temperature up to 1 000 K if the H_2 pressure is lower than 10^{-9} bar. For a typical reduction temperature (775 K) the HCl pressure must be carefully considered: $PtCl_2$ is stable up to $P(H_2) = 10^{-7}$ bar for $P(HCl) = 10^{-6}$ bar. However, considering realistic reduction conditions, higher $P(H_2)$, implies the stabilization of full reduction of Pt either as Pt(0) or $Pt(H_2)$ depending on both temperature and H_2 pressure. Hydrated and hydrogenated Pt(II) complexes such as $PtH_2(OH)_2(H_2O)$ (in absence of chlorine), or $PtH_2Cl_2(H_2O)$ and $PtHCl_2H^*$ in chlorinated systems are stabilized for the low temperatures. However, at these temperatures the water is not expected to be gaseous (black line in **Figure V-6**) hence, we are out of the validity domain of our model. Among them only $PtHCl_2H^*$ can be expected at $P(HCl) = 10^{-6}$ bar and $P(H_2) > 10^{-3}$ bar.

We showed that the description of the reduction of such platinic complexes in gas phase may need to go beyond simple GGA functionals.[60] In particular, it was observed that PBE-dDsC underestimates the stability of reduced Pt atom with respect to ACFDT-RPA and HSE06 approaches. Hence, the same diagrams were also calculated at the PBE-dDsC level (**Figure SV-6)**. Contrasting with this discrepancy on the reduction diagrams in gas phase[60], the exchange correlation impact is relatively small for the case of the supported complexes. In particular, the reduction temperature of Pt species does not depend on the level of theory which is an important result for the following investigation of the reduction mechanism at PBE level. For unchlorinated and $P(HCl) = 10^{-12}$ bar cases, a slight increase of the stability domain of PtH(OH) is observed. For both chlorinated systems, the remaining of the differences are mainly observed for low temperature at which the validity of the model is discussable as the water is not expected to be gaseous.

Thus, the surface tends to minimize the impact of the exchange-correlation functional on the thermodynamic diagram. However, the precise explanation of this phenomenon is beyond the scope of the present work.

V.3.3. Kinetic aspects of the reduction of Pt complexes

Thermodynamics diagrams revealed the stabilizing role of Cl on the Pt(II) species such as $PtCl_2$. However, for H_2 pressure superior to 10^{-6} bar, for the typical temperatures encountered during reduction[21], platinum is supposed to be reduced at the Pt(0) state from a thermodynamic point of view. Hence the chlorine role on the stabilization of single atom might be from another nature. As the impact of chlorine during the reduction from a kinetic point of view is still unknown, we propose to study the reduction under H_2 of the post-calcinated species from **Chapter IV**. After calcination, three species are expected according to the quantity of chlorine in the system: PtO_2, $PtOCl_2$ and $PtCl_4$ hence we will focus our study on these species. However, they are intrinsically strongly different:

PtO_2 is adsorbed on a different alumina site than the two others, $PtOCl_2$ is square planar while $PtCl_4$ corresponds to a pentahedral platinum. Therefore, the impact of chlorine might be convoluted with differences in initial coordination states. In order to focus on the role of chlorine, the reduction of the fully hydroxylated pentahedral $Pt(OH)_4$ is considered as a reference.

At this point it has to be noticed that desorption mechanisms are hard to describe using a static approach such as we did. Hence, most of them are described as inactivated steps by considering only the thermodynamic aspect of the desorption.

V.3.3.a) Reduction of Pt(IV) into Pt(II)

By considering H_2 as the reducing agent, four Pt(II) species are formed from the considered Pt(IV) species : $PtCl_2$, PtCl(OH), $Pt(OH)_2$ and PtO (**Figure V-7**). While $PtCl_4$ and $Pt(OH)_4$ produce $PtCl_2$ and $Pt(OH)_2$ or PtO respectively, three Pt(II) can be obtained from the reduction of $PtOCl_2$: $PtCl_2$, PtCl(OH) or PtO. (**Figure V-7**) Thermodynamically, at 775 K, PtO can be expected for P(HCl) lower than ~10^{-10} bar, PtCl(OH) for P(HCl) between 10^{-10} bar and $10^{-8.5}$ bar and $PtCl_2$ in expected for the remaining pressures up to 1 bar (**SI.9**). Hence, because of existence domain of $PtOCl_2$ after calcination (**section IV.3.4**) $PtCl_2$ should be expected. However, as we will see later, the formation of $PtCl_2$ and PtCl(OH) share many similarities and kinetically the formation of PtCl(OH) can be envisaged. The reduction of PtO_2 can lead to two theoretical Pt(II) products: $Pt(OH)_2$ and PtO. (**Figure V-7**) While the formation of $Pt(OH)_2$ is highly favorable at 0 K, the formation of PtO is favored with the increase of temperature due to the release of H_2O and at 775 K there is an inversion of the expected product (**SI.10, Part I**).

In summary, the five following global equations are considered during the reduction of Pt(IV) into Pt(II).

$$PtCl_4 + H_2 \rightarrow PtCl_2 + 2HCl \quad \textbf{Eq.11}$$

$$Pt(OH)_4 + H_2 \rightarrow Pt(OH)_2 + 2(H_2O) \quad \textbf{Eq.12}$$

$$PtOCl_2 + H_2 \rightarrow PtCl_2 + H_2O \quad \textbf{Eq.13}$$

$$PtOCl_2 + H_2 \rightarrow PtCl(OH) + HCl \quad \textbf{Eq.14}$$

$$PtO_2 + H_2 \rightarrow PtO + H_2O \quad \textbf{Eq.15}$$

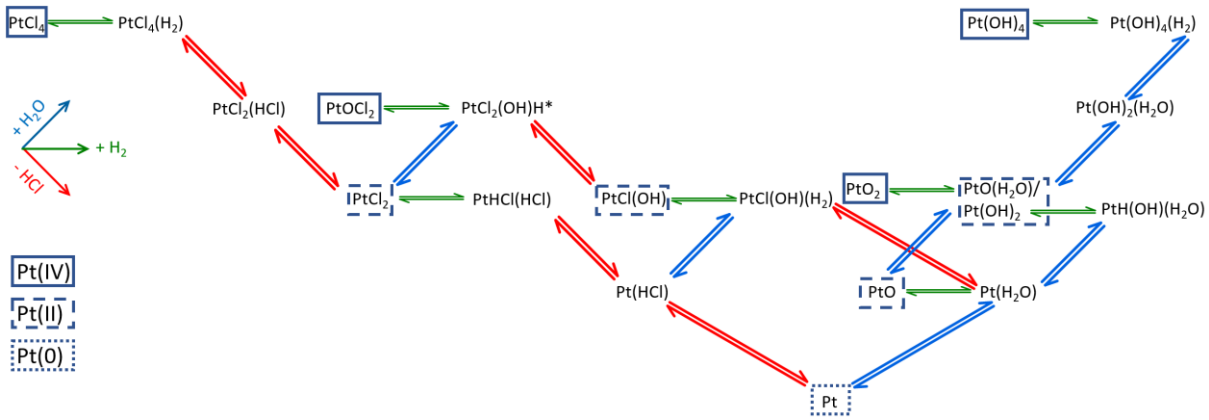

Figure V-7. Simplified representation of the network of reactions considered for the reduction of $PtCl_4$, $PtOCl_2$, $Pt(OH)_4$ and PtO_2 into Pt. Some relevant intermediates species (no frames) encountered along the reduction pathways are represented for the sake of clarity.

We report in **Figure V-8** the free energy profiles for the reduction of the Pt(IV) into Pt(II) and complementary information on the TS such as imaginary frequencies are reported in **Table SV-5**. As expected from the thermodynamic diagrams of the calcination, $PtOCl_2$ is the most stable Pt(IV) species at the considered conditions (T = 775 K, $P(H_2)$ = 1 bar, $P(H_2O) = 10^{-6}$ bar, P(HCl) = 10^{-6} bar), closely followed by PtO_2 then $PtCl_4$ and finally $Pt(OH)_4$. The absence of Pt(IV) in the reduction thermodynamic diagrams that were presented in the previous section resonates strongly with the highly negative reaction free energies for the reduction of all these Pt(IV) into Pt(II) from -436.4 kJ/mol for the reduction of $Pt(OH)_4$ into $Pt(OH)_2$ to -186.4 kJ/mol for the reduction of $PtOCl_2$ into PtCl(OH).

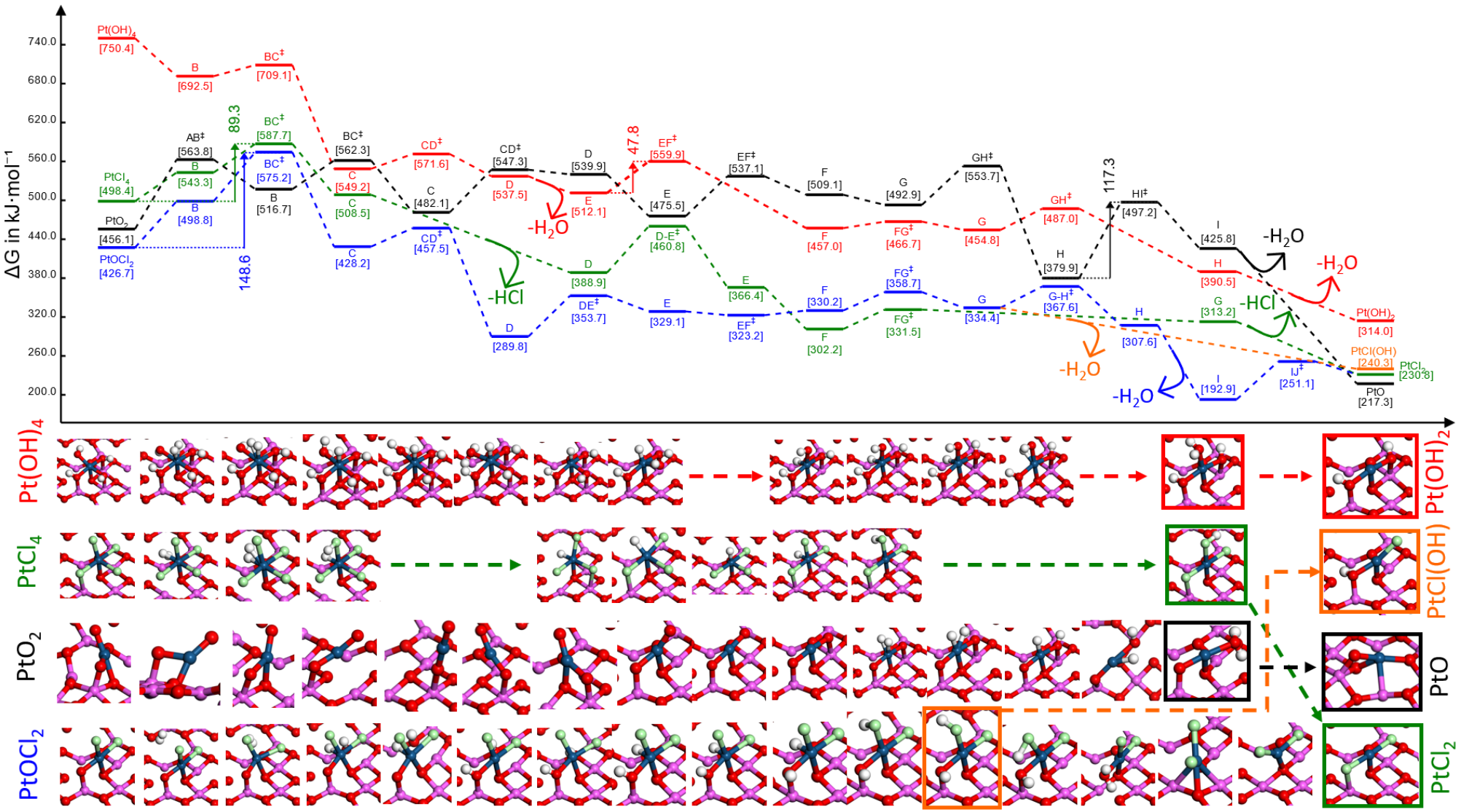

Figure V-8. Free energy profiles calculated at T = 775 K, P(H_2O) = P(HCl) = 10^{-6} bar and P(H_2) = 1 bar for Pt(IV) reduction into Pt(II) in the presence of H_2. The free energies are referenced with Pt/Al_2O_3 being at 0 kJ/mol. Transition states are indicated through the two letter and a double dagger (ex : $BC^{‡}$). Color code for atomic structures: Pt: blue; Cl: green; O: red; Al: pink, H: white. The higghest energy barrier is indicated by a vertical arrow for each profile.

Case of $Pt(OH)_4$ and $PtCl_4$

The main steps of the reduction of $PtCl_4$ and $Pt(OH)_4$ by H_2 (**Eq.11** and **Eq.12**) can be summed up as in the following **Eq**. 16 (with X = Cl or OH), with full pathways represented in green ($PtCl_4$) and red ($PtOH_4$) in **Figure V-8**.

$$PtX_4 + H_2 \rightarrow PtX_4(H_2) \rightarrow PtHX_3(HX) \xrightarrow{-HX} PtHX_3 \rightarrow PtX_2(HX) \xrightarrow{-HX} PtX_2 \quad \textbf{Eq. 16}$$

As it was previously described, the stability of platinum complexes is highly dependent on their geometries and ligands environment. And while the two penta-coordinated complexes $PtCl_4$ and $Pt(OH)_4$ share similar reduction mechanisms the free energies are clearly distinct. Because of their geometric similitude, we pin these differences to a chlorine effect. The first difference is the adsorption of H_2 which is exergonic at 775 K in presence of hydroxyls with - 57.7 kJ/mol for the formation of $Pt(OH)_4(H_2)$ (B_{red}) while + 44.9 kJ/mol are needed for the formation of $PtCl_4(H_2)$ (B_{green}) from $PtCl_4$. Moreover, the dissociation of H_2 is more activated in presence of chlorine with activation barriers of $\Delta G^{\ddagger}_{(BC-B)_{green}} = 44.4$ kJ/mol (with $\Delta G^{\ddagger}$calculated as the energy difference between the TS $BC^{\ddagger}$ and the reactant B for the green pathway. The ‡ indicates that one TS is considered) against $\Delta G^{\ddagger}_{(BC-B)_{red}} = 16.6\ kJ/mol$ for the formation of HCl and H_2O respectively.

Not only it is harder to form HCl rather than H_2O but the formation of H_2O results in a stronger stabilization of the system compared to the formation of HCl (C_{green} for $PtCl_3$(HCl) and D_{red} for $Pt(OH)(H_2O)$). While the formation of HCl leads to a small stabilization of - 34.8 kJ/mol compared to $PtCl_4(H_2)$ (B_{green}) the formation of H_2O is more stabilizing with - 171.6 kJ/mol compared to $Pt(OH)_4(H_2)$ (B_{red}). However, in the following steps, the desorption of HCl results in a stronger stabilization of the complex than the desorption of H_2O with $\Delta G_{(D-C)_{green}} = -119.6$ kJ/mol and $\Delta G_{(E-D)_{red}} = -25.4$ kJ/mol.

After some rearrangements (which require to overpass high activation barrier in the case of $PtCl_4$ with $\Delta G^{\ddagger}_{(DE-D)_{green}} = 71.9$ kJ mol-1), an almost square planar platinum is obtained in a configuration suitable to the formation of HCl or H_2O in apical position. The activation free energy barrier of this second formation of HCl/H_2O is similar in both cases with $\Delta G^{\ddagger}_{(FG-F)_{green}} = 29.3$ kJ/mol for $PtCl_4$ and $\Delta G^{\ddagger}_{(GH-G)_{red}} = 32.2$ kJ/mol for $Pt(OH)_4$, but once again, and despite the fact that the H_2O in apical position cannot interact with the surface, the formation of H_2O is more favored (– 64.3 kJ/mol, $G_{red} \rightarrow H_{red}$) whereas the formation of HCl ($F_{green} \rightarrow G_{green}$) is an endergonic step of + 11.0 kJ/mol.

The last desorption of water or HCl is energetically similar with – 76.5 kJ/mol for the formation of $Pt(OH)_2$ and -82.4 kJ/mol for $PtCl_2$.

Case of $PtOCl_2$

The main steps of the reduction of $PtOCl_2$ by H_2 into $PtCl_2$ (Eq.**13**) can be summed up as in the following **Eq. 17**, with full pathways represented in blue in **Figure V-8**. The alternative path leading to the formation of PtCl(OH) as described in **Eq. 18** for which steps until the formation of PtCl(OH)(HCl) are the same.

$$PtOCl_2 + H_2 \rightarrow PtHOCl_2H^* \rightarrow PtCl_2(OH)H^* \rightarrow PtHCl_2(OH) \rightarrow PtCl(OH)(HCl) \xrightarrow{-HCl} PtCl_2(H_2O) \xrightarrow{-H_2O} PtCl_2 \quad \textbf{Eq. 17}$$

$$PtOCl_2 + H_2 \rightarrow PtHOCl_2H^* \rightarrow PtCl_2(OH)H^* \rightarrow PtHCl_2(OH) \rightarrow PtCl(OH)(HCl) \xrightarrow{-HCl} PtCl(OH) \quad \textbf{Eq. 18}$$

The reduction of $PtOCl_2$ (blue pathway in **Figure V-8**) differs from the previous cases on many aspects, not only because of the square planar nature of the complex but also because of the presence of an oxo ligand which require two hydrogen atoms to be released as H_2O. First of all, no $PtOCl_2$ + H_2 systems were found stable with undissociated H_2 adsorbed on it. Thus, the adsorption of H_2 on the square planar $PtOCl_2$ starts with its dissociation leading to the formation of Pt-H and a hydroxyl on the alumina surface (C_{blue}) which has a Gibbs free energy very close to the naked $PtOCl_2$ (+ 1.5 kJ/mol). The role of Pt in the dissociation of H_2 being limited, the activation energy of H_2 is the highest calculated ($\Delta G^{\ddagger}_{(BC-C)_{blue}} = +148.5\ kJ/mol$). This more difficult activation may also be linked to the very stable nature of the square planar starting state, reluctant to coordination extension up to five, contrary to $PtCl_4$ and $Pt(OH)_4$ which are pentahedral, prone to become octahedral upon H_2 adsorption and dissociation.

The formation of a hydroxyl in place of the oxo ligand (C_{blue}→ $CD^{\ddagger}_{blue}$ →D_{blue}) is a highly stabilizing step ($\Delta G^{\ddagger}_{(D-CD)_{blue}} = -167.7$ kJ/mol) with a small activation barrier of $\Delta G^{\ddagger}_{(CD-C)_{blue}} = +29.3$ kJ/mol. Once D_{blue} is obtained, the proton of the alumina surface migrates to the platinum as exhibited in the $D_{blue} \rightarrow DE^{\ddagger}_{blue} \rightarrow E_{blue}$ steps (**Figure V-8**). Losing the stabilizing square planar nature of Pt between D_{blue} and E_{blue} results in a destabilization of $\Delta G_{(D-E)_{blue}} = +39.2$ kJ/mol. In order to form $PtCl_2$ or PtCl(OH) from F_{blue}, the hydrogen has to migrate, either on OH to form H_2O or on the apical Cl to form HCl. During our research of competitive pathways, we found out that in both cases the formation of HCl was the energetically more interesting mechanism. The transition state ($FG^{\ddagger}_{blue}$) leads to the formation of HCl with an activation free energy of + 38.5 kJ/mol, which is

consistent with the one calculated for the second formation of HCl in the $PtCl_4$ case. From the G_{blue} intermediate, HCl desorption leads to PtCl(OH) with an energy gain of -94.1 kJ/mol (orange path in **Figure V-8**). The formation of $PtCl_2$ (as expected from thermodynamic diagrams (**SI.9**) requires the formation of $PtCl_2(H_2O)$ (H_{blue}) through the transition state $GH^{\ddagger}_{blue}$. As this step is only weakly activated ($\Delta G^{\ddagger}_{(GH-G)_{blue}} = +33.2$ kJ/mol) it can considered as a kinetically competitive pathways from the formation of PtCl(OH). From H_{blue}, the desorption of H_2O and some internal rearrangements lead to $PtCl_2$.

Case of PtO_2

The main steps of the reduction of PtO_2 by H_2 into PtO (**Eq.15**) can be summed up as in the following **Eq.19**, with full pathways represented in black in **Figure V-8**. The reaction can be decoupled in two parts, the first one related to the change of adsorption site of PtO_2, and the second one for the formation and desorption of H_2O.

$$PtO_2^{(O_A-O_C)} \rightarrow PtO_2^{O_B} \rightarrow PtO_2 + H_2 \rightarrow PtO_2(H_2) \rightarrow PtHO(OH) \rightarrow PtO(H_2O) \rightarrow PtO \qquad \text{Eq.19}$$

Because of its bi-grafted nature, the reduction mechanism of PtO_2 is also different than the three others. Indeed, no H_2 adsorption was found possible on Pt as long as the complex is in this optimal adsorption site (O_A-O_C). Thus, we looked for preliminary step (before the reduction) and found that a relevant one consists in the diffusion of PtO_2 into another adsorption site (oxygen O_B, F_{black} in **Figure V-8**) where it can be reduced. Due to the strong nature of the bridging Pt-O-Al bonds, the activation barrier for diffusion is high ($\Delta G^{\ddagger}_{(AB-A)_{black}} = +107.7$ kJ/mol). At this point it has to be noted that no TS was successfully optimized between the two intermediates D_{black} and E_{black}. The exergonic adsorption of H_2 on F_{black} results in a stable square planar intermediate. The limiting step is the subsequent formation of the water molecule through the $HI^{\ddagger}_{black}$ TS with $\Delta G^{\ddagger}_{(HI-I)_{black}} = +117.3\ kJ/mol$. From I_{black} the water molecule desorbs to form PtO which is the most stable product from the thermodynamic point of view. However, from the H_{black} intermediate, it is also possible to form $Pt(OH)_2$ which is kinetically slightly more interesting (**SI. 10 Part II**).

With the previously presented pathways, and under the hypothesis about the inactivated desorption of H_2O or HCl, we observe that the surface almost does not contribute directly to the reduction of Pt(IV) into Pt(II) and that H_2O is desorbed as soon as it is formed in the coordination sphere of platinum. Starting from $Pt(OH)_4$, we considered in **Figure SV-11,** the formation of the second water molecule on the alumina surface (**Figure SV-11**, $ef'^{\ddagger}_{black}$). However, this requires overcoming a free energy barrier higher than 200 kJ/mol while only 32.2 kJ/mol were needed for the formation of the

second water molecule in the coordination sphere of Pt. We also consider the possibility that the platinum might act as a water reservoir and thus that multiple water molecules might be formed on the platinum (blue and green paths of **Figure SV-11**). However, in such hydrated environment, the formation of the second water molecule requires to overcome barriers between + 106.7 kJ/mol ($\Delta G^{\ddagger}_{(de''_{blue}-D_{red})} = +106.7$ kJ/mol) and ($\Delta G^{\ddagger}_{(de'''_{green}-D_{red})} = +151.1$ kJ/mol) depending on which hydroxyls are used to form H_2O (**Figure SV-11**). Thus, the preferred pathways are clearly those allowing the formation of water on platinum and its release each time right after its formation.

Accounting for the entropic and enthalpic effects largely impact the conclusion that could be drawn from the energy profile obtained at 0 K. (**SI.12**).

Many factor impact the reduction of the Pt(IV) into P(II). For a given geometry, higher activation barriers are calculated for chlorinated complexes rather than their hydroxylated counterpart. Moreover, the chlorine hardens the adsorption of H_2 on the platinum. This is the case for the pentahedral complexes ($PtCl_4$ and $Pt(OH)_4$) where the adsorption of undissociated H_2 becomes endergonic for $PtCl_4$. The square planar geometry of $PtOCl_2$, whose formation is favored by the presence of chlorine during the calcination (**Chapter IV**), lead to difficulties to start the reduction as the Pt center cannot participate to the dissociation of H_2. Finally, because of its different adsorption site PtO_2 its diffusion is first required before being reduced.

V.3.3.b) Reduction of Pt(II) into Pt(0)

Following the reduction of Pt(IV) into Pt(II), we might expect the formation of different species, $PtCl_2$ from $PtCl_4$ and $PtOCl_2$, $Pt(OH)_2$ from $Pt(OH)_4$, $PtCl(OH)$ from $PtOCl_2$ and PtO from PtO_2. (**Figure V-7**) We now consider the reduction of these four Pt(II) species into the reduced Pt(0) in presence of H_2. These reductions can be summed up as:

$$PtCl_2 + H_2 \rightarrow Pt + 2HCl \quad \textbf{Eq. 20}$$

$$PtCl(OH) + H_2 \rightarrow Pt + HCl + H_2O \quad \textbf{Eq. 21}$$

$$Pt(OH)_2 + H_2 \rightarrow Pt + 2H_2O \quad \textbf{Eq. 22}$$

$$PtO + H_2 \rightarrow Pt + H_2O \quad \textbf{Eq. 23}$$

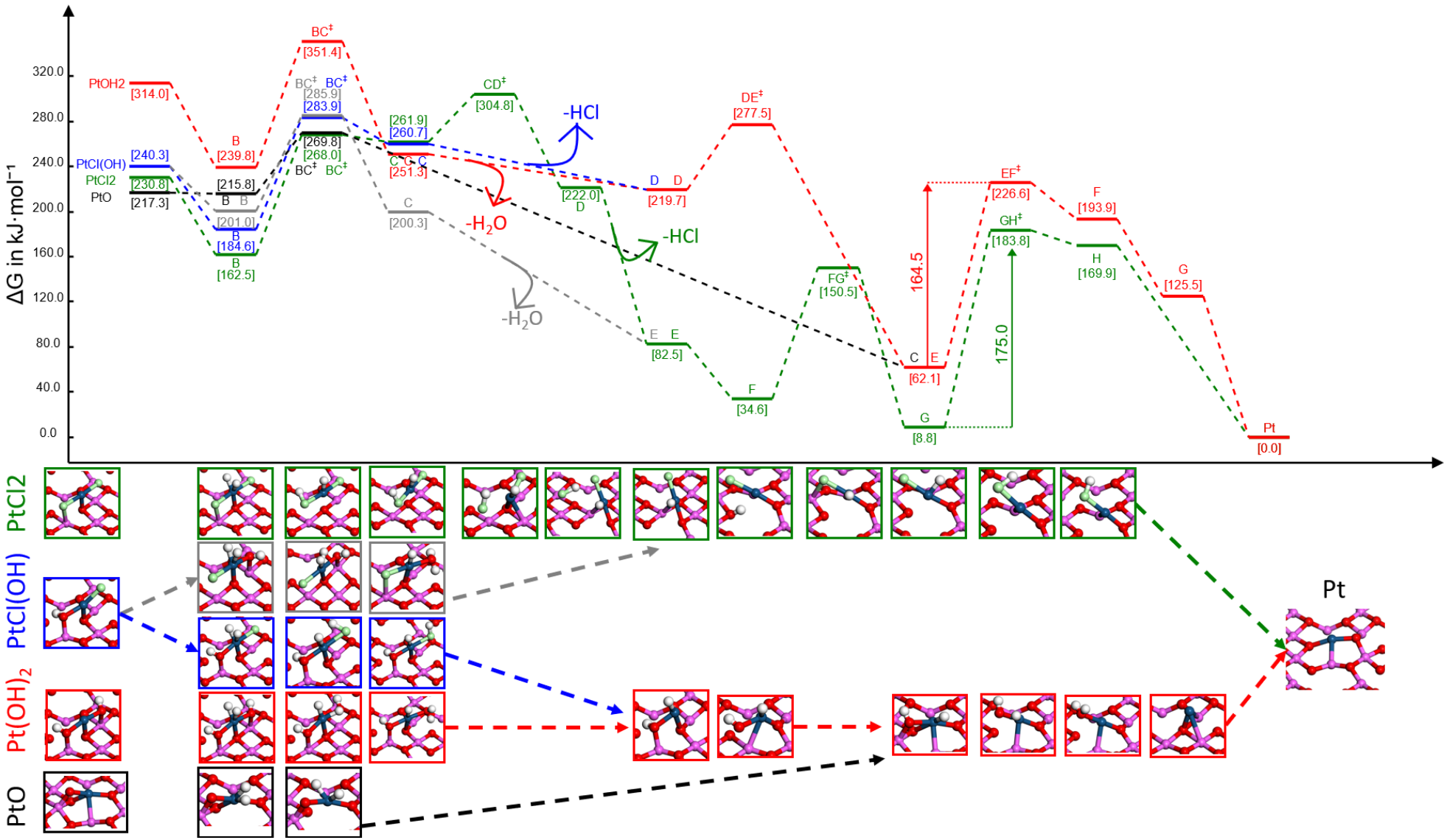

Figure V-9. Free energy profiles calculated at T = 775 K, $P(H_2O) = P(HCl) = 10^{-6}$ bar and $P(H_2) = 1$ bar for Pt(II) reduction into Pt(0) in the presence of H_2. The free energies are referenced with Pt/Al_2O_3 being at 0 kJ/mol. Transition states are indicated through the two letter and a double dagger (ex : $BC^{‡}$). Color code for atomic structures: Pt: blue; Cl: green; O: red; Al: pink, H: white.

The detailed pathways are presented in **Figure V-9** and details on the TS are reported in **Table SV-6**. Overall, and as predicted by the thermodynamic diagrams (**Figure V-6**), at P(H_2) = 1 bar, oxidized platinum (+II) species are not thermodynamically stable with respect to the final product Pt(0) and energy gains range between -314 kJ/mol for $Pt(OH)_2$ reduction to -217.3 kJ/mol for PtO reduction.

Among the four Pt(II) species, three of them share a similar geometry and adsorption site ($PtCl_2$, PtCl(OH) and $Pt(OH)_2$). Notably, we consider here the species at the locations they were formed starting from Pt(IV), without additional diffusion, which will be discussed in the next part. Conversely, PtO is adsorbed on another adsorption site (**Figure V-9**). Because of the PtCl(OH) asymmetry, different intermediates can be obtained through its reduction, and thus two possibilities were considered and are represented by the grey and blue pathways on **Figure V-9**. The blue one is the case where HCl is first formed and desorbed, while the grey one corresponds to H_2O formation and desorption. It has to be noted that an approximation has been made for the grey path where the B_{grey} and B_{blue} are conformers with B_{grey} obtained after a 180° rotation along the axis perpendicular to the surface, leading to a slightly less stable intermediate (+ 16.4 kJ/mol). Here, we neglected the presence of activation barriers during this process. In both cases, as soon as the first molecule (H_2O or HCl) is formed and desorbed, the remaining pathways are equivalent to the reduction of $PtCl_2$ or $Pt(OH)_2$ after their first desorption of HCl or H_2O respectively. In spite of differences at the initial state, the reduction of PtO pathway quickly merges with the reduction of $Pt(OH)_2$ (C_{black} is equivalent to E_{red}). In the end, while five possibilities were considered for the first activation of H_2, only two remain for the second activation (green and red paths). The limiting steps occur in all cases during the formation of the last labile molecule (HCl with the $EF^{\ddagger}_{red}$ transition state and water with the $GH^{\ddagger}_{green}$ transition state) and their barriers are almost equal with $\Delta G^{\ddagger}_{(EF-E)_{red}} = 164.5\ kJ/mol$ and $\Delta G^{\ddagger}_{(GH-G)_{green}} = 175.0\ kJ/mol$.

$$PtX_2 + H_2 \rightarrow PtX_2(H_2) \rightarrow PtHX(HX) \xrightarrow{-HX} PtHX \rightarrow Pt(HX) \xrightarrow{-HX} Pt \qquad \textbf{Eq.24}$$

$$PtO + H_2 \rightarrow PtH(OH) \rightarrow Pt(H_2O) \xrightarrow{-H_2O} Pt \qquad \textbf{Eq.25}$$

The reduction is again highly dependent on the geometry of complexes with similar behavior for the three $PtCl_2$, PtCl(OH) and $Pt(OH)_2$ (**Eq.24**) whereas PtO differs in its first part (**Eq.25**). On one hand, the H_2 adsorption on PtO (B_{black}) is almost thermo-neutral and does not result in changes on the Pt adsorption site. The activation of H_2 to form OH (C_{black}) requires overcoming a barrier of + 54 kJ/mol through the $BC^{\ddagger}_{black}$ transition state. As soon as C_{black} is formed the following steps of the reduction are described by the red path. On the other hand, the adsorption of H_2 on the three other Pt(II)

species results in the formation of more stable square planar platinum. As for Pt(IV), the absence of chlorine favors H_2 adsorption by -74.2 kJ/mol calculated for the formation of $Pt(OH)_2(H_2)$ (B_{red}), while the lowest energy gain is calculated for B_{blue} with -55.7 kJ/mol. The case of B_{grey} is slightly different, due to the configurational change with respect to B_{blue} which implies sub-optimal bonding with the support. The complex (B_{grey}) is intrinsically destabilized compared to B_{blue} and an overall stabilization of only - 39.3 kJ/mol is calculated for the rotation of the complex and the adsorption of H_2. The next step is the dissociation of H_2 and formation of the labile molecule through the $BC^{\ddagger}$ transition states. The formation barrier of HCl is almost independent on the nature of the non-contributing ligand with $\Delta G^{\ddagger}_{(BC-B)_{green}} = +105.5$ kJ/mol and $\Delta G^{\ddagger}_{(BC-B)_{blue}} = +99.3$ kJ/mol, while in the case of the formation of water, the presence of chlorine in the coordination sphere of the platinum lowers the barrier with $\Delta G^{\ddagger}_{(BC-C)_{red}} = +111.6$ kJ/mol and $\Delta G^{\ddagger}_{(BC-B)_{grey}} = +84.9$ kJ/mol. As soon as the $C_{green,red,blue,grey}$ intermediates are formed, the desorption of HCl/H_2O occurs. However, in the case of $PtCl_2$, a metastable intermediate (D_{green}) was found with desorbed HCl in proximity to the platinum and a TS ($CD^{\ddagger}_{green}$) for the desorption of HCl was obtained. After the first desorption, rearrangements are needed to get the highly stable E_{red} and G_{green} from D_{red} and E_{green} (**Figure V-9**). In the case of $PtCl_2$, the support plays a role by capturing the proton (F_{green}) as the complex rotates, but around + 116 kJ/mol are needed to form $G_{green}$where the hydrogen is back on Pt. We acknowledge that a more direct and less activated simple rotation from E_{green} to G_{green} might exist to link these two states. However, such transition was not found during this study. The final step, as described previously, is the reduction of these two complexes (E_{green} and G_{green}) through a direct migration of H from the platinum to the ligand in order to get the labile molecule.

As for the reduction of Pt(IV) into Pt(II) the importance of accounting for the entropic and enthalpic effect is highlighted by the highly distinct energy profile obtained at 0 K. (**SI.15**). In the search of the presented reduction profiles, we found out that in the case of $PtCl_2$ and $Pt(OH)_2$ the role of the surface and the position of the first ligand to be removed from the Pt impact the energetic profile of the reduction. We report these cases in **SI.16** for $PtCl_2$ and **SI.17** for $Pt(OH)_2$.

The reduction of the considered Pt(II) share many similitudes, and compared to the reduction of Pt(IV) into Pt(II), the impact of the nature of the coordination sphere is lower. In all cases, the highest activation barrier is calculated for the formation of the last labile molecule. The very high stability of the intermediates obtained prior to this last step (PtH(OH) and PtHCl) is exacerbated in presence of chlorine, however this stabilization due to the chlorine is also reported to the next TS (**Figure V-9**), hence similar activation barriers are observed for the reduction of PtH(OH) and PtHCl into Pt.

V.3.3.c) Migration of bi-grafted complexes

For the Pt(II) complexes with two ligands, the most stable conformations were obtained on different adsorption sites with respect to those obtained from reduction of Pt(IV). In the latter case, platinum is bound to a single oxygen atom from the support, whereas in the former, platinum is bonded to two oxygens of the alumina surface (**Figure SV-5**). Indeed, during the reduction of the Pt(IV) complexes ($PtCl_4$, $PtOCl_2$ and $Pt(OH)_4$), the reduced Pt(II) complexes $PtCl_2$, PtCl(OH) and $Pt(OH)_2$ are generated on the same adsorption sites than their Pt(IV) precursors, but this does not correspond to the most stable adsorption site. Thus, the question of the migration of these species during the reduction arises. Either the partially reduced Pt(II) remain on the same adsorption site and the reduction into Pt(0) occur as we saw in the previous section, or they migrate into stabilizing adsorption site (**Figure V-3**). Alongside the stabilization of the complexes, the most stable adsorption site for bi-grafted complexes (O_A-O_C) strongly hardens the reaction (adsorption) of H_2 on the platinum complex. Indeed, despite numerous attempts, we were never able to adsorb H_2 on these bi-grafted complexes leading to the conclusion that the O_A-O_C site could be responsible for stopping the reduction of the platinum and trapping oxidized Pt(II) complexes. Moreover, the self-reduction of $PtCl_2$ into Pt by release of Cl_2, or through the migration of Cl on the surface is not expected to occur after adsorption starting from this bidentate site, due to thermodynamical reasons (**SI 21**). Similar results were obtained for the self-reduction for $Pt(OH)_2$ and the migration of OH on the surface (**SI 21**).

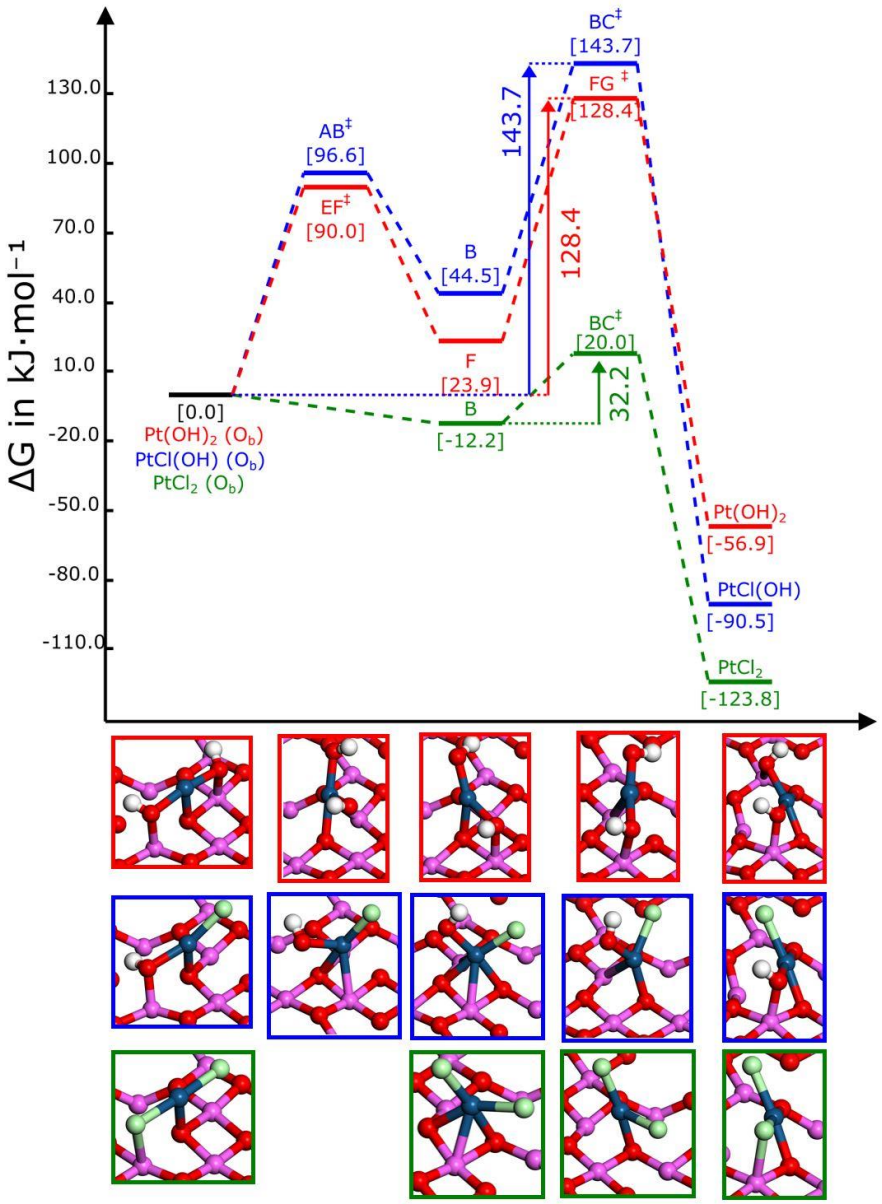

Figure V-10. Free energy profiles calculated at T = 775 K, P(H_2O) = P(HCl) = 10^{-6} bar and P(H_2) = 1 bar for the key steps of the bi-grafted Pt(II) migration. Steps that are not limiting to the migration are reported with the full pathways in SI.12. Transition states are indicated through the two letter and a double dagger (ex: BC‡). Highest activation barriers of the migration are reported. The free energies are referenced for the reactant of each profile are chosen at 0 kJ/mol. Color code for atomic structures: Pt: blue; Cl: green; O: red; Al: pink, H: white.

As we can expect, the coordination sphere of platinum plays a key role on its migration. **Figure V-10** shows that the migration of $PtCl_2$ is almost not activated ($\Delta G^{\ddagger}_{(BC-B)_{green}} = +32.2$ kJ/mol) accompanied by -123.8 kJ/mol of free energy gain for the final migration. Replacing at least one chlorine by an hydroxyl leads to a significant higher activation barriers with $\Delta G^{\ddagger}_{(BC-C)_{blue}} = +143.7$ kJ/mol for PtCl(OH) and $\Delta G^{\ddagger}_{(FG-F)_{red}} = +128.4$ kJ/mol for $Pt(OH)_2$. In addition to these higher activation barriers, the stabilization free energy due to the change of adsorption site is lowered as

chlorines are replaced by hydroxyls, and thermodynamically the migration leads to an energy gain of -90.5 kJ/mol and -56.9 kJ/mol only for PtCl(OH) and $Pt(OH)_2$, respectively. Thus, for the migration of Pt(II) species, Cl ligands play a dual role, while it speeds up the migration by lowering the activation barrier, it also highly stabilizes the product of the migration in higher proportions.

The first step of the $PtCl_2$ migration is not activated and weakly stabilizes $PtCl_2$. It corresponds to the bonding of the Pt to both an oxygen (O_A) and an aluminum in addition to the rupture of a Cl-Al bond (B_{green}) (**Figure V-10** (green path)). Only one TS separates this intermediate to the bi-grafted $PtCl_2$ (O_A-O_C). The Pt-Al bond is then elongated and in $BC^{\ddagger}_{green}$ the platinum is only bonded to the O_A site. The distance between the surface and the platinum remains similar for the three intermediates $PtCl_2$ (O_B), B_{green} and $PtCl_2$ (O_A-O_C) but is slightly elongated for the TS $BC^{\ddagger}_{green}$. During the migration, the platinum and one chlorine remain at an almost constant distance to the surface, while the remaining Al-Cl-Pt bond is highly elongated in B_{green} and $BC^{\ddagger}_{green}$ which suggest that this second chlorine does not participate much to the migration process (**Table V-3**).

The case of PtCl(OH) is very similar with one supplementary TS corresponding to the breaking of the OH-Al bond at the beginning of the process ($AB^{\ddagger}_{blue}$ in **Figure V-10**). The anchoring of the reactant and product of the diffusion of PtCl(OH) is mostly done through the hydroxyl, however its influence on the stabilization of the complex along the migration is lessened as HO-surface distances are elongated of more than 1Å (compared to the reactant) during all the diffusion (**Table V-3**).The Pt-surface distances are only slightly modified along the migration. The Cl remains far from the surface during all the migration, but it can be noted that this is also the case for the product and reactant where the distance between the chlorine and the surface is more than 1 Å longer than for $PtCl_2$ (**Table V-3**). In the PtCl(OH) case, the migration is mostly driven by the diffusion of the platinum while the ligands remain dangling, hence few intermediates are encountered, but they are energetically high.

Replacing the second chlorine by a hydroxyl gives rise to many more intermediates and transition states due to the stronger interaction between the hydroxylated complex and the surface. (**Figure SV-4**) Moreover, because of the lower flexibility of the complex, at least one Pt-OH-Al bond with the surface is kept all along the migration (**Table V-3**), hence, and contrasting with the previous cases, not only Pt-surface bonds are involved but also O(H)-Al bonds are broken and formed during all the diffusion which harden the diffusion of the complex. The first step is the breaking of one (OH)-Al bond (**Figure V-10** (red path)). The activation barrier is more than twice smaller than the one calculated for the breaking of the (OH)-Al bond in PtCl(OH), but note that the hydroxyl implicated is not the same. This forms the B_{red} intermediate, almost as stable as the reactant (+4.3 kJ/mol)

because of entropic stabilization at 775 K (**Figure SV-15**). Again, numerous intermediates and TS are then needed to transfer the hydroxyl from the former Al on which the reactant was bonded to the Al on which it is bonded in the product as exhibited in F_{red}. During all these successive steps, Pt remains bonded to O_B. Finally, by using as an anchor the newly formed Al-OH-Pt bond in F_{red} the platinum migrates in the O_A-O_C adsorption site after breaking the Pt-O bond which requires overcoming the highest activation barrier of the process with $\Delta G^{\ddagger}_{(FG-A)_{red}} = 128.4$ kJ/mol.

Intermediate	Shortest Pt-O_{surf} (Å)	Shortest Cl-Al_{surf} (Å)	Shortest HO-Al_{surf} (Å)
$PtCl_2$ migration			
$PtCl_2$ (O_B)	1.99	2.39 2.53	NC
B_{green}	2.09	2.53 4.28	NC
$BC^{\ddagger}_{green}$	2.16	2.48 4.63	NC
$PtCl_2$ (O_A-O_C)	2.03	2.40 2.96	NC
PtCl(OH) migration			
PtCl(OH) (O_B)	1.99	3.92	1.85
$AB^{\ddagger}_{blue}$	2.09	4.52	2.89
B_{blue}	2.18	3.78	4.19
$BC^{\ddagger}_{blue}$	2.12	4.3	3.9
PtCl(OH) (O_A-O_C)	2.04	3.23	1.89
$Pt(OH)_2$ migration			
$Pt(OH)_2$ (O_B)	1.95	NC	1.90 1.96
$EF^{\ddagger}_{red}$	2.08	NC	2.69 3.84
F_{red}	2.07	NC	1.94 4.06
$FG^{\ddagger}_{red}$	2.56	NC	1.94 3.53
$Pt(OH)_2$ (O_A-O_C)	1.98	NC	1.91 2.11

Table V-3. Key distances along the diffusion process of the bi-grafted Pt(II): $PtCl_2$, PtCl(OH) and $Pt(OH)_2$. NC indicates that the value has not been calculated.

Interestingly, we can compare the migration of these bi-grafted Pt(II) species to the first part of the reduction of PtO_2 which also correspond to its migration (**SI.18**). While we could expect that PtO_2 would be at least as hard as $Pt(OH)_2$ to move on the surface, it appears that the activation barrier is slightly lowered and calculated at $\Delta G^{\ddagger}_{(AB-E)_{black}} = 88.3\ kJ/mol$.

The temperature eases the migration of the species over the surface as the activation barriers calculated at 0 K (**Figure SV-16**) are between 15 kJ/mol and 20 kJ/mol higher than those calculated at 775 K (**Figure V-10**). However, as the impact of the temperature is limited to the vibrational component of the Gibbs free energies (no desorption is considered) both profiles share many similitudes.

Overall, the pathways describing the migration of these species remain are quite similar in term of mechanisms encountered. Adding hydroxyls or oxo ligands increases the number of intermediates along the migration path, notably because they are more prone to interact with the surface

aluminum and in fine this highly harden the diffusion of the platinum complex (**Figure SV-15**). While the chlorine did not impact much the reduction of the Pt(II) into Pt(0), its impact on the migration of the Pt(II) is striking. In comparison with hydroxyl ligands, not only does chlorine accelerate the migration of platinum complexes into the O_A-O_C adsorption site but it also stabilizes the product of such migration in bigger proportion.

V.4. Discussion

The reduction of the SA platinum obtained after calcination has been investigated both from a thermodynamic and a kinetic point of view. The importance of a fine control over the calcination condition is exhibited by the highly distinct responses of $PtCl_4$, $PtOCl_2$ and PtO_2 to the reduction by H_2. The nature of the species obtained post calcination will substantially impact the intermediates encountered along the reduction and in fine, the product of the reduction step. These complexes, because of their single atom nature, are highly impacted by the nature of the coordination sphere, or the complex geometry. We retrieve some results such as the intrinsic stability of square planar and octahedral complexes or the higher stability of chlorinated complexes that were observed in a study dedicated to similar platinum complexes but in absence of the support.[60] However the surface actively participates in the complexes chemistry through various possible adsorption sites which add a layer of complexity in the chemistry that need to be considered to describe these SA species. Thermodynamically, the chlorine, through the formation of a bi-grafted $PtCl_2$, enhances the resistance of oxidized platinum towards reduction against temperature and H_2 pressure. Its stability increases as the HCl pressure in the system increases (and thus the quantity of chlorine). For the highest HCl pressure considered ($P(HCl)=1.10^{-6}$ bar), $PtCl_2$ was found stable at 775 K for $P(H_2)$ up to 10^{-6} bar. Kinetically, the chlorine acts differently depending on the stage of the reduction. A condensed representation of the most relevant reduction and migration steps according to the platinum oxidation level is reported in **Figure V-11**. For each stage of the reduction, the TS with highest activation barrier is reported in addition to the key intermediates. Numerical values for the highest activation barriers are reported in **Table V-4**. For the first step of the reduction (Pt(IV) → Pt(II)), chlorine plays a double role. The first one is inherited from the calcination through the stabilization of a square planar $PtOCl_2$ which kinetically hardens the adsorption and reaction of the first H_2 molecule on it (+148.6 kJ/mol in **Table V-4**) because of its geometry and thus refrains the start of the reduction. In a second time, in the case of complexes geometrically similar, chlorine lowers the affinity of the Pt for H_2 and increases the required energy to overcome the activation barriers along the reduction process with a limiting step calculated at + 89.3 kJ/mol for with

$BC^{\ddagger}_{green}(IV)$ for $PtCl_4$ against 32.2 kJ/mol with $E^{\ddagger}_{red}(IV)$ for $Pt(OH)_4$ (**Table V-4** and **Figure V-11**). Since in **Figure V-11**, several intermediates or TS share the same name, in what follows, we will annotate (IV) species involved in reduction Pt(IV) into Pt(II), and (II) for species involved in the reduction of Pt(II) into Pt(0). Finally, the species from the diffusion process will be annotated with $(migration)$. PtO_2 is different from the other Pt(IV) as it first needs to migrate in a similar fashion than for the bi-grafted Pt(II) before it can adsorb H_2. This migration step requires to overcome the highest free energy of the pathway ($AB^{\ddagger}_{black}$) in **Figure V-8** and omitted for the sake of clarity in **Figure V-11**), but the highest activation barrier is encountered for the formation of the water molecule through $HI^{\ddagger}_{black}(IV)$.

During the second part of the reduction Pt(II) → Pt(0), the impact of chlorine is less pronounced with respect to oxygen ligands. The limiting steps exhibit similar activation free energies: +175 kJ/mol for $PtCl_2$ against +164.5 kJ/mol for $Pt(OH)_2$. Moreover, we can note that the intermediate from which these barriers are calculated are relatively stable with respect to our reference Pt(0), with only + 8.8 kJ/mol for $G_{green}(II)$ $(PtHCl)$ and +62.1 kJ/mol for $E_{red}(II)$ $(PtH(OH))$. Thus, in absence of chlorine PtH(OH) might be able to last the reduction step while. In presence of chlorine, PtHCl become also a strong candidate for the single atoms located on the (100) surface, moreover, because of its higher stability compared to PtH(OH) we might suspect it might be responsible for an increase of the SA population in presence of chlorine. Hence we could suspect that both PtHCl, and in a lower proportion PtH(OH), might represent a proportion of the platinum single atom species reluctant to reduction. (**Figure V-11**)

The adsorption of H_2 is quite similar with -68.3 kJ/mol for the formation of $PtCl_2(H_2)$ and -76.9 kJ/mol for the formation of $Pt(OH)_2(H_2)$. In both cases high activation barriers of +142.3 kJ/mol ($CD^{\ddagger}_{green}(II)$) and +116.6 kJ/mol ($BC^{\ddagger}_{red}$ (II)) have to be overcome in order to form PtHCl ($G_{green}(II)$) and PtH(OH) ($E_{red}(II)$). However, at this step, these Pt(II) species are not adsorbed in their most favorable adsorption, thus, alongside their reduction into Pt(0), a competing migration process might occur. (**Figure V-11**)

The migration of $PtCl_2$ is highly stabilizing (-123.8 kJ/mol) and require to overcome a very small barrier of 32.2 kJ/mol ($BC^{\ddagger}_{green}(migration)$), however, adding at least one hydroxyl not only diminishes the gain from the migration but also largely increases the activation barrier (up to 143.7 kJ/mol in the case of PtCl(OH) and 128.4 kJ/mol for $Pt(OH)_2$) (**Table V-4**). Hence, in the case of $PtCl_2$, the competition between reduction and migration is clearly in favor of the migration, while for PtCl(OH) and $Pt(OH)_2$ both pathways are competitive. (**Figure V-11**)

By itself, the migration is not enough to explain the reluctance of $PtCl_2$ to undergo its reduction into Pt(0). However, we found out that H_2 (dissociated or not) could not be adsorbed on the platinum as long as the platinum was bi coordinated to the surface through the two oxygens O_A and O_C (**Figure V-3**). Moreover, as the self-reduction of $PtCl_2$ into Pt through the migration of Cl onto the surface or the release of Cl_2 is also not thermodynamically expected (**SI.21**), this specific adsorption site for Pt(II) species could thus act as an inhibitor against the reduction**.**

From these results, we suspect that a larger proportion of $PtCl_2$ species that are expected after the reduction of the chlorinated $PtCl_4$ or $PtOCl_2$ species obtained themselves after calcination in presence of Cl, end up in this irreducible and highly stable form that is the bi-grafted $PtCl_2$. By contrast, for PtCl(OH) and $Pt(OH)_2$ the competition between the migration and the adsorption of a second H_2 to continue the reduction and obtain Pt(0) is tighter. In addition, along the path leading to Pt(0) a higher proportion of PtHCl could be stabilized with the increase of the chlorine loading. This combination could be part of the explanation for the experimentally observed increase of the number of SA in presence of chlorine during the reduction[21–23,31,53]. As a consequence, the Pt SAs that are favored under high chlorine loading[21] could be this highly stable but lowly reactive $PtCl_2$. The low activity hypothesis of such species is based on the difficulties that we encountered to adsorb something on it, and while a study dedicated to the reactivity of such species might be needed to reach a definite conclusion on the subject, it echoes with experimental observation relation the lower activity of chlorinated catalysts.

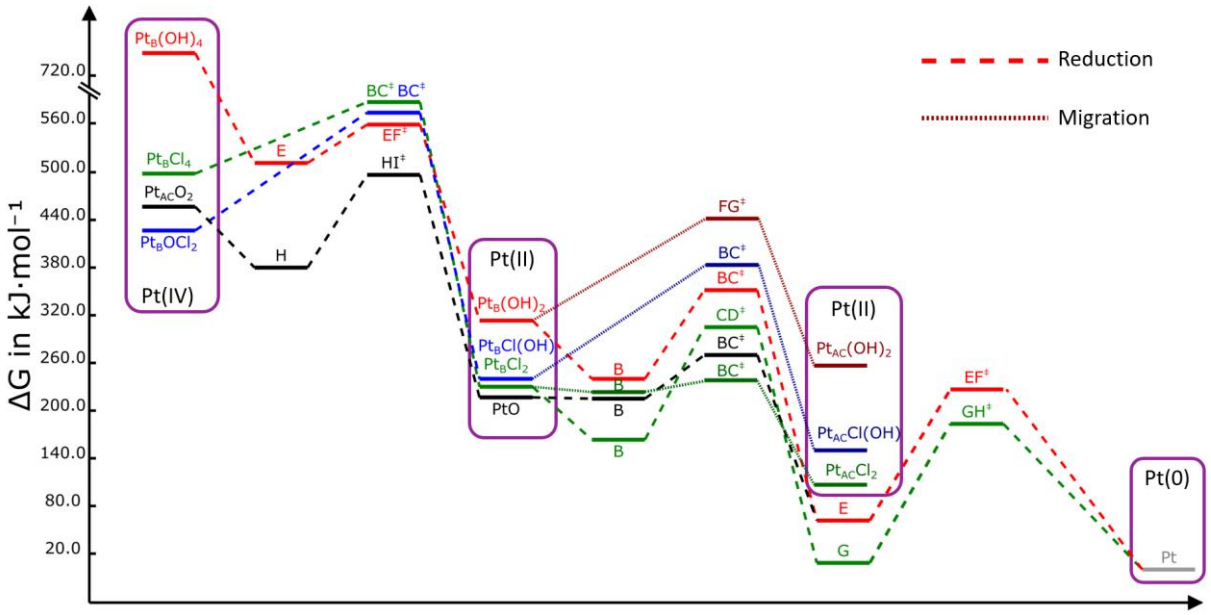

Figure V-11. Simplified representation of the reduction of Pt(IV) into Pt(0). For each complex and for each step investigated (Pt(IV) → Pt(II), Pt(II) → Pt(0) and Pt(II) migration) highest free energy TS with the intermediate from which the barrier is calculated are reported in addition to key intermediates. The same nomenclature than for each step has been used. (Pt(IV) → Pt(II) : Figure V-8; Pt(II) → Pt(0) : Figure V-9; Pt(II) migration : Figure V-10. The adsorption site of the intermediate is indicated through indices when required. Numerical values for highest free energy activation barriers are reported in Table V-4.

Type	Reaction	Highest activation barrier (kJ/mol)
Pt(IV) → Pt(II)	$PtCl_4$-(O_B) + H_2 → $PtCl_2$-(O_B) + 2HCl	89.3
	$Pt(OH)_4$-(O_B) + H_2 → $Pt(OH)_2$-(O_B) + 2H_2O	47.8
	$PtOCl_2$-(O_B) + H_2 → $PtCl_2$-(O_B) + H_2O	148.6
	PtO_2-(O_A-O_C) + H_2 → PtO-(O_B -O_C-Al_I) + H_2O	117.3
Pt(II) → Pt(0)	$PtCl_2$-(O_B) + H_2 → Pt-(O_B -O_C-Al_I) + 2 HCl	175.0
	$Pt(OH)_2$-(O_B) + H_2 → Pt-(O_B -O_C-Al_I) + 2 H_2O	164.5
Migration	$PtCl_2$-(O_B) → $PtCl_2$-(O_A-O_C)	16.8
	PtCl(OH)-(O_B) → PtCl(OH)-(O_A-O_C)	128.4
	$Pt(OH)_2$-(O_B) → $Pt(OH)_2$-(O_A-O_C)	143.7

Table V-4. Summary of the highest free energy activation barriers at 775K for every stage of reduction considered.

The existence of such post-reduction $PtCl_2$ is supported by various studies and its properties could rationalize experimental observations. Quite explicitly Smolikov et al.[42] suggested that the reduction of the catalyst made from H_2PtCl_6 precursors lead to ~10% of the supported platinum that could be Pt(II) with chloride ligands coexisting with disperse metallic particles.[42] This estimation is relatively close to more recent observations from Batista et al. who suggested from HAADF-STEM that around 20% of the platinum were present as single atoms.[30]

Moreover, the reluctance of $PtCl_2$ upon H_2 adsorption is consistent with an observation from Samoila et al.[85] who noticed that during the preparation of various supported metals (Ir, Pt and Rh) on Al_2O_3 the adsorption of hydrogen atoms on metals decreased with the amount of Cl in the system. Moreover, our difficulties to adsorb H_2 on such bi-grafted $PtCl_2$ seem to be in lines with experimental observations about the poisoning effect of Cl during oxidation reactions[23–26]. In their study on the oxidation of methane catalyzed by Pt/Al_2O_3 catalysts, Marceau et al.[24,25] observed a the decrease of the activity of freshly reduced catalyst obtained from chlorinated precursors, while after hours of reaction the activity becomes independent of the nature of the precursors. They suspected that chlorine could remain bonded to platinum after the reduction and thus prevent adsorption of methane, similarly to what we observed for the adsorption of H_2 on $PtCl_2$. The chlorine is then progressively removed during the use of the catalyst until the platinum sintering dominates, and the activity of the catalyst drops. This last observation highlights how the presence of chlorine is necessary to maintain the SA population. However, it has to be noticed that the oxidation of methane and other considered reactions are carried out in oxidizing conditions, which is different from what we considered here to establish the existence of $PtCl_2$ after reduction. As the conditions of preparation of these catalysts are however similar to what we modelled[24], we can suspect that our calculated $PtCl_2$ exists after the preparation of the catalyst. By considering its relative stability under oxidant conditions as developed in **SI 22** we show that if the bi-grafted $PtCl_2$ supported on the (100) surface of the γ-Al_2O_3 is formed during the reduction, it is expected to remain thermodynamically stable under the conditions used for the considered reactions (**Figure SV-19**). Hence, our calculations tend to corroborate the hypothesis of Marceau et al.[24,25] on the nature of the platinum species responsible for the decrease of activity during oxidation reactions.

As such, $PtCl_2$ species seem to not be used as a proper metallic site, its role as a catalytic system remains unclear. On one hand it could act as a chlorine reservoir on the (100) surface. Recently it was found that the γ-Al_2O_3 edges could endorses such role as the replacement of the hydroxyls adsorbed on edges by chlorine was calculated to be favorable from DFT calculations[21]. These complexes could act in a similar way on the (100) surface where chlorines are not expected to remain adsorbed on the surface (**S.15**). This hypothesis could be in line with the observation of Lieske et al.[35] who suggested that chlorines should remain on the surface after the reduction. Finally, we can speculate that by maintaining a population of chlorine on the (100) surface, the complex could help stabilize other reduced platinum single atoms. Indeed, in the XAS study of Stakheev et al.[43], they found out that by depleting electronically the oxygen of the support supported chlorine was responsible for stronger $Pt\text{-}O_{support}$ bonds. While this was established for platinum cluster, we can suspect that such result

remains true in case of SA. In that case, the stabilization of chlorine on the (100) through $PtCl_2$ could reduce the mobility of the reduced Pt(0) and restrain their aggregation on the same surface.

V.5. Conclusion

Platinum single atom ($PtO_xCl_y(OH)_z(H_2O)_n(H_2)_m$) with oxidation degrees ranging from 0 to +IV and supported on the (100) γ-Al_2O_3 surface have been studied by periodic DFT simulations. The evolution of these complexes, inherited from the calcination, under a reducing atmosphere has been described from both thermodynamical and kinetical points of view. The structural and energetic properties of these complexes highlighted the role of the surface in the stabilization of undercoordinated platinum and a relationship between the number of ligands in the coordination sphere of the platinum and the favored adsorption site was established. The intrinsic stability of square planar and octahedral platinum has been noticed and take an important place in the chemistry of these supported SA.

The relative stability of these supported complexes during the reduction has been assessed from the calculation of first principles thermodynamic diagrams. By accounting for realistic conditions, we highlighted how the chlorine could enhance the resistivity against reduction through the formation of Pt(II) species such as SA $PtCl_2$. Chlorine not only increases the reduction temperature, but also lower the affinity of the Pt for H_2, even if under $P(H_2)$ = 1 bar, the reduction into Pt(0) is still thermodynamically expected.

As a consequence, $PtCl_2$ is a kinetically key species during reduction of the supported Pt complexes. By considering the reduction mechanism of four relevant Pt(IV) species into a reduced Pt(0), we showed that higher activation barriers had to be overcome in presence of chlorine to reduce the Pt(IV) into Pt(II). Moreover, as soon as Pt(II) are formed and alongside the continuation of the reduction into Pt(0), chlorine, through the formation of $PtCl_2$, offers an energetically competitive migration of the complex into an adsorption site where its reduction will be greatly hardened. We also establish that $PtCl_2$ supported on the (100) γ-Al_2O_3 would subsist under the oxidizing conditions used in oxidation reaction, and thus might help rationalize the lower activity of Pt/Al_2O_3 catalyst in presence of chlorine for these oxidation reactions. Hence, while chlorine might increase the proportion of SA after reduction by stabilizing a highly stable $PtCl_2$, the role of such species as an active metallic site remains blurry and might need further investigations.

For the first time, we provided through an ab initio approach a rational description of the role of chlorine on the dispersion of platinum. We expect this study to provide a better understanding of the

activation (reduction) step of alumina supported platinum catalysts and hence a better control over the genesis of the Pt SA on γ-Al_2O_3.

V.6. References

1. Kaiser, S. K., Chen, Z., Faust Akl, D., Mitchell, S. & Pérez-Ramírez, J. Single-Atom Catalysts across the Periodic Table. *Chem. Rev.* **120,** 11703–11809 (2020).
2. Serp, P. & Minh, D. P. *Supported Metal Single Atom Catalysis* (Wiley, 2022).
3. Liu, J. Catalysis by Supported Single Metal Atoms. *ACS Catal.* **7,** 34–59 (2017).
4. Chen, A. & Holt-Hindle, P. Platinum-based nanostructured materials: synthesis, properties, and applications. *Chem. Rev.* **110,** 3767–3804 (2010).
5. Farrauto, R. J. & Heck, R. M. Catalytic converters: state of the art and perspectives. *Catal. Today* **51,** 351–360 (1999).
6. Huber, G. W., Cortright, R. D. & Dumesic, J. A. Renewable alkanes by aqueous-phase reforming of biomass-derived oxygenates. *Angew. Chem. Int. Ed.* **43,** 1549–1551 (2004).
7. Zhang, F. *et al.* Polyethylene upcycling to long-chain alkylaromatics by tandem hydrogenolysis/aromatization. *Science* **370,** 437–441 (2020).
8. Ertl, G., Knözinger, H., Schüth, F. & Weitkamp, J. *Handbook of Heterogeneous Catalysis, 2nd ed.,* (Wiley-VCH; Weinhei, 2008).
9. Sattler, J. J. H. B., Ruiz-Martinez, J., Santillan-Jimenez, E. & Weckhuysen, B. M. Catalytic dehydrogenation of light alkanes on metals and metal oxides. *Chem. Rev.* **114,** 10613–10653 (2014).
10. Cui, X. *et al.* Synthesis of Single Atom Based Heterogeneous Platinum Catalysts: High Selectivity and Activity for Hydrosilylation Reactions. *ACS Cent. Sci.* **3,** 580–585 (2017).
11. V. Haensel. *Alumina-Platinum-Halogen Catalyst And Preparation Thereof. U.S. Patent 2,479,109* (1949).
12. Sinfelt, J. H. Catalysis by alloys and bimetallic clusters. *Acc. Chem. Res.* **10,** 15–20 (1977).
13. Yu, W., Porosoff, M. D. & Chen, J. G. Review of Pt-based bimetallic catalysis: from model surfaces to supported catalysts. *Chem. Rev.* **112,** 5780–5817 (2012).
14. Burch & R. Platinum-tin reforming catalysts I. The oxidation state of tin and the interaction between platinum and tin. *J. Catal.* **71,** 348–359 (1981).
15. Antos, G. J. & Aitani, A. M. (eds.). *Catalytic naphtha reforming.* 2nd ed. (Marcel Dekker, New York, 2004).
16. Karim, W. *et al.* Catalyst support effects on hydrogen spillover. *Nature* **541,** 68–71 (2017).
17. Jang, E. J., Lee, J., Jeong, H. Y. & Kwak, J. H. Controlling the acid-base properties of alumina for stable PtSn-based propane dehydrogenation catalysts. *Appl. Catal. A* **572,** 1–8 (2019).
18. Jahel, A. N. *et al.* Effect of Indium Doping of γ-Alumina on the Stabilization of PtSn Alloyed Clusters Prepared by Surface Organostannic Chemistry. *J. Phys. Chem. C* **116,** 10073–10083 (2012).
19. Digne, M., Raybaud, P., Sautet, P., Guillaume, D. & Toulhoat, H. Atomic scale insights on chlorinated gamma-alumina surfaces. *J. Am. Chem. Soc.* **130,** 11030–11039 (2008).
20. Guillaume, C., Jean-Miche, G. & Daniel, C. Chlorination of alumina: an IR spectroscopic study. *Bulletin de la Societe Chimique de France,* 223–233 (1997).
21. Batista, A. T. F. *et al.* Atomic Scale Insight into the Formation, Size, and Location of Platinum Nanoparticles Supported on γ-Alumina. *ACS Catal.* **10,** 4193–4204 (2020).
22. Berdala, J., Freund, E., Lynch J. P. Environment of platinum atoms in a H2 PtCl6/Al2O3 catalyst : Influence of metal loading and chlorine content. *J. Phys. Colloques* **47,** C8-269-C8-272 (1986).
23. Svintsitskiy, D. A. *et al.* Insight into the Nature of Active Species of Pt/Al 2 O 3 Catalysts for low Temperature NH 3 Oxidation. *ChemCatChem* **12,** 867–880 (2020).
24. Marceau, E., Lauron-Pernot, H. & Che, M. Influence of the Metallic Precursor and of the Catalytic Reaction on the Activity and Evolution of Pt(Cl)/δ-Al2O3 Catalysts in the Total Oxidation of Methane. *J. Catal.* **197,** 394–405 (2001).
25. Marceau, E., Che, M., Saint-Just, J. & Tatibouët, J. M. Influence of chlorine ions in Pt/A12O3 catalysts for methane total oxidation. *Catal. Today* **29,** 415–419 (1996).

26. Gracia, F. J., Miller, J. T., Kropf, A. J. & Wolf, E. E. Kinetics, FTIR, and Controlled Atmosphere EXAFS Study of the Effect of Chlorine on Pt-Supported Catalysts during Oxidation Reactions. *J. Catal.* **209,** 341–354 (2002).
27. Yentekakis, I. V., Lambert, R. M., Konsolakis, M. & Kallithrakas-Kontos, N. On the effects of residual chloride and barium promotion on Pt/gamma-Al2O3 catalysts in the reduction of NO by propene. *Catal. Lett.* **81,** 181–185 (2002).
28. Ali, L. I., Ali, A.-G. A., Aboul-Fotouh, S. M. & Aboul-Gheit, A. K. Hydroconversion of n-paraffins in light naphtha using Pt/Al2O3 catalysts promoted with noble metals and/or chlorine. *Appl. Catal. A: Gen.* **205,** 129–146 (2001).
29. Davis, B. H. Alkane dehydrocyclization mechanism. *Catal. Today* **53,** 443–516 (1999).
30. Batista, A. T. F. *et al.* Evaluating acid and metallic site proximity in Pt/γ-Al2O3-Cl bifunctional catalysts through an atomic scale geometrical model. *Nanoscale* **14,** 8753–8765 (2022).
31. Lynch, J. Development of Structural Characterisation Tools for Catalysts. *Oil & Gas Science and Technology - Rev. IFP* **57,** 281–305; 10.2516/ogst:2002020 (2002).
32. Mondloch, J. E., Bayram, E. & Finke, R. G. A review of the kinetics and mechanisms of formation of supported-nanoparticle heterogeneous catalysts. *J. Mol. Catal. A Chem* **355,** 1–38 (2012).
33. Marceau, E., Carrier, X. & Che, M. Impregnation and Drying. In *Synthesis of Solid Catalysts,* edited by K. P. de Jong (Wiley-VCH Verlag GmbH & Co. KGaA, Weinheim, Germany, 2009), pp. 59–82.
34. Marceau, E. *et al.* Interfacial coordination chemistry for catalyst preparation. *J. Catal.* **396,** 104–121 (2021).
35. Lieske, H. Reactions of platinum in oxygen- and hydrogen-treated Pt/gamma-Al2O3 catalysts I. Temperature-programmed reduction, adsorption, and redispersion of platinum. *J. Catal.* **81,** 8–16 (1983).
36. Lietz, G. Reactions of platinum in oxygen- and hydrogen-treated Pt/gamma;-Al2O3 catalysts II. Ultraviolet-visible studies, sintering of platinum, and soluble platinum. *J. Catal.* **81,** 17–25 (1983).
37. Sinkler, W. *et al.* Aberration-Corrected Transmission Electron Microscopy and In Situ XAFS Structural Characterization of Pt/γ-Al 2 O 3 Nanoparticles. *ChemCatChem* **7,** 3779–3787 (2015).
38. Lee, J., Jang, E. J. & Kwak, J. H. Effect of number and properties of specific sites on alumina surfaces for Pt-Al2O3 catalysts. *Appl. Catal. A: Gen.* **569,** 8–19 (2019).
39. Dessal, C. *et al.* Atmosphere-dependent stability and mobility of catalytic Pt single atoms and clusters on γ-Al2O3. *Nanoscale* **11,** 6897–6904 (2019).
40. Bradley, S. A. *et al.* Behavior of Pt Atoms on Oxide Supports During Reduction Treatments at Elevated Temperatures, Characterized by Aberration Corrected Stem Imaging. *Catal. Lett.* **142,** 176–182 (2012).
41. Finzel, J. *et al.* Limits of Detection for EXAFS Characterization of Heterogeneous Single-Atom Catalysts. *ACS Catal.,* 6462–6473 (2023).
42. Smolikov, M. D. *et al.* New data about platinum state in reduced Pt/Al2O3(Cl) catalysts. *React. Kinet. Catal. Lett.* **37,** 437–442 (1988).
43. Stakheev, A. Y. *et al.* Separation of Geometric and Electronic Effects of the Support on the CO and H 2 Chemisorption Properties of Supported Pt Particles: The Effect of Ionicity in Modified Alumina Supports. *J. Phys. Chem. C* **111,** 3938–3948; 10.1021/jp0651182 (2007).
44. Hohenberg, P. & Kohn, W. Inhomogeneous Electron Gas. *Phys. Rev.* **136,** B864-B871 (1964).
45. Kohn, W. & Sham, L. J. Self-Consistent Equations Including Exchange and Correlation Effects. *Phys. Rev.* **140,** A1133-A1138; 10.1103/PhysRev.140.A1133 (1965).
46. Chizallet, C. Achievements and Expectations in the Field of Computational Heterogeneous Catalysis in an Innovation Context. *Top. Catal.* **65,** 69–81 (2022).
47. Chizallet, C. & Raybaud, P. Density functional theory simulations of complex catalytic materials in reactive environments: beyond the ideal surface at low coverage. *Catal. Sci. Technol.* **4,** 2797–2813 (2014).
48. Hu, C. H. *et al.* Modulation of catalyst particle structure upon support hydroxylation: Ab initio insights into Pd13 and Pt13/γ-Al2O3. *J. Catal.* **274,** 99–110 (2010).

49. Erfani, G. S., Hong, S. & Rahman, T. S. Effects of γ-Al 2 O 3 Support on the Morphology and Electronic Structure of Pt Nanoparticles. *J. Phys. Chem. C* **123,** 16893–16901 (2019).
50. Mager-Maury, C., Bonnard, G., Chizallet, C., Sautet, P. & Raybaud, P. H2-Induced Reconstruction of Supported Pt Clusters: Metal-Support Interaction versus Surface Hydride. *ChemCatChem* **3,** 200–207 (2011).
51. Gorczyca, A. *et al.* Monitoring morphology and hydrogen coverage of nanometric Pt/γ-Al2 O3 particles by in situ HERFD-XANES and quantum simulations. *Angew. Chem. Int. Ed. Engl.* **53,** 12426–12429 (2014).
52. Mager-Maury, C., Chizallet, C., Sautet, P. & Raybaud, P. Platinum Nanoclusters Stabilized on γ-Alumina by Chlorine Used As a Capping Surface Ligand: A Density Functional Theory Study. *ACS Catal.* **2,** 1346–1357 (2012).
53. Ana Teresa Fialho Batista. Atomic scale insight into platinum based catalysts supported on chlorinated gamma-alumina. PhD thesis, 2016-2019.
54. Xu, Y., Shelton, W. A. & Schneider, W. F. Effect of particle size on the oxidizability of platinum clusters. *J. Phys. Chem. A* **110,** 5839–5846 (2006).
55. Mei, D. *et al.* Unique Role of Anchoring Penta-Coordinated Al 3+ Sites in the Sintering of γ-Al 2 O 3 -Supported Pt Catalysts. *J. Phys. Chem. Lett.* **1,** 2688–2691 (2010).
56. Liu, Y. *et al.* First principles study on the adsorption of Ptn (n=1–4) on γ-Al2O3(110) surface. *Appl. Surf. Sci.* **313,** 424–431 (2014).
57. Valero, M. C. & Raybaud, P. Computational chemistry approaches for the preparation of supported catalysts: Progress and challenges. *J. Catal.* **391,** 539–547 (2020).
58. Sahu, A., Steinmann, S. N. & Raybaud, P. Genesis of MoS2 from model-Mo-oxide precursors supported on γ-alumina. *J. Catal.* **408,** 303–315 (2022).
59. Zhou, X., Zhang, Y. & Wang, J. DFT study on the regeneration of Pt/γ-Al2O3 catalyst: The effect of chlorine on the redispersion of metal species. *Appl. Surf. Sci.* **545,** 148988 (2021).
60. Hellier, A., Chizallet, C. & Raybaud, P. PtOxCly(OH)z H2O)n Complexes under Oxidative and Reductive Conditions: Impact of the Level of Theory on Thermodynamic Stabilities. *Chemphyschem* **24,** e202200711 (2023).
61. Kresse & Hafner. Ab initio molecular-dynamics simulation of the liquid-metal-amorphous-semiconductor transition in germanium. *Phys. Rev. B* **49,** 14251–14269 (1994).
62. Kresse, G. & Furthmüller, J. Efficiency of ab-initio total energy calculations for metals and semiconductors using a plane-wave basis set. *Comput. Mater. Sci.* **6,** 15–50 (1996).
63. Perdew, J. P., Burke, K. & Ernzerhof, M. Generalized Gradient Approximation Made Simple. *Phys. Rev. Lett.* **77,** 3865–3868 (1996).
64. Steinmann, S. N. & Corminboeuf, C. A generalized-gradient approximation exchange hole model for dispersion coefficients. *J. Chem. Phys.* **134,** 44117 (2011).
65. Steinmann, S. N. & Corminboeuf, C. Comprehensive Benchmarking of a Density-Dependent Dispersion Correction. *J. Chem. Phys.* **7,** 3567–3577 (2011).
66. Kresse, G. & Joubert, D. From ultrasoft pseudopotentials to the projector augmented-wave method. *Phys. Rev. B* **59,** 1758–1775 (1999).
67. Hirshfeld, F. L. Bonded-atom fragments for describing molecular charge densities. *Theoret. Chim. Acta* **44,** 129–138 (1977).
68. Heyd, J. & Scuseria, G. E. Efficient hybrid density functional calculations in solids: assessment of the Heyd-Scuseria-Ernzerhof screened Coulomb hybrid functional. *J. Chem. Phys.* **121,** 1187–1192 (2004).
69. Heyd, J., Scuseria, G. E. & Ernzerhof, M. Hybrid functionals based on a screened Coulomb potential. *J. Chem. Phys.* **118,** 8207–8215 (2003).
70. Krukau, A. V., Vydrov, O. A., Izmaylov, A. F. & Scuseria, G. E. Influence of the exchange screening parameter on the performance of screened hybrid functionals. *J. Chem. Phys.* **125,** 224106 (2006).
71. Digne, M., Sautet, P., Raybaud, P., Euzen, P. & Toulhoat, H. Hydroxyl Groups on γ-Alumina Surfaces: A DFT Study. *J. Catal.* **211,** 1–5 (2002).

72. Digne, M. Use of DFT to achieve a rational understanding of acid?basic properties of ?-alumina surfaces. *J. Catal.* **226,** 54–68 (2004).
73. Krokidis, X. *et al.* Theoretical Study of the Dehydration Process of Boehmite to γ-Alumina. *J. Phys. Chem. B* **105,** 5121–5130 (2001).
74. Pigeon, T., Chizallet, C. & Raybaud, P. Revisiting γ-alumina surface models through the topotactic transformation of boehmite surfaces. *J. Catal.* **405,** 140–151 (2022).
75. Henkelman, G., Uberuaga, B. P. & Jónsson, H. A climbing image nudged elastic band method for finding saddle points and minimum energy paths. *J. Chem. Phys.* **113,** 9901–9904 (2000).
76. Henkelman, G. & Jónsson, H. Improved tangent estimate in the nudged elastic band method for finding minimum energy paths and saddle points. *J. Chem. Phys.* **113,** 9978–9985 (2000).
77. Henkelman, G. & Jónsson, H. A dimer method for finding saddle points on high dimensional potential surfaces using only first derivatives. *J. Chem. Phys.* **111,** 7010–7022 (1999).
78. Fukui, K. Formulation of the reaction coordinate. *J. Phys. Chem.* **74,** 4161–4163; 10.1021/j100717a029 (1970).
79. Fukui, K. The path of chemical reactions - the IRC approach. *Acc. Chem. Res.* **14,** 363–368; 10.1021/ar00072a001 (1981).
80. Hratchian, H. P. & Schlegel, H. B. Following Reaction Pathways Using a Damped Classical Trajectory Algorithm. *J. Phys. Chem. A* **106,** 165–169 (2002).
81. Paul Fleurat-Leussard. Opt'n Path.
82. Henkelman Group. VTST Tools. Vasp Transition State Tools for Vasp. Available at https://theory.cm.utexas.edu/vtsttools/.
83. R.A. Angnes. mechaSVG (2020).
84. Jørgensen, C. Differences between the four halide ligands, and discussion remarks on trigonal-bipyramidal complexes, on oxidation states, and on diagonal elements of one-electron energy. *Coord. Chem. Rev.* **1,** 164–178 (1966).
85. Samoila, P., Epron, F., Marécot, P. & Especel, C. Influence of chlorine on the catalytic properties of supported rhodium, iridium and platinum in ring opening of naphthenes. *Appl. Catal. A: Gen.* **462-463,** 207–219 (2013).

V.7. Supporting Information

SI 1. Structural and electronic properties of the various simulated Pt complexes.

System	d(Pt-O_{surf}) (Å)	d(Pt-Cl) (Å)	d(Pt-OH) (Å)	d(Pt-O) (Å)	d(Pt-H) (Å)	d(Pt-OH_2) (Å)	Pt charge (e)	OD
PtO_2	2.07 2.15			1.79 1.94			0.580	IV
$PtOCl_2$	2.08	2.24 2.26		1.86			0.490	IV
PtOCl(OH)	2.05	2.24	1.96	1.85			0.543	IV
$PtO(OH)_2$	2.05		1.91 1.98	1.94			0.604	IV
$PtCl_4$	2.11	2.26 2.28 2.29 2.32					0.498	IV
$PtCl_3(OH)$	2.00	2.23 2.28 2.34	2.05				0.543	IV
$PtCl_2(OH)_2$	2.04	2.27 2.27	2.01 2.04				0.621	IV
$PtCl(OH)_3$	1.98	2.23	2.00 2.04 2.04				0.637	IV
$Pt(OH)_4$	1.97		1.90 2.00 2.03 2.05				0.684	IV
$PtCl_4(OH)H$*	2.11	1.90 2.00 2.03 2.05	2.07				0.493	IV
$PtCl_3(OH)_2H$*	2.09	2.28 2.29 2.30	2.05 2.06				0.537	IV
$PtCl_2(OH)_2(H_2O)$	2.05	2.29 2.30	2.01 2.04			2.05	0.597	IV
$PtCl(OH)_3(H_2O)$	2.02	2.30	2.00 2.01 2.03			2.05	0.643	IV
$Pt(OH)_4(H_2O)$	2.04	1.99 2.00 2.02 2.03				2.05	0.683	IV
$PtHCl_4H$*	2.29	2.29 2.33 2.33 2.34			1.54		0.386	IV+H_2
$PtHCl_3(OH)H$*	2.24	2.29 2.33 2.33	2.07		1.54		0.438	IV+H_2
$PtHCl_2(OH)_2H$*	2.19	2.33 2.33	2.03 2.07		1.55		0.485	IV+H_2
$PtHCl(OH)_3H$*	2.16	2.32	2.01 2.05 2.05		1.55		0.528	IV+H_2
$PtH(OH)_3(H_2O)$	2.11		2.01 2.02 2.04		1.56		0.578	IV+H_2
PtOCl	2.05 2.07	2.27		1.92			0.468	III
PtO(OH)	1.98 2.05		2.10	1.94			0.510	III
$PtCl(OH)_2$	2.04	2.24	1.95 1.98				0.464	III
$Pt(OH)_3$	1.96		1.91 2.01 2.04				0.530	III
PtHOClH*	2.19	2.23		1.93	1.55		0.315	III+H_2
PtHO(OH)H*	2.14		1.98	1.91	1.56		0.366	III+H_2
$PtHHCl(OH)_2$	2.16	2.49	2.00 2.04		1.55 1.55		0.445	III+H_2
$PtHH(OH)_3$	2.15		2.00 2.03 2.20		1.55 1.56		0.477	III+H_2
PtO	1.97 2.07			1.98			0.464	II
$PtCl_2$	2.03 2.10	2.28 2.34					0.308	II
PtCl(OH)	2.04 2.07	2.27	2.09				0.353	II
$Pt(OH)_2$	1.98 2.06		2.09 2.13				0.396	II
$PtCl_2(OH)H$*	2.11	2.25 2.25	2.05				0.234	II

System	d(Pt-O_{surf}) (Å)	d(Pt-Cl) (Å)	d(Pt-OH) (Å)	d(Pt-O) (Å)	d(Pt-H) (Å)	d(Pt-OH_2) (Å)	Pt charge (e)	OD
$PtCl(OH)_2H$*	2.06	2.26	2.02 2.03				0.265	II
$Pt(OH)_2(H_2O)$	1.97		2.01 2.04			2.11	0.335	II
$PtHCl_2(OH)(H_2O)$	2.19	2.28 2.29	2.05		1.55	2.07	0.481	II
$PtHCl(OH)_2(H_2O)$	2.14	2.29	2.01 2.05		1.55	2.05	0.532	II
$PtH(OH)_3(H_2O)$	2.11		2.01 2.01 2.03		1.56	2.06	0.580	II
PtH(OH)	2.07 2.23		2.07		1.55		0.334	II+H_2
$PtHCl_2H$*	2.28	2.28 2.28			1.54		0.098	II+H_2
PtHCl(OH)H*	2.23	2.28	2.05		1.55		0.147	II+H_2
$PtH(OH)_2H$*	2.17		2.05 2.05		1.56		0.184	II+H_2
$PtHHCl_2(H_2O)$	2.26	2.29 2.31			1.54 1.54	2.21	0.352	II+H_2
$PtHHCl(OH)(H_2O)$	2.20	2.28	2.04		1.54 1.55	2.21	0.400	II+H_2
$PtHH(OH)_2(H_2O)$	2.15		2.01 2.04		1.55 1.56	2.19	0.454	II+H_2
PtHHHHO	2.18				1.55 1.56 1.67 1.68		0.453	II+H_2
$PtHHCl_2(H_2)$	2.24	2.29 2.32			1.54 1.55 1.93 2.00		0.368	II+H_2
PtHHHCl(OH)H*	2.24	2.27	2.07		1.54 1.59 1.76		0.339	II+H_2
$PtHHH(OH)_2H$*	2.17		2.01 2.07		1.55 1.60 1.75		0.389	II+H_2
PtCl	2.06 2.25	2.33					0.276	I
Pt(OH)	2.05 2.23		2.11				0.306	I
$PtCl(H_2)$	2.25 2.42	2.50			1.55 1.55		0.266	I+H_2
$Pt(OH)(H_2)$	2.23 2.46		2.22		1.54 1.55		0.303	I+H_2
Pt	2.03 2.06						0.077	0
$Pt(H_2O)$	1.99					2.09	-0.009	0
PtHH	2.23 2.26				1.55 1.56		0.198	0+H_2

Table SV-1. Geometric description and platinum charge of supported complexes. Grafting refers to the number of bonds between Pt and the support. OD is for oxidative degree use in the paper to rank the systems.

SI 2. Charges difference, impact of support.

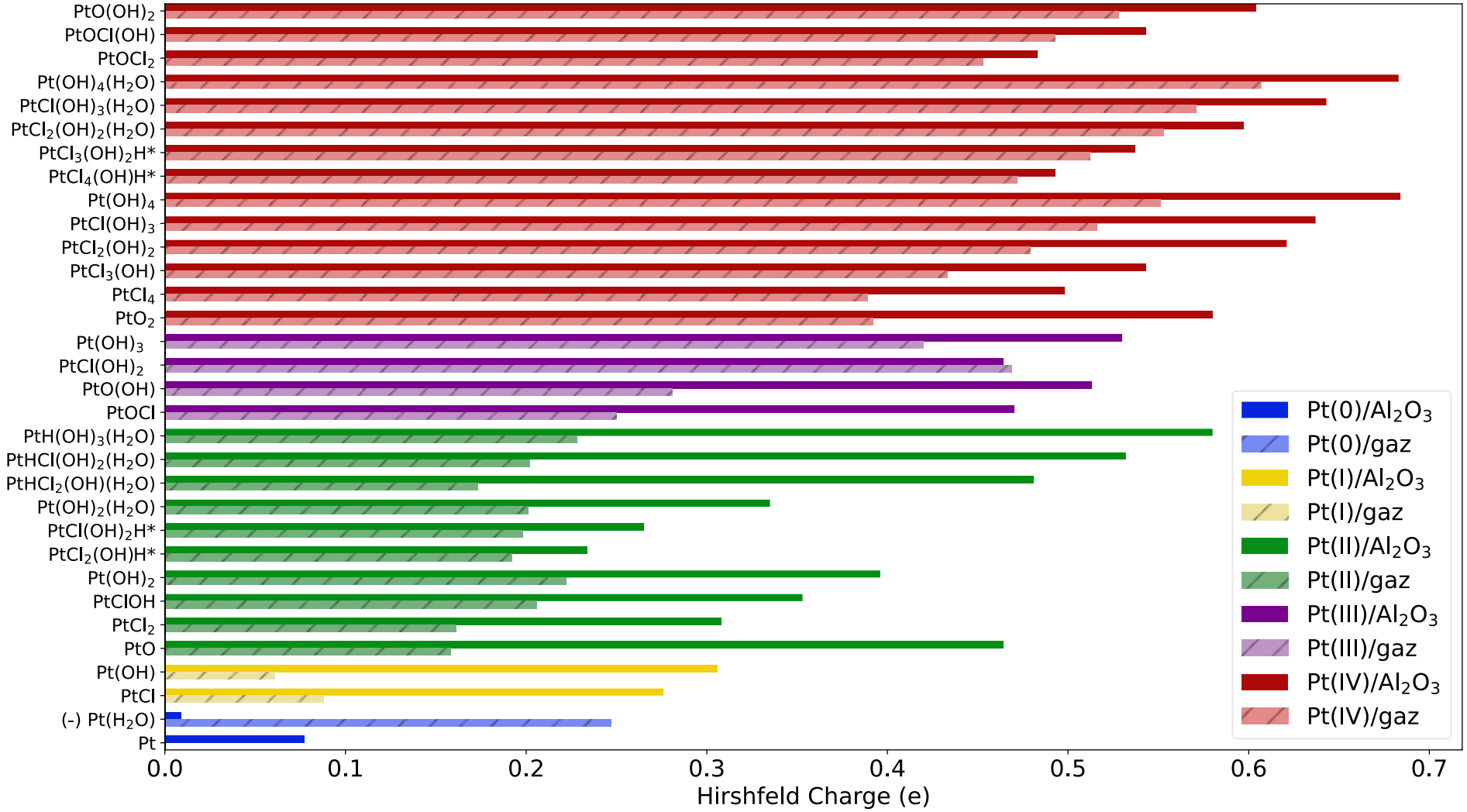

Figure SV-1. Impact of the support on the platinum Hirshfeld charge for a given stoichiometry. Gas phase models are taken from Ref [1]. The stoichiometry reported is the one used in this paper as detailed in the method, to link them to the corresponding gas phase species, the reader is referred to the Table SV-1. No species with adsorbed H_2 were considered as they were not treated in Ref [1].

SI 3. Adsorption modes of H_2 on Pt(II).

System	Undissociated system	Dissociated system
$PtCl_2 + 2H_2$	-1813.45	-1813.40
$PtCl(OH) + 2H_2$	-1821.18	-1821.27
$Pt(OH)_2 + 2H_2$	-1828.84	-1829.01

Table SV-2. Total energies (eV) of the Pt(II) + $2H_2$ according to the adsorption mode of the second H_2.

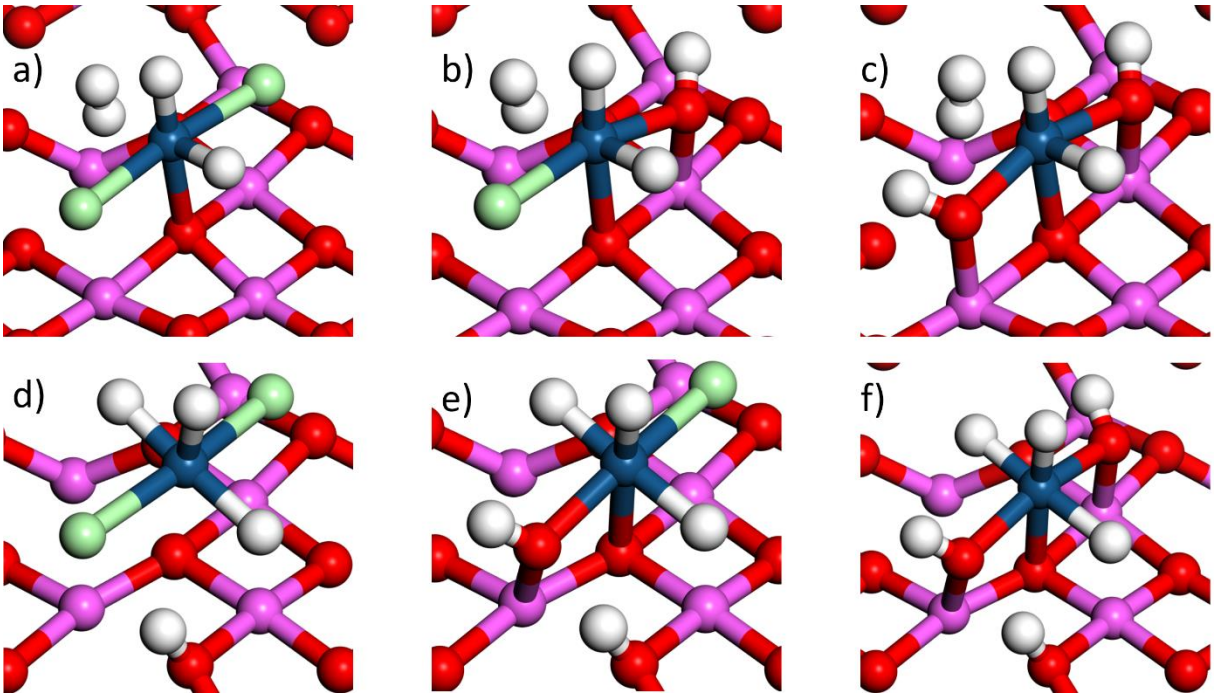

Figure SV-2. Adsorption mode of the second H_2 molecule on the three Pt(II) species: $PtCl_2$, $PtCl(OH)$ and $Pt(OH)_2$. a): $PtH_2Cl_2(H_2)$, b): $PtH_2Cl(OH)(H_2)$, c): $PtH_2(OH)_2(H_2)$, d):PtH_2Cl_2H*, e):$PtH_2Cl(OH)H$*, f): $PtH_2(OH)_2H$*. Color code for atomic structure: Pt: blue; Cl: green; O: red; Al: pink, H: white.

In every case, the first H_2 is always dissociated. The second one however is impacted by the nature of the coordination sphere. $PtCl_2$ is the only case where the smallest energy was calculated by keeping H_2 undissociated, even though the dissociated system (**Figure SV-2**, **a) and d)**) is extremely close in energy. In the two others cases, the dissociation of the second H_2 stabilize the system with a stronger stabilization for the fully hydroxylated case (0.11 eV for PtCl(OH) and 0.17 eV for $Pt(OH)_2$).

SI.4 Different hydration mechanisms.

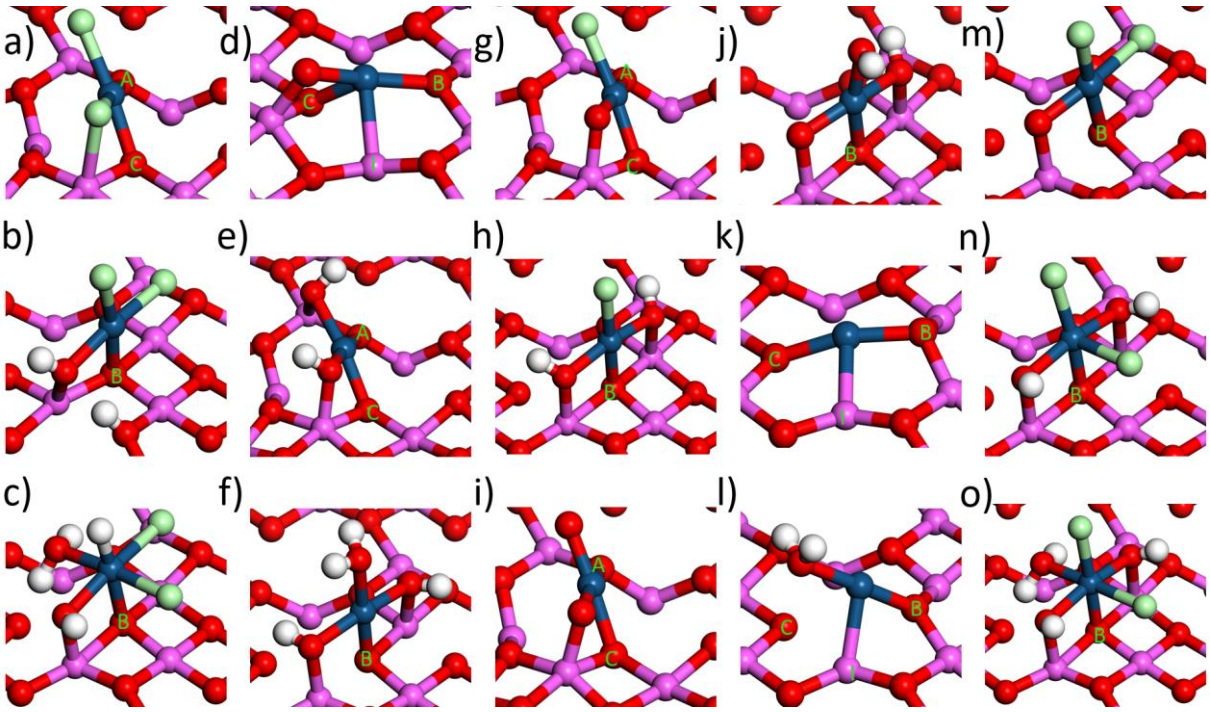

Figure SV-3. Impact of the hydration on the geometry of various complexes. a) $PtCl_2$, b) $PtCl_2(OH)H^*$, c) $PtHCl_2(OH)(H_2O)$, d) PtO, e) $Pt(OH)_2$, f) $Pt(OH)_2(H_2O)$, g) PtOCl, h) $PtCl(OH)_2$, i) PtO_2, j) $PtO(OH)_2$, k) Pt, l) $Pt(H_2O)$, m) $PtOCl_2$, n) $PtCl_2(OH)_2$, o) $PtCl_2(OH)_2(H_2O)$. Color code for atomic structure: Pt: blue; Cl: green; O: red; Al: pink, H: white.

SI 5. Reaction energies of supported platinum complexes.

Pt(IV)	**ΔE (kJ/mol)**	**Pt(II)**	**ΔE(kJ/mol)**
Ligand Exchange		**Ligand Exchange**	
$PtCl_4 + H_2O \rightarrow PtCl_3(OH) + HCl$	14.1	$PtCl_2 + H_2O \rightarrow PtCl(OH) + HCl$	41.0
$PtCl_3(OH) + H_2O \rightarrow PtCl_2(OH)_2 + HCl$	21.3	$PtCl(OH) + H_2O \rightarrow Pt(OH)_2 + HCl$	91.8
$PtCl_2(OH)_2 + H_2O \rightarrow PtCl(OH)_3 + HCl$	23.9	$PtCl_2(OH)H^* + H_2O \rightarrow PtCl(OH)_2H^* + HCl$	37.0
$PtCl(OH)_3 + H_2O \rightarrow Pt(OH)_4 + HCl$	46.1	$PtCl(OH)_2H^* + H_2O \rightarrow Pt(OH)_2(H_2O) + HCl$	73.1
$PtCl_4(OH)H^* + H_2O \rightarrow PtCl_3(OH)_2H^* + HCl$	17.0	$PtHCl_2(OH)(H_2O) + H_2O \rightarrow PtHCl(OH)_2(H_2O) + HCl$	30.2
$PtCl_3(OH)_2H^* + H_2O \rightarrow PtCl_2(OH)_2(H_2O) + HCl$	20.0	$PtHCl(OH)_2(H_2O) + H_2O \rightarrow PtH(OH)_3(H_2O) + HCl$	55.5
$PtCl_2(OH)_2(H_2O) + H_2O \rightarrow PtCl(OH)_3(H_2O) + HCl$	29.8	**MAV**	**54.7**
$PtCl(OH)_3(H_2O) + H_2O \rightarrow Pt(OH)_4(H_2O) + HCl$	89.9	**Hydration**	
$PtOCl_2 + H_2O \rightarrow PtOCl(OH) + HCl$	42.3	$PtCl_2 + H_2O \rightarrow PtCl_2(OH)H^*$	-27.9
$PtOCl(OH) + H_2O \rightarrow PtO(OH)_2 + HCl$	64.9	$PtCl(OH) + H_2O \rightarrow PtCl(OH)_2H^*$	-31.8
MAV	**36.9**	$Pt(OH)_2 + H_2O \rightarrow Pt(OH)_2(H_2O)$	-50.6
Hydration		$PtCl_2(OH)H^* + H_2O \rightarrow PtHCl_2(OH)(H_2O)$	-67.0
$PtCl_4 + H_2O \rightarrow PtCl_4(OH)H^*$	-196.0	$PtCl(OH)_2H^* + H_2O \rightarrow PtHCl(OH)_2(H_2O)$	-73.8
$PtCl_3(OH) + H_2O \rightarrow PtCl_3(OH)_2H^*$	-193.1	$Pt(OH)_2(H_2O) + H_2O \rightarrow PtH(OH)_3(H_2O)$	-91.6
$PtCl_2(OH)_2 + H_2O \rightarrow PtCl_2(OH)_2(H_2O)$	-194.3	$PtO + H_2O \rightarrow Pt(OH)_2$	-208.9
$PtCl(OH)_3 + H_2O \rightarrow PtCl(OH)_3(H_2O)$	-188.4	**MAV**	**-78.8**
$Pt(OH)_4 + H_2O \rightarrow Pt(OH)_4(H_2O)$	-144.7	**Reduction**	
$PtOCl_2 + H_2O \rightarrow PtCl_2(OH)_2$	-108.4	$PtO + H_2 \rightarrow Pt + H_2O$	-132.9
$PtOCl(OH) + H_2O \rightarrow PtCl(OH)_3$	-126.9	$PtCl_2 + H_2 \rightarrow Pt + 2\ HCl$	208.7
$PtO(OH)_2 + H_2O \rightarrow Pt(OH)_4$	-145.6	$PtCl(OH) + H_2 \rightarrow Pt + HCl + H_2O$	167.8
$PtO_2 + H_2O \rightarrow PtO_2(H_2O)$	-106.6	$Pt(OH)_2 + H_2 \rightarrow Pt + 2\ H_2O$	76.0
MAV	**-156.0**	$Pt(OH)_2 + H_2 \rightarrow Pt(H_2O) + H_2O$	69.4
Reduction		$PtCl_2(OH)H^* + H_2 \rightarrow Pt(H_2O) + 2HCl$	230.0
$PtO_2 + H_2 \rightarrow PtO + H_2O$	-130.4	$PtCl(OH)_2H^* + H_2 \rightarrow Pt(H_2O) + HCl + H_2O$	193.0
$PtOCl_2 + H_2 \rightarrow PtCl_2 + H_2O$	-258.2	$Pt(OH)_2(H_2O) + H_2 \rightarrow Pt(H_2O) + 2H_2O$	119.9
$PtOCl(OH) + H_2 \rightarrow PtCl(OH) + H_2O$	-259.6	**MAV**	116.5
$PtO(OH)_2 + H_2 \rightarrow Pt(OH)_2 + H_2O$	-232.7	**Pt(II) + H_2**	
$PtCl_4 + H_2 \rightarrow PtCl_2 + 2\ HCl$	-114.5	**Ligand Exchange**	
$PtCl_3(OH) + H_2 \rightarrow PtCl_2 + HCl + H_2O$	-128.5	$PtHCl_2H^* + H_2O \rightarrow PtHCl(OH)H^* + HCl$	29.5
$PtCl_2(OH)_2 + H_2 \rightarrow PtCl_2 + 2H_2O$	-149.8	$PtHCl(OH)H^* + H_2O \rightarrow PtH(OH)_2H^* + HCl$	59.2
$PtCl(OH)_3 + H_2 \rightarrow PtCl(OH) + 2H_2O$	-132.7	$PtH_2Cl_2(H_2O) + H_2O \rightarrow PtH_2Cl(OH)(H_2O) + HCl$	31.4
$Pt(OH)_4 + H_2 \rightarrow Pt(OH)_2 + 2\ H_2O$	-87.0	$PtH_2Cl(OH)(H_2O) + H_2O \rightarrow PtH_2(OH)_2(H_2O) + HCl$	40.0
$PtCl_4(OH)H^* + H_2 \rightarrow PtCl_2(OH)H^* + 2\ HCl$	53.7	**MAV**	**40.0**
$PtCl_3(OH)_2H^* + H_2 \rightarrow PtCl_2(OH)H^* + HCl + H_2O$	36.7	**Hydration**	
$PtCl_2(OH)_2(H_2O) + H_2 \rightarrow PtCl_2(OH)H^* + 2H_2O$	16.7	$PtCl_2(H_2) + H_2O \rightarrow PtCl_2(H_2O)(H_2)$	-63.9
$PtCl(OH)_3(H_2O) + H_2 \rightarrow PtCl(OH)_2H^* + 2H_2O$	23.9	$PtCl(OH)(H_2) + H_2O \rightarrow PtCl(OH)(H_2O)(H_2)$	-62.0
$Pt(OH)_4(H_2O) + H_2 \rightarrow Pt(OH)_2(H_2O) + 2\ H_2O$	7.0	$Pt(OH)_2(H_2) + H_2O \rightarrow Pt(OH)_2(H_2O)(H_2)$	-81.2
MAV	**-96.8**	**MAV**	**-69.0**
Pt(IV) + H_2		**H_2 Adsorption**	
Ligand Exchange		$PtCl_2 + H_2 \rightarrow PtHCl_2H^*$	-59.9
$PtHCl_4H^* + H_2O \rightarrow PtHCl_3(OH)H^* + HCl$	23.9	$PtCl(OH) + H_2 \rightarrow PtHCl(OH)H^*$	-71.4
$PtHCl_3(OH)H^* + H_2O \rightarrow PtHCl_2(OH)_2H^* + HCl$	30.9	$Pt(OH)_2 + H_2 \rightarrow PtH(OH)_2H^*$	-104.1
$PtHCl_2(OH)_2H^* + H_2O \rightarrow PtHCl(OH)_3H^* + HCl$	37.0	$PtO + H_2 \rightarrow PtH(OH)$	-278.5
$PtHCl(OH)_3H^* + H_2O \rightarrow PtH(OH)_3(H2O) + HCl$	47.8	**MAV**	**-128.5**

MAV	**34.9**		
Adsorption H_2	**ΔE(kJ/mol)**	**Pt(II) + H_2 -- H_2 Adsorption**	**ΔE(kJ/mol)**
$PtCl_4 + H_2 \rightarrow PtHCl_4H^*$	-271.0	$PtHCl_2H^* + H_2 \rightarrow PtH_2Cl_2(H_2)$	17.4
$PtCl_3(OH) + H_2 \rightarrow PtHCl_3(OH)H^*$	-261.2	$PtHCl(OH)H^* + H_2 \rightarrow PtH_3Cl(OH)H^*$	17.8
$PtCl_2(OH)_2 + H_2 \rightarrow PtHCl_2(OH)_2H^*$	-251.5	$PtH(OH)_2H^* + H_2 \rightarrow PtH_3(OH)_2H^*$	-3.1
$PtCl(OH)_3 + H_2 \rightarrow PtHCl(OH)_3H^*$	-238.4	$PtHO(OH) + H_2 \rightarrow PtH_2O(H_2)$	110.6
$Pt(OH)_4 + H_2 \rightarrow PtH(OH)_3(H_2O)$	-236.8	**MAV**	**59.8**
$PtO_2 + H_2 \rightarrow Pt(OH)_2$	-339.3	**Pt(I)**	
$PtOCl_2 + H_2 \rightarrow PtCl_2(OH)H^*$	-286.1	**Ligand Exchange**	
$PtOCl(OH) + H_2 \rightarrow PtCl(OH)_2H^*$	-291.4	$PtCl + H_2O \rightarrow Pt(OH) + HCl$	48.5
$PtO(OH)_2 + H_2 \rightarrow Pt(OH)_2(H_2O)$	-283.3	**MAV**	**48.5**
MAV	**-273.2**	**Reduction**	
Pt(III)		$PtCl + 0.5H_2 \rightarrow Pt + HCl$	82.9
Ligand Exchange		$Pt(OH) + 0.5H_2 \rightarrow Pt + H_2O$	34.3
$PtOCl + H_2O \rightarrow PtO(OH) + HCl$	92.2	**MV**	58.6
$PtCl(OH)_2 + H_2O \rightarrow Pt(OH)_3 + HCl$	68.2	**Pt(I) + H_2**	
MAV	**80.7**	**Ligand Exchange**	
Hydration		$PtCl(H_2) + H_2O \rightarrow Pt(OH)(H_2) + HCl$	38.9
$PtOCl + H_2O \rightarrow PtCl(OH)_2$	-107.1	**MAV**	**38.9**
$PtO(OH) + H_2O \rightarrow Pt(OH)_3$	-131.0	**H_2 Adsorption**	
MAV	**-119.1**	$PtCl + H_2 \rightarrow PtCl(H_2)$	-25.2
Reduction		$Pt(OH) + H_2 \rightarrow Pt(OH)(H_2)$	-34.9
$PtOCl + H_2 \rightarrow PtCl + H_2O$	-103.4	**MAV**	**-30.0**
$PtO(OH) + H_2 \rightarrow Pt(OH) + H_2O$	-147.1	**Pt(0)**	
$PtCl(OH)_2 + H_2 \rightarrow PtCl + 2H_2O$	3.7	**Hydration**	
$Pt(OH)_3 + H_2 \rightarrow Pt(OH) + 2H_2O$	-16.1	$Pt + H_2O \rightarrow Pt(H_2O)$	-6.6
MAV	**-65.7**	**MAV**	**-6.6**
Pt(III) + H_2		**Pt(0) + H_2**	
Ligand Exchange		**H_2 Adsorption**	
$PtHOClH^* + H_2O \rightarrow PtHO(OH)H^* + HCl$	45.1	$Pt + H_2 \rightarrow PtH_2$	-148.9
$PtH_2Cl(OH)_2 + H_2O \rightarrow PtH_2(OH)_3 + HCl$	31.5	**MAV**	**-148.9**
MAV	**38.3**		
Hydration			
$PtHOClH^* + H_2O \rightarrow PtH_2Cl(OH)_2$	-22.2		
$PtHO(OH)H^* + H_2O \rightarrow PtH_2(OH)_3$	-35.8		
MAV	**-29.0**		
H_2 Adsorption			
$PtOCl + H_2 \rightarrow PtHOClH^*$	-116.7		
$PtO(OH) + H_2 \rightarrow PtHO(OH)H^*$	-163.7		
$PtOCl(H_2O) + H_2 \rightarrow PtH_2Cl(OH)_2$	-31.9		
$PtO(OH)(H_2O) + H_2 \rightarrow PtH_2(OH)_3$	-68.5		
MAV	**-95.2**		

Table SV-3. Reaction energies for various types of reactions calculated at 0 K and ranked according to the oxidation degree of the reactants.

SI. 6 Energy descriptors calculated at 0 K.

To describe the strength of the adsorption process, adsorption energy was calculated for each complex at 0 K without accounting for the zero-point energy correction (**Eq.S1**). Interaction energies describe how strongly complexes are interacting with the support by excluding the energy cost for deformation (**Eq.S2**). The deformation energy of the Pt complex is the destabilization resulting from the constrained geometry after the adsorption of the complex on the support (**Eq.S3**). Similarly, the deformation of the surface is the difference between the optimized surface in absence of the complex and the surface in the geometry resulting from the adsorption of the complex (**Eq.S4**). The adsorption energy can be expressed in term of **Eq.S2-S4** as the strength of the interaction between the complex and the support to which is subtract the destabilizing deformations resulting from the adsorption process. (**Eq.S5**)

$$E^{ads} = E_{system} - E_{complex} - E_{surface} \quad \textbf{Eq.S1}$$

$$E^{int} = E_{system} - E'_{complex} - E'_{surface} \quad \textbf{Eq.S2}$$

$$E^{def}_{complex} = E'_{complex} - E_{complex} \quad \textbf{Eq.S3}$$

$$E^{def}_{surface} = E'_{surface} - E_{surface} \quad \textbf{Eq.S4}$$

$$E^{ads} = E^{int} - E^{def}_{complex} - E^{def}_{system} \quad \textbf{Eq.S5}$$

With E_{system} being the energy of the optimized system (adsorbed complex + support) , $E'_{complex}$ is the energy of the Pt complex in gas phase but with the same geometry as when absorbed. The spin state was also fixed to be the same as for the supported complex system. $E_{complex}$ is the energy of the complex in gas phase but with an optimized geometry and spin state as it is in gas phase. Similarly, $E'_{surface}$ is the energy of the surface without the adsorbed complex but with the geometry after adsorption and $E_{surface}$ is the energy of the optimized surface in absence of the complex. The spin state of the surface was considered to be a singlet.

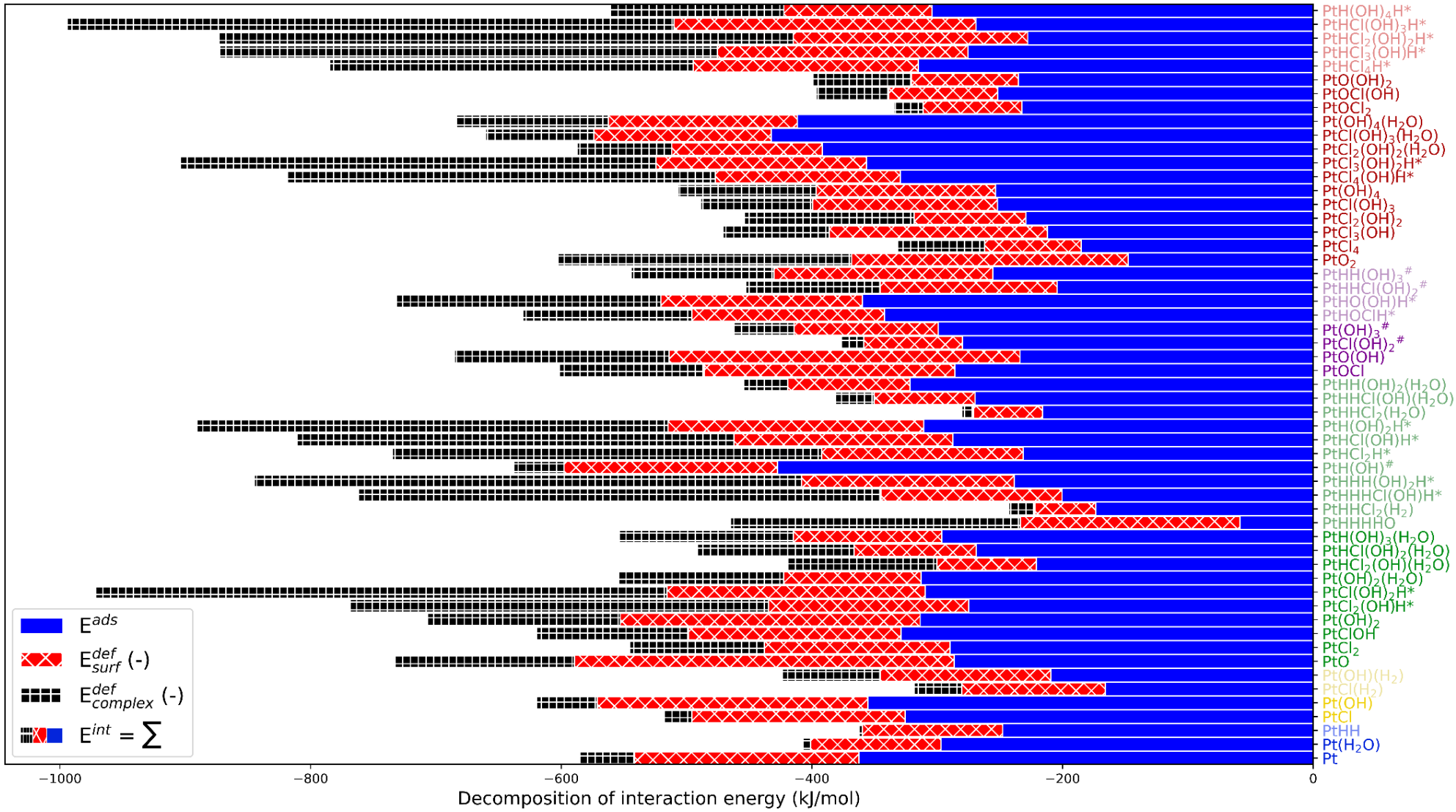

Figure SV-4. Decomposition of the interaction energy for supported complexes. Both deformations are reported as negative value for the sake of clarity. The interaction energy is the sum of the three quantities: E^{ads} + E^{def} (surf) + E^{def}(complex) as described by Eq. S1-4. The color code adopted for the complexes is blue for Pt^0, yellow for Pt^I, green for Pt^{II}, purple for Pt^{III} and red for Pt^{IV}. Lighter colors indicate the complexes with H_2 adsorbed.

SI. 7 The impact of the high stability of $PtCl_2$ in the conclusion on the reducibility of Pt complexes.

The very high stability of supported $PtCl_2$ induces a change in the reduction trends according to the ligands implicated. Our reasoning is based on three points:

First of all, by considering the reduction of $PtCl_y(OH)_{4-y}$ complexes, three of them have $PtCl_2$ as a product: $PtCl_4$, $PtCl_3(OH)$ and $PtCl_2(OH)_2$. If we restraint the study to these three reductions, then decreasing the amount of chlorine in the coordination sphere of the Pt eases the reduction (**Table SV-3**), as for the others oxidation degree. The same effect is predicted for the reduction of the octahedral $PtCl_y(OH)_{4-y}(H_2O)$ which share $PtCl_2(OH)H^*$ as product. (**Table SV-3**)

Secondly, this change is not observed for the gas phase species[1] where we calculated that the more chlorinated was the coordination sphere of the Pt the harder the reduction would be. Hence, we can suspect that this effect might be caused by the surface.

Finally, because of the convention we choose to only consider the most stable conformer for a given stoichiometry we are missing that the reduction we are describing is also accompanied by the migration of the platinum (**Figure SV-5**). Indeed, as the number of ligands become two after the reduction, a change of the adsorption site is expected. If we do not consider the migration of the platinum during the reduction, then we retrieve that chlorines harden the reduction of the platinum in comparison to hydroxyls with +42.5 kJ/mol for the reduction of $PtCl_4$ into $PtCl_2$ against +2.5 kJ/mol for the reduction of $Pt(OH)_4$ into $Pt(OH)_2$. For the reduction of Pt(II) into Pt(0), we observed that the reduction is harder for $PtCl_2$ than $Pt(OH)_2$ but by accounting for the migration of Pt(II) the effect is exacerbated. (**Table SV-4**)

Hence the bi-grafted $PtCl_2$ is stable enough to impact the conclusion that one can obtain on the reducibility of chlorinated platinum compared to hydroxylated platinum.

We will detail these migration phenomena in in the part dedicated to the kinetic analysis of the reduction.

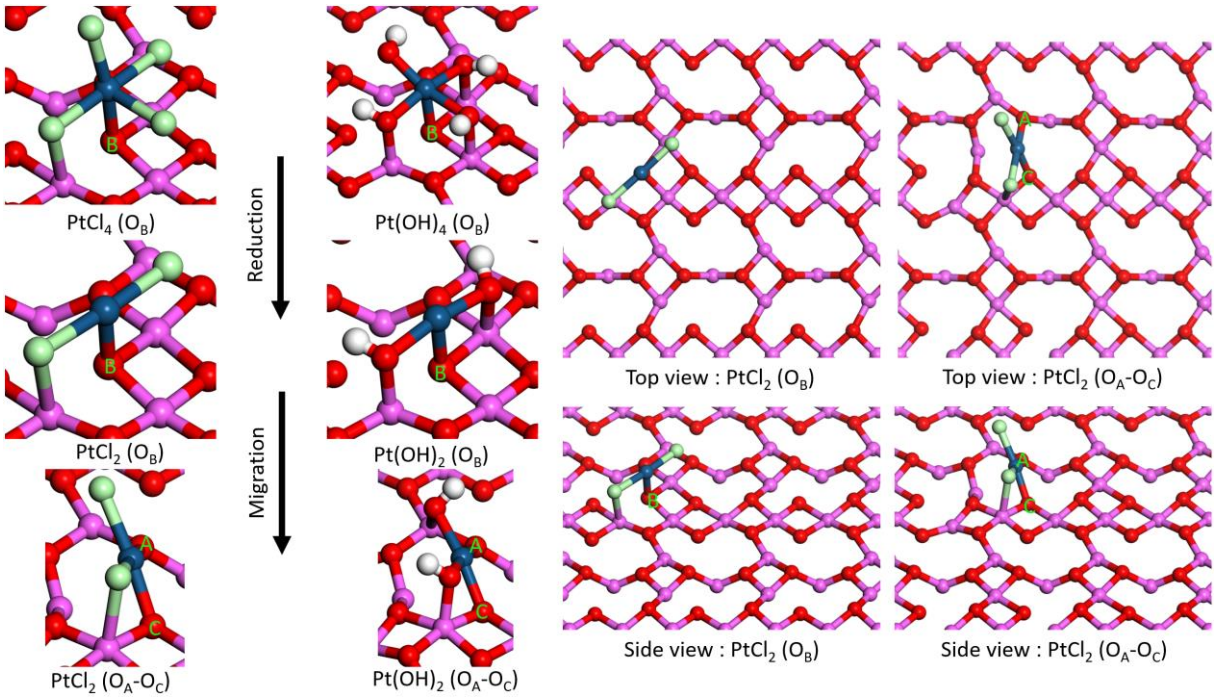

Figure SV-5. Atomistic representation of the reduction of $PtCl_4$ and $Pt(OH)_4$ into $PtCl_2$ and $Pt(OH)_2$, with spatial details regarding the adsorbed complexes on the (100) surface. Color code for atomic structure: Pt: blue; Cl: green; O: red; Al: pink, H: white.

Reduction without migration	**ΔE (kJ/mol)**	**Reduction with migration (Table S4)**	**ΔE (kJ/mol)**
$PtCl_4 + H_2 \rightarrow PtCl_2(O_b) + 2\ HCl$	42.5	$PtCl_4 + H_2 \rightarrow PtCl_2(O_A\text{-}O_C) + 2\ HCl$	-114.5
$Pt(OH)_4 + H_2 \rightarrow Pt(OH)_2(O_b) + 2\ H_2O$	2.5	$Pt(OH)_4 + H_2 \rightarrow Pt(OH)_2(O_A\text{-}O_C) + 2\ H_2O$	87.0
$PtCl_2(O_b) + H_2 \rightarrow Pt + 2\ HCl$	52.2	$PtCl_2(O_b) + H_2 \rightarrow Pt + 2\ HCl$	208.7
$Pt(OH)_2 + H_2 \rightarrow Pt + 2\ H_2O$	-13.5	$Pt(OH)_2 + H_2 \rightarrow Pt + 2\ H_2O$	76.0

Table SV-4. Reduction energies by excluding the migration of the platinum into the adsorption site O_A-O_C during the formation of Pt(II). For comparison the values by including the migration as reported in Table SV-3 are added.

SI 8. Calcination and reduction thermodynamic diagrams calculated at the PBE-dDsC level.

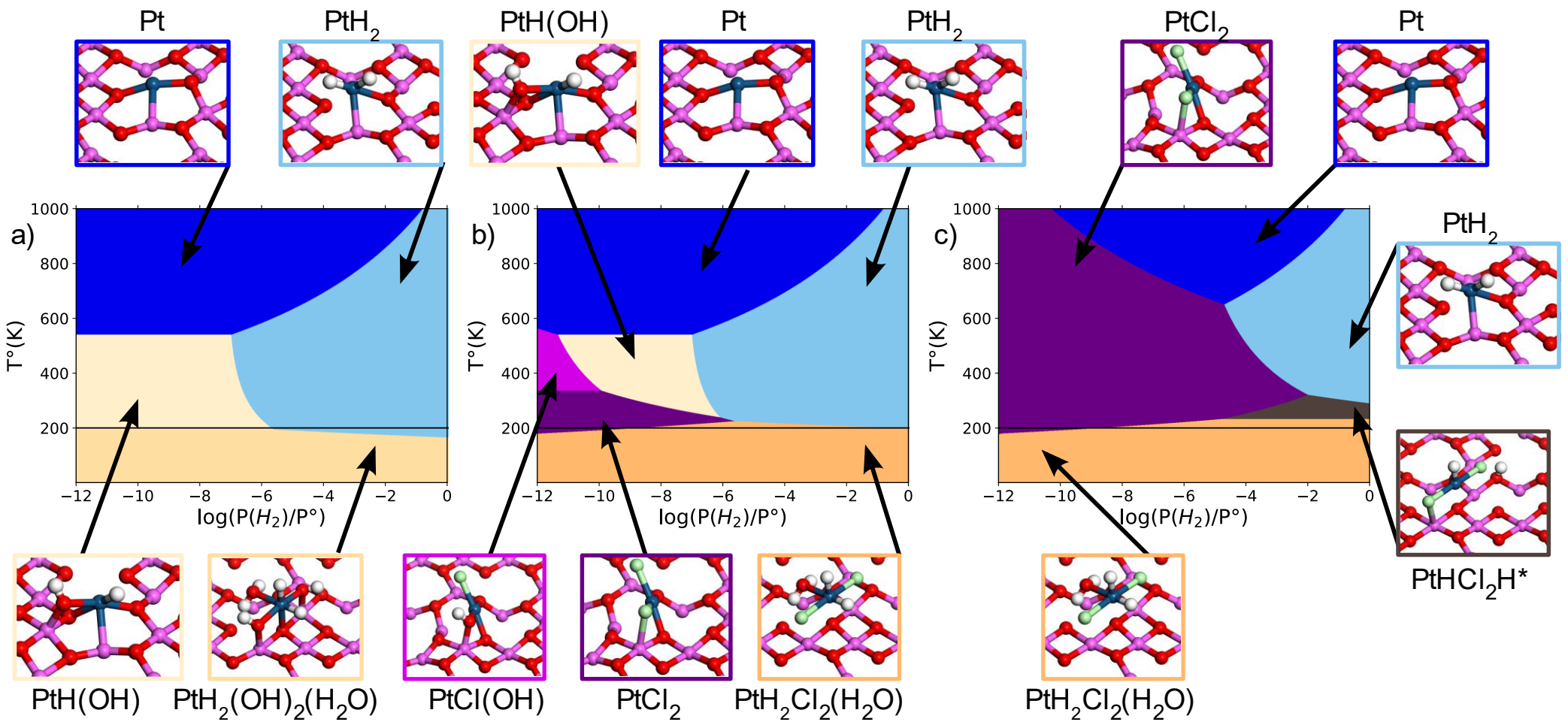

Figure SV-6. Thermodynamic diagrams calculated at the PBE-dDsC level of the most stable species under reductive conditions at $P(H_2O) = 1.10^{-6}$ bar for three chlorine loadings: a : Without chlorine; b : $P(HCl) = 1.10^{-12}$ bar; c : $P(HCl) = 1.10^{-6}$ bar. Color code for atomic structure: Pt: blue; Cl: green; O: red; Al: pink, H: white. The gas phase domain of water is located above the black straight line.

SI 9. On the reduction of $PtOCl_2$.

$$PtOCl_2 + H_2 \rightleftarrows \mathrm{PtO} + 2\mathrm{HCl} \quad \textbf{Eq.S6}$$

$$PtOCl_2 + H_2 \rightleftarrows \mathrm{PtCl(OH)} + \mathrm{HCl} + \mathrm{H_2O} \quad \textbf{Eq.S7}$$

$$PtOCl_2 + H_2 \rightleftarrows \mathrm{PtCl_2} + 2\mathrm{H_2O} \quad \textbf{Eq.S8}$$

In order to establish the relative stability between products of the reduction of $PtOCl_2$ by H_2, we calculate the Gibbs free energies of reaction according to the three equation **Eq. S5-S7**. From our previous considerations on the calcination step we established that the stability domain of $PtOCl_2$ at $P(H_2O) = 1.10^{-6}$ bar at 775 K was comprised between $P(HCl) = 1.10^{-7}$ bar and 1.1^{-4} bar (**Chapter IV** and **Figure IV-8**).

The results are reported in **Figure SV-7** where the relative stability of the product is considered according to the HCl pressure and temperature for $P(H_2O) = 1.10^{-6}$ bar and $P(H_2) = 1$ bar. For the HCl pressure corresponding to the stability of $PtOCl_2$ post-calcination, we can see that $PtCl_2$ is expected for $P(HCl) > 1.10^{-9}$ bar.

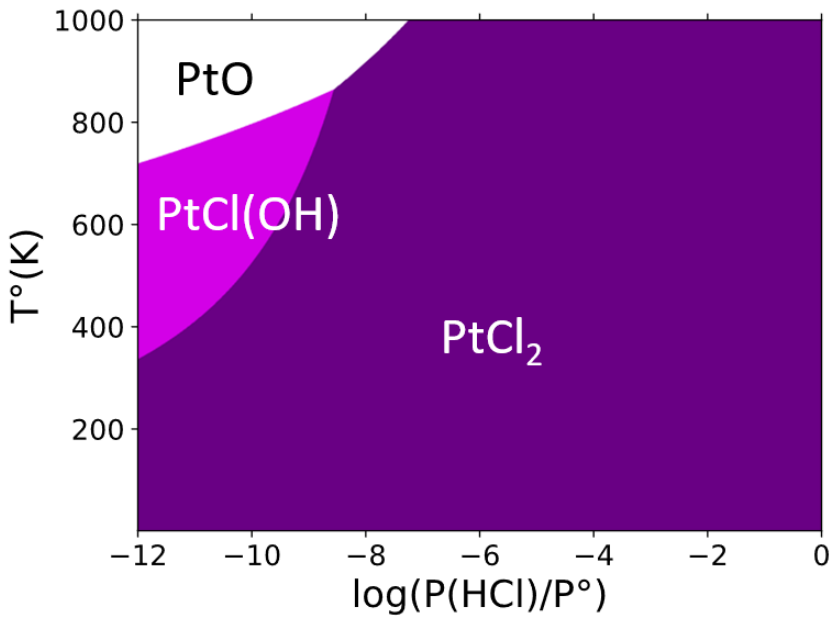

Figure SV-7. Thermodynamic diagram of the most stable product of the reduction of $PtOCl_2$ at $P(H_2O) = 1.10^{-6}$ bar and $P(H_2) = 1$ bar.

SI 10. On the reduction of PtO_2.

Part I:

At 0 K, $\Delta E = 129$ kJ/mol for the formation of PtO against $\Delta E = -248$ kJ/mol for the formation of $Pt(OH)_2$ (simply grafted to the surface). However, by accounting for the temperature and the water pressure we calculated at reduction conditions (T = 775 K, $P(H_2O) = 10^{-6}$ bar and $P(H_2) = 1$ bar), the free enthalpy of the reaction $PtO_2 + H_2 \rightarrow PtO + H_2O$ is -238.8 kJ/mol against -142 kJ/mol for $PtO_2 + H_2 \rightarrow Pt(OH)_2$. While the formation of $Pt(OH)_2$ is favored for its intrinsic stability over PtO, high temperatures and low water pressure will favors the formation of the latter for entropic reason (**Figure SV-8**).

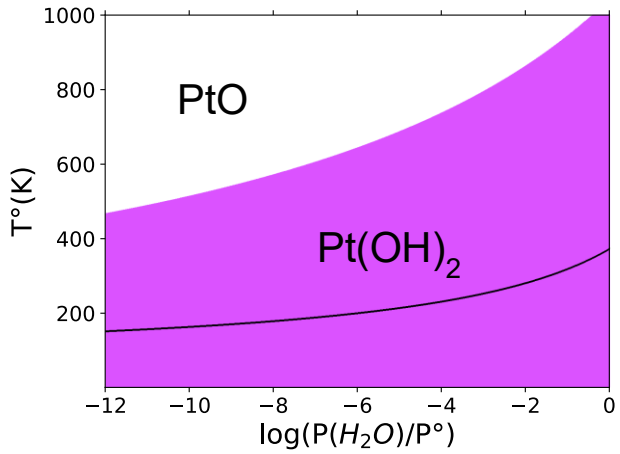

Figure SV-8. ***Relative stability of the products from the reduction of PtO2 under H2 according to the temperature and the pressure. H2 pressure is fixed at 1 bar. The gas phase domain of water is located above the black curved line.***

Part II:

The pathways to form PtO or $Pt(OH)_2$ from PtO_2 are highly similar and only differ on the last transition step where the proton will either go on the remaining oxo ligand to form $Pt(OH)_2$ or on the hydroxyl to form $PtO(H_2O)$ which will be followed by the desorption of water. As we saw in **Figure SV-8** at 775 K and $P(H_2O) = 10^{-6}$ bar, PtO is the thermodynamical product.

If we consider kinetic aspects, the comparison of the two profiles reveal that they are very similar at 775 K (**Figure SV-9**). While being energetically less interesting, the formation of $PtO(H_2O)$ allows through the desorption of H_2O at 775 K the formation of PtO which is relatively more stable than $Pt(OH)_2$ adsorbed on a O_B.

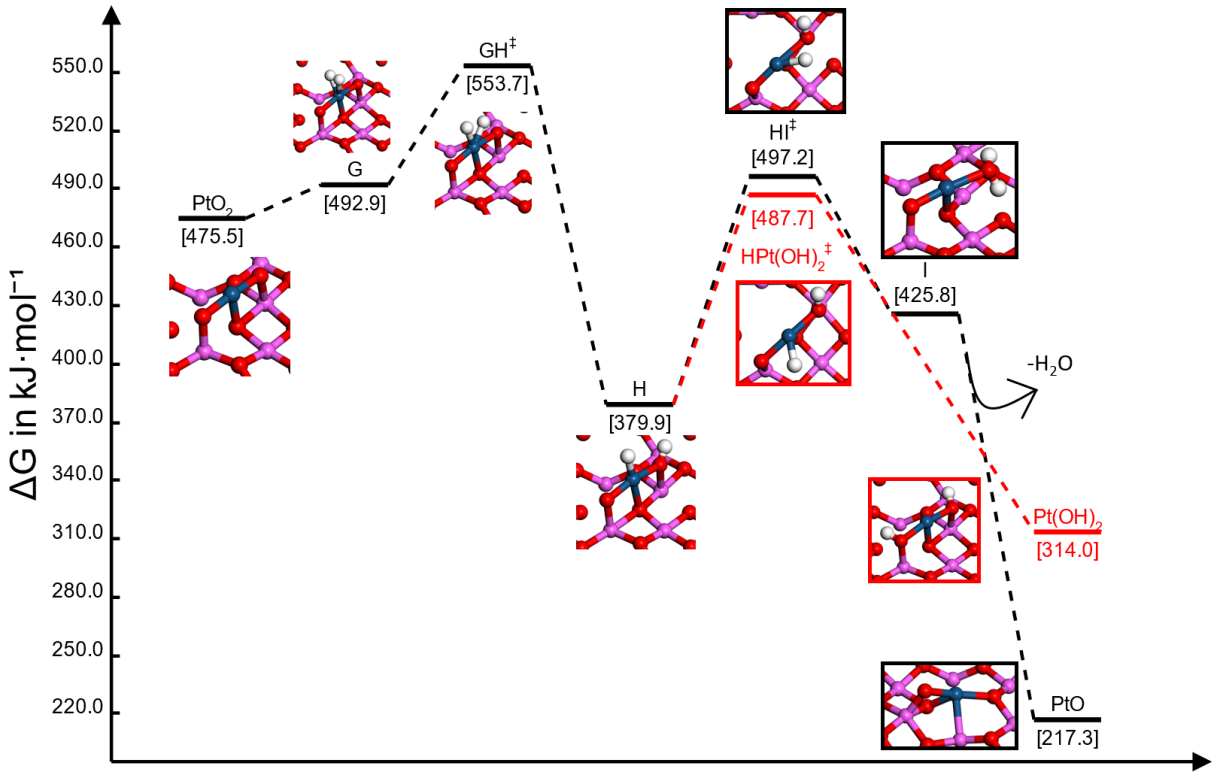

Figure SV-9. Free energy profiles calculated at T = 775 K, $P(H_2O) = P(HCl) = 10^{-6}$ bar and $P(H_2) = 1$ bar for the comparison of the products of PtO_2 reduction by H_2. Color code for atomic structure: Pt: blue; Cl: green; O: red; Al: pink, H: white. Highest energy barrier is indicated for each profile.

SI 11. Details on transition states for the reduction of Pt(IV) into Pt(II)

Name	Imaginary frequencies (cm^{-1})	Energy (kJ/mol)	Description
Reduction of $PtCl_4$ into $PtCl_2$			
BC‡	735.9	587.7	HCl formation
DE‡	733.3	460.8	Internal rearrangement
FG‡	562.7	331.5	HCl formation
Reduction of $Pt(OH)_4$ into $Pt(OH)_2$			
BC‡	724.55	709.1	H_2O formation
CD‡	536.44	571.6	H_2O rotation
EF‡	123.05	559.9	Internal rearrangement
FG‡	331.54	466.7	OH rotation
GH‡	719.68	487.0	H_2O formation
Reduction of $PtOCl_2$ into $PtCl_2$			
BC‡	442.8	575.2	H_2 dissociation
CD‡	101.6	457.5	OH formation
DE‡	316.9	353.7	Pt-H formation
EF‡	312.3	323.2	OH rotation
FG‡	581.1	358.7	HCl formation
GH‡	473.1	367.6	OH formation
IJ‡	25.6	251.1	Pt-O_{surf} bond breaking
Reduction of PtO_2 into PtO			
AB‡	98.5	563.8	O-Al bond breaking
BC‡	116.7	562.3	Pt-O_{surf} bond breaking
CD‡	109.0	547.3	Pt-O_{surf} bond breaking
EF‡	188.6	537.1	O-Al bond breaking
GH‡	1204.7	553.7	Ho formation
HI‡	886.5	497.2	H_2O formation

Table SV-5. Details on the transition states for the main pathways presented in Figure SV-8.

SI.12 Impact of the temperature on the reduction of supported Pt(IV) into Pt(II)

Using high temperature is known to favor the reduction of the Pt(IV) into Pt(II). By comparing the free energy profile at 775 K (**Figure SV-8**) and the electronic energy profile at 0 K (**Figure SV-10**) the reduction of Pt(IV) into Pt(II) species is indeed much less favorable at low temperature.

The reduction of $PtCl_4$ into $PtCl_2$ (and to a lower extent, of $Pt(OH)_4$ into $Pt(OH)_2$) is even endothermic at 0 K. The activation barriers are greatly increased in different proportion for each species $\Delta G^{\ddagger}_{(DE-C)_{green}} = +188.3$ kJ/mol, $\Delta G^{\ddagger}_{(EF-D)_{red}} = +249.6$ kJ/mol, $\Delta G^{\ddagger}_{(IJ-D)_{blue}} = +187.7$ kJ/mol and $\Delta G^{\ddagger}_{(CD-A)_{black}} = 138.7$ kJ/mol. Moreover, as it could be expected, the release of HCl or H_2O is not a stabilizing factor anymore at 0 K. These values highlight the beneficial contribution of the temperature in the reduction process, also from a kinetic perspective. We can notice that the first part of the reduction of PtO_2 (the diffusion, from A_{black} up to F_{black}) is only slightly impacted by the temperature.

The high energy profile of PtO_2 can be rationalized by the nature of the reaction required to form it from $PtCl_4$. Four chlorines have to be exchanged for four hydroxyls, which is an endothermic process. Then a double dehydration is required. As we saw in **Figure SV-10** and in the **Table SV-3** dehydrations are also endothermic.

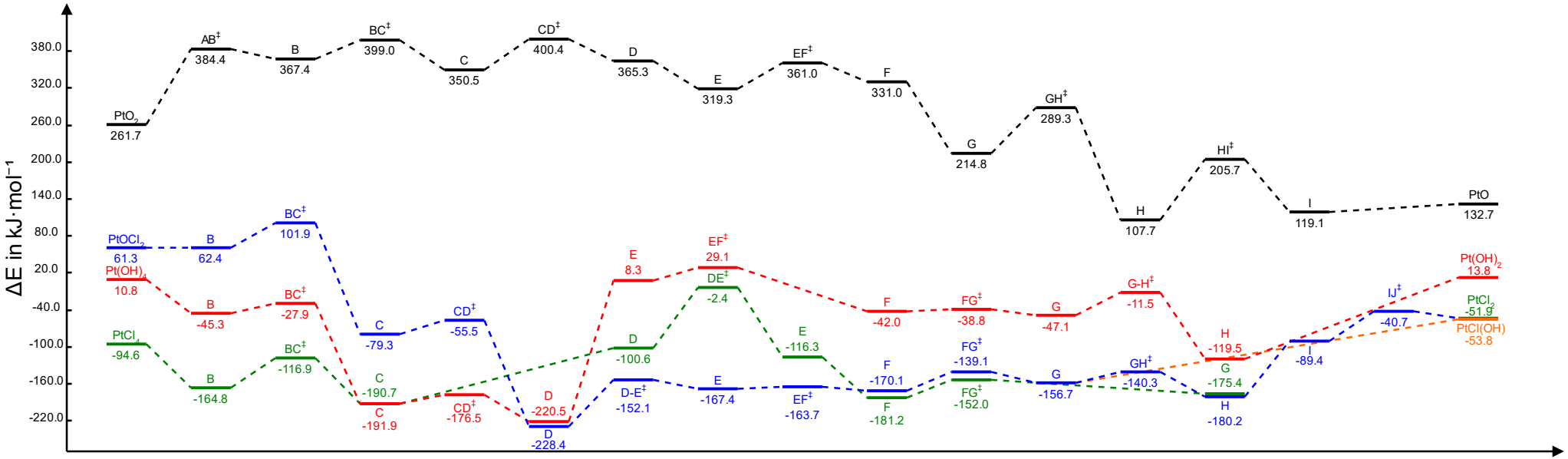

Figure SV-10. Electronic energy profiles of the Pt(IV) reduction into Pt(II) in the presence of H_2 at T = 0 K. The energies are referenced with the Pt/Al_2O_3 being at 0 kJ/mol. The colors used for each pathway are the same than in Figure SV-8 where the structures are visible. Transition states are indicated through the two letter and a double dagger (ex : BC‡).

SI 13. Reduction of $Pt(OH)_4$ into $Pt(OH)_2$. Alternative surface-assisted pathways

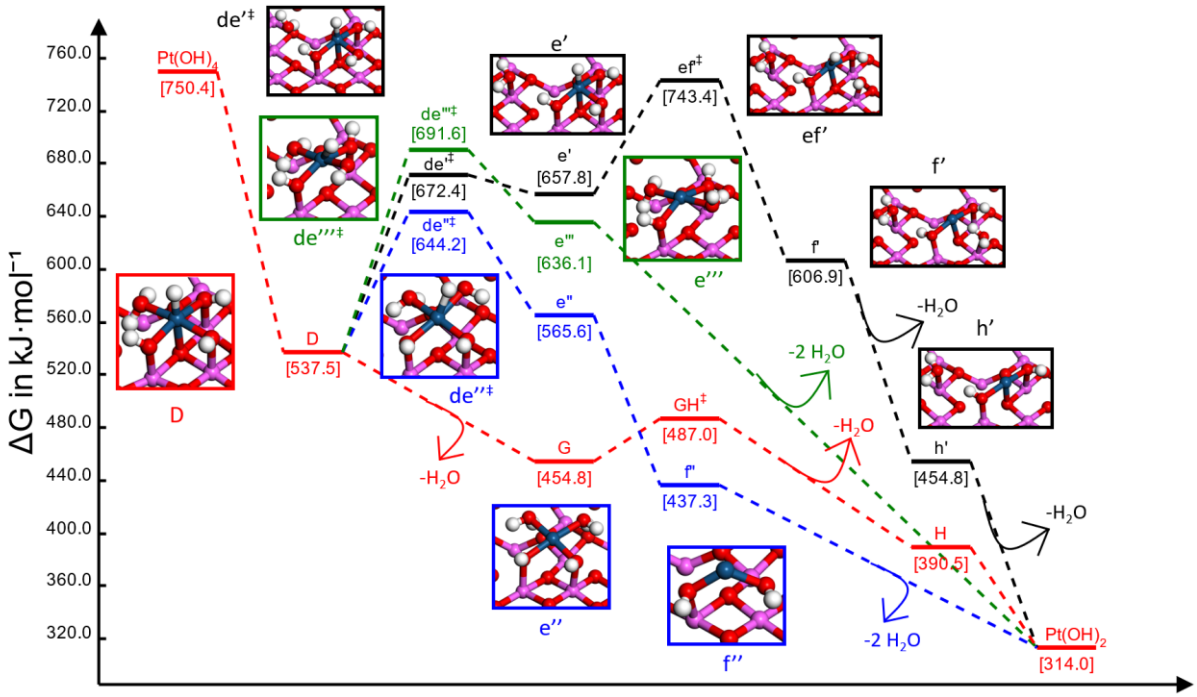

Figure SV-11. Free energy profiles calculated at T = 775 K, $P(H_2O) = P(HCl) = 10^{-6}$ bar and $P(H_2) = 1$ bar for competitive pathways for the reduction of $Pt(OH)_4$ into $Pt(OH)_2$. The blue and green paths consider the possible accumulation of water on the Pt during the reduction. The black one describes the participation of the surface during the reduction process of the platinum. In all three cases, they were found less favorable than the path presented in Figure SV-8 (red). $GH^{\ddagger}_{red}$ correspond to the most activated water formation of the red path in Figure SV-8. Transition states are indicated through the two letter and a double dagger (ex : $BC^{\ddagger}$). Color code for atomic structure: Pt: blue; Cl: green; O: red; Al: pink, H: white. Structures are framed in the same color as their corresponding pathway and the corresponding intermediate is indicated.

SI 14. Details on transitions states for the reduction of Pt(II) into Pt(0)

Name	Imaginary frequency (cm^{-1})	Energy (eV)	Description
Reduction of $PtCl_2$ into Pt			
BC‡	597.5	268.0	HCl Formation
CD‡	74.8	304.8	HCl desorption
FG‡	442.4	150.5	Pt-H formation
GH‡	663.9	183.8	HCl formation
Reduction of $Pt(OH)_2$ into Pt			
BC‡	984.2	351.4	H_2O formation
DE‡	155.3	277.5	HO-Al bond breaking
EF‡	970.0	226.6	H_2O formation
Reduction of PtO into Pt			
BC‡	461.66	269.8	OH formation
Reduction of PtCl(OH) into Pt (Blue path)			
BC‡	645.09	283.9	HCl formation
Reduction of PtCl(OH) into Pt (Grey path)			
BC‡	991.67	285.9	H_2O formation

Table SV-6. Details on the transition states for the main pathways presented Figure SV-9.

SI.15 Impact of the temperature on the reduction of Pt(II) into Pt(0)

The effect of the temperature is far from being negligible and highlight the importance of considering entropic and enthalpic effect in the modelling of processes occurring at high temperature. The relative stability of Pt(II) against Pt(0) is totally revisited (**Figure SV-12**) by considering that the reduction occurs at 0 K. In that case, only the reductions of PtO and $Pt(OH)_2$ (in a smaller extent) are thermodynamically favorable. As it could be expected, adsorptions of H_2 result in strong stabilization, and the formation of the three square planar $PtCl_2(H_2)$, $PtCl(OH)(H_2)$ and $Pt(OH)_2(H_2)$ is now highly exothermic. The limiting steps require higher activation energy (between +48.3 kJ/mol for the reduction of $PtCl_2$ and +34.9 kJ/mol for the reduction of $Pt(OH)_2$) and the presence of the highly stables intermediates such as the $B_{green,red,blue,grey}$ or G_{green} and E_{red} highlight how increasing the temperature can ease the reduction.

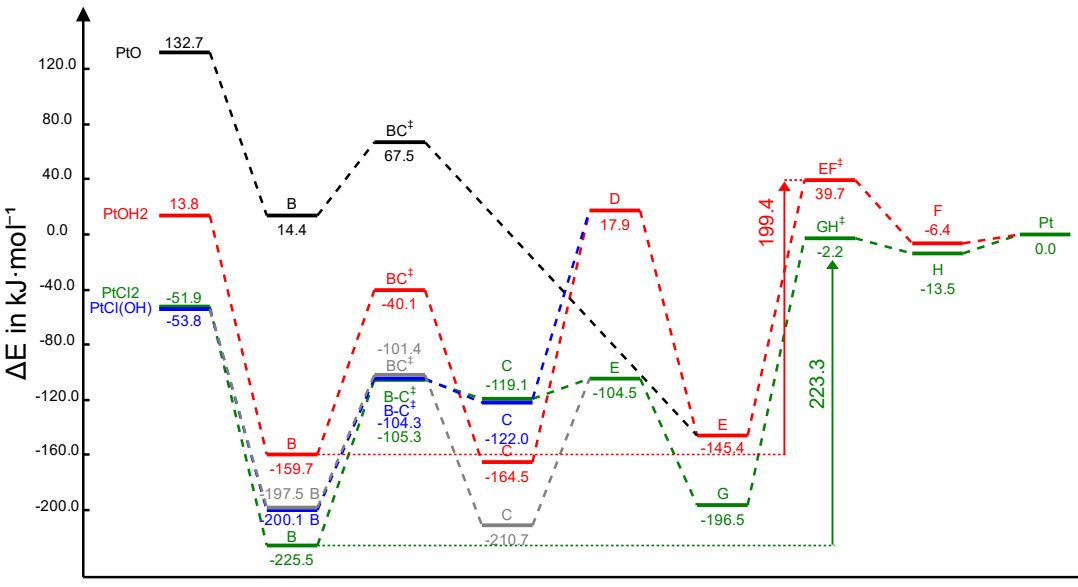

Figure SV-12. Electronic energies for key steps of the reduction of Pt(II) complexes into Pt(0). Color code for profile is taken from the full pathways available in Figure SV-9. If two pathways lead to the same intermediate, only one of them is reported after, in this case, red and green lines were chosen. The free energies are referenced with Pt/Al_2O_3 being at 0 kJ/mol. Transition states are indicated through the two letter and a double dagger (ex: $BC^{‡}$). Color code for atomic structure: Pt: blue; Cl: green; O: red; Al: pink, H: white. Highest energy barrier is indicated for each profile.

SI 16. Alternative pathways for the reduction of $PtCl_2$ into Pt(0)

In the case of $PtCl_2$ the formation of the first labile molecule occurs in a different position than for the other Pt(II) species. Trying to get HCl in the same position as the others (**Figure SV-13,** ${e'}_{red}$) requires a stronger participation of the surface which results in a higher free energy pathway and the migration of a proton to the support was first needed (**Figure SV-13**, d'_{red},). The following formation of HCl and its desorption require to overcome higher activation barriers with at $\Delta G^{\ddagger}_{(de'-d')_{red}} = +180$ kJ/mol and $\Delta G^{\ddagger}_{(ef'-d')_{red}} = 199.5$ kJ/mol. The formation of the second HCl is, however, less activated ($\Delta G^{\ddagger}_{(jk'-j')_{red}} = 133.4$ kJ/mol) than for the principal pathway presented previously as we avoid the formation of the highly stable G_{green} (**Figure SV-9**). This formation of the second HCl is a multi-step process as the required proton was first adsorbed on the surface to allow the formation of the first HCl. It is thus necessary to consider its diffusion to Pt. Surprisingly, we found out that it is easier to bring closer the adsorbed PtCl (h'_{red}) to the proton than doing the opposite as the diffusion the of proton over the (100) γ-Al_2O_3 surface requires to overcome very high activation barriers (>300 kJ/mol) (not reported in **Figure SV-13**).

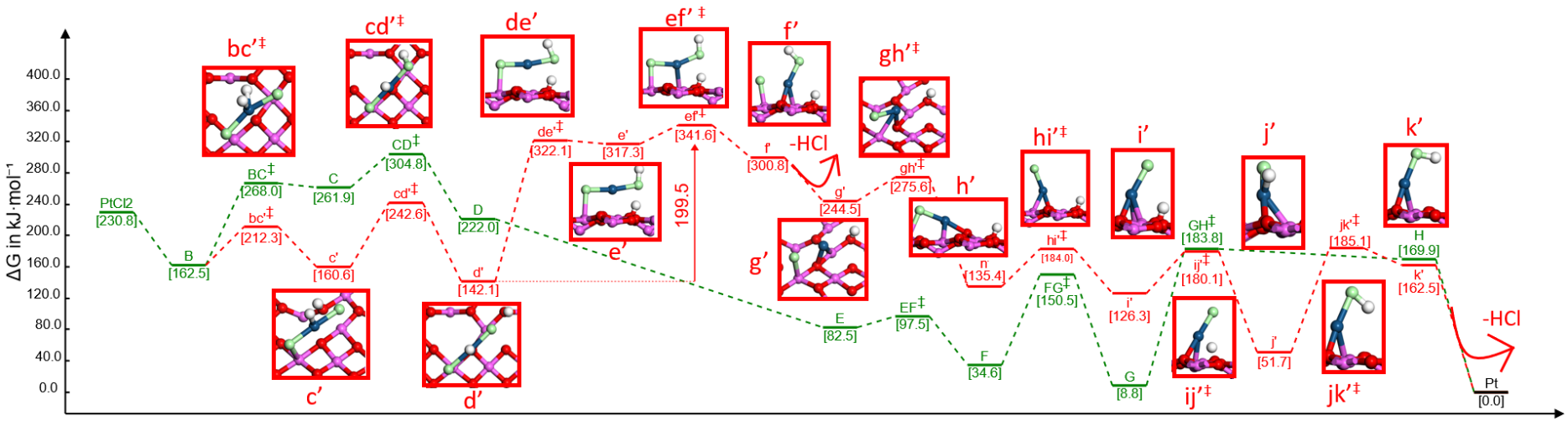

Figure SV-13. Free energy profiles calculated at T = 775 K, $P(H_2O) = P(HCl) = 10^{-6}$ bar and $P(H_2) = 1$ bar for the comparison of two pathways for the reduction of $Pt(Cl)_2$ into Pt. The green path with capital letters is the principal one as presented in Figure SV-9, while the red one with lower case letters and single quotation marks is the alternative. The free energies are referenced with Pt/Al_2O_3 being at 0 kJ/mol. Transition states are indicated through the two letter and a double dagger (ex : $BC^‡$). Color code for atomic structure: Pt: blue; Cl: green; O: red; Al: pink, H: white. Highest energy barrier is indicated for each profile. Irrelevant steps such as rotation of hydroxyls, that are lowly activated, were omitted here.

SI 17. Alternative pathways for the reduction of $Pt(OH)_2$ into Pt

Unlike the reduction of $PtCl_2$ the reduction of $Pt(OH)_2$ is independent of the choice of the first hydroxyl to be desorbed, as it is highlighted with the blue profile in **Figure SV-14.** Similar activation energies are calculated for the formation of the second H_2O ($\Delta G^{\ddagger}_{(h''-i'')_{blue}} = 164.3$ kJ/mol while the formation of the first water molecule is less activated ($\Delta G^{\ddagger}_{(c''-d'')_{blue}} = 99.3$ kJ/mol) than in the path proposed in **Figure SV-9**. However, this implies a less stable intermediate (d''_{blue}). As it is represented with the green profile, the surface can change the reduction profile of PtH(OH) by avoiding the formation of the highly stables E_{red} (**Figure SV-9**)or h''_{blue} (**Figure SV-14**) intermediates which could limit the reduction. As the first H_2O is desorbed and D_{red} is formed, another alternative is to form H_2O on the surface as exhibited in f'_{green}. By doing so, the highest barrier is lowered to $\Delta G^{\ddagger}_{(ef'-e')_{green}} = 134.8$ kJ/mol but intermediates with higher energies are expected through this path (green path of **Figure SV-14**).

In the end, the blue profile is energetically competitive with the one presented in the manuscript for the reduction of $Pt(OH)_2$ into Pt. The choice of the red over the blue one is based on the level of verification done on the transition states. While for the pathways presented in the manuscript, all TS have been verified through an IRC analysis, these alternative pathways have been subject to less constrained exigences, and the IRC analysis has not been performed on all of these alternative TS. However, it has to be noted that vibrational calculation has been performed in order to ensure that they are first order saddle point of the PES and that the vibrational mode correspond to the desired reaction.

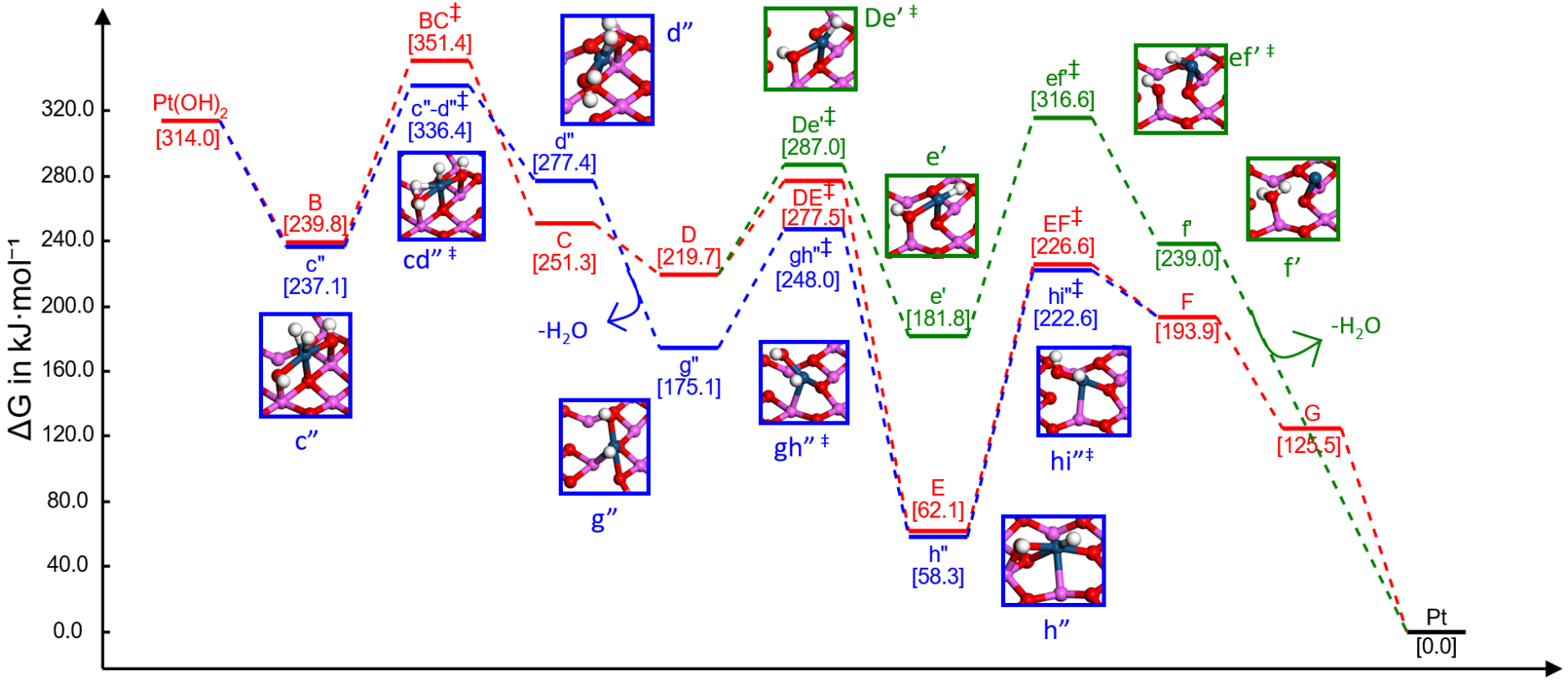

Figure SV-14. Free energy profiles calculated at T = 775 K, $P(H_2O) = P(HCl) = 10^{-6}$ bar and $P(H_2) = 1$ bar for the comparison of two pathways for the reduction of $Pt(OH)_2$ into Pt. The red profile with capital letters is the principal one as reported in Figure SV-9. The green and blue profiles with lower case letters and quotation marks are alternatives. The free energies are referenced with Pt/Al_2O_3 being at 0 kJ/mol. Transition states are indicated through the two letter and a double dagger (ex : $BC^‡$). Color code for atomic structure: Pt: blue; Cl: green; O: red; Al: pink, H: white. Highest energy barrier is indicated for each profile. Irrelevant steps such as rotation of hydroxyls, that are lowly activated, were omitted here.

SI 18. Migration of bi-grafted complexes.

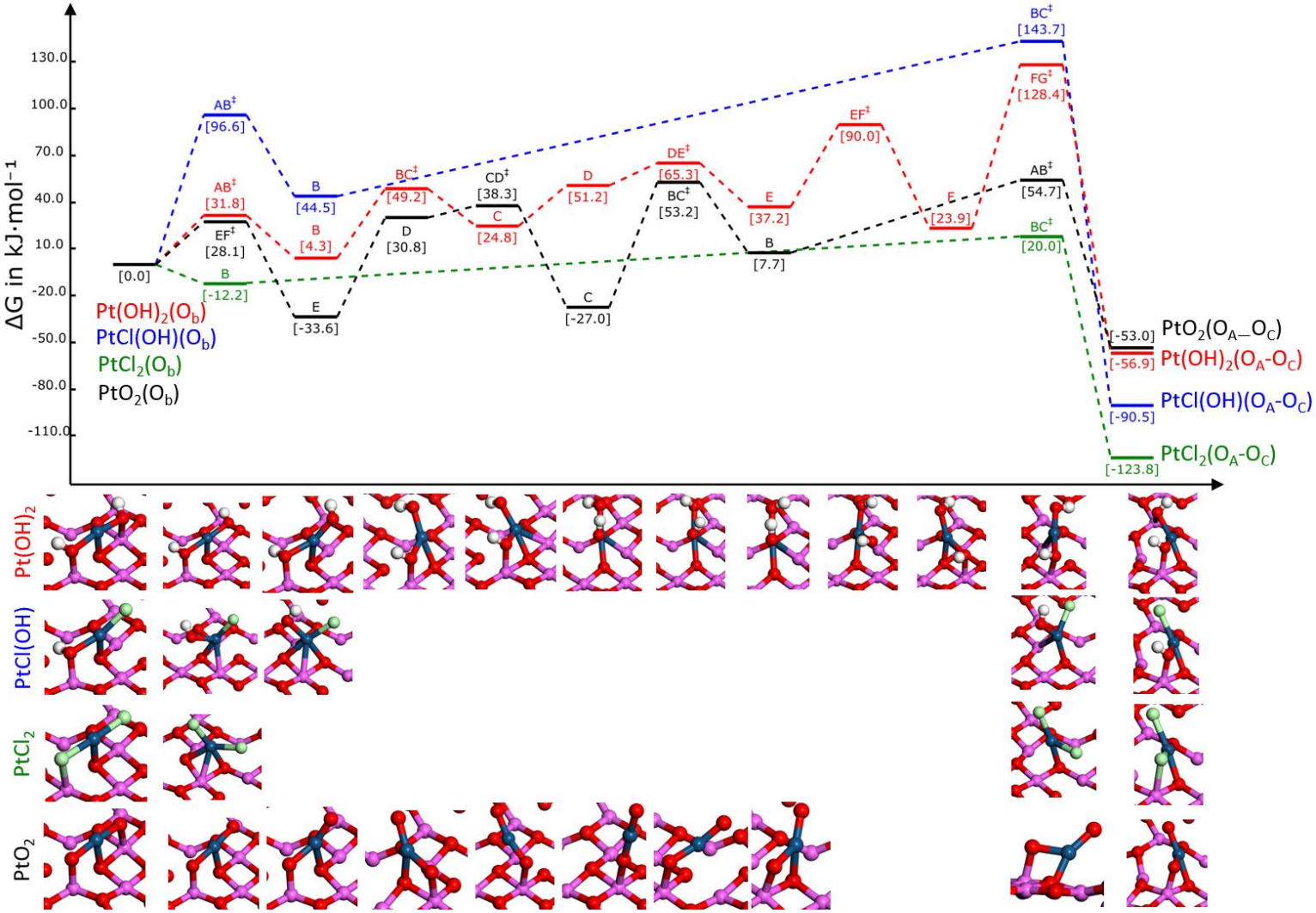

Figure SV-15. Free energy profiles calculated at T = 775 K, P(H_2O) = P(HCl) = 10^{-6} bar and P(H_2) = 1 bar for migration of bi-grafted complexes. The free energies are referenced with the reactant of each profile being at 0 kJ/mol. Transition states are indicated through the two letter and a double dagger (ex : $BC^{‡}$). Color code for atomic structure: Pt: blue; Cl: green; O: red; Al: pink, H: white. Highest energy barrier is indicated for each profile.

SI 19. Details on transition states of the migration of bi-grafted Pt(II).

Name	Imaginary frequencies (cm^{-1})	Energy (kJ/mol)
Migration of $PtCl_2$		
$BC^{‡}$	49.5	20.0
Migration of PtCl(OH)		
$AB^{‡}$	97.4	96.6
$BC^{‡}$	101.2	143.7
Migration of $Pt(OH)_2$		
$AB^{‡}$	177.4	31.8
$BC^{‡}$	47.6	49.2
$DE^{‡}$	212.4	65.3
$EF^{‡}$	78.5	90.0
$FG^{‡}$	163.0	128.4

Table SV-7. Details on the transition states for the main pathways presented in Figure SV-15

SI 20. Impact of temperature on the migration of supported Pt(II) complexes.

In all cases, the final product is less stabilized (between + 24.3 kJ/mol for PtCl(OH) and + 34.5 kJ/mol for $PtCl_2$) compared to the reactant with the increase of temperature probably due to the constraints induced by the O_A-O_C adsorption site which brings the platinum closer to the surface. At 0 K, the intermediates and TS along the migration of both PtCl(OH) and $Pt(OH)_2$ are stabilized in similar proportions leading to small changes to the kinetics of these reactions with the temperature. The activation barriers are lowered by 14.7 kJ/mol in the case of PtCl(OH) (158.4 kJ/mol at 0 K and 143.7 kJ/mol at 775 K) and 16.9 kJ/mol for $Pt(OH)_2$ (with 145.3 kJ/mol at 0 K and 128.4 kJ/mol at 775 K). The case of $PtCl_2$ is different as the stabilization of the intermediates and TS are not consistent along the migration and the intermediate B_{green} is relatively more stabilized at 0 K than the $BC^{\ddagger}_{green}$ TS (**Figure SV-16**) but the activation barrier remains extremely low: 36.4 kJ/mol at 0 K and 32.2 kJ/mol at 775 K. Overall, migrations are slightly eased with the increase of temperature.

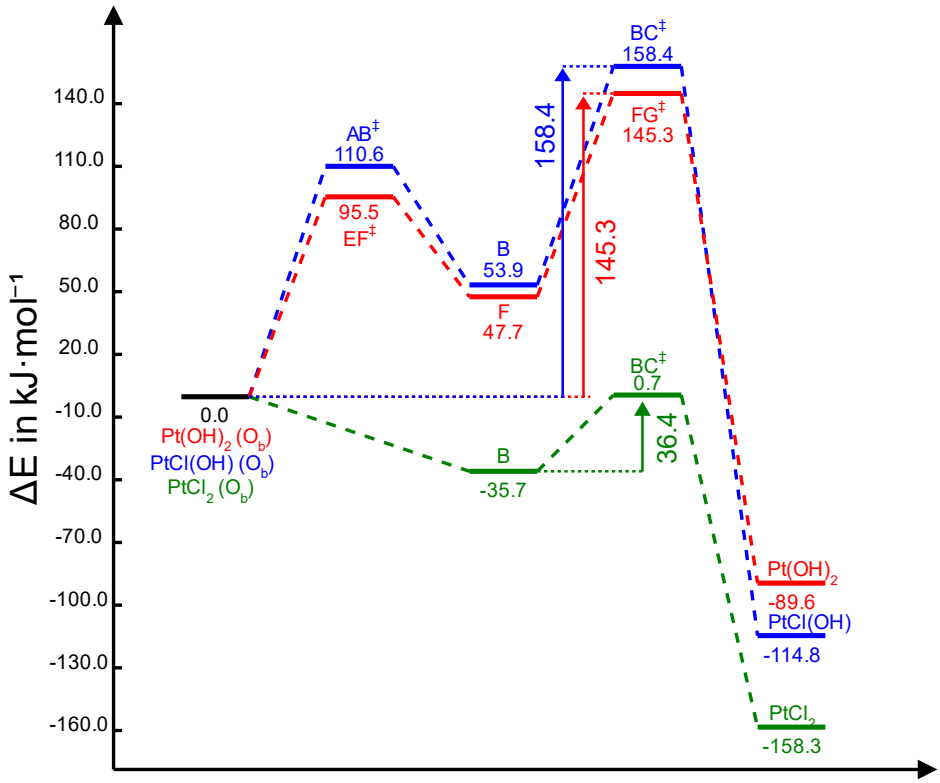

Figure SV-16. Electronic energies for key steps of the migration of Pt(II) complexes. The color code for the pathways is the following: red for $Pt(OH)_2$, blue for PtCl(OH) and green for $PtCl_2$. Name of intermediates are taken from the full pathways available in Figure SV-15. Transition states are indicated through the two letters and a double dagger (ex : $BC^{\ddagger}$).

SI 21. Self-reduction of bi-grafted Pt(II)

As exhibited by the calculation of the Gibbs free energies (**Figure SV-17**, **a)**) the self-reduction of $PtCl_2$, either by the release of Cl_2 or through the migration of the chlorine on the (100) is thermodynamically prohibited. In a lesser extent, the reduction of $Pt(OH)_2$ with a similar mechanisms leading to the formation of surface hydroxyls is also unfavored.

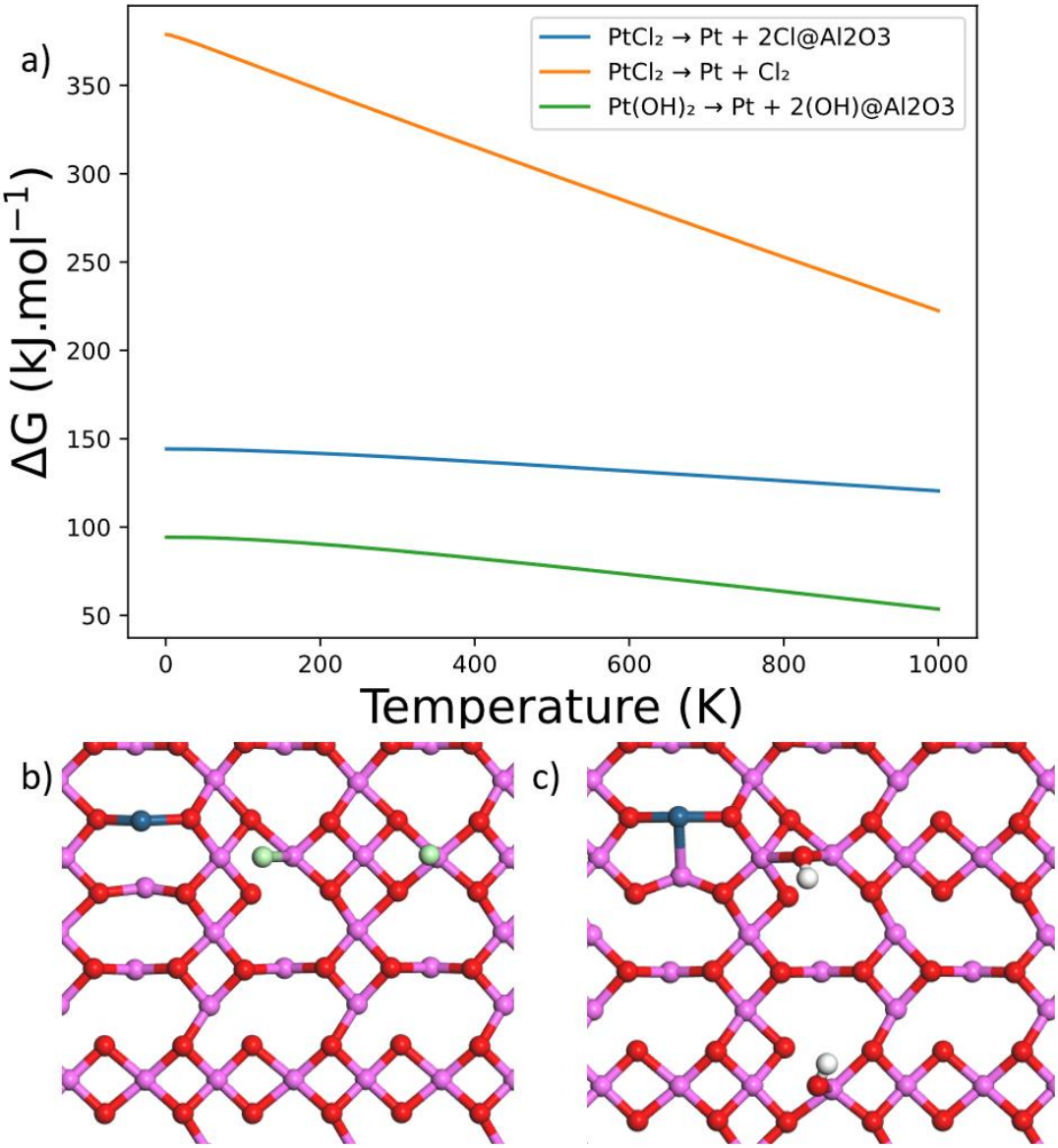

Figure SV-17. a) Gibbs free energy of reaction for various mechanisms of self-reduction of $PtCl_2$ and $Pt(OH)_2$. Two mechanisms are considered, the release of Cl_2 for $PtCl_2$ and the migration of ligand onto the surface for both $PtCl_2$ and $Pt(OH)_2$. b) Most stable adsorption sites for chlorine on the (100) γ-Al_2O_3. c) Most stable adsorption sites for OH on the (100) γ-Al_2O_3.

SI.22 About the stability of $PtCl_2$ under oxidizing atmosphere

We established the existence of the bi-grafted supported $PtCl_2$ under a reducing atmosphere and thus it is necessary to check in what extent such species could be stable under the oxidizing atmosphere used by Marceau et al.[2,3] during methane oxidation. Similar to the calculation of the thermodynamic stability of platinic species during the reduction (**Figure V-6**) we simulate here the relative stability of relevant species under oxidizing conditions. By following the experimental protocol of Marceau et al.[3] we fixed the O_2 pressure at 0.21 bar and the temperature at 725 K. The quantity of chlorine is controlled via the HCl pressure which can range from 1.10^{-12} bar to 1 bar and the same variation are used for H_2Os pressure. The pool of species considered is described in **Figure SV-18**.

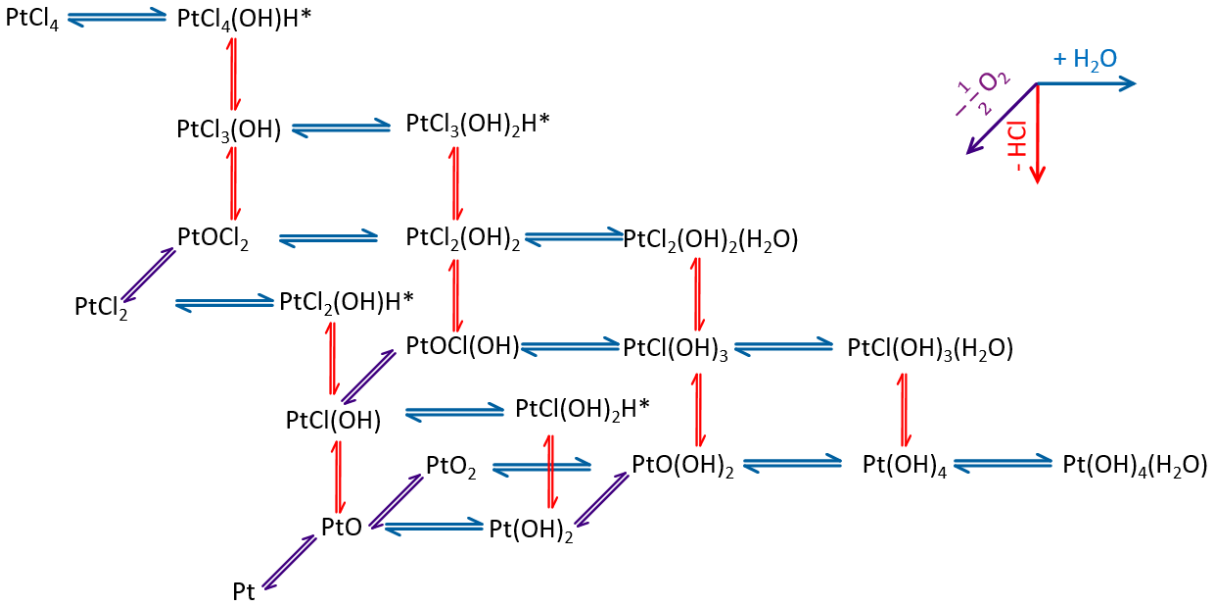

Figure SV-18. Network of species and their link used to describe the stability of $PtCl_2$ under an oxidizing atmosphere.

The pool of species is considered assuming the following reasoning:

The catalysts have been reduced prior to their use, hence, according to our kinetic results, both Pt and $PtCl_2$ can be considered as present on the surface. As H_2O is present on the system because of the oxidation of the methane, ligand exchanges are considered to be possible. At the opposite of what we considered for the calcination step, here we authorize changes in the oxidation degree of the platinum. While we are, as for the calcination, in presence of only one metallic center, we suppose that a methane from the environment might capture half of the O_2.

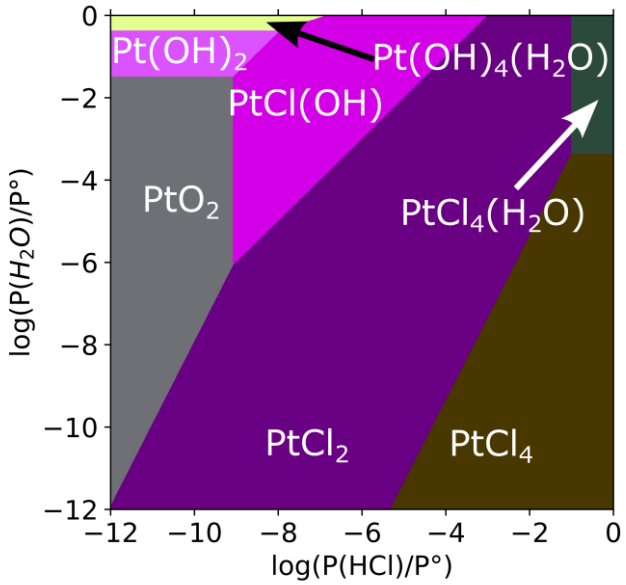

Figure SV-19. Thermodynamic diagrams of the most stable species under oxidizing atmosphere and T = 725 K mimicking Marceau et al.[3] protocol.

As exhibited in **Figure SV-19** if formed during the reduction, $PtCl_2$ remains a stable surface platinum species at 725 K under $P(O_2)$ = 0.21 bar over a wide range of H_2O and HCl pressures.

SI 23. Desorption of Cl on the (100) γ-Al_2O_3 surface.

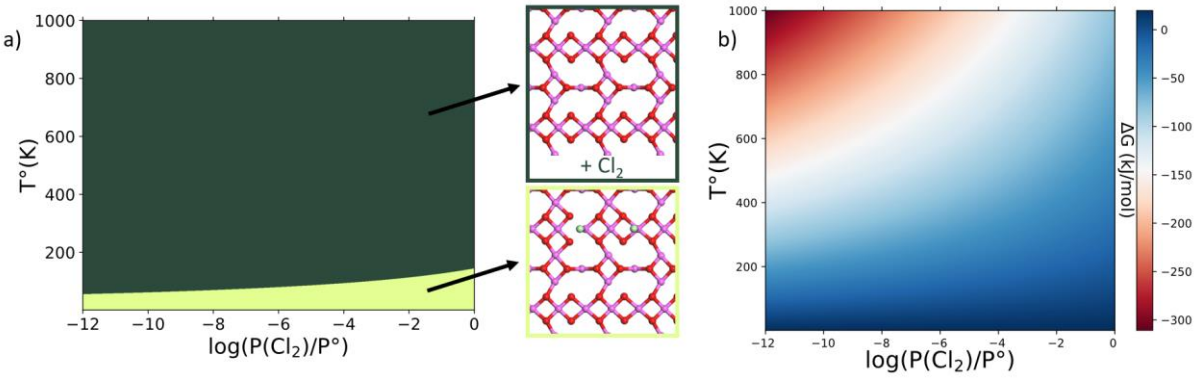

Figure SV-20. a) Thermodynamic diagrams of the state of the (100) surface in presence of chlorine. The chlorinated (100) is considered in yellow, while in green the chlorine is desorbed as Cl_2 and in gas phase. b): Corresponding Gibbs free energy for the desorption of chlorine.

By calculating the Gibbs free energy for the (100) with two chlorine atoms onto it and for the naked (100) with Cl_2 desorbed in gas phase we evaluate the capacity of the (100) to retain the chlorine as a function of the temperature and the Cl_2 pressure. As exhibited by the **Figure SV-20**, no chlorine is expected to stay on the (100), not even at room temperature.

SI References

(1) Hellier, A.; Chizallet, C.; Raybaud, P. PtOxCly(OH)z H2O)n Complexes under Oxidative and Reductive Conditions: Impact of the Level of Theory on Thermodynamic Stabilities. *Chemphyschem* **2023**, *24*, e202200711.

(2) Marceau, E.; Lauron-Pernot, H.; Che, M. Influence of the Metallic Precursor and of the Catalytic Reaction on the Activity and Evolution of Pt(Cl)/δ-Al2O3 Catalysts in the Total Oxidation of Methane. *J. Catal.* **2001**, *197* (2), 394–405.

(3) Marceau, E.; Che, M.; Saint-Just, J.; Tatibouët, J. M. Influence of chlorine ions in Pt/A12O3 catalysts for methane total oxidation. *Catal. Today* **1996**, *29* (1-4), 415–419.

Conclusion and perspectives

This PhD work was carried out with the objective to contribute to the current understanding of the genesis of the active phase of platinum supported on γ-alumina by using an ab initio approach. Indeed, being able to precisely tune the active phase of a catalyst for a specific reaction requires a high level of control and knowledge on its preparation steps from impregnation to activation. Moreover, it might be a key leading to more efficient catalysts. However, because of the highly complex and intricated nature of the chemical phenomena involved in the preparation steps, these steps remain only partially understood at an atomic scale and their tuning often relies on empirical observations. γ-Al_2O_3 supported Pt is a prototypical catalytic system, illustrating well these challenges. Since, it is also a very important system for heterogeneous catalysis, from the laboratory to the industrial scale, we have investigated it during this PhD work. In particular, the nature of Pt intermediates formed as well as the mechanisms involved in the calcination and reduction activation steps are still questioned even if numerous experimental results are available**.** In addition, the role of chlorine added during the preparation of the catalyst, favoring a more dispersed metallic phase, is not clearly explained although this cause-and-effect relationship is known since the pioneering works of Haensel in the 50s'.[1]

Based on the empirical knowledge of these systems, the study of supported single atoms of platinum, with various oxidation states and various ligands such as O^{2-}, Cl^-, OH^-, H_2O or H_2 (dissociated or not in the last two cases), has been undertaken through periodic DFT calculations in order to reveal their evolution under calcination and reduction conditions. A peculiar attention has been devoted to the effect of the chlorine ligand whose impact (beneficial, or not depending on the targeted reaction) on the catalyst's chemical state and on its reactivity is experimentally observed.

This work started with the study of platinum complexes ($[Pt_1O_xCl_y(OH)_z(H_2O)_n]$), built from experimental observations on the Pt/γ-Al_2O_3(-Cl) system, in gas phase. Without the complexity brought by the support, it was possible to get the intrinsic dependence between the platinum complex electronic properties and its coordination sphere. The high stability of the square planar and octahedral geometries as well as the higher affinity of the platinum for chlorine rather than hydroxyls or oxo ligand was established. The impact of a reactive atmosphere as it can be encountered during the calcination and reduction steps of the catalyst was evaluated through the determination of thermodynamic diagrams based on Gibbs free energy calculations. The calculation of the stability of

all species in calcination conditions revealed that three complexes ($PtCl_4$, $PtOCl_2$ and PtO_2) could be expected at high temperature according to the quantity of chlorine (monitored by the HCl partial pressure in our approach) and water present in the system. The calculation of the stability of all species in reduction conditions highlighted that chlorine stabilizes oxidized platinum (+II) through the stabilization of $PtCl_2$. The relatively low number of electrons of these unsupported systems allowed to tackle down the inextricable issue of the choice of the exchange-correlation functional. We benchmarked exchange correlation functionals that are computationally tractable on larger systems, against ACFDT-RPA results. It was shown that for studying platinum complexes stable under calcination conditions, a GGA corrected for dispersive forces such as PBE-dDsC is adapted. However, in the cases where changes in the oxidation degree of the platinum are expected, as it can be encountered in reduction conditions, hybrid functionals and especially HSE06 were found to be a more suitable choice rather than meta-GGAs such as SCAN, TPSS or RTPSS which should be avoided for such reactions.

Secondly, the impact of the γ-alumina support was investigated. For that, Pt(IV) complexes from the gas phase study were adsorbed on the dehydrated (100) surface of a γ-Al_2O_3 to model more realistically the calcination. Through the comparison with the gas phase, the impact of the support on these systems has been deciphered. Most of the $PtO_xCl_y(OH)_z(H_2O)_n$ complexes were found mono-grafted to the same surface site of the γ-Al_2O_3 surface through one Pt-O_{surf} bond with ligands participating to the anchoring of the Pt and only PtO_2 is bi-grafted with the platinum bonded to two oxygens of the alumina surface. Thus, the support modifies the properties and the chemistry of the platinum single atom complexes. The charge analysis revealed that with respect to the gas phase, the surface oxidizes the platinum. Moreover, exchanging hydroxyls for chlorine is easier than in the gas phase because of the stronger nature of the Al-OH-Pt bridging bonds.

The relative stability of these supported Pt(IV) species during calcination was evaluated by the determination of thermodynamic diagrams in which realistic conditions (T, $P(H_2O)$ and P(HCl)) were accounted for. At 800 K, PtO_2 is expected in the absence of chlorine while $PtOCl_2$ and $PtCl_4$ are formed in the presence of chlorine, the latter being favored by a high chlorine loading. At room temperature, octahedral Pt(IV) species ($PtCl_x(OH)_y(H_2O)$) are expected and the impact of P(HCl) is even stronger. Very low amounts of Cl are required to form hydroxy chlorinated $PtCl_x(OH)_y(H_2O)$ from the fully hydroxylated $Pt(OH)_4(H_2O)$ that is expected in the absence of chlorine.

A very good correspondence was found between the structural and electronic properties of these predicted octahedral $PtCl_y(OH)_{4-y}(H_2O)$, stable at room temperature, and XAS results, obtained on Pt/γ-Al_2O_3(Cl) in similar conditions with two different chlorine loadings during a former IFPEN PhD

thesis work.[2] EXAFS fitting results obtained for both chlorine loadings are consistent regarding the Pt coordination number as well as the Pt-Cl or Pt-O distances. The XANES simulation of these calculated octahedral species by using the FDMNES software revealed a specific signature related to the presence of chlorine coordinated to the platinum. The whiteline is shifted toward lower energies and a remarkable bump appears between 11575 eV and 11585 eV whose intensity increases with the number of chlorine atoms present in the Pt coordination sphere. Moreover, fitting the experimental spectra with computed ones allowed a quantification of the $PtCl_y(OH)_z(H_2O)$ speciation.

Finally, the reduction of the $PtO_xCl_y(OH)_z(H_2O)_n(H_2)_m$ for various oxidation numbers ranging from +IV to 0 and supported on the (100) γ-Al_2O_3 surface was modelled both from kinetic and thermodynamic points of view. Similarly, to what was done for calcination, the structural and energetic properties of the most stable complexes were quantified. The stabilizing role of the surface on the undercoordinated complexes was revealed through migration to different surface adsorption sites depending on the number of ligands of Pt. This relation between the adsorption site and coordination number of Pt makes the role of the surface on the platinum chemistry more difficult to be unraveled.

The impact of the reduction temperature as well as the nature of the atmosphere was accounted for by the calculation of the Gibbs free energy of the supported platinum complexes. The reduction in the absence of chlorine is expected to have occurred at room temperature for H_2 pressure superior to 10^{-8} bar. Adding chlorine results in the stabilization of Pt(II) species more resistant to typical H_2 pressure and temperature. Following the benchmark achieved on gas phase systems, thermodynamic diagrams have been determined at the HSE06 level. Compared to the gas phase, the differences between HSE06 and PBE-dDsC results are less pronounced and PBE-dDsC can be considered as a good compromise for simulating alumina supported systems.

The mechanistic description and kinetic barriers involved in the reduction of four Pt(IV) complexes inherited from the calcination thermodynamic diagram (PtO_2, $PtOCl_2$, $Pt(OH)_4$ and $PtCl_4$) highlighted how chlorine could stabilize single atom on the (100) alumina surface. Not only chlorine hardens the reduction by increasing the energy required to overcome the reduction of Pt(IV) into Pt(II) but most importantly it allows the stabilization of $PtCl_2$ at the end of this first reduction step. This highly mobile chlorinated complex can easily migrate into a specific adsorption site of alumina where its reduction will be greatly hardened. In the other hand, any other Pt(II) that might be obtained during the reduction of Pt(IV) was found much more reluctant to undergo the same migration. The potential existence of $PtCl_2$ as post-reduction species resonates directly or indirectly with various experimental

studies. However, its suspected high chemical inertia raises the question of its value and role as a catalyst.

The study of the genesis of an active phase from an ab initio approach such as done during this PhD thesis allowed to gain some insight on the nature of the surface species as well as their evolution during the calcination and reduction steps of their preparation. While these results are relatively promising regarding the use of an approach of this kind, it is necessary to go further along this path to enrich our understanding of the catalyst preparation.

As short-term perspectives, we can propose that a similar DFT mechanistic study of the hydration and ligand exchange reactions could be addressed to complete the thermodynamic description of the calcination step done in this work, by a kinetic perspective. This might help getting further insights on the relation between the calcination condition and the obtained species that will be reduced. This part is currently being investigated, but the results are not consolidated enough to be reported in the present manuscript.

On a longer term, feeding a multi-scale model (such as kinetic Monte Carlo or microkinetic model for example) with the energies of intermediates, and with activation barriers found during this work could be proposed to allow the simulation of the evolution of both nature and surface concentration of the platinum single atom during the calcination and reduction as a function of time.

On a broader timescale, it will be highly instructive to carry the same approach used in this work on the other surfaces and edges of the γ-Al_2O_3. Numerous atomistic models of relevant faces and edges of the γ-Al_2O_3 have already been developed[3,4] and would help getting a deeper understanding of the experimental observations during the calcination and reduction of these catalysts. The adsorption sites present on the hydrated sites of (110) alumina surfaces and of edges might reveal different behavior of platinum complexes, that cannot be grasped by considering the (100) surface only.

The aggregation of the platinum species especially during the reduction would also be an interesting complement to this work which was mostly devoted to single atoms. However such work would require to get relevant intermediates for complexes with stoichiometry such as $Pt_nO_XCl_Y(OH)_Z(H_2O)_N(H_2)_M$. The exploration of the potential energy surface of such species could require the use of more sophisticated theoretical methods as chemical intuition might not be enough for such complicated structures. Thus, two consequential projects lie behind the Pt aggregation problem: the search for relevant supported intermediates and then the description of the growth mechanisms linking the SA studied in this part to $Pt_nO_XCl_Y(OH)_Z(H_2O)_N(H_2)_M$ clusters.

To complete this work, one could investigate the impact of metallic dopants (Sn, Re) that are used industrially against coke or to promote specific reactions.[5] For example, by using a similar approach as the one used here, it would be interesting to see how the Sn precursors (typically, $SnCl_4$) evolve during calcination and reduction. Similar questions to the ones asked during this work could be investigated, knowing that experimentally, Sn(II) and Sn(IV) usually co-exist with Sn(0) on the final catalysts.[6–8] What are the preferred adsorption sites of the γ-Al_2O_3 and how do they coexist with the Pt SA? How does their oxidation degree and coordination sphere evolve during calcination and reduction, and finally how adding a new species impact the structure and properties of platinum species?

At last, even if that deviates more significantly from the original framework of this work which is related to the genesis of the active phase, the reactivity of the supported single atom of platinum on the γ-Al_2O_3 could be the subject of an investigation. As a direct consequence of this work, the elucidation of the reactivity of the $PtCl_2$ species, that appears to be a potential candidate among the platinum species obtained after reduction could be suggested for future studies.

References

1. V. Haensel. *Alumina-Platinum-Halogen Catalyst And Preparation Thereof. U.S. Patent 2,479,109* (1949).
2. Ana Teresa Fialho Batista. Atomic scale insight into platinum based catalysts supported on chlorinated gamma-alumina. PhD thesis, 2016-2019.
3. Pigeon, T., Chizallet, C. & Raybaud, P. Revisiting γ-alumina surface models through the topotactic transformation of boehmite surfaces. *J. Catal.* **405,** 140–151 (2022).
4. Batista, A. T. *et al.* Beyond γ-Al2O3 crystallite surfaces: The hidden features of edges revealed by solid-state 1H NMR and DFT calculations. *J. Catal.* **378,** 140–143 (2019).
5. Antos, G. J. & Aitani, A. M. (eds.). *Catalytic naphtha reforming.* 2nd ed. (Marcel Dekker, New York, 2004).
6. Gorczyca, A., Raybaud, P., Moizan, V., Joly, Y. & Chizallet, C. Atomistic Models for Highly-Dispersed PtSn/γ-Al 2 O 3 Catalysts: Ductility and Dilution Affect the Affinity for Hydrogen. *ChemCatChem* **11,** 3941–3951 (2019).
7. Audo, C., Lambert, J. F., Che, M. & Didillon, B. Synthesis of platinum–tin/alumina reforming catalysts from a well-defined platinum–tin precursor complex. *Catal. Today* **65,** 157–162 (2001).
8. Jahel, A. N. *et al.* Effect of Indium Doping of γ-Alumina on the Stabilization of PtSn Alloyed Clusters Prepared by Surface Organostannic Chemistry. *J. Phys. Chem. C* **116,** 10073–10083 (2012).